Numerical and experimental studies of two-phase flows interacting with a bundle of tubes

Clément Bazin

To cite this version:

Clément Bazin. Numerical and experimental studies of two-phase flows interacting with a bundle of tubes. Fluid mechanics [physics.class-ph]. Institut Polytechnique de Paris, 2023. English. NNT : 2023IPPAX106 . tel-04496140

HAL Id: tel-04496140
https://theses.hal.science/tel-04496140v1
Submitted on 8 Mar 2024

INSTITUT
POLYTECHNIQUE
DE PARIS

NNT : 2023IPPAX106

Thèse de doctorat

Numerical and experimental studies of two-phase flows interacting with a bundle of tubes

Thèse de doctorat de l'Institut Polytechnique de Paris
préparée à l'École polytechnique

École doctorale n°626 École doctorale de l'Institut Polytechnique de Paris (EDIPP)
Spécialité de doctorat : Ingénerie mécanique et énergétique

Thèse présentée et soutenue à Gif-sur-Yvette, le 21 décembre 2023, par

Clément BAZIN

Composition du Jury :

Olivier Doaré Professeur, ENSTA Paris	Président du jury
Eric Goncalves Professeur, ISAE-ENSMA, Université de Poitiers	Rapporteur
Hélène Mathis Professeure, Université de Montpellier	Rapporteur
Guillaume Bois Ingénieur de recherches, CEA, Université Paris-Saclay	Examinateur
Sergio Chibbaro Professeur, Université Paris-Saclay	Examinateur
Gloria Faccanoni Maîtresse de conférence, Université de Toulon	Examinatrice
Christophe Josserand Directeur de recherches, CNRS, l'Ecole polytechnique	Directeur de thèse
Maria Giovanna Rodio Ingénieur de recherches, CEA, Université Paris-Saclay	Encadrante
Romain Lagrange Ingénieur de recherches, CEA, Université Paris-Saclay	Invité - encadrant

Acknowledgements

En premier lieu, je souhaite exprimer ma profonde gratitude envers Hélène Mathis et Eric Goncalves pour avoir accepté la responsabilité de rapporteurs de cette thèse. Mes remerciements vont également à Sergio Chibbaro, Gloria Faccanoni, et Guillaume Bois pour leur précieuse participation en tant que membres de mon jury, et à Olivier Doaré pour avoir présidé ma soutenance. Je tiens à exprimer ma reconnaissance envers l'ensemble du jury pour leurs questions judicieuses et leurs commentaires constructifs qui ont grandement contribué à l'enrichissement de mon travail de recherche. Mes remerciements vont également à Maria-Giovanna et Romain, mes encadrants au CEA, ainsi qu'à Christophe, mon directeur de thèse, pour leur implication et leurs conseils. Je souhaite adresser une gratitude particulière à Giovanna pour ses encouragements constants et sa bienveillance au cours de ces trois années.

Je tiens à exprimer ma reconnaissance envers mes collègues du LMSF, dont les échanges et le partage ont grandement enrichi mon expérience en thèse et permettent d'avoir une ambiance de travail exceptionnelle. Je tiens à remercier particulièrement Nikos pour sa gentillesse et les jeux de rôles qui permettent de vraies pauses hors thèse le midi. Merci à Julie pour son humour et sa gentillesse qui permettent de s'épanouir au labo. Merci à mon co-bureau de toujours Andrew de me supporter depuis 2020 et pour j'espère encore longtemps ! Merci à l'ancienne promo COVID de stagiaires du LMSF, Gabibi, Paupau et Mathis d'avoir été là et d'avoir ensoleillé avec humour mes journées au cours de cette thèse. Merci aux thésard de la zone *51, en particulier Nathalie, Téo, Jiayi, Loïc, Matthieu, Sanae, Antonin et Capucine pour l'ambiance au labo, les soirées, les bars et leur bonne humeur.

Mes pensées vont également à toutes les personnes qui ont participé de près ou de loin à ce projet de recherche, que ce soit par des discussions stimulantes, des collaborations fructueuses ou des conseils précieux.

Merci à tous mes amis de m'avoir permis de souffler en dehors de la thèse. Je pense à mes amis de longue date Manon, Elodie, Léa, Laura, Sarah, Julia et toutes les personnes dont le prénom fini par « a », pour toujours ensoleiller mes fin de semaines, mes vacances, ma vie et j'espère pour encore longtemps. Je remercie également mes amis de l'ENSMA, Benja, Baptiste, Marine, Damien, Benoit, Clarisse et Robin. En particulier Clarisse pour les soirées films nuls et émissions télé sans retenue. Un grand merci à l'homme pub, grosse DIVA, rageux de première, expert du air-contrebasse de m'avoir supporté pendant 3 ans. Je n'ai aucun doute que tout roulera pour toi en Allemagne.

Pour terminer, un immense merci à ma famille, mes parents et ma sœur d'être toujours là pour me soutenir et m'encourager. Mais heureusement pour vous c'est bon j'arrête les études, promis, je travaille maintenant !

Contents

Nomenclature

List of acronyms

$CATHARE$	Code for Analysis of THermalhydraulics during Accident of Reactor and safety Evaluation
CEA	Commisariat à l'Energie Atomique
CFD	Computational Fluid Dynamics
DNS	Direct Numerical Simulations
$EBRSM$	Elliptic Blending-Reynolds Stress Model
FSI	Fluid-Stucture Interaction
$GEMMA$	GEeneralized Multifluid Modelling Approach
$GENTOP$	GENeralized TwO-Phase flow concept
GV	Générateur de vapeur
$HD-LIS$	Hybrid Dispersed-Large Interface Solver
$i-MUSIG$	inhomogeneous-MUltiple SIze Group
$IATE$	Interfacial Area Transport Equation
$IRIS$	International Reactor Innovative and Secure
$IRSN$	Institut de Radioprotection et de Surêté Nucléaire
LBM	Lattice-Boltzmann Method
LES	Large Eddy Simulations
LIM	Large Interface Model
Mom	Method of Momentums
PSD	Power Spectral Density
PWR	Pressurized Water Reactor
$RANS$	Reynolds Average Navier-Stokes

RC	Random Collisions
SG	Steam Generator
SI	Surface Instability
SO	Shearing-off
TI	Turbulent Impacts
$TRACE$	Transient Reactor Analysis Code
$TRITON$	Two-phase RegIme TransitiON
VK	Von Karman
WE	Wake Entrainment

List of math symbols

Δ	Difference between phases
i	Imaginary unit
∂	Partial difference
$\underline{\underline{I}}$	Identity matrix

List of physics constants and variables

α	Void fraction
β_1	Ratio between Lagrangian time and Eulerian time
β_Q	Volumetric quality
χ	Bubble aspect ratio
χ^{phase}	Tracker
χ_e	Bubble aspect ratio for high Weber number
χ_r	Bubble aspect ratio for low Weber number
$\ddot{x}$	Modal acceleration
$\dot{m}$	Mass flow rate
$\dot{Q}$	Volumetric flow rate
$\dot{q}$	Body heating
$\dot{x}$	Modal velocity
η^{inter}	Intergroup mass source term
η_r	Ratio between turbulence characteristic time and Drag characteristic time
$\mathbf{\Omega}$	Velocity curl

$\mathbf{F}_{l->g}^{D}$	Dispersed drag force
$\mathbf{F}_{l->g}^{L}$	Dispersed lift force
$\mathbf{F}_{l->g}^{T}$	Turbulent dispersion force
$\mathbf{F}_{l->g}^{WL}$	Wall Lubrication force
$\mathbf{F}_{l->g}^{WR}$	Wall repulsion force
$\mathbf{M}^{k}$	Interfacial model
$\mathbf{n}_{w}$	Wall normal
$\mathbf{v}$	Velocity
μ	Dynamic viscosity
ν	Kinematic viscosity
ϕ	Field
$\psi^{intergroup}$	Intergroup source term in IATE equation
$\psi^{internal}$	Internal source term in IATE equation
ρ	Density
σ	Suface tension
τ_{b}	Bubble relaxation time
$\underline{\underline{\tau}}^{T}$	Turbulent stress tensor
$\underline{\underline{\tau}}$	Shear stress tensor
$\underline{\underline{R}}$	Reynolds stress tensor
$\underline{\underline{T}}$	Stress Tensor
ξ_{d}	External parameter in Boltzmann equation
A_{i}	Particle surface area
a_{i}	Interfacial area concentration
A_{s}	Cross-sectional area
b	Ratio of inertia coeffient between liquid and gas
C_{W}^{*}	Wall lubrification coefficient
C_{L}^{S}	Spherical bubble Lift coefficient
C_{L}^{SH}	Spherical bubble contribution high-Reynolds Lift coefficient
C_{L}^{SL}	Spherical bubble contribution low-Reynolds Lift coefficient
C_{0}	Kolmogorov constant

C_D	Drag coefficient
C_f	Fluid damping coefficient
C_L	Lift coefficient
C_s	Structure damping coefficient vaccum
C_{AM}	Added Mass coefficient
D	Diameter
D_{sm}	Sauter Mean Diameter
e	Internal Energy
Eo	Eötvös
F^D	Interfacial Drag force
F^f	Interfacial friction force
f_0	Characteristic vibration frequency
f_d	Distribution in Boltzmann equation
f_f	Flow frequency
$F_{coupling}$	Fluid coupling force
F_{Random}	Random excitation force
Fr	Modified Froude number
g	Gravity
GTD	Generalized turbulent dispersion coefficient
h	Enthalpy
I	Interfacial source term
j	Superficial velocity
k	Turbulent kinetic energy
K_f	Fluid rigidity coefficient
K_s	Structure rigidity coefficient vaccum
m	Mass
M_f	Fluid mass coefficient
M_s	Structure mass coefficient in vaccum
N	Modeling in turbulence model
P	Pressure

p	Fluctuating pressure
p	Kinematic viscosity
q	Heat flux
Re	Reynolds number
Sr	Shear rate
St	Strouhal number
Sto	Stokes number
t	Time
U	Flow mean velocity
u	Flow fluctuating velocity
V	Volume
V_Ω	Control volume
V_r	Reduced velocity
We	Weber number
X	Spatial frame
x	Modal displacement
y_w	Wall distance

List of subscripts and superscript

$\overline{\overline{X}}$	Ensemble average in proper volume
$\overline{X}$	Ensemble average in volume
$\tilde{X}$	Favre average
X'	Fluctuation
X^t	Transpose
X''	Fluctuation in Favre averaging
X_a	Interface
X_g	Gas
X_k	Phase k
X_l	Liquid
X_m	Mix quantity
X_{bm}	Bubble-liquid mix

X_b	Bubble
X_{cap}	Cap bubble
X_c	Critical
X_{dm}	Droplet-gas mix
$X_{ellipse}$	Distorted bubble
X_{g1}	IATE 1st gas group
X_{g2}	IATE 2nd gas group
X_{gc}	Continuous gas
X_{gd}	Dispersed gas
X_H	Hydraulic
X_{lc}	Continuous liquid
X_{ld}	Dispersed liquid
X_{max}	Maximum

List of Figures

List of Tables

Chapter 1

Introduction

Summary

This chapter provides an introduction to the physical problem addressed in this thesis and the associated issues.

The first section focuses on the general industrial issue that led to the thesis's open questions. It includes a description of a steam generator and the vibrational risks encountered, as well as the industrial tools used to apprehend and predict these phenomena.

The second section deals with the experimental study of flows similar to those in steam generators. The first part presents the current understanding of flow regimes and their interaction with a cylinder in academic cases. The second part explores the understanding of flows in industrial configurations.

The third section addresses numerical physical modeling for the description of flows in steam generators. The first part provides a brief overview of models one can found in the literature and their limitations regarding our study, while the second part presents the model developed at CEA and its limitations.

The final section outlines the challenges in reproducing multiphase flows for fluid-structure interaction. It raises questions about modeling and introduces essential modeling components for accurately replicating these flows.

General introduction

The flows studied in this thesis lie at the intersection of two major fields within fluid mechanics: multiphase and turbulence. Multiphase focuses on the interaction between two phases, often a liquid and a gas or a gas and solid particles, while turbulence aims to study the dynamics of a fluid when its velocity is high enough to exhibit a wide range of fluid scales. When considered separately, both of these areas present numerous open questions and are characterized by high complexity.

The interaction between multiphase flows and turbulence, especially in the presence of walls, remains far from being a fully understood domain. Indeed, there exists a wide collection of complex dynamic and thermodynamic phenomena that can lead to the development or disappearance and movement of drops, bubbles, or spray. These flows are encountered both in nature, through phenomena like particle dispersion in the atmosphere or bubbles in ocean currents, and in industrial applications such as steam production for energy generation or combustion in rocket engines.

Thus, understanding and modeling turbulent multiphase flows present a significant challenge due to the variability and complexity of the encountered structures. It becomes necessary to take into account property discontinuities between the fluids, interactions between the phases, the forces acting between these phases and their topology, among other factors. This complexity then translates into the systems of equations to be solved, which are often non-linear and involve numerous equations in order to predict their behavior accurately.

The wonder of fluid mechanics lies precisely in these recurring phenomena in nature and industry, which seem so simple to us because they are easily observable but are incredibly challenging to describe using our mathematical tools. An essential part of understanding flows thus involves finding similarities between phenomena that may be closely related, but on a slightly different system or on a reduced scale. In this chapter, we will attempt to present an easily observable phenomenon that we try to replicate using similarities or reduced scales in an effort to better understand it. Ultimately, this will help us understand the challenges associated with its modeling.

1.1 The primary circuit failure accident in steam generators

1.1.1 Flow induced vibrations in steam generators

Pressurized Water Reactors (PWRs) are a type of nuclear power plant that uses water as coolant and neutron moderator. They are composed of a primary circuit, a secondary circuit, and a cooling circuit as presented in Figure 1.1.

The primary circuit is a closed system that operates water under high pressure (about 155 bar) to transfer heat generated by the nuclear reaction in the reactor to the secondary circuit. The water in the primary circuit is heated to a temperature of around 300 °C and high pressure to keep it in a liquid state. This closed circuit also acts as a barrier to prevent the spread of radioactive materials. The secondary circuit uses a Steam Generator (SG) to recover heat from the primary circuit and turn it into steam, which is then used to drive a turbine to generate electricity. The steam is produced at a pressure of 50-80 bar. After passing through the turbine, the steam is condensed in the cooling circuit using water from a cold source, such as a river or the ocean. This water is either returned to the source at a slightly higher temperature or cooled in an air cooler and re-injected into the cooling circuit. PWRs typically have two to four SGs

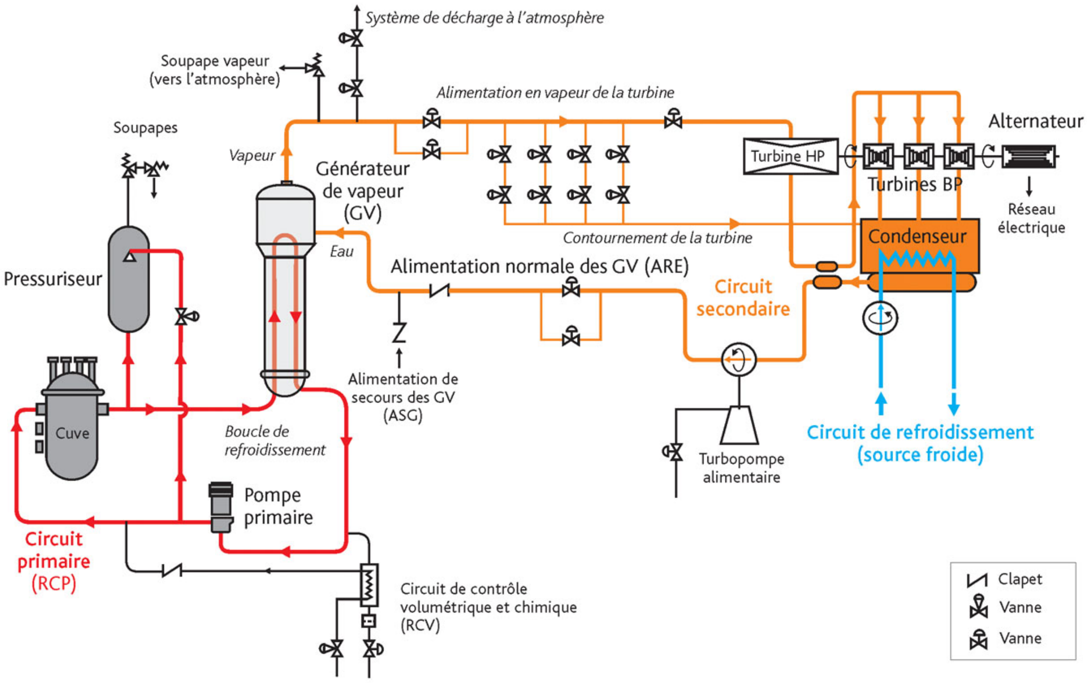

Figure 1.1: Main components of the primary and secondary circuits of a nuclear reactor. In red the primary circuit, in orange the secondary circuit and in blue the cooling circuit. The steam generator is translated by Générateur de vapeur (GV). From Georges Goué/Médiathèque IRSN via IRSN website.

(GV in Figure 1.1), which are large, circular chambers containing thousands of tubes (inverted U-shaped tubes called tubular beams) that carry water from the primary circuit. These tubes are about 20 mm in diameter and 10m high, and are held in place by spacer plates and anti-vibration bars , as presented in Figure 1.2. The curved portion of the tubes, located at the top of the SG, has a maximum radius of curvature of 1.5 m. As the water passes through the tubes and spacer plates, it gradually turns into steam as presented in Figure 1.2.

A monitoring system is in place to detect any leaks between the primary and secondary circuits through the tubes. This helps prevent contamination of the secondary circuit and prevents SG tube rupture accidents. In the event of an accident, the difference in pressure between the primary and secondary circuits can cause a spill of contaminated water and steam, which can escape as steam. To prevent further damage, it is important to isolate the SG from the rest of the system.

The phenomenon of rupture is caused by the repeated vibrations and stresses on the structures over large cycles due to the two-phase flow. These types of accidents are rare, can have various causes, and are generally not dangerous. They tend to occur in the top cross-flow part of the SG, where the tubes are horizontal and the void fraction (the proportion of the volume occupied by the vapor) is high. However, they can still require an extended shutdown of the SG to repair it. For example, in 1991, a leakage accident at the Mihama Power Plant in Japan led to a shutdown of the SG for two years. The accident was caused by misaligned vibration bars. To prevent such accidents, SG tubes are regularly inspected during scheduled shutdowns to check for wear and damage. If the condition of the materials is not sufficient, the SG may need to be replaced through a series of heavy operations. According to the French Institute

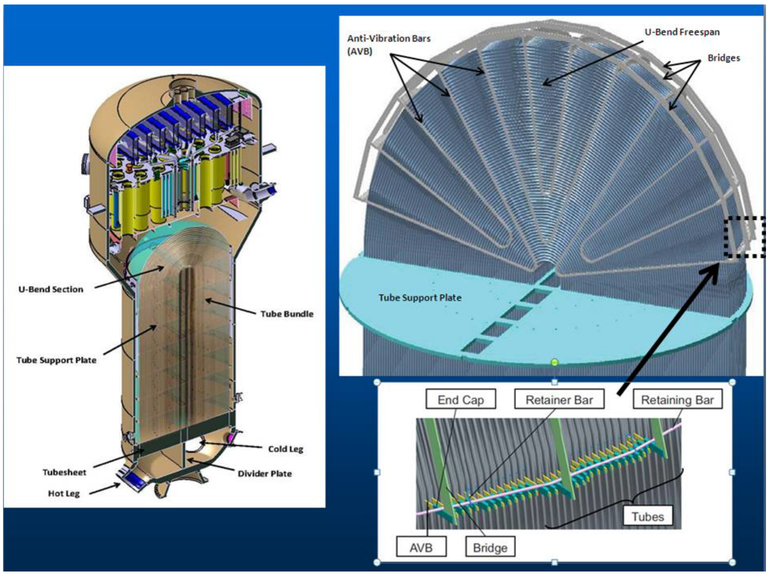

Figure 1.2: Scheme of a steam generator. From US Nuclear Regulatory Commision (NRC) website.

of Radiation Protection and Nuclear Safety (IRSN), 18 replacements were carried out between 1990 and 2010, or about one per year. In 2008, the Fessenheim Reactor No. 2 in Alsace, France experienced a leak from the primary circuit to the secondary circuit. This led to a shutdown of the reactor. The leak was caused by a crack at the beginning of the SG U-tube curvature, which was determined to be the result of fatigue due to excessive vibration. This vibration was traced back to the non-uniform installation of the anti-vibration bars during the construction of the Fessenheim reactor in 1978. It is then critical to understand what kind of phenomenon can lead to such excessive vibrations leading to the rupture of the tubes. Some clues can be found studying single phase flows.

Another configuration where this phenomenon could occur is the design of new modular architectures. These more compact designs have the potential to lead to the exploration of novel configurations, such as IRIS (International Reactor Innovative and Secure)[7] presented in Figure 1.3 or the one proposed in Korea presented in Figure 1.4, which feature a helical arrangement of tubes of the primary circuit in the SG. Tubes can be installed in triangular and square configurations or any combination of the previous configuration. This design are intended to enhance heat transfer between the primary and secondary circuits. Six to eight of these SGs can be installed between the core support body and the reactor pressure vessel.

1.1.2 Modeling the vibrations of tubes in steam generators

The U-bend tubes at the top of the SG are subjected to an upward flow of steam and water with a high void fraction. These tubes are exposed to random forces caused by turbulence and intermittent impacts from bubbles or gas pockets. There are two types of fluid-structure interactions that can occur in this situation:

- When the forces acting on the tubes are not coupled to the motion of the tube. The problem can be separated into a fluid mechanical problem and a structural problem. In

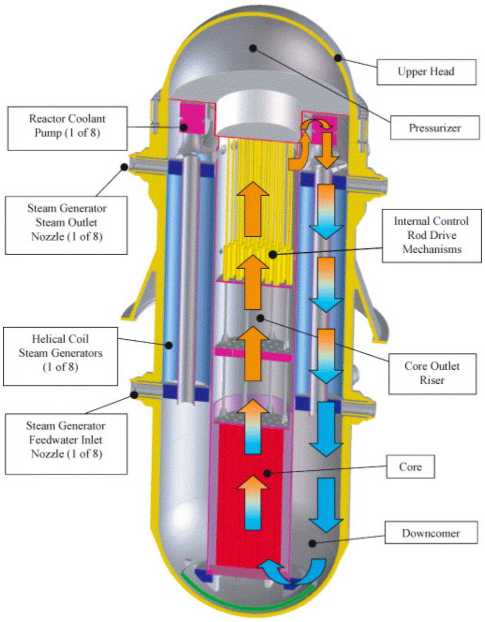

Figure 1.3: Internals of the International Reactor Innovative and Secure (IRIS). From [7].

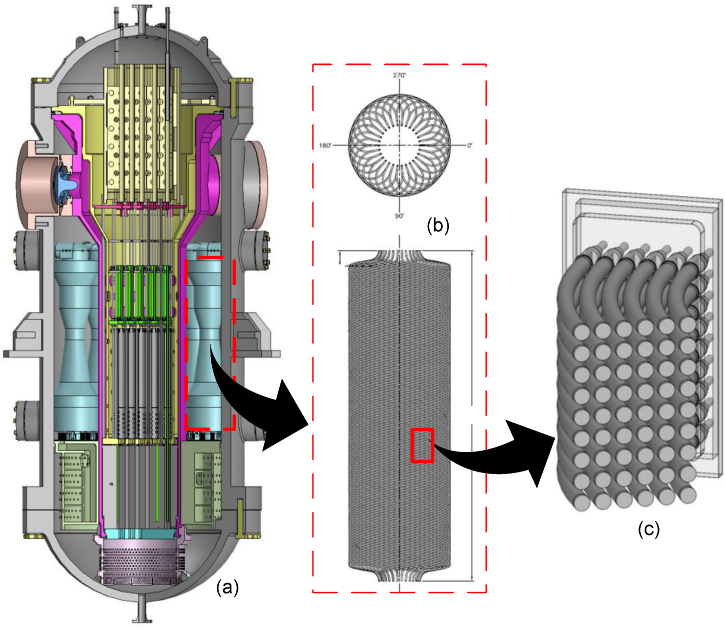

Figure 1.4: Scheme of a modular Korean reactor(a) showing the helical coiled steam generator tubing(b) and the sectional tube array (c) from [66].

two-phase flow, this interaction can be caused by turbulence and the intermittent presence of bubbles or gas pockets. Random excitations due to turbulence are called Turbulence Induced Vibrations.

- When the forces acting on the tubes are coupled to the tube motion. This can be seen as the fluid adapting its motion to the motion of the tubes. This phenomenon can lead to instabilities. Because of the strong amplitudes at stack, the coupling between the fluid and the structure can be dangerous as presented in Figure 1.5.

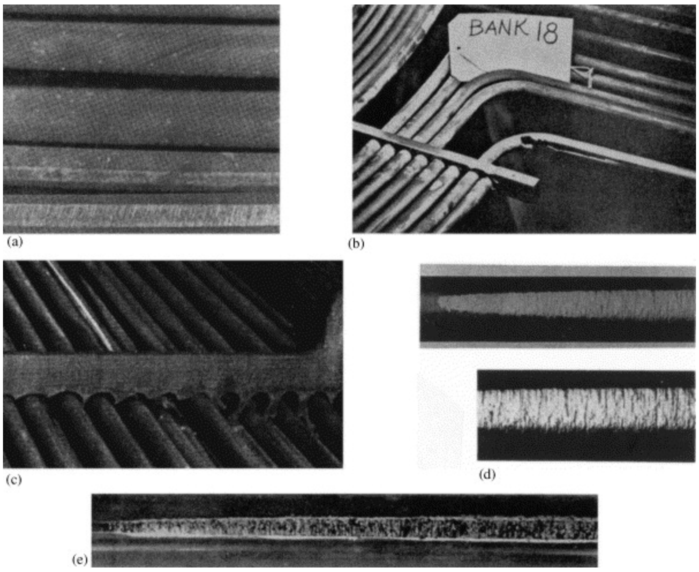

Figure 1.5: Examples of damage of tube arrays from SG due to fluidelastic instability. From [93].

The modeling of the mechanical loading exerted by the flow on a flexible tube is predicated on the hypothesis that the fluid force can be separated into two distinct phenomena : a random excitation and a coupling phenomenon. The random excitation is modeled as a fluid force F_{Random} independent of the tube motion. It is related to the turbulent fluctuations generated by the flow through the bundle. The increase of flow velocity leads to a linear growth of the vibratory amplitude of the structure. The coupling phenomenon is modeled as a fluid force $F_{coupling}$ that depends on the modal displacement x, velocity $\dot{x}$ and acceleration $\ddot{x}$, as follows :

$$F_{coupling}(\ddot{x},\dot{x},x,t) = -\underbrace{M_f\ddot{x}(t)}_{Inertia} - \underbrace{C_f\dot{x}(t)}_{Damping} - \underbrace{K_f x(t)}_{Stiffness}, \tag{1.1}$$

with M_f, C_f and K_f respectively the added mass, damping and rigidity coefficients that depend on the flow velocity.

The modal displacement x is then assumed to satisfy the following equation of motion :

$$\underbrace{M_s\ddot{x}(t)}_{Inertia} + \underbrace{C_s\dot{x}(t)}_{Damping} + \underbrace{K_s x(t)}_{Stiffness} = \underbrace{F_{coupling}(\ddot{x},\dot{x},x,t)}_{Coupling\ force} + \underbrace{F_{Random}}_{Random\ excitation}, \tag{1.2}$$

with M_s, C_s and K_s respectively the mass, damping and rigidity coefficients in vacuum.

As depicted in Figure 1.6, for a critical flow velocity V_c, the total damping $C_f + C_s$ of the system becomes zero, resulting in a fluid-elastic instability that manifests as an exponential growth of the vibration amplitude. This velocity can be studied through the reduced velocity V_r, a dimensionless number that represents the ratio between the flow velocity and a characteristic vibration velocity of the tube. It is defined as $V_r = \frac{U}{f_0 D}$, where U is the flow velocity, D is the diameter of the tube, and f_0 is a characteristic vibration frequency. It can also be seen as the ratio between the inertia associated with the flow and the flexibility of the tube.

Fluid-elastic instability can lead to wear and even rapid rupture of SG tubes. However, this instability does not allow us to predict the phenomenon of tube fatigue that emerges over much

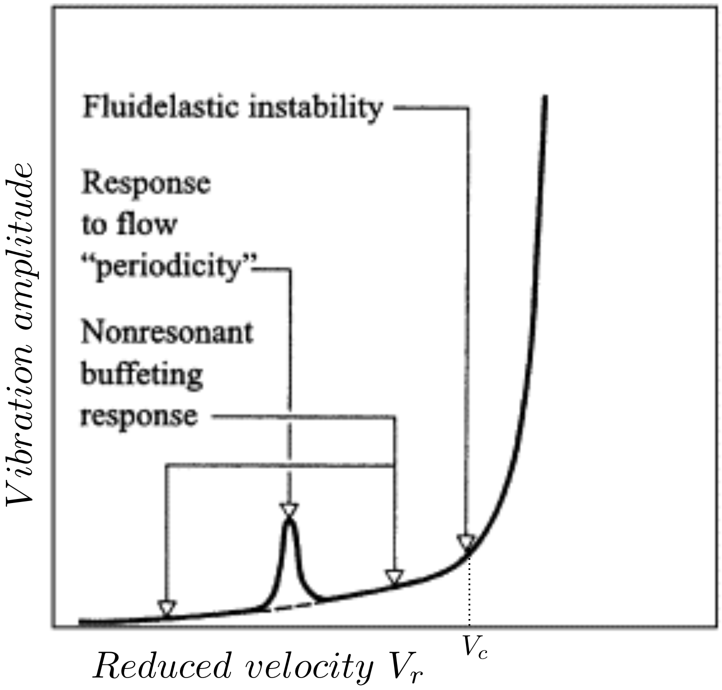

Figure 1.6: Idealized response according to the reduced velocity of a structure in cross-flow. Adapted from [93].

longer periods of time. To do this, the computation of the general system response with all the terms by time integration is necessary. The complexity arises from the random nature of the excitation caused by flow fluctuations, which makes it challenging to analyze the system's temporal behavior directly.

A deterministic signal is characterized by its amplitude and frequency, following a known mathematical law with respect to time. The knowledge of this law enables a definite and unique determination of the signal at any given time. In contrast, a random signal can result in various outcomes within a given time interval, and it can only be described using mean values derived from probability density functions. Since these functions are often unknown in practice, statistical analyses rely on sets of means. However, for a stationary random signal, a powerful tool known as spectral analysis can be applied. Spectral analysis allows the identification of the frequency content existing in the signal. It involves a study into Fourier's space. This allows the signal to be analyzed in terms of energy distribution across different frequency bands. This analysis of a signal's frequency content is referred to as its spectrum. In the context of studying forces, we focus on the Power Spectral Density (PSD, see section 2.4.1), which quantifies the variance of power within the examined physical process and is expressed in units of N^2/Hz. Figure 1.7 is an example of a force spectrum applied to a cylinder in a tubular beam.

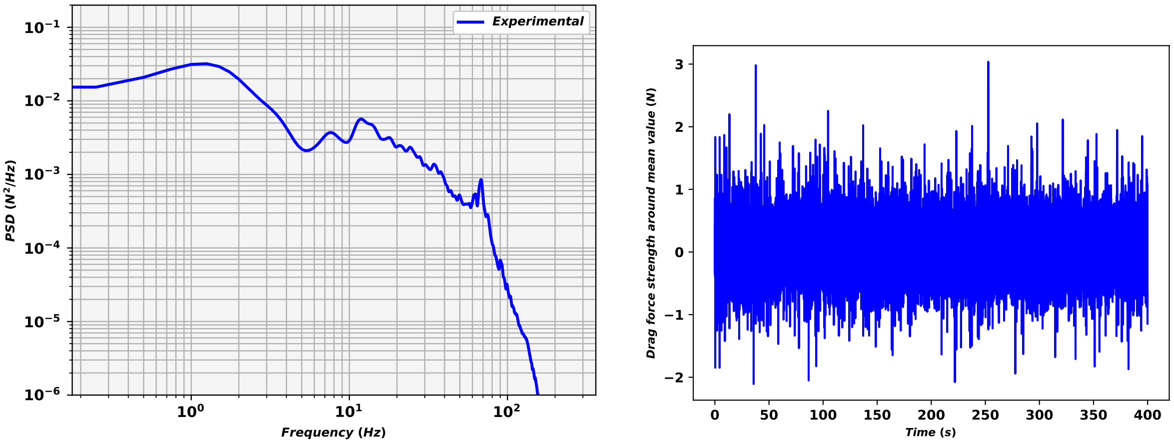

Figure 1.7: Example of power spectral density (left) of the drag force signal (right) exerted on a tube of a tubular beam.

Two-phase flows are notably different from single-phase flows due to the diverse hydrodynamic regimes they create. The combination of physical properties from the different fluids and flow characteristics within the two-phase fluid can result in various spatial distributions between phases, corresponding to different flow regimes. To conduct a precise analysis of FSI in two-phase flow, it becomes crucial to take into account these distinct flow regimes.

1.2 Understanding phenomena in steam generators through experiments

1.2.1 Topology of two-phase flows in experiments

In order to understand the physical processes that can happen in a SG, it is important to identify the topology of the flow, called flow regime. A flow regime is a specific pattern of fluid behavior within a two-phase flow system, characterized by the distribution and properties of the phases. These regimes can be classified into three main categories:

- Separated flows are characterized by isolated phases, such as film flow on a plate, annular flow in a pipe, jet flow, or stratified flow.
- Dispersed flows operate with numerous individual bubbles of various types, such as bubbly flow with small, spherical or distorted bubbles.
- Transitional (or intermittent) flows can be depicted as the transition between separated and dispersed flows, and can include slug flow with merging bubbles to form large cylindrical gas regions, cap-bubbly flow with cap-shaped bubbles, or churn-bubbly flow with erratic shape bubbles.

It is important to note that two-phase flow behavior is highly dependent on system geometry, bubble topology, bubble distribution, and flow conditions, making it difficult to create a universal map of flow regimes. However, this classification system provides a general understanding of the different types of flow patterns that can occur in two-phase systems.

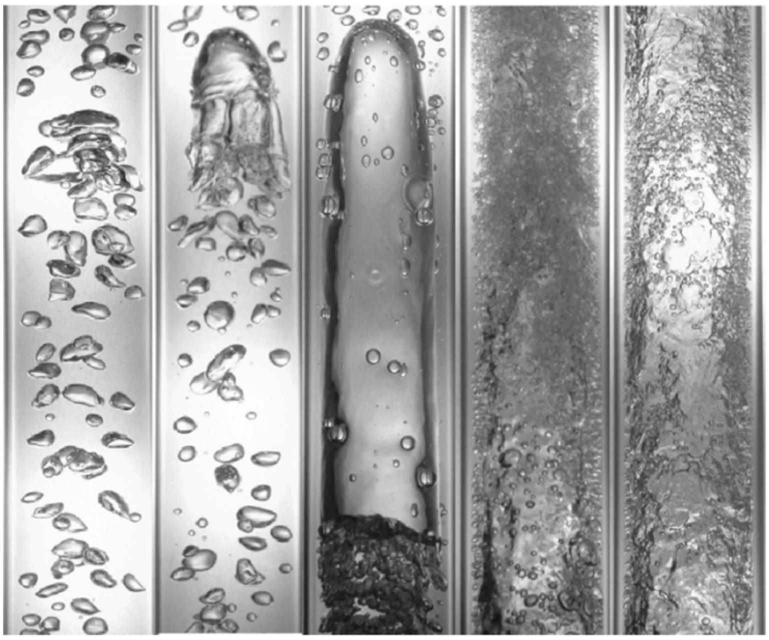

Figure 1.8: Images observed in a vertical 25.4 mm diameter pipe for different regimes. From left to right bubbly (dispersed), cap-bubbly (transitional), slug (transitional), churn-turbulent (transitional) and annular flows (separated). From [85].

In a SG various flow regimes occur, ranging from bubbly flow (dispersed) in the lower portion to separated flow in the upper portion, with intermittent regimes (such as cap and slug flow) in the middle. To study those regimes crossing the tubular beam of the SG, experimental platforms of tube bundles were developed. K.Mao and T.Hibiki [79] proposed a flow regime map for cross-flow tube bundles based on 8 experimental studies found in the literature, gathering parallel triangular, normal square and normal triangular configurations with various gaps and tube diameters. Figure 1.9 presents [79]'s map. The classification is based on the 5 following categories, as presented in Figure 1.8: bubbly flow, cap bubbly flow, churn flow and annular flow.

The bubbly flow is characterized by a continuous liquid phase with dispersed small gas bubbles (smaller than the tube spacing). It is observed for low superficial gas velocities (flow rate of gas over cross-sectional area, often denoted as j_g) but a wide range of superficial liquid velocities (flow rate of liquid over cross-sectional area, often denoted as j_l). The finely dispersed bubbly flow is characterized by a highly turbulent flow with small bubbles prevented from coalescing and large ones breaking-up. It is observed for high superficial liquid velocities and intermediate superficial gas velocities.

The cap bubbly flow is a bubbly flow with cap bubbles that can be larger than the tube spacing. It is observed for intermediate superficial gas velocities and low/intermediate superficial liquid velocities. Actually, the rise of gas flow rate impulses the coalescence of smaller bubbles whereas moderate liquid flow rate doesn't induce high intensity turbulence that could break large bubbles.

The churn flow is characterized by a chaotic mixture of liquid and gas driven by gravitational effects. It is observed for intermediate superficial velocities of both gas and liquid. It can be noticed that downward movements can happen for short periods.

The annular flow is characterized by continuous gas with liquid droplets in the core of the tube bundle and continuous liquid films over walls and tubes. It is observed for reduced liquid superficial velocities and high gas superficial velocities.

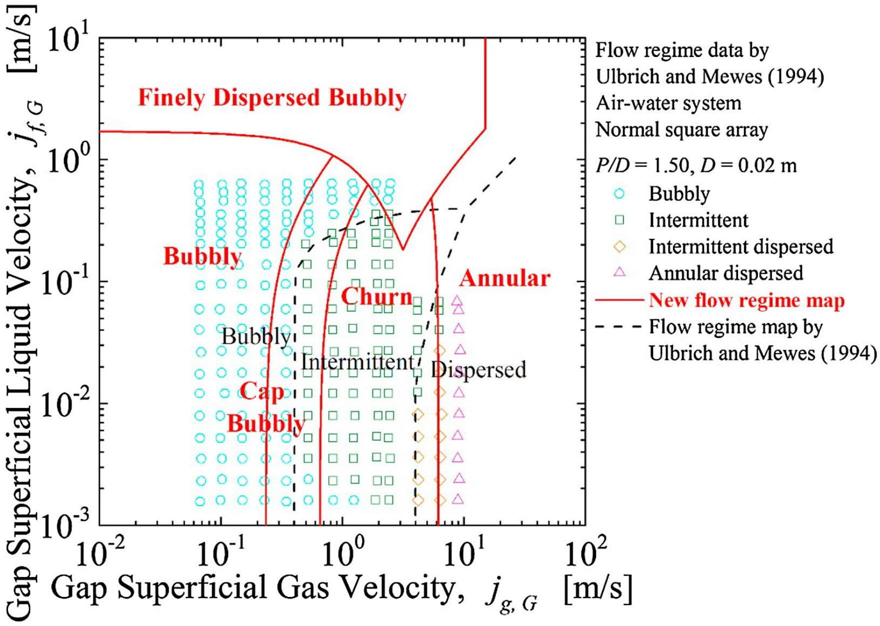

Figure 1.9: Comparison of [79] flow regime map with the data of [136].

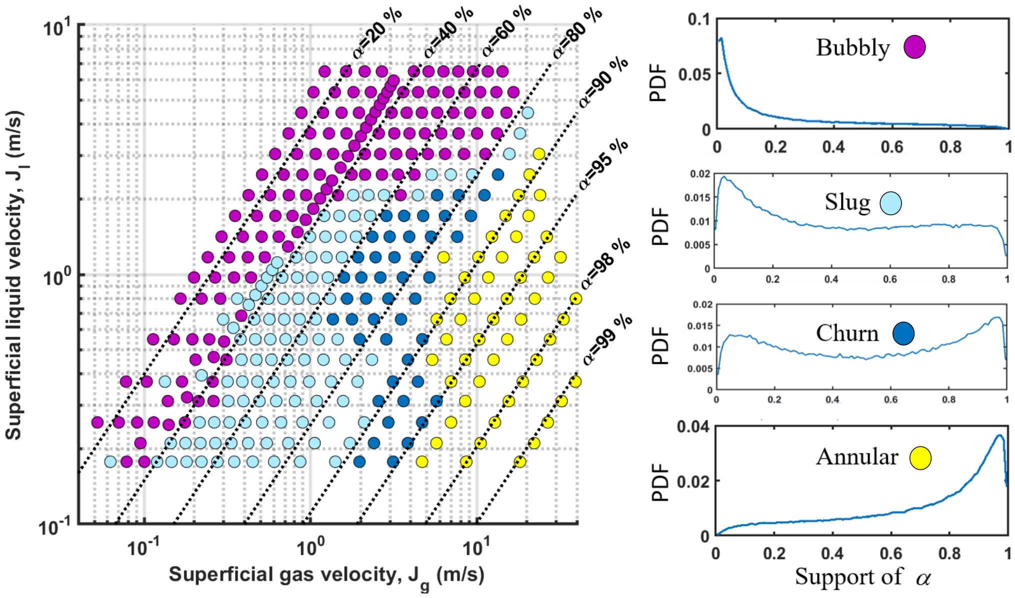

Figure 1.10: Regime flow map of DIVA experiment (left), described in the following section. The superfacial velocities are based on the gap between the tubes as for [79]. The categories are based on void fraction α PDF observations, as presented next to the map (right).

The DIVA experiment, carried out at CEA, involves a tube bundle configuration similar to those found in steam generators. Its primary purpose is to investigate vibrations occurring in square-pitch bundles. The experimental setup is composed of an upward channel with a

rectangular cross-section measuring 0.18 m × 0.3 m, hosting a square tube bundle of 5 × 3 rigid tubes, with a pitch ratio of 1.5. This setup allows for experimentation with various flow scenarios, including water flow, air flow, or air-water flow. The following section will provide a full description of the experimental configuration and its relevance to the study of vibrations in steam generators. Figure 1.10 is the flow regime map of DIVA experiment. The void fraction PDF of each flow operating conditions allowed to distinguish the experimental tests into 4 categories : bubbly (dispersed), slug (transitional), churn (transitional) and annular (separated).
Figure 1.9 shows the map proposed by [79] by comparison with the experiment made by [136], with 5×10 normal square configuration with a tube diameter of $D = 2$ cm and a gap of $1.5D$. It highlights the good agreement between the DIVA, [136] and [79] configurations. The comparison between the map and experimental data reveals a good agreement between the two and DIVA, indicating the reliability of the proposed maps. Although, the flow regimes are similar, [79] gives a more detailed map and identifies the so-called slug category from DIVA as a cap-bubbly regime. The DIVA experiment lacks visual data for the different flow regimes. To address this limitation, [136] provides visualizations of some regimes, as shown in Figure 1.11. These visualizations offer valuable insights into the characteristics of different flow regimes within the tube bundle configuration. At the left a bubbly flow around the tubes is presented. It highlights the presence of some bubble clusters and few $3D$ effects (along the tube). At the center a churn flow is presented. It highlights the heterogeneity of the flow, $3D$ effects and the presence of gas pockets. At the right an annular flow is presented. It highlights liquid ligaments, some $3D$ effects and mostly separated phases interactions.

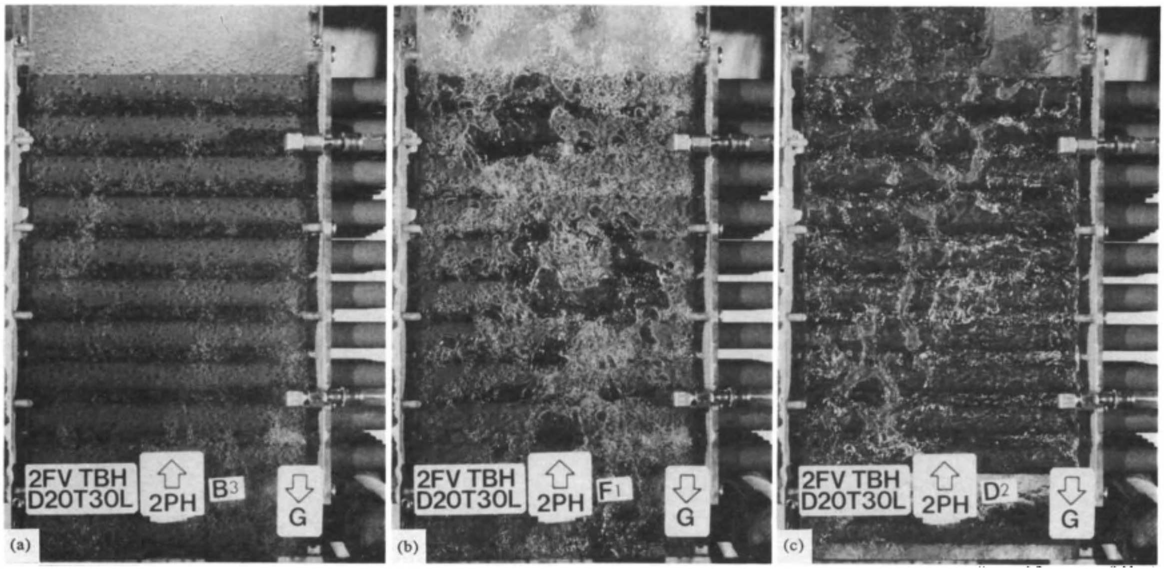

Figure 1.11: Cross-flow patterns for (a) bubbly, (b) intermittent and (c) annular regimes from R.Ulbrich and D.Mewes [136].

Such maps are useful to understand the different topologies but give no information on local phenomena arising from those regimes. Then experimental studies of the interaction between cylinders and the different regimes are important. The study of single-phase flow around a cylinder is a well-established area of research. For example, in single-phase flow, different patterns was observed according to the Reynolds number $Re = \frac{\rho U D}{\mu}$, with ρ the density, U the velocity, D the diameter of the tube and μ the dynamic viscosity :

- When $Re < 5$, viscosity is dominant so that the flow is laminar. Trajectories follow the curvature of the cylinder.

- When $5 < Re < 49$, viscosity is less dominant but the flow is still laminar. A detachment point can be observed but the vorticies behind the cylinder are stable.

- When $49 < Re < 300$, the so-called Von Karman vortex appears. It creates alternate vorticies behind the cylinder with the characteristic frequency of the configuration.

- When $300 < Re < 10^5$, the flow transitions to turbulence in the wake but the boundary layer is still laminar.
- When $10^5 < Re < 4.10^6$, the boundary layer over the cylinder transitions to turbulence.
- When $Re > 4 \times 10^6$, the flow is completely turbulent.

The instability of Von Karman (VK) is manifested by an alternating swirling detachment that induces fluctuating stress. The vortex is a phenomenon where the speed of the fluid is higher and the pressure lower than in the main flow. Thus, at the back of a cylinder this area is characterized by the presence of a depression area. In order to understand this phenomenon, we can define the number of Strouhal St which links the upstream speed U, the diameter of the cylinder D and the flow frequency f_f of the instability, by:

$$St = \frac{f_f D}{U}. \tag{1.3}$$

In single phase, for Re between 10^2 and 10^6 we can observe a characteristic St_{VK} of the order of 0.2 with a quasi-random distribution of standard deviation of the order of 10%. Regarding two-phase flow around a single cylinder, Inoue and al.[44] described the behavior of an upward uniform bubbly air-water flow around a cylinder for void fractions between 0 and 0.24 and Re between 10^4 and 10^5. He listed some important observations. The area near the separation point produces high local void fraction 3 to 4 times the homogeneous volume fraction. A high void fraction area is situated behind the cylinder. As the liquid velocity increases, its void fraction peak increases and its position come closer to the cylinder. A liquid layer where bubbles can hardly penetrate can be produced in the front and in the rear of the cylinder due to the static pressure gradient. Its thickness respectively increases and decreases in the front and in the rear with increasing flow velocity. This phenomenon is visible on Figure 1.12. Compared to single phase flow, the width and the length of the wake are smaller due to the buoyancy force on bubbles and higher turbulent intensity.

1.2.2 Two-phase flows in industrial configurations

Most of the literature dealing with upward two-phase flows giving interesting local data involve flows going through tube bundles or spacer grid [146, 147, 31, 137, 70]. Regarding two-phase flow across horizontal in-line tube bundles, the local data available is still limited [144]. Iwaki [46] performed bubbly flows around an upward tube bundle at low void fraction. He observed that for liquid superficial velocities under 0.1 m/s bubbles stay between the tubes whereas when the liquid superficial velocities is over 0.1 m/s, bubbles are driven into the wake behind the tubes.

Murakawa [89] experimental setup operated with the bubbly, transitional (called transition) and separated (called intermittent) flow regimes for square (called in-line) and triangular (called staggered) configurations as presented in Figures 1.13 and 1.14. In this study, we focus on

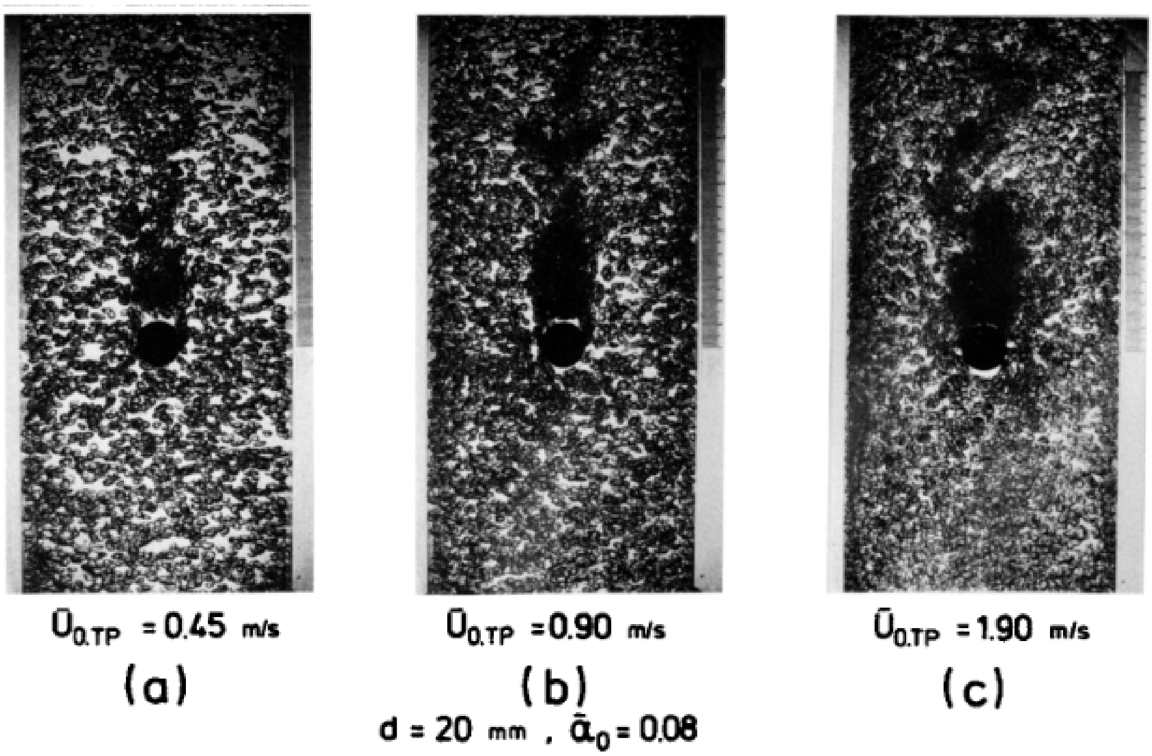

Figure 1.12: Photographs of a cylinder wake for several flow conditions from [44].

only triangular configuration observations of bubbly, intermittent, and separated flows. For bubbly flow, numerous bubbles were observed passing between the tubes, with some bubbles also observed behind the tubes, as noted by Iwaki [46]. This resulted in a higher void fraction in the upstream region compared to behind the tubes. In the case of intermittent flow, the void fraction was found to be almost uniformly distributed throughout the tube bundle. For separated flow, large gas structures were observed passing intermittently, accompanied by reverse flow in the near-wall region. Large bubbles were observed to occupy the horizontal maximum and vertical minimum gaps, leading to a lower void fraction in the horizontal minimum gap.

However, experimental data for all the regimes is still lacking. Indeed, to fully understand these mechanisms under the other regimes, experimental studies using specialized instrumentation for water-steam flow are necessary. Moreover, this instrumentation is not yet fully operational, and constructing a water-steam experimental facility is cost-prohibitive. As a result, research and development efforts in this area currently rely on tests using simulating fluids (such as water-freon and water-air) or analytical experiments.

In order to better understand and quantify the vibratory phenomena of SG tubes, experimental work has been carried out for about forty years at CEA, on a reduced scale. In order to limit the cost of installations and for safety reasons, these studies are carried out with simulating fluids, in this case water and air instead of water and steam. The DIVA experimental setup hosted at CEA, presented in Figure 1.15, is dedicated to the study of vibrations in square-pitch bundle. It thus reproduces on a reduced scale the FSI in the SG which currently equip the 32 nuclear reactors of 900 MWe and the 20 reactors of 1300 MWe of France. The loop is equipped with a pump able to deliver 5 to 300 L/s of water and an air compressor able to deliver up to 3000 m^3/h at an absolute pressure of 8 bar. The loop can thus operate in water flow, air flow

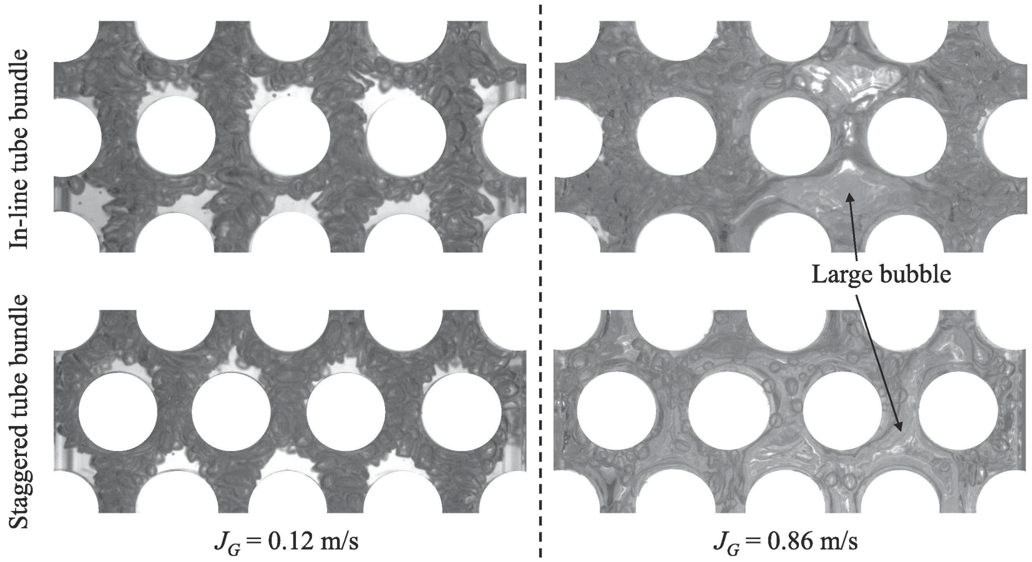

Figure 1.13: Instantaneous visualizations of the flow in the tube bundles for $j_g = 0.12$ m/s (left) and $j_g = 0.86$ m/s (right), as superficial gas velocities and $j_l = 0.2$ m/s (both), as superficial liquid velocities. The upstream flow originates from the bottom side. From [89].

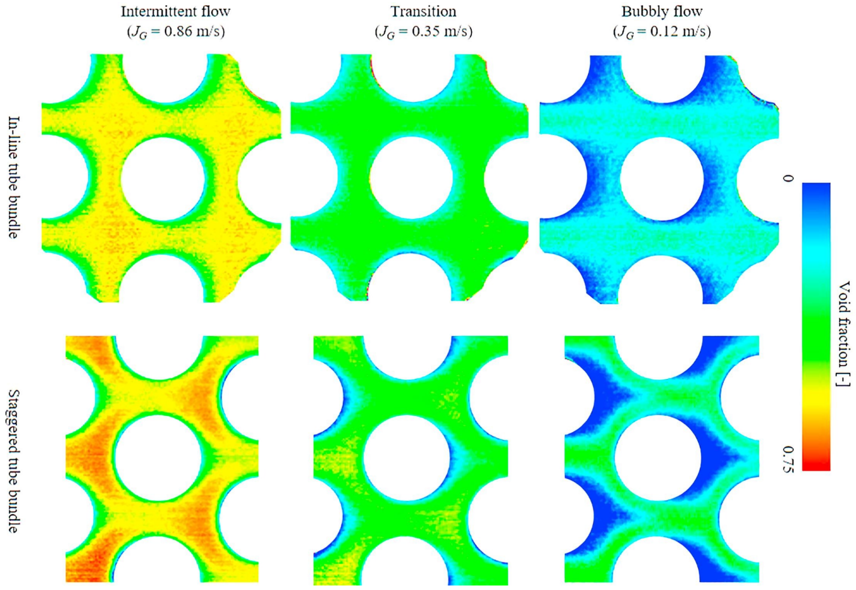

Figure 1.14: Experimental two-dimensional averaged void fraction distributions for $j_l = 0.2$ m/s, as liquid superficial velocity. The upstream flow originates from the left-hand side. From [89].

or air-water flow. It allows reproducing regimes similar to the ones encountered in the SG. The experimental setup is composed of an upward channel of 0.18 m × 0.3 m rectangular section in which can be set a square tube bundle made of 5 × 3 rigid tubes, with a pitch ratio 1.5, as presented in [95] and in Figure 1.15. A central flexible tube can be set but will not be discussed in this manuscript.

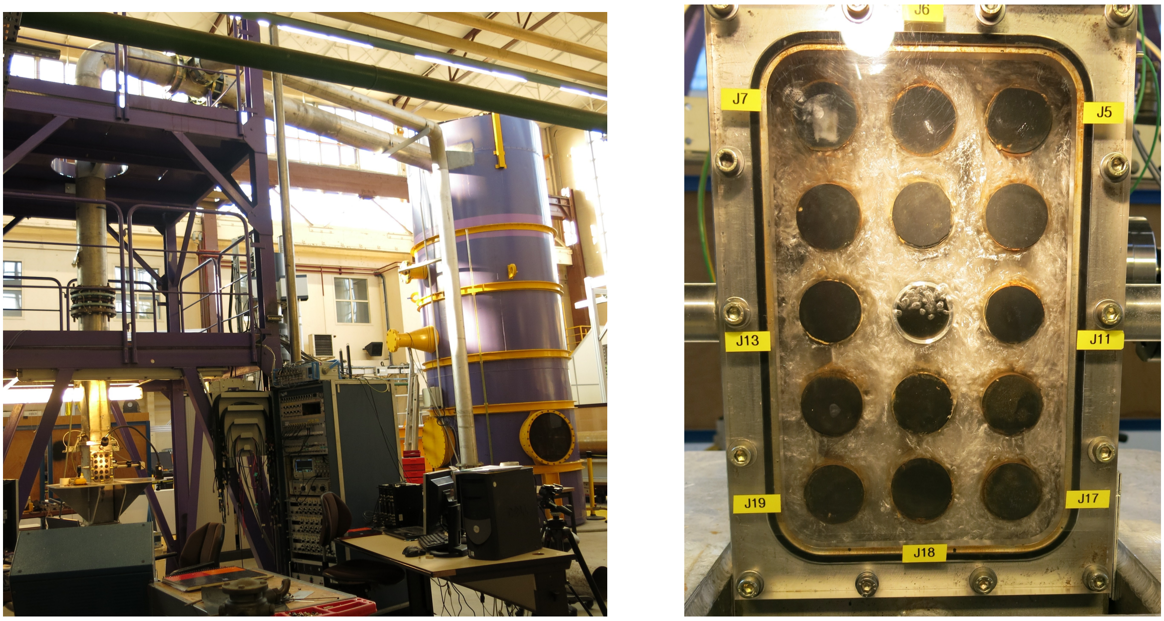

Figure 1.15: Photos of the DIVA experiment.

The Power Spectral Density (PSD) of the fluid force (drag and lift directions) acting on the central tube is calculated by measuring the random excitation for various volume flow rates of air and water. Specifications and verifications for single phase flows were performed in Piteau and al. [95]. It aims to understand and take into account the fluctuations of the two-phase flow for the fluid-elastic interaction. However, due to the complexity of the phenomenon (such as bubble swarms, the emergence and the transition of several bubbly turbulent regimes, etc.), it is not always possible experimentally to access to all flow conditions and information because of limited instrumentation. Then in order to get additional local information, the idea is to get a numerical twin. Indeed, numerical simulation can play a fundamental role, as it allows access to all quantities of interest and information that are not accessible or observable experimentally.

In order to simulate any configuration similar to a SG, a quasi-steady general numerical model must be built. Such a model is said "All-regimes". It describes flow configurations where multiple dispersed and continuous regions can be met. It can be seen as a smooth transitional flow between the different flow topologies previously introduced.

1.3 Advanced numerical models for two-phase flows

1.3.1 Literature overview

In order to reproduce two-phase flows it exists several methods that are suitable for specific applications [148, 32, 150, 85]. Then a compromise between precision and prediction must be done. A more precise description is given in the appendix. To summarize, direct approaches like DNS and LBM can only be used for precise small portion of industrial configurations because of their computational cost and the need of further development. Statistical approaches are accessible in industrial codes and their computational cost is relevant for our applications. Statistical approaches to fluid flow can be divided into two aspects: the statistical behavior within each phase, known as Reynolds Averaged Navier-Stokes (RANS), and the statistical presence of interfaces. The first aspect involves decomposing any quantity into a mean field and a fluctuating field. The mean field is calculated, while the fluctuations are modeled. Unsteady methods called URANS were developed to capture timescales separated from turbulence, but they violate the principle of ergodicity, which states that ensemble averages and time averages are the same. From a mathematical perspective, the filtered equations of Large Eddy Simulations (LES) and URANS equations are identical, with the only difference being the closure models. The second aspect arises from the averaged equations, as the mean quantities eliminate the interfaces. Additional equations are needed to account for the presence of interfaces. The popular approach is called Euler-Euler because it treats both phases as coexisting fluids, both as the "stage" fluid, and their mixture is characterized by a void fraction. This approach is much less computationally demanding and allows for the simulation of real industrial geometries.

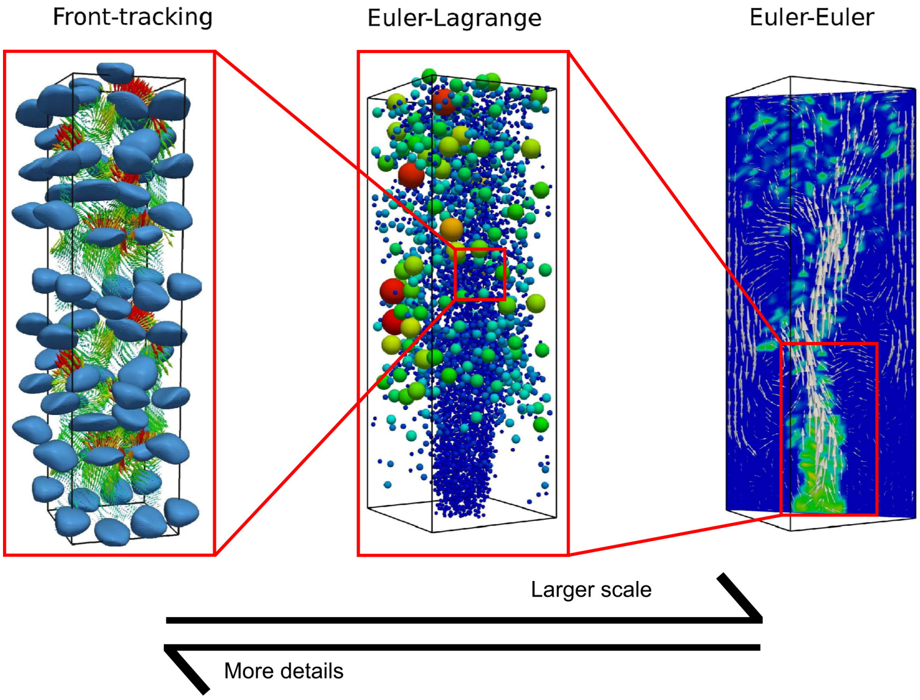

Figure 1.16: Comparison between Front-Tracking, Euler-Lagrange and Euler-Euler methods from [63].

Numerical models that can simulate the complexity of two-phase flows in a SG are called "all regimes" and only few approaches have been proposed in the literature (see [102] and section 2.2.2). The Eulerian-Eulerian approach suggests solving both phases, with mass, momentum and energy equations. These equations are coupled by the volume fraction of the phase and the interfacial exchange terms for all three equations. The fundamental concept behind all-regimes models is to define appropriate interfacial exchange terms for each regime topology. These models combine a formulation able to define interfacial terms for dispersed bubbly regime with another formulation that defines them for continuous flows. Consequently, these methods do not explicitly track or reconstruct the geometry of the liquid/gas interfaces, as Level-Set, Phase Fields, or Volume Of Fluid method would typically do [135]. All-regimes models primarily focus on solving the dynamics for average quantities across the phases. As a result, they are particularly well-suited for scenarios involving multiple and complex bubble/droplet topologies. The changes among different "all-regimes" models primarily lie in how the intermediate regimes between the two extremes (bubbly and continuous) are solved.
The initial approach taken to address this challenge involved flow regime-dependent correlations and regime transition criteria based on experimental data [54], as demonstrated in [113].

However, as highlighted in [57], this approach fails at reproducing the dynamics of developing flows, transition regimes, and inlet effects. Moreover, correlations based on experimental data inherently suffer from a considerable margin of errors, limitations in operational conditions and geometries, and can introduce artificial discontinuities and numerical instability. To overcome these limitations, the first family of models introduced algebraic blending techniques for intermediate regimes. One inherent weakness of the blending approach is its inability to accurately define the gradual transitions between different two-phase regimes.[102, 29, 142]. According to Frederix et al. [27], the success of the transitions in GEMMA approach [102] is dependent on capturing the dynamics on the computational grid. Indeed, most algebraic models suffer from implicit transitions that only take into account the void fraction dependency, disregarding other important factors.

The second family, known as the "multi-field" method, divides the gas field into N subfields based on the size distribution of the gas bubbles being computed [60, 43, 80]. For each gas field, an additional set of conservative equations needs to be solved. While this leads to a significant increase in the number of interfacial terms that need to be modeled, it allows for a more accurate treatment of different flow regimes. The "multi-field" family of models has gained popularity due to its ability to handle dynamics associated with bubbles of different shapes and bubble interactions. Many models in the literature, such as GENTOP [43] or HD-LIS [82], are based on combinations of the inhomogeneous MUlti-SIze Group (I-MUSIG) method [58] and a continuous gas field with an interface segregation method. One notable weakness of these models is their high dependence on the computational grid, primarily caused by the transition condition between the dispersed and continuous gas fields. The accuracy and performance of these models are significantly influenced by the way the transition is handled on the grid. It prevents to have a convincing grid convergence for mesh sensitivity study, as illustrated in 1.17. Furthermore, it prevents correct validation of some mesh progression strategies like in boundary layers or around complex geometries. It makes the models not suitable for specific turbulent models.

The model handled in this thesis belongs to the same family of models lastly discussed but introduces a different approach. It relies on differential equations for the interfacial area concentration (IATE) [55] for two groups of bubbles, along with an interface detection method. A detailed description of this model is presented in the following section.

1.3.2 The Two-phase RegIme Transition model

The TRITON (Two-phase RegIme TransitiON) model , developed by Kuidjo [60], combines a two-group IATE with an interface detection method developed by Coste [16]. In this approach, each of the two gas groups has separate momentum equations, and only the mean level of each group is computed. The transition between the dispersed and continuous gas fields is then determined based on the prediction of local void fraction and its gradient, enabling the identification of gas pockets. One notable advantage of this model is that it is not grid-dependent in its formulation, making it well-suited for mesh progression strategies such as those used in boundary layers. By dividing the gas into two distinct fields, we are able to effectively model separately and take into account with their unique characteristics and behavior the following regimes topologies :

- Dispersed bubbly flows with one distribution of small bubbles.
- Transitional flows such as cap and churn flows, thanks to a hybrid large bubble dispersed-continuous field.

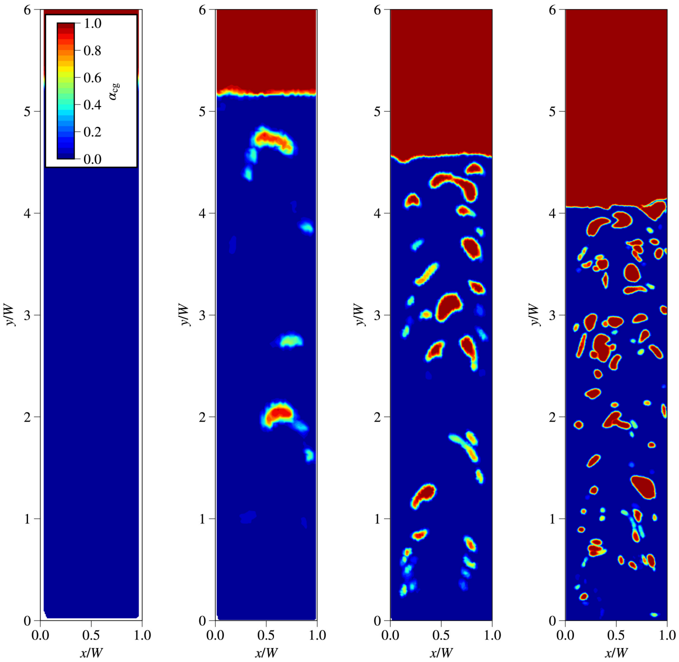

Figure 1.17: Void fraction α_{cg} prediction contour of the continuous gas field from Four-Field-LIS with finer mesh from left to right. From [27].

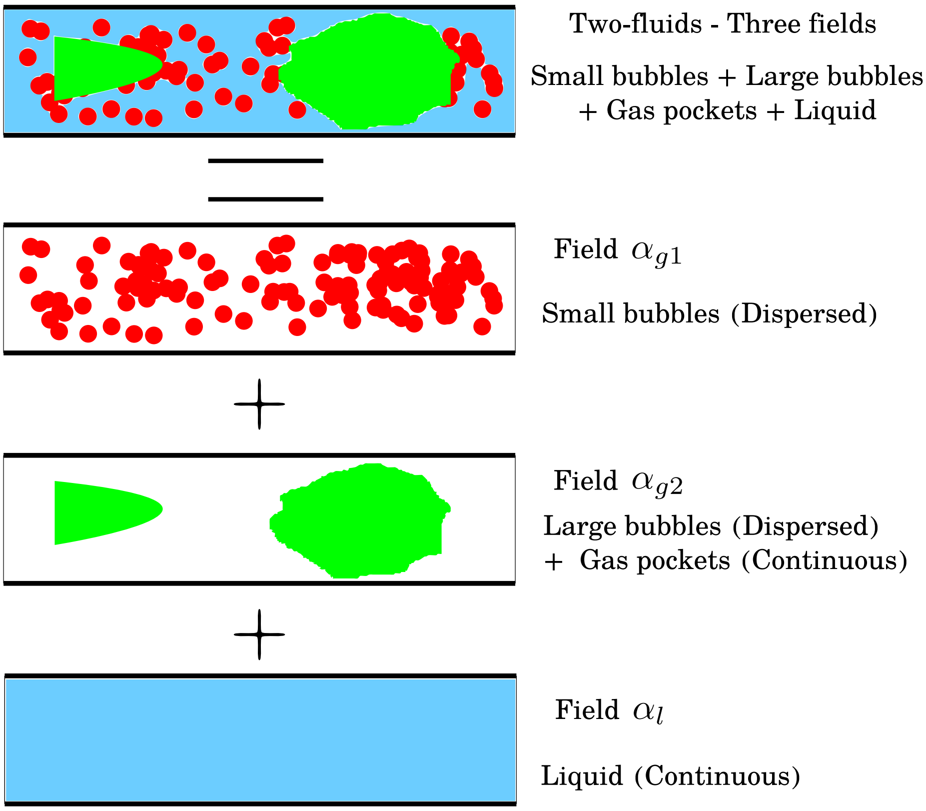

Figure 1.18: Principle of the "all-regimes" model developped at CEA. 🟥 Small bubbles, 🟩 Continuous gas and large bubbles, 🟦 Liquid.

- Separated flows, thanks to the hybrid field using the continuous part.

By solving the IATE, there is no need for an algebraic blending function to define the interfacial transfer terms for the intermittent regimes, as the IATE 2-Groups model [121] already incorporates them. However, it is essential to establish the conditions that enable two transitions.

From bubbly to intermittent: It is ensured as critical diameter D_c between the two distribution of bubbles, based on the Laplace length scale proposed by Ishii and Zuber [84] as :

$$D_c = 4\sqrt{\frac{\sigma}{g\Delta\rho}}, \tag{1.4}$$

where σ is the surface tension, g is the gravitational acceleration and $\Delta\rho$ is the difference between the liquid and gas densities.
Wang and Sun tested a two-group IATE model in 3D configurations on a wide range of conditions for bubbly flows, in [140], and for cap-bubbly flows, in [141], in channel geometry and obtained good results.

From intermittent to separated: the LIM is an interface-holding method that identifies regions where the gas must be computed as a continuous phase based on a criterion defined by the volume fraction gradient[16, 17, 18]. Unlike interface tracking methods [8] (VOF [39] *etc.*), the LIM does not reproduce the interface but only identifies cells where interfacial forces (specific to this regime) are applied. It is based on a three cells recognition, activated with criteria based on the void fraction gradient that clearly identifies the liquid continuous side, the gas continuous side and an intermediate interface cell as presented in Figure 1.19.

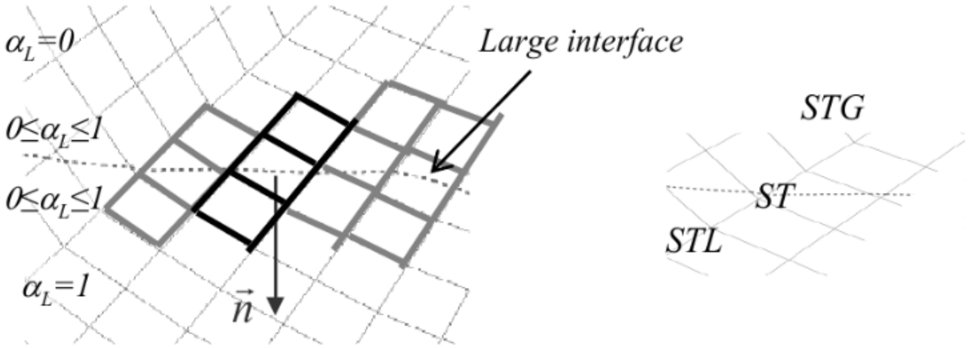

Figure 1.19: Graphical concept of the LIM method from [16].

However, the model was designed mathematically for channel flows and was validated on few test cases. In order to reproduce the FSI problem, these types of models must undergo a double validation necessary on the one hand to estimate the ability of the model to reproduce the hydrodynamics of the flow and the interactions between bubbles and on the other hand to estimate the ability of the model to reproduce the good fluctuations on tubes. Indeed, to reproduce the flows occurring in DIVA it is necessary to understand and validate the different modeling bricks but also for the interaction aspect with the structure and the turbulence. In particular, it is necessary to further investigate in order to correctly couple the TRITON model with the modeling of the fluctuations.

1.4 The challenge of two-phase fluid-stucture interaction simulations

The experimental setup known as DIVA, hosted at CEA, is dedicated to replicating and studying the fluctuations experienced by tubes in steam generators. Its primary objective is to develop models that can effectively prevent tube ruptures. However, due to the intricate nature of two-phase flow and the limited availability of instrumentation, it is necessary to incorporate additional local information through numerical simulations. Although several numerical approaches have been proposed in the literature, their validation, particularly under conditions of high void fraction, is not yet convincing. One promising model, called TRITON, is based on experimental observations and aims to simulate various flow regimes encountered in a steam generator. However, further validation and modeling are essential to accurately reproduce the fluctuations observed in two-phase flow.

The primary objectives of this study are to address the following questions: How can we replicate DIVA, and to what extent? What insights can we gain from simulations to enhance our understanding of DIVA? What kind of modeling is necessary to reproduce two-phase fluid-structure interaction? How can we effectively manage areas with a high void fraction?

By answering these questions, this work aims to contribute to the advancement of understanding and modeling of FSI in the context of two-phase flow, particularly in scenarios similar to the DIVA experimental setup.

Figure 1.20 provides an overview of the key decomposition of the DIVA experiment. In this thesis, we investigate a fluid-structure interaction problem, which involves the interaction between a two-phase fluid and a structure. However, for the purpose of this research, our focus will be only on the fluid aspect with fixed tubes. Prior to simulating the movements of the structure, it is crucial to validate the behavior of the fluid and the forces exerted on the tube. This will be achieved by reproducing the force spectra, ensuring accurate representation and understanding of the fluid dynamics. We simulate, via the NEPTUNE_CFD code, the different flow regimes that can be observed in the DIVA analytical setup. In particular, we want to reproduce the mechanical loading on the tubes in order to analyse and understand the observed vibratory phenomena.

Bestion demonstrates in [3] that developing an "all-regimes" fluid model for DIVA confronts several challenges, even from a theoretical perspective. These challenges arise from the need for accurate modeling of various physical processes within the averaged equations of the two-phase flow, as depicted in Figure 1.20. The behavior of bubbles dispersion, large interfaces, and turbulence play crucial roles in the model. To address these processes, the TRITON model incorporates coupling forces and IATE for the dispersed aspect, a turbulence model, and the LIM transition for the large interfaces. Extensive work has been carried out to select and adapt the different components of the model. Initially developed for channel flow, only a limited literature addresses the particular challenges and modifications required to accurately replicate the dynamic behavior of a two-phase averaged flow around tubes.

The interdependencies among the various building blocks of the model is one key problem. The accuracy of each fundamental aspect's prediction is essential because the computations of these aspects rely on the predictions of each other, as depicted on Figure 1.21. Therefore, any shortcomings in predicting one fundamental aspect can have a prejudicial effect on the overall predictive capability of the model.

Best practices for two-phase flow modeling in nuclear reactor thermal hydraulics are outlined in [2]. These practices involve identifying important flow processes, such as regime type,

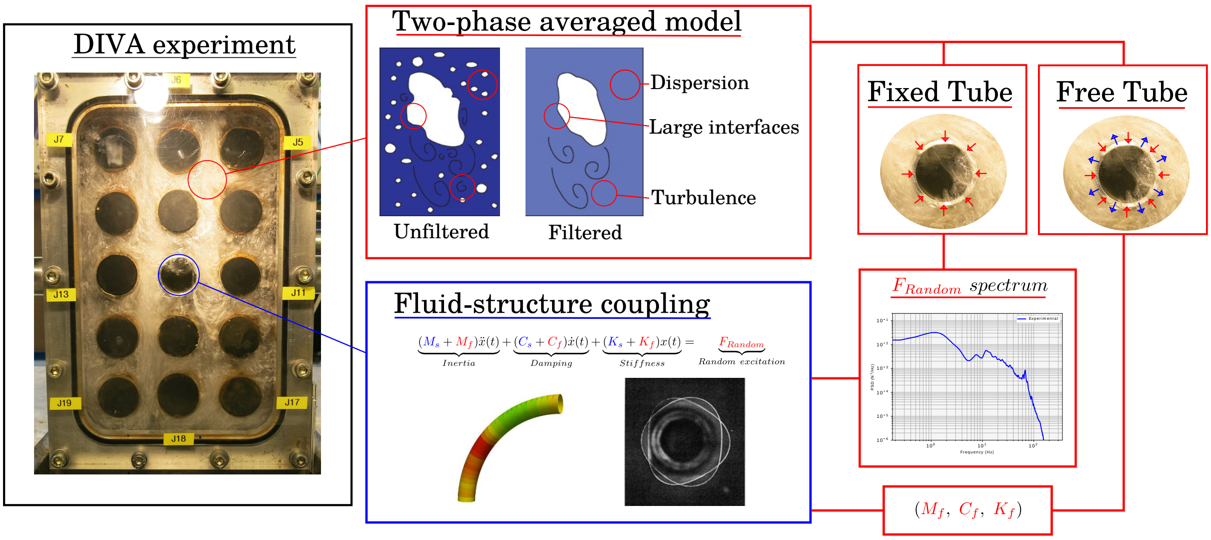

Figure 1.20: Illustration of the numerical modeling for DIVA. Images from Europlexus website, [93] and [3].

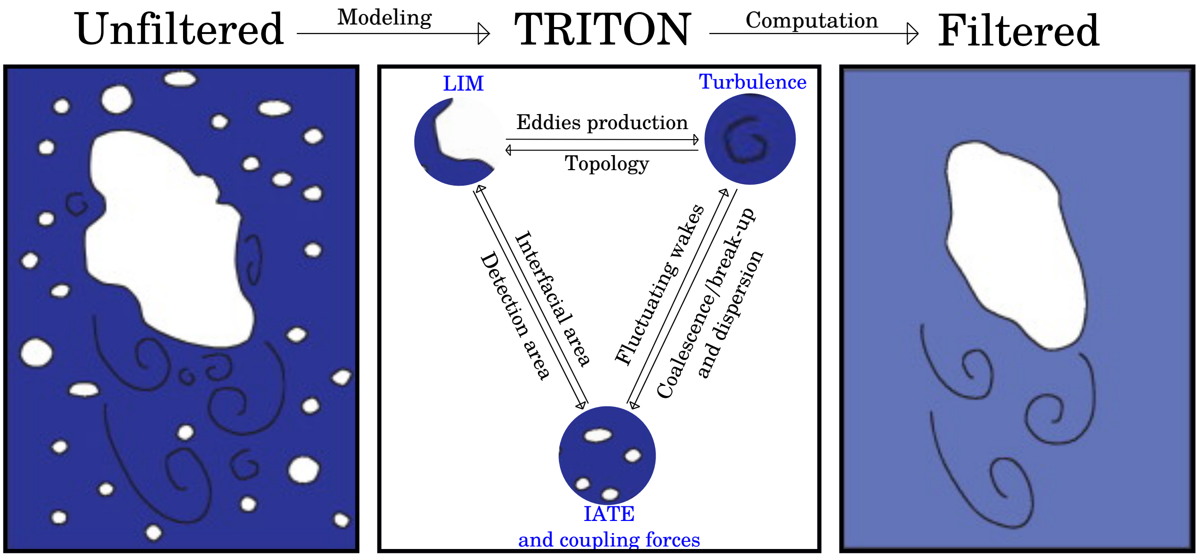

Figure 1.21: Illustration of the different numerical modelings of TRITON and their interactions. Images from [3].

space and time resolutions, physical processes, and relevant non-dimensional numbers. Modeling choices should be made and justified especially for the interface treatment. Closure laws should be selected, justifying the modeling of interfacial transfers, turbulence. Coherence and consistency of choices should be verified and compared with literature and experimental data for simple cases. The model should be validated using more complex experimental data or down-scaling comparisons. Finally, uncertainties in predictions should be evaluated, but will not be discussed in this thesis.

This work is divided into 4 parts. The first part (Chapter 2) focuses on describing the modeling used and the state of the art to justify our approach and starting points. The second part (Chapter 3) aims to identify the influence of some parts of the model and their issues, and propose solutions to improve it. The third part (Chapter 4) deals with the simulation of averaged two-phase flows in the presence of a single cylinder, including experimental comparisons to understand the model's sensitivity and behavior. This part aims to identify the strengths, challenges, and possible improvements. The final part (Chapter 5) focuses on simulating DIVA experiments (tube bundle), attempting to establish links between our numerical model and the experiment to understand the physical insights achievable with our model.

Chapter 2

Two-phase averaged modeling for flows in tubular geometries

Summary

This chapter is a state-of-the-art review and a description of two-phase averaged modeling for the reproduction of fluid-structure interaction in a channel with a tube bundle.

The first section outlines the general principles of two-phase averaged modeling. The initial part introduces various tools and approaches available for replicating experimental flows. The second part outlines what the averaged modeling should be able to reproduce regarding experimental data and justifies the use of our model.

The second section focuses on interfacial stress modeling in the literature and for our model. The first part describes interfacial force models for dispersed and continuous phases. The next part introduces the concept of interfacial area equations required for forces modeling, especially the Interfacial Area Transport Equation (IATE) 2 group model used in this thesis. The last part briefly showcases, in a non-exhaustive way, various source terms available in the literature and those used in this thesis.

The third part offers a description of turbulence modeling in single-phase and two-phase cases. The first part provides a simple introduction to single-phase turbulence modeling to better understand the subsequently modeled terms. The following part introduces the Elliptic Blending – Reynolds Stress Model and justifies its use. The last part details current approaches to modeling pseudo-turbulence in the liquid phase, associated with the transit of bubbles.

The final part presents two-phase simulations with a single cylinder before modifying the model. The first part introduces the geometry, mesh, and post-processing aspects relevant to reproducing force spectra. The next part addresses the issues related to the modeling in the presence of an obstacle, along with the results obtained using a simpler model to apprehend and address specific problems arising from the presence of the cylinder.

2.1 The two-phase averaged Navier-Stokes equations

2.1.1 Averaging the Navier-Stokes equations

The simulation of an adiabatic system of incompressible water-air requires the computation of the instantaneous local Navier-Stokes equations in each phase k. The conservation equations for mass in each phase is given by :

$$\underbrace{\nabla.(\rho_k \mathbf{v}_k)}_{Transport} = \underbrace{\Gamma_k}_{Source} , \tag{2.1}$$

with t the time, ρ_k the density of phase k, $\mathbf{v}_k$ the velocity of phase k and Γ_k a mass source term of phase k. The conservation equation for momentum in each phase is :

$$\frac{\partial}{\partial t}\rho_k \mathbf{v}_k + \underbrace{\nabla.(\rho_k \mathbf{v}_k \mathbf{v}_k)}_{Transport} = \underbrace{-\nabla P_k}_{Pressure} + \underbrace{\nabla \cdot \underline{\underline{\tau}}_k}_{Diffusion} + \underbrace{\rho_k \mathbf{g}}_{Gravity} , \tag{2.2}$$

with P_k the pressure, $\underline{\underline{\tau}}_k$ the viscous stress tensor and $\mathbf{g}$ gravity.

Equations 2.1 and 2.2 are defined within each phase, but it is necessary to introduce jump conditions on either side of the interface, which is the boundary between the two phases (see [85] for more details). From the balance equations, boundary and jump conditions, and constitutive laws, emerge dimensionless numbers that are crucial scaling parameters. These dimensionless numbers play a significant role in establishing the similarity between simulations and experiments. However, fixing these scaling parameters in two-phase flow rises a challenge due to the inherent complexity of the system. Nonetheless, they are still used to account for specific effects within the equations. In fact, in certain configurations, scaling effects can be notably significant, emphasizing the need to extrapolate using physical similarities. Furthermore, the use of dimensionless parameters enables a deeper understanding of flow regimes, structures, and mechanisms. Considering an isothermal incompressible gas-liquid channel flow allows us to define several essential dimensionless numbers, presented in Table 2.1, based on the following independent physical quantities :

- The velocities of the liquid U_l and gas phases U_g.
- The dynamic viscosities of the liquid μ_l and gas phases μ_g.
- The densities of the liquid ρ_l and gas phases ρ_g.
- The characteristic lengths for the liquid D_l and gas phases D_g. They are commonly chosen as the hydraulic diameter for the liquid phase and the bubble diameter for bubbly flow.
- The surface tension σ.
- The gravitational acceleration g.

The similarity between simulations also relies on operating conditions known as inlet conditions for the simulation. It leans on key dimensional and non dimensional parameters that are in Table 2.2. They are characterized by the mass flow rates $\dot{m}$ of the liquid $\dot{m}_l$ and the gas $\dot{m}_g$, volumetric flow rates $\dot{Q}$ of the liquid $\dot{Q}_l$ and the gas $\dot{Q}_g$, the cross-sectional area A_s occupied by the liquid and the gas and the velocities of the liquid v_l and the gas v_g.

Number	Expression	Ratio of	over
Reynolds	$Re_k = \frac{\rho_k U_k D_k}{\mu_k}$	Inertia	Viscosity
Modified Froude	$Fr_k = \frac{\rho_k U_k^2}{\Delta\rho g D_k}$	Kinetic energy	Gravity
Weber	$We_k = \frac{\rho_k U_k^2 D_k}{\sigma}$	Inertia	Suface tension
Eötvös	$Eo_k = \frac{\Delta\rho g D_k^2}{\sigma}$	Buoyancy	Surface tension

Table 2.1: Table of significant dimensionless numbers.

Operating parameter	Symbol	Expression
Quality	x_Q	$\frac{\dot{m}_g}{\dot{m}} = \frac{\dot{m}_g}{\dot{m}_g+\dot{m}_l}$
Volumetric quality	β_Q	$\frac{\dot{Q}_g}{\dot{Q}} = \frac{\dot{Q}_g}{\dot{Q}_g+\dot{Q}_l}$
Superficial velocity of phase k	j_k	$\frac{\dot{Q}_k}{A_s}$
Void fraction of phase k	α_k	$\frac{j_k}{v_k}$

Table 2.2: Table of significant operating inlet numbers.

In the case of a system like DIVA, simulating thousands of deformable bubbles of different sizes and shapes while tracking their interface through the bundle of tubes with very fine mesh to capture the fluctuations would be necessary. However, due to the computational power required, it is unrealistic to be able to compute the spectra of forces exerted on tubes with our current means. Then, it becomes necessary to consider a statistical flow to reproduce the water-air flow at a low cost. To ease the understanding of the averaging principles, the formalism of Ishii and Hibiki [85] is adopted. The general form of the Navier-Stokes equations can then be written, as follows, to describe how a specific quantity, denoted as ϕ_k changes:

$$\frac{\partial}{\partial t}\rho_k\phi_k + \underbrace{\nabla.(\rho_k\phi_k\mathbf{v}_k)}_{Transport} = \underbrace{-\nabla\cdot\mathbb{J}}_{Diffusion} + \underbrace{\rho_k s_k}_{Source} . \tag{2.3}$$

Table 2.3 provides the corresponding quantities for the mass (equation 2.1) and momentum conservation (equation 2.2).

The averaged Navier-Stokes equations predict the average behavior of fluid motion and properties by filtering out local instant fluctuations. However, precise modeling of all microscopic scales is still necessary for an accurate reproduction of the averaged flow. To handle multiple phases within the averaged framework, it becomes essential to introduce a variable that defines the phase mixture. Let χ_k^{phase} be a tracer of phase k, which defines whether or not we are in this phase. It takes the value 1 if we are in the phase, 0 otherwise. The void fraction of phase

Quantity	ϕ_k	$\mathbb{J}$	s_k
Mass	1	0	Γ_k
Momentum	$\mathbf{v}_k$	$\underline{\underline{T}}_k = P_k \underline{\underline{I}} - \underline{\underline{\tau}}_k$	$\mathbf{g}$

Table 2.3: Table of the conserved quantities in balance equations.

k, denoted as α_k, in a volume $V_{\Omega k}$ within a reference frame (X,t), is defined as follows:

$$\alpha_k = \frac{1}{V_\Omega} \int_{V_\Omega} \chi_k^{phase}(X,t) dV_\Omega = \frac{V_{\Omega k}}{V_\Omega}. \tag{2.4}$$

As depicted in Figure 2.1, the void fraction primarily captures smooth periodic macroscopic phenomena. However, it can also account for interacting phenomena and disequilibrium. For instance, to accurately depict the overall spreading phenomenon resulting from dynamic behavior, it becomes essential to consider the wake's disequilibrium behind the tube, depicted in red. Similarly, we can draw parallels to Monet's painting approach. By observing and gathering information daily, he performs an ensemble average to convey the comprehensive impression of the phenomenon he wishes to represent. Given his continuous observations, he captures the fluctuating behavior and its macroscopic consequences, such as the breaking waves influenced by their interactions with the sand.

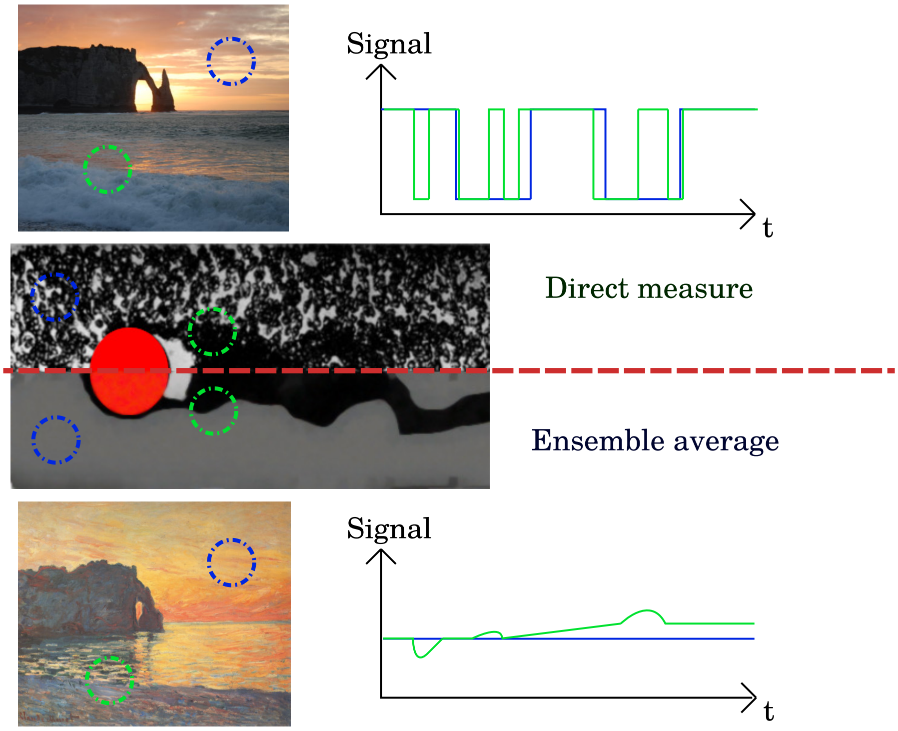

Figure 2.1: Link between the instantaneous presence of the tracker and its void fraction. Comparison between direct measure and ensemble averaged for a two-phase flow crossing a tube [44] and for Etretat cliffs between a photo and Monet painting.

The volume averaged method introduces two different mean quantities for a property ϕ: the mean of a field k in the volume $\bar{\phi}_k$ and the mean of a field in its proper volume $\overline{\overline{\phi_k}}$. With the void fraction α_k of the field k in a volume $V_{\Omega k}$ in a reference frame (X,t), they are defined by :

$$\bar{\phi}_k = \frac{1}{V_\Omega}\int_{V_\Omega} \phi_k(X,t)dV_\Omega, \tag{2.5}$$

$$\overline{\overline{\phi_k}} = \frac{1}{V_{\Omega k}}\int_{V_{\Omega k}} \phi_k(X,t)dV_\Omega = \frac{\bar{\phi}_k}{\alpha_k}. \tag{2.6}$$

To ensure accuracy, the mean values must satisfy a fundamental assumption of regularity, which ensures that the average of a mean value remains consistent with the mean value itself. In order to account for the zero mean value of the fluctuation ϕ', another commonly used approach is the Favre averaging. The Favre average of the quantity ϕ for the field k is defined as $\tilde{\phi_k} = \frac{\overline{\rho\phi_k}}{\bar{\rho}}$, where the overline represents the averaging operation.

A new fundamental relation arises by summing the differential equations of each phase to get the differential equations for the mixture. Assuming that the subscript "m" denotes the quantity for the mixture, the relation can be expressed as follows:

$$\begin{aligned}\sum_k \overline{\rho_k\phi_k\mathbf{v}_k} &= \sum_k \alpha_k(\overline{\overline{\rho_k}}\overline{\overline{\phi_k\mathbf{v}_k}} + \overline{\overline{\rho_k'\phi_k\mathbf{v}_k}}) = \sum_k \alpha_k(\overline{\overline{\rho_k}}\tilde{\phi}_k\tilde{\mathbf{v}}_k + \overline{\overline{\rho_k\phi_k'\mathbf{v}_k'}})\\ &= \underbrace{\rho_m\phi_m\mathbf{v}_m}_{Mean\ transport} + \underbrace{\sum_k \alpha_k\overline{\overline{\rho_k}}\tilde{\phi}_k(\mathbf{v}_k - \mathbf{v}_m)}_{Phase\ transport} + \underbrace{\sum_k \alpha_k\overline{\overline{\rho_k\phi_k'\mathbf{v}_k'}}}_{Turbulent\ and\ interfacial\ transport}.\end{aligned} \tag{2.7}$$

This relation provides the basis for separating the mixture and individual phases into distinct sets of equations. Two approaches stem from this separation: simulating only the mixture while modeling phase phenomena, known as the drift-flux model, or simulating the behavior of each phase while incorporating turbulent and interfacial phenomena, known as the two-fluid model. According to Ishii et al. [85], the last approach offers several advantages, including the ability to simulate segregated dynamics and non-equilibrium interactions between phases.

The difficulties in the averaged modeling are mainly found in the momentum conservation equation since the mass conservation equation is almost unchanged. The momentum balance equation of the two-fluid model can be expressed as follows:

$$\frac{\partial}{\partial t}\alpha_k\overline{\overline{\rho_k}}\tilde{\mathbf{v}}_k + \underbrace{\nabla.(\alpha_k\overline{\overline{\rho_k}}\tilde{\mathbf{v}}_k\tilde{\mathbf{v}}_k)}_{Transport} = \underbrace{-\nabla.(\alpha_k(\underline{\underline{T}}_k + \underline{\underline{T}}_k^T))}_{Stress\ and\ turbulence} + \underbrace{\alpha_k\overline{\overline{\rho_k}}\tilde{\mathbf{g}}}_{Gravity} + \underbrace{\mathbf{I}_k}_{Interfacial\ transfer}, \tag{2.8}$$

with $\mathbf{I}_k$ interfacial transfer for the phase k, $\overline{\overline{\underline{\underline{T}}_k}}$ the stress tensor and $\underline{\underline{T}}_k^T$ the turbulent stress and $\mathbf{g}$ gravity.
The interfacial transfer in the momentum balance equation can be expressed as follows:

$$\begin{aligned}\mathbf{I}_k &= -\frac{1}{\Delta t}\sum_j \frac{1}{v_{ni}}(\rho_k\mathbf{n}_k(\mathbf{v}_k - \mathbf{v}_i)\mathbf{v}_k - \underline{\underline{T}}_k\mathbf{n}_k))\\ &= -\frac{1}{\Delta t}\sum_j \frac{1}{v_{ni}}(\rho_k\mathbf{n}_k(\mathbf{v}_k - \mathbf{v}_i)\mathbf{v}_k - (\underline{\underline{T}}_k - \underline{\underline{T}}_k^{interface})\mathbf{n}_k)) + \frac{1}{\Delta t}\sum_j \frac{1}{\mathbf{v}_{ni}}\underline{\underline{T}}_k^{interface}\mathbf{n}_k,\end{aligned} \tag{2.9}$$

with v_{ni} the interfacial normal velocity, $\mathbf{n}_k$ the interfacial normal vector, $\mathbf{v}_i$ the interfacial velocity and $\underline{\underline{T}}^{interface}$ interfacial stress tensor.
A new variable, called interfacial area concentration, can be introduced to simplify the formulation: $a_{ij} = \frac{1}{\Delta t v_{ni}}{}_j$, with Δt a time interval. We can also notice that $\frac{1}{\Delta t}\sum_j \frac{1}{v_{ni}}\mathbf{n}_k = -\nabla\alpha$. By

decomposing the stress into pressure and shear-stress components, subscripted i at the interface, and incorporating the mass loss rate $\dot{m}$, we obtain the following expression :

$$\begin{aligned}\mathbf{I}_k = \underbrace{\Gamma_k \tilde{\mathbf{v}}_{ki}}_{Mass\ transfer} + \underbrace{\sum_j a_{ij}(\overline{\overline{P_{ki}}} - P_k)\mathbf{n}_k}_{Interfacial\ pressure\ imbalance} + \underbrace{\sum_j a_{ij}(\underline{\underline{\tau}}_k - \overline{\overline{\underline{\underline{\tau}}_{ki}}})\mathbf{n_k}}_{Interfacial\ shear-stress\ imbalance} \\ + \underbrace{\overline{\overline{P_{ki}}}\nabla\alpha_k}_{Interfacial\ pressure\ dispersion} - \underbrace{\overline{\overline{\underline{\underline{\tau}}_{ki}}}\nabla\alpha_k}_{Interfacial\ shear-stress\ dispersion} ,\end{aligned} \tag{2.10}$$

with quantities denoted with an i as quantities at the interface and Γ_k the mass transfer term. In order to accurately determine the mean values of the variables of interest, a common and simple assumption is to consider that all interfacial quantities are equal to the corresponding average quantities. However, this approach overlooks significant factors such as the interfacial pressure imbalance that contributes to drag and lift caused by the presence of bubbles, as well as the interfacial shear stress that influences skin drag.

In order to obtain the mean values of variables of interest, we have the classical field equations of mass and momentum for each field. The system must be closed by adding models for:

- Turbulent stress $\underline{\underline{\tau}}_k^T$, described in section 2.3,
- Interfacial transfers of mass Γ_k, described in section 2.2,
- Interfacial transfers of momentum $\mathbf{I}_k$, described in section 2.2.

Before modeling exchanges between phases, it is necessary to fix the number of phases to be modeled, which then imposes the number of equations. Modeling the dynamics of two-phase flows presents significant challenges due to the diverse range of scenarios encountered, including steady and transient behaviors, as well as losses in homogeneity and thermal effects. To address these complexities, researchers have proposed various modeling approaches. One notable approach is the four-fields model, initially introduced by Lahey and Drew [61]. The four-fields model partitions the flow into distinct regions, each associated with specific characteristics. These regions include the liquid phase, bubbly phase, droplet phase, and gas phase. Within this model, a continuous liquid field (lc) is managed to represent the presence of liquid, a continuous gas field (gc) captures the behavior of large gas pockets, a dispersed gas field (gd) models the dispersed bubbles, and a dispersed liquid field (ld) represents the behavior of liquid droplets (as illustrated in Figure 2.2).

While the four-fields model offers a comprehensive approach to capture the complex dynamics of two-phase flows, it can be computationally intensive. This model requires the solution of twelve balance equations, accounting for mass, momentum, and energy conservation. Additionally, closure models are needed to describe the interfacial transfers and interactions between the different fields. Implementing the four-fields model accurately demands careful consideration of the closure models and numerical techniques to ensure reliable predictions of the system behavior. To reduce the number of equations, Morel [86] proposed two degenerate four-fields to two-fields models that combines the Two-fluid and Drift-flux approaches. The first proposition involves using two dispersed fields of bubbles carried by liquid (bm) and droplets carried by gas (dm), and then drifting the mixture made by the dispersed field.

Another proposition is to use two separated fields for gas (g) and liquid (l), with each field being a hybrid of dispersed and continuous phases.

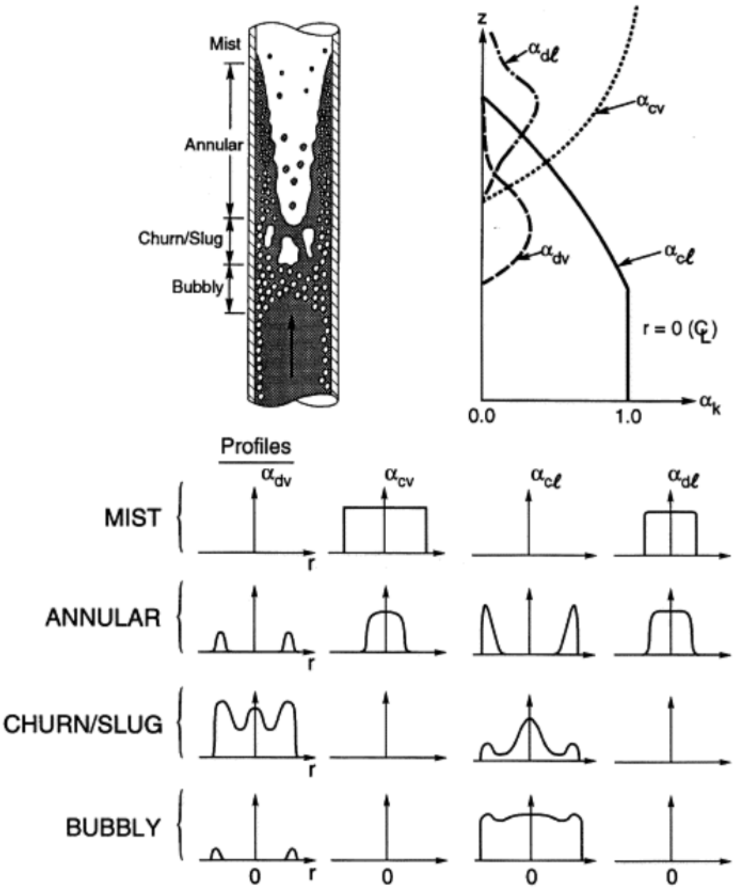

Figure 2.2: Principle of a four-field model handling any kind of topology of interest. From [61]. The subscripts v and l refer respectivly to vapor and liquid whereas d and c denote respectivly the dispersed and the continuous phases.

The benefit is the reduction of the number of closure models to 6 balance equations. However, these approaches have limitations, such as the inability to handle non-equilibrium physical phenomena.

The most preferred approach at present is to use a Two-fluid model and to neglect the droplets. This approach uses a continuous liquid field (l) and a hybrid continuous-dispersed gas field (g), which eliminates the need for a dispersed liquid model and reduces the number of closure models and balance equations. However, the challenge is to find a way to transition between dispersed and continuous phases in any topology. To address this challenge, some models deviate from the two-field model and use a three-field model with a continuous liquid field (lc), a dispersed gas field (gd), and a continuous gas field (gc). This approach can handle gas in any topology but still requires some model to transition between dispersed and continuous phases.

The model used in this work is based on the last approach, where continuous gas regions arise from large bubbles. The model uses a three-field model with a dispersed gas field for small bubbles ($g1$), a hybrid dispersed-continuous gas field ($g2$) to handle large bubbles and gas pockets, and a liquid continuous field (l). A summary of the various approaches is presented in Table 2.4

This model aims to capture the fundamental topological interfaces observed in experimental studies. Therefore, it is imperative to precisely model different aspects of the system, such as interfacial stress and turbulent stress. The upcoming section focuses on experimental obser-

Model	Field 1	Field 2	Field 3	Field 4
Four Fields	α_{gd}	α_{gc}	α_{ld}	α_{lc}
Hybrid Drift	$\alpha_{bm} = \alpha_{gd} + \alpha_{lc}$	$\alpha_{dm} = \alpha_{ld} + \alpha_{gc}$		
Hybrid Two-fluid	$\alpha_g = \alpha_{gd} + \alpha_{gc}$	$\alpha_l = \alpha_{ld} + \alpha_{lc}$		
TRITON	$\alpha_{g1} = \alpha_{gd1}$	$\alpha_{g2} = \alpha_{gd2} + \alpha_{gc}$	α_{lc}	

Table 2.4: Table of the different approaches for "all-regimes" modelling.

vations to fully comprehend their complexity. By studying experimental data, we can better understand and account for the dynamics associated with those terms and justify the number of phases computed in this work.

2.1.2 A bridge between experiments and equations

In the context of a liquid-gas system, such as in a gas-liquid flow, the interface behavior can be considered dispersed due to the presence of numerous relatively small bubbles. However, the local distribution of these bubbles can exhibit variations in shape and size. While providing a precise classification of interface characteristics can be challenging, it is possible to categorize them into five general categories, offering a broad understanding of their properties and behavior :

- The spherical bubbles that stands for small spherical bubbles.
- The distorted bubbles that stands for almost spherical bubbles (ellipsoidal). They source from little distortion of spherical bubbles.
- The cap bubbles that stands for cap shaped bubbles. They source from very distorted bubbles.
- The Taylor bubbles are bullet shaped large bubbles. Their development is conditional on the presence of walls.
- The churn-turbulent bubbles are very deformed bubbles because of high intensity turbulence. They can not be characterized by a specific shape because of their erratic interfacial topology.

By increasing their inner volume, bubbles modify their interface and allow local deformations, crossing the different types of bubbles. This deformability can be characterized by the Eötvös number Eo. The larger Eo is, the more the bubble is deformed. Furthermore, two bubbles can merge or one can be divided into 2, it is the coalescence/break-up mechanism. This mechanism is sourced by random collision, wake entrainment or turbulent impact. Then, it becomes more difficult to link their diameter with their interfacial surface with a simple expression. However, thanks to their topology, it is possible to characterised them by equivalent spherical bubble diameter that represents a spherical bubble of equivalent volume. As for the volume, an equivalent surface can be defined to represent the surface of the interface. While the minimum bubble diameter depends on injection conditions and turbulent intensity, the different categories can be segregated by maximum size/shape. To this end, Ishii and Zuber [84] proposed some bubbles size limit:

- For the distorted bubbles, the upper diameter limit D_{ld} before becoming cap-shaped: $D_{ld} = 4\sqrt{\frac{\sigma}{g\Delta\rho}}$, with $\Delta\rho = \rho_l - \rho_g$. In normal conditions, $D_{ld} = 11$ mm. It corresponds to $Eo = 15.77$.

- For the cap bubbles, the diameter upper limit D_{lc} is: $D_{lc} = 40\sqrt{\frac{\sigma}{g\Delta\rho}}$. In normal conditions, $D_{lc} = 11$ cm. It corresponds to $Eo = 1.57 \times 10^3$.

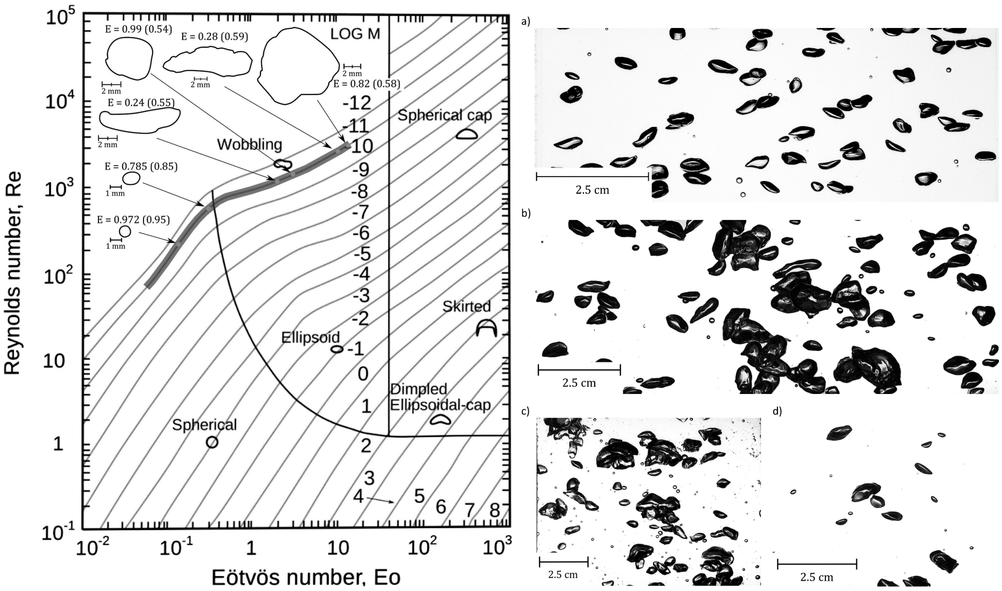

Figure 2.3: Shapes diagram and photos of different bubbles. (a) homogenous bubble column,(b) bubble plume,(c) airlift reactor,(d) single needle experiment. From T. Ziegenhein and D. Lucas [155].

The maximum stable Taylor bubble diameter imposes an upper limit on the bubble sizes. Configurations that have a diameter $D_H^* = \frac{D_H}{\sqrt{\frac{\sigma}{g\Delta\rho}}} > 40$ are considered "large" because no Taylor bubble can exist. This limit segregates "small" configurations" from "large" one. In large diameter configurations, small and large bubbles can coexist easily and create stronger turbulence. This turbulence enhances the mixture diffusion [122], can reduce the wall-peak [152], increase the bubble breakup. Furthermore, according to Smith and al. [121] the injection conditions can have strong effects on the flow pattern by creating already deformed bubbles at the inlet.
According to Shen and al.[115], in "large" diameter pipes a core-peak phase distribution pattern exits in most flow regimes and can be linked to the presence of large and deformed bubbles. On another hand, wall-peak distribution is met only for undisturbed bubbly flow or mostly one-dimensional flows. Indeed, the lift force acts on bubbles that moves in a shear flow with radial velocity gradient at low gas superficial velocity, creating a wall-peak. Furthermore, in upward flows, the average bubble size along the vertical axe increases due to the change of regime. According to Shawkat and al.[110], in large diameter pipes, the average liquid velocity profile is

more uniform than in single phase flow for wall-peak void fraction configurations whereas higher average velocities can be met in core-peak void fraction configuration. Furthermore, in [111], Shawkat and al. stand that the distribution of turbulence in bubbly flows is similar to that in single-phase flow but with a more uniform distribution in the core region, clue of a decrease of the turbulent diffusion in this region. However, in the near wall region, the intensity was found to be much higher than in single-phase. It is also essential to notice that a turbulence suppression process was observed for void fraction less than 5% and for liquid velocities above 1 m/s in the core.

In experimental studies the access to local information is limited. With the development of special probes configurations local flow characterization is increasingly accessible and comparisons with numerical simulation are becoming possible. Indeed for example with the four-sensor optical probe, that consists of one front optical sensor and three rear optical sensors allows getting good local information of the interfacial concentration. However, data is still very local. The probes can give the information of the presence of the bubbles, their time residence, their chord or their velocity.

The figures 2.4 and 2.5 are probe visualizations for different flow regimes in downward flow.

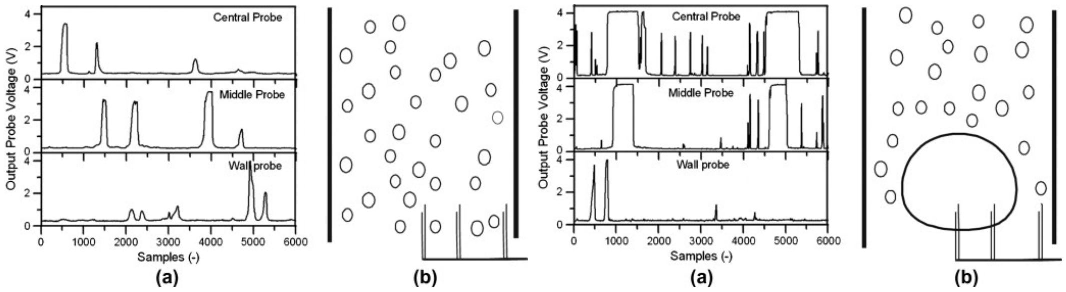

Figure 2.4: Visualization of probe signals for bubbly and cap bubbly regimes from [50].

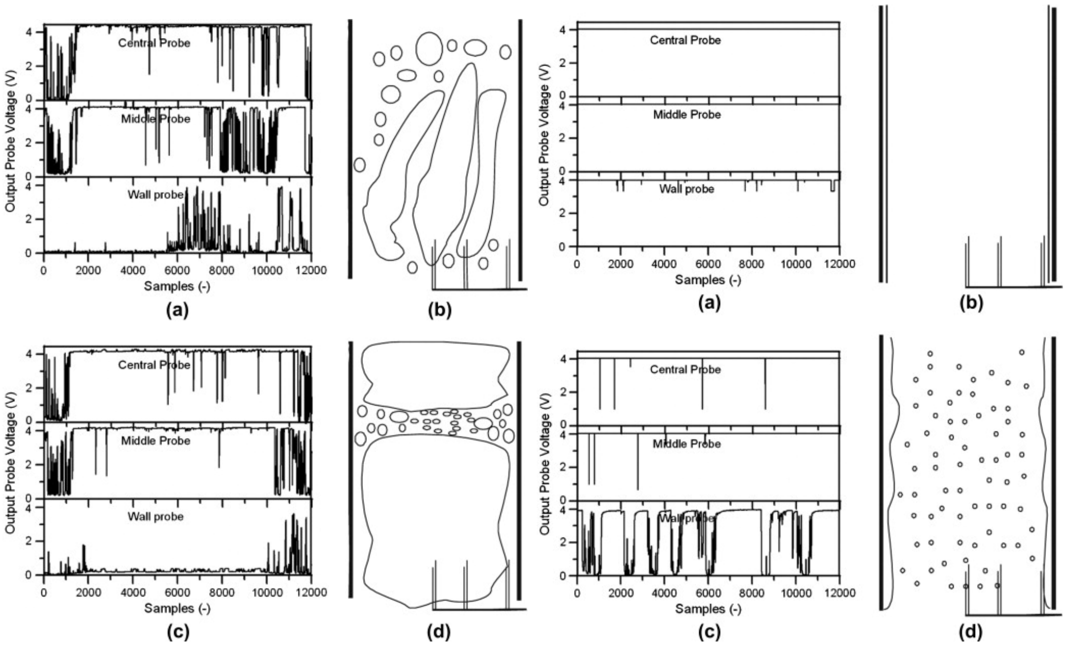

Figure 2.5: Visualization of probe signals for bubbly and cap bubbly regimes from [50].

It highlights noticeable differences between bubbles according to their shape or even for gas pockets. Those differences must be included in the model in order to capture "all-regimes" flow. Indeed, depending on the topology of the flow it can be homogeneous, heterogeneous, intermittent, quasi-static. However, the statistical approach erases the interfacial information so that the model by itself needs to include sources able to reproduce those very different configurations.

The figure 2.6 shows the different time signals of the void fraction for different regimes. It highlights that in order to get a complete description of cap-bubbly and churn turbulent flows, intermittency must be reproduced by the model. Then unsteadiness from quasi-periodic phenomena must be taken into account. In particular, Churn-turbulent flows depends on unsteadiness and turbulence. Then unsteady average equations are necessary to capture this regime.

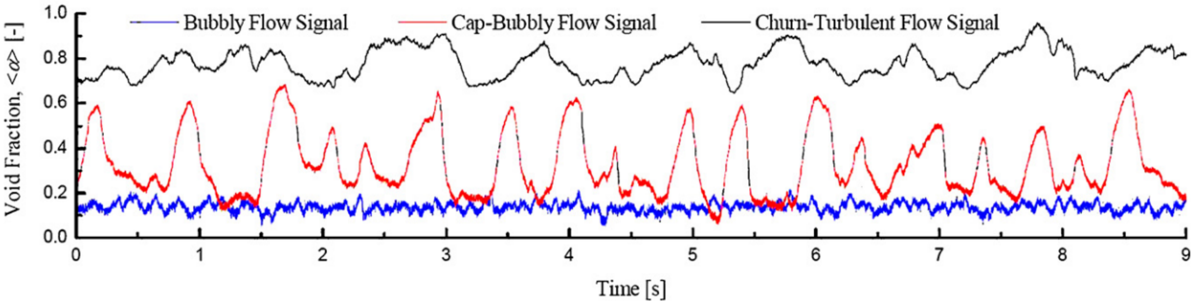

Figure 2.6: Differences between temporal signals according to the flow regime from Shlegel and al. [105].

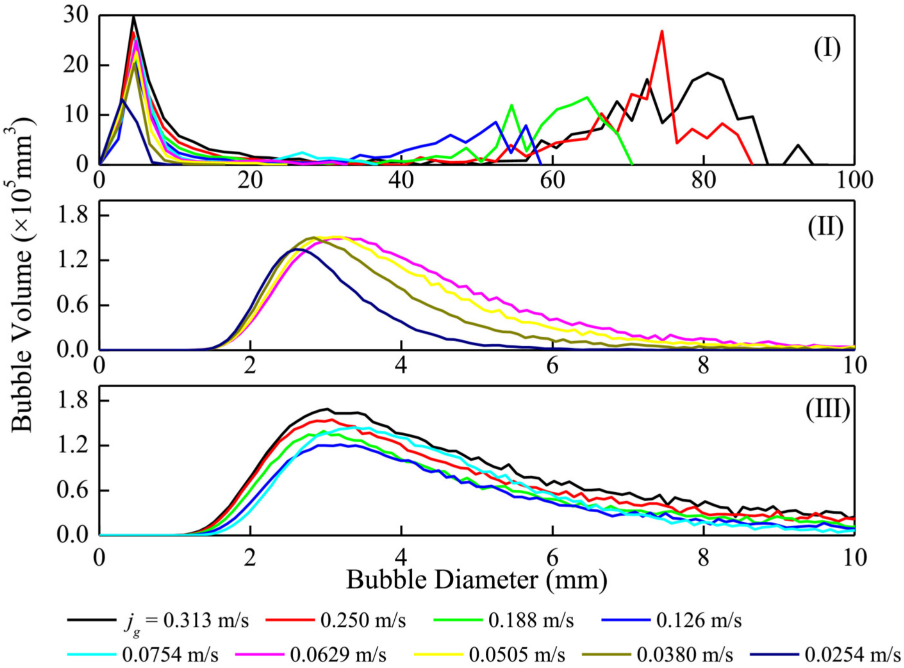

Figure 2.7: Bubble size distribution for liquid injection $j_l = 0.765$ m/s and different gas injections in a square channel of side 66 mm. Subfigures: (I) bubble size distribution with bin width of 2 mm for the bubbly and cap-bubly regimes, (II) bubble size distribution zoom with bin width of 0.1 mm for the bubbly regime, (III) bubble size distribution zoom with bin width of 0.1 mm or the cap-bubbly regime. From [153].

The figure 2.7 shows the statistical distribution of the bubble equivalent diameters in a square channel of side 66 mm for liquid injection $j_l = 0.765$ m/s and different gas injections from [153]. The first subfigure illustrates the distribution of the different flow conditions with a 2 mm bin for the bubbly and cap-bubbly regimes. The two other subfigures illustrate a zoom of the first subfigure respectively for the cap-bubbly and bubbly regimes. The bottom subfigure shows that in bubbly flows, any bubble is smaller than 10 mm, agreeing with the bubble limit of distorted bubbles and displays only one peak. In the top subfigure showing the cap-bubbly flows, the distribution displays two peaks, one around 3 mm and another one around $4 - 8\ cm$ whereas in between few bubbles are detected. It highlights a transition region between two distinct "groups" of bubbles. The small bubbles group and the large bubbles group. Furthermore, for this regime the small bubbles' distribution is wider than for the bubbly regime. It is due to the interactions between the two groups of bubbles. Then the model needs to capture the behavior of the two "groups" of bubbles and their interactions.

We have just presented the general averaged two-phase modeling for steam generator-type flows, highlighting the presence of two groups of bubbles and a field designed to replicate erratic, unsteady structures. However, the method of averages needs the inclusion of closure models to faithfully reproduce the encountered structures. To achieve this, two major families of closures must be studied: turbulent stresses ($\underline{\underline{T}}_k^T$) and interfacial models (Γ_k and $\mathbf{I}_k$). The following two sections deals with these two aspects.

2.2 Modeling of the interfacial transfers

2.2.1 Interfacial momentum transfers

As a reminder, the TRITON (Two-phase RegIme TransitiON) model handles two gas groups with separate momentum equations, and only the mean level of each group is computed. The transition between the dispersed and continuous gas fields is then determined based on the prediction of local void fraction and its gradient, enabling the identification of gas pockets thanks to the LIM. We finally get three fields as presented in Figure 1.18 :

- One dispersed field of small bubbles - less than 10.8 mm.
- One hybrid field of bigger dispersed bubble - more than 10.8 mm - and continuous field.
- One continuous liquid field.

Indeed, the dispersed approach proved to be inadequate when dealing with irregular interfaces. Interfaces that are significantly large and cannot be considered similar to a bubble present challenges for dispersed methods, and relying on averaging alone is insufficient to address them. To accurately capture the behavior of these interfaces and accurately simulate their interactions with the liquid field, a new method that incorporates an additional skin drag force is necessary. Various methods are based on a shared principle: initially, an interface detection method is managed to identify the location of the interface. This can be achieved through techniques such as Volume of Fluid (VoF [39]) methods, the use of blending functions, or other defined criteria. The LIM (Large Interface Model) method [16, 17, 18], for example, is based on detecting volume fraction gradients. In some cases, the interface detection method is coupled with an interface sharpening technique involving interface compression or blending functions. Subsequently, a specific drag model is handled, and some methods even incorporate surface tension effects. These approaches aim to enhance the accuracy of simulations by considering the characteristics of the interface and its dynamic behavior. Regarding the LIM method, the idea is to model the skin drag $\mathbf{I}_{LIM}$ in the normal direction $\mathbf{n}$ to the large interface using the classical drag force F^D and in the tangential direction $\mathbf{t}$ using a friction model F^f that is specific to large interfaces. The underlying hypothesis is that the interface behaves like a moving wall.

$$\mathbf{I}_{LIM} = F^D\mathbf{n} + F^f\mathbf{t}, \tag{2.11}$$

$$F^f = \rho_g U_g^{*2} a_{i,LIM}, \tag{2.12}$$

with U_g^{*2} the friction velocity computed thanks to suitable large-interface friction laws and $a_{i,LIM}$ an evaluation of the interfacial area concentration.

$$a_{i,LIM} = \frac{\sum_{i=1,3} \nabla_i \alpha_{gi} V_i}{\sum_{i=1,3} \alpha_{gi} V_i}, \tag{2.13}$$

with V_i the volume of the cells used in the LIM.

As previously mentioned, the expression for the averaged interfacial momentum transfers, excluding mass transfers, can be expressed as follows :

$$\begin{aligned}\mathbf{I}_k = \; & \underbrace{\sum_j a_{ij}(\overline{\overline{P_{ki}}} - P_k)\mathbf{n}_k}_{Interfacial\ pressure\ imbalance} + \underbrace{\sum_j a_{ij}(\underline{\underline{\tau}}_k - \overline{\overline{\underline{\underline{\tau}}_{ki}}})\mathbf{n_k}}_{Interfacial\ shear-stress\ imbalance} \\ & + \underbrace{\overline{\overline{P_{ki}}}\nabla\alpha_k}_{Interfacial\ pressure\ dispersion} - \underbrace{\overline{\overline{\underline{\underline{\tau}}_{ki}}}\nabla\alpha_k}_{Interfacial\ shear-stress\ dispersion} .\end{aligned} \tag{2.14}$$

Regarding the dispersed forces, the expression for the averaged interfacial momentum transfers depends on the hydrodynamical models, denoted as M^k. :

$$\mathbf{I}_k = \underbrace{\sum_j a_{ij}\mathbf{M}^k}_{Hydrodynamical\ forces} + \underbrace{\mathbf{M}^k\nabla\alpha_k}_{Interfacial\ dispersion\ force} . \tag{2.15}$$

Two types of hydrodynamical forces F are classically used : the steady forces like the Drag and the Lift and the transient forces like the Added mass forces. The interfacial dispersion forces can be seen as transient forces because it tries to reproduce the spread by fluctuations of the steady forces. As suggested in [85], the simplest way to model the momentum transfer between the gas and the liquid $I_{l\to g}$ is to express them as a linear combination of several forces $F^k_{l\to g}$. The momentum transfers are then proportional to the void fraction α_g and the representative volume of the bubble V_g :

$$\mathbf{I}_{l\to g} = \sum_k \mathbf{F}^k_{l\to g} = \sum_k \frac{\alpha_g}{V_g}(\mathbf{M}^k_g). \tag{2.16}$$

Drag force

The standard drag force $F^D_{l\to g}$ accounts for the form drag and the viscous friction. The model developed by Ishii and Zuber [84] was determined with single bubble flow of different shapes and has a strong effect on terminal velocities. However, the model doesn't seem to capture transient bubble deformation, contamination or swarm effect. This term stands for the force that goes against the movement of bubbles in the flow direction. It is expressed as :

$$\mathbf{F}^D_{l->g} = -\frac{1}{8} a_i \rho_l C_D (\mathbf{U}_g - \mathbf{U}_l)|U_g - U_l|, \tag{2.17}$$

with $a_i = \frac{6\alpha_g}{D_{sm}}$ the interfacial area concentration of the gas, D_{sm} the Sauter mean diameter and C_D the drag coefficient. This drag coefficient depends on the type of bubble. For ellipsoidal bubbles the coefficient is $C_D = min(C_{Dellipse}, C_{Dcap})$ with :

$$C_{Dellipse} = \frac{2}{3} D_{sm} \sqrt{\frac{g|\rho_g - \rho_l|}{\sigma}} \left(\frac{1 + 17.67(1-\alpha_g)^{9/7}}{18.67(1-\alpha_g)^{3/2}} \right)^2. \tag{2.18}$$

For cap and churn bubbles, the drag coefficient is calculated as follows:

$$C_{Dcap} = \frac{8}{3}(1-\alpha_g)^2. \tag{2.19}$$

Figure 2.8 illustrates the behavior of the two previous drag coefficients, for an ellipsoidal bubble of 4 mm and a cap bubble.
The previous correlations are correct in turbulent regions where $Re_b > 1000$, then in viscous regions another correlation must be used. For low velocity area like behind cylinders and in the near-wall region, another drag coefficient can be used:

$$C_{Dlow} = \frac{24}{Re_b}(1 + 0.15 Re_b^{0.687}). \tag{2.20}$$

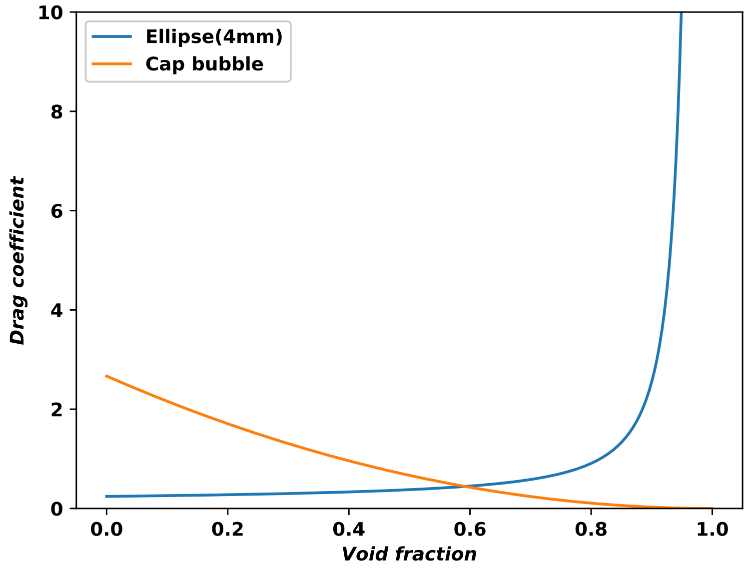

Figure 2.8: Drag coefficient according to the value of α.

Other models were proposed to take into account the shear induced[68], the bubble deformation [99] or even swarm effects [76]. However, those models still need validation over a wide variety of configurations and the contribution of these complex models compared to simpler ones is necessary to demonstrate their usefulness.

Added mass force

The added mass force $F_{l\to g}^{AM}$ accounts for the apparent mass from relative acceleration. This transient force is often used to stabilize the simulation but is based on a real physical process. The model used was developed by Zuber [90]. However, it doesn't take into account effect of the bubble size. This term stands for the inertia of the liquid due to the bubble acceleration. It is expressed as:

$$\mathbf{F}_{l->g}^{AM} = -C_{AM}\alpha_g \frac{1+2\alpha_g}{1-\alpha_g}\rho_l\left(\frac{D\mathbf{U}_g}{Dt} - \frac{D\mathbf{U}_l}{Dt}\right), \tag{2.21}$$

with C_{AM} the added mass coefficient often taken as equal to 0.5.

Lift force

The lift force $F_{l\to g}^{L}$ accounts for the relative velocity in the normal direction, developed by Auton [134] with the correlation of Tomiyama [133]. Actually, the lift force is very sensitive about bubble size and can even change of sign. The Tomiyama correlation well capture the sign change for air-water flows at ambient conditions (around 5.8mm) and so seems to be the best to use. However, the model doesn't seem to capture turbulence interaction, swarm effect or near-wall interaction. This term stands for the force that goes against the movement of bubble normal to the flow direction. An overview of different models for the lift coefficient is proposed in [36]. It is expressed as :

$$\mathbf{F}_{l->g}^{L} = -C_L\alpha_g\rho_l(\mathbf{U}_g - \mathbf{U}_l)\times(\nabla\times\mathbf{U}_l), \tag{2.22}$$

with C_L the lift coefficient. In case of potential flow, this coefficient is equal to 1/2 (Auton, 1987). It has been empirically modeled by Tomiyama et al. (2002) as follow :

$$C_L = \begin{cases} min(0.288tanh(0.121Re), 0.00105Eo_H^3 - 0.0159Eo_H^2 - 0.0204Eo_H + 0.474) & if\ Eo_H < 4, \\ 0.00105Eo_H^3 - 0.0159Eo_H^2 - 0.0204Eo_H + 0.474 & if\ 4 \leq Eo_H \leq 10, \\ -0.27 & if\ 10 < Eo_H, \end{cases} \tag{2.23}$$

with $Eo_H = \frac{g(\rho_g-\rho_l)D_H^2}{\sigma}$, $D_H = D_b(1+0.163Eo^{0.757})^{1/3}$, $Eo = \frac{g(\rho_g-\rho_l)D_b^2}{\sigma}$ and D_b the bubble diameter.

Figure 2.9 illustrates the behavior of the lift coefficient according to the value of the diameter for a velocity of 0.332 m/s.

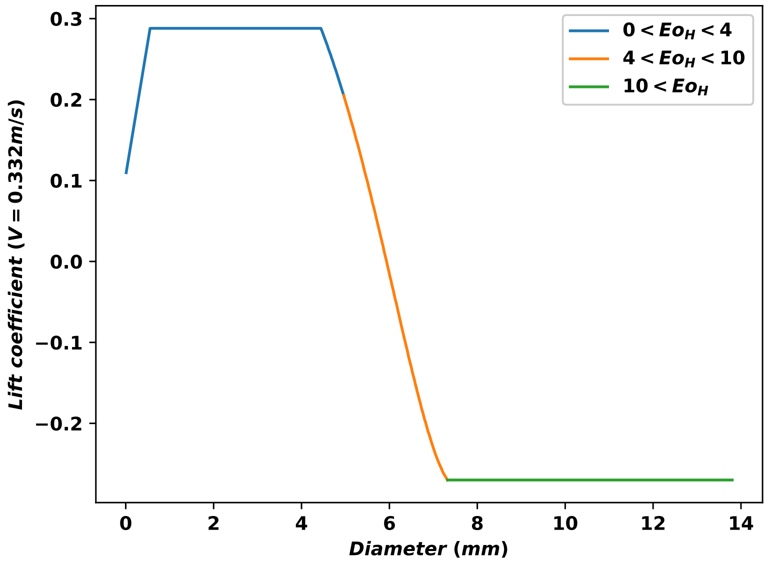

Figure 2.9: Lift coefficient according to the value of the diameter for a velocity of 0.332 m/s.

The strength of this model is that it distinguishes the transversal behavior of small and large bubbles. It is then adapted for the all-regimes used for the two groups. Other models were proposed to take into account the low velocities [67, 36] and wall effects [68]. However, as for the Drag force their usefulness need to be demonstrated in a wide variety of configurations.
Hayashi and al. [33] proposed an interesting new correlation for the lift coefficient, gathering several previous works and that can reproduce the negative lift. The first assumption is based on the calculation of Legendre standing that the lift depends on a pure lift contribution and a drag contribution that allows the total lift to be negative :

$$C_L = C_L^S - f(\chi, Re_b, M)C_D. \tag{2.24}$$

Then C_L^S is the euclidian norm between the low Reynolds contribution C_L^{SL} and the high Reynolds contribution C_L^{SH}.

$$C_L^{SL} = \frac{6}{\pi}\frac{2.255}{\sqrt{SrRe_b}(1+0.2\frac{Re_b}{Sr})^{3/2}}, \tag{2.25}$$

$$C_L^{SH} = \frac{1}{2}\frac{1+\frac{16}{Re_b}}{1+\frac{29}{Re_b}}, \tag{2.26}$$

with $Re_b = \frac{UrD_{sm}}{\nu_l}$ and $Sr = \frac{\omega D_{sm}}{Ur}$.
Then there is a distinction between the viscous $\mu - regime$ and the surface tension- inertial $\sigma - i\ regime$. Regarding the $\mu - regime$, the correlation depends on the aspect ratio χ and the Morton number $M = \frac{\mu_L^4 \Delta\rho g}{\rho_L \sigma^3}$. Its expression is :

$$C_L = C_L^S - \frac{g(M)(\chi - 1)^{h(M)}}{Re_b} C_D^*, \tag{2.27}$$

with $g(M) = 500exp(-6M^{0.0735})$, $h(M) = 3.46exp(-5.M^{0.191})$ and $C_D^* = \frac{16}{Re}(1+0.25\chi^{1.9}Re_b^{0.32}$.
Regarding the $\sigma - i\ regime$, the correlation depends on the Eotvos E_o and on the aspect ratio

χ. Its expression is :

$$C_L = C_L^S - 0.048\omega_{max}\frac{E_o + 4}{E_o + 16\frac{\chi^2-1}{\chi^{8/3}}}C_D, \tag{2.28}$$

with the maximum vorticity $\omega_{max} = \frac{2\chi^{5/3}(\chi^2-1)^{3/2}}{\chi^2 cos(\chi^{-1}) - \sqrt{(\chi^2-1)}}$.
In order to avoid discontinuities, a fast increase of the lift and to get a criteria for the transition between the $\sigma - i$ *regime* and the $\mu -$ *regime*, we use:

$$\chi = min(\chi_r, \chi_e), \tag{2.29}$$

$$\chi_r = 1 + \frac{9}{64}We + \frac{0.04We^2}{\sqrt{3.7 - We}}, \tag{2.30}$$

$$\chi_e = 1 + 0.62We^{0.376}. \tag{2.31}$$

Then, the transition happens when $We = \frac{\rho_L U_r^2 D_{sm}}{\sigma} \approx 3.121$.

Turbulent dispersion force

The turbulent dispersion force $F^T_{l\to g}$ tries to model the transport of the dispersed phase by large fluid turbulent eddies. Several original models were proposed. For example, on one hand, the complex model proposed by Simonin et al. [118] is based on Tchen‘s theory of two-phase dispersed turbulence. On the other hand, Lopez [73] proposed a diffusive model with a simple diffusive constant. Another interesting model was proposed by Burns[5] is based on the Favre average of the drag force. The Generalized Turbulent Dispersion developed by J.Laviéville and al. [64] is used because it gathers multiple already working dispersion models and so seems to be more general. It depends on local variables that reduces the diffusion in the near wall-region. However, this model is not widespread so that it still lacks of diversity in validation. It is expressed as :

$$\mathbf{F}^T_{l->g} = -GTD\rho_l\frac{2}{3}k_l\frac{\partial}{\partial x_i}\alpha_g. \tag{2.32}$$

$$GTD = (f^D\tau^t_{lg} - 1)\frac{b + \eta_r}{1 + \eta_r} + C_{AM}\frac{b^2 + \eta_r}{1 + \eta_r}, \tag{2.33}$$

$$\eta_r = \frac{\tau^t_{lg}}{\tau^F_{lg}},\ b = \frac{\rho_l + \rho_l C_{AM}}{\rho_g + \rho_l C_{AM}},\ \tau^t_{lg} = \frac{3}{2}C_\mu\frac{k_l}{\varepsilon_l}(1 + \beta_1\frac{V_r^2}{k_l})^{-1/2}, \tag{2.34}$$

$$\tau^F_{lg} = \frac{1}{f^D}(\frac{\rho_g}{\rho_l} + C_{AM}), f^D = \frac{3}{4}\frac{C_D}{D_{sm}}\rho_l U_r, \tag{2.35}$$

$$\beta_1 = (\frac{1}{2} + \frac{3}{4}C_0) = 2.07,\ C_0 = 2.1. \tag{2.36}$$

β_1 represents the ratio between the Lagrangian time and the Eulerian integral time scales. C_0 is called Kolmogorov constant.

Wall lubrication force

The wall lubrication force $F_{l\to g}^{WL}$ accounts for the redistribution of the velocity in the near-wall regions that the lift force can not take into account. Most of the models are based on the lubrication theory. The model developed by Tomiyama [131] is used because it is the most used and validated one. However, this model needs the information of the hydraulic diameter. To avoid this problem a new formulation was proposed to make it cancel at a distance D_b and inspired by the wall lubrication of Lubchenko and al. This term stands for the force that repel bubble from the wall. It is expressed as follows :

$$\mathbf{F}_{l->g}^{WL} = C_W \rho_l |U_g - U_l|^2 \mathbf{n}_w, \tag{2.37}$$

$$C_W = C_W^* \frac{D_b}{2} \left(\frac{1}{y_w^2} - \frac{1}{(D_h - y_w)^2} \right), \tag{2.38}$$

$$C_W^* = \begin{cases} 0.47 & if\ Eo_H < 1, \\ e^{-0.933Eo+0.179} & if\ 1 \leq Eo_H < 5, \\ 0.00599Eo - 0.187 & if\ 5 \leq Eo_H \leq 33, \\ 0.179 & if\ 33 \leq Eo_H. \end{cases} \tag{2.39}$$

Figure 2.10 illustrates the lubrication coefficient according to the value of the diameter.

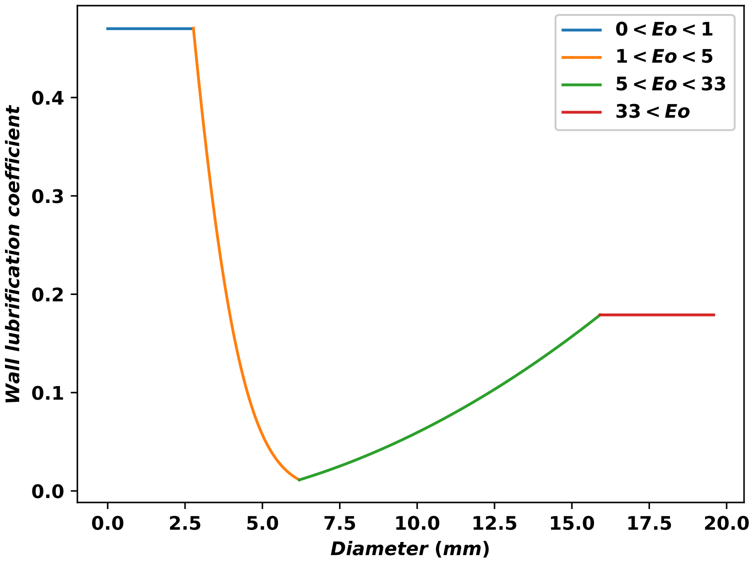

Figure 2.10: Lubrication coefficient according to the value of the diameter.

The problem with this force is that it depends on the hydraulic diameter. In case of infinite hydraulic diameter compared to the bubble size, this force still has effect on long range. Simulations showed that it is necessary to have a repelling force near the stagnation point of a cylinder to prevent gas stagnation and numerical problem. Then the aim of this force is just to prevent this phenomenon. It is then modified as follows by replacing the hydraulic diameter by twice the mean Sauter diameter and to calibrate the force to match the infinite hydraulic diameter strength at a radius of the wall :

$$C_W = \alpha_g \frac{D_b}{2} C_W^* \frac{1 - y_w^*}{y_w^{*2}}\ if\ y_w < D_b,\ 0\ if\ not. \tag{2.40}$$

The strength of this formulation is that it allows getting a liquid lubrication on few cells in the near wall region and doesn't always induce a wall peak. A force that try to reproduce the bouncing due to the presence of the wall, called Bubble-Wall Collision Force, was proposed by Chuang and Hibiki [11]. However, it depends on a pre-factor that still needs validation over a wide range of configurations.
Another wall lubrication force popular F_p^R accounts for the bubble void fraction gradient within a bubble. It was proposed by Lubchenko and al. [71]. It was derived for the regularization of the turbulent dispersion force in the near-wall region. The result was compared against Liu and Bankoff database. It allows imposing a parabolic void fraction profile in the near wall region. It is expressed as follows with the use of the generalized turbulent dispersion :

$$\mathbf{F}_{l->g}^{WR} = \frac{2}{3} GTD \rho_l k_l \frac{a_i}{6} \frac{1-2y_w^*}{y_w^* - y_w^{*2}} \; if \; y_w^* < 0.5, \; 0 \; if \; not. \tag{2.41}$$

The main problem with this force is that it is a static force that is not really suitable for flows around cylinder. Indeed, this force is not able to repulse the dispersion toward the stagnation point. In case of low flow rate, the pressure do not repulse the bubbles, this force neither and so allow non-physical local stagnant high void fraction in few cells around the stagnation point.

An essential aspect of modeling the coupling forces between the liquid and gas phases is accurately predicting the interfacial area concentration. Indeed some forces are proportional to the interfacial area concentration a_i ($\mathbf{F}_{l\to g}^k \propto a_i$) or to an equivalent diameter D_{sm} ($\mathbf{F}_{l\to g}^k \propto D_{sm}$). To tackle this challenge, it is beneficial to introduce a new equation that governs the transport of the interfacial area concentration. With this additional equation, it becomes possible to explicitly account for the transport of interfacial area concentration to get $\mathbf{I}_k$ and the mechanisms of bubbles coalescence and break-up to get Γ_k.

2.2.2 Obtaining the Interfacial Area Transport Equation

The two-fluid model, due to averaging, can't accurately represent the volume and presence of interfaces. To address this limitation, an alternative approach is adopted, assuming that the two fluids can be segregated into distinct roles: a continuous stage fluid and a dispersed local actor fluid that can dynamically influence the stage fluid. In this context, the dispersed fluid is represented as a population of bubbles with varying diameters, which serves as a topological characteristic for the stage fluid. The dispersed fluid is characterized by two interconnected attributes: a distribution of bubble diameters and the concentration of interfaces.
We can define the Sauter-Mean Diameter of the distribution f_d of sizes D as :

$$D_{sm} = \frac{\int f_d D^3 dD}{\int f_d D^2 dD}, \tag{2.42}$$

the area concentration per unit of volume A_i so that in dispersed bubbly hypothesis $A_i = \pi D^2$, the interfacial area concentration $a_i = \int f_d A_i dV$ and the void fraction α. The relation between those variables is :

$$D_{sm} = \frac{\int f_d D^3 dD}{\int f_d D^2 dD} = 6 \frac{\int f_d V dV}{\int f_d A_i dV} = \frac{6\alpha}{a_i}. \tag{2.43}$$

Then two approaches are commonly used to compute the interfacial area concentration. The first naive method, often called monodispersed, is to use flow regime dependent correlations and regime transition criteria based on experimental data[113]. However, this approach can not reproduce the dynamics of developing flows [57], transition regimes and inlet effects. Furthermore, by nature, experimental data correlations can suffer of high percentage of errors, are limited in operational conditions and geometries and cause artificial discontinuities and numerical instability [35].

The second approach, often called polydispersed, is based on a differential equation for the interfacial area concentration that can reproduce dynamic phenomena, eliminate discontinuities and allow modeling of bubble mechanism. The distribution of diameters and of interfacial presence can be modelled by a Boltzmann transport equation of the distribution called population balance equation.

Then, two approaches can be used to solve the problem of linked diameter/interfacial concentration : the Method of Momentums (MoM) [150] or size-group methods [58] .

The MoM is the most mathematically elegant method. With this method the distribution f_d is discretized into classes. We can then solve the Boltzmann equation for each class and then compute the moment associated (surface, diameter) for the equations. However, the different moments are convected by the same velocity whereas it has no physical meaning.

While the idea of the MoM is to transport a discrete distribution of pics, the idea behind the size-group methods is to fix the groups so that the distribution stays continuous but to transport only the mean level. Then the distribution is discretised into fixed classes so that we can define the fraction α_i and its corresponding level of each class. The difference with the MoM is that each class has its proper velocity. Because experimental data shows differences in velocity for specific bubbles classes, the size-group method is used. Two separated size-group methods was proposed. One based on having an arbitrary number of groups to reproduce a distribution, referred as MUSIG of i-MUSIG [139, 20, 69] and the other reproducing the distribution thanks to the Mean Sauter diameter referred as IATE. The generalized Interfacial Area Transport Equation (IATE) developed by Kocamustafaogullari and Ishii [55, 56] is obtained by multiplying the number density transport equation by the particle surface area A_i, integrating over the range of possible volumes and simplifying the terms to get a simple differential equation for the IAC (cf. [85]). The general expression for adiabatic flows with $\psi_j^{internal}$ a source term and $\psi_j^{intergroup}$ an intergroup term is then :

$$\frac{\partial a_{ik}}{\partial t} + \underbrace{\nabla.(\mathbf{U}_k a_{ik})}_{Transport} = \underbrace{\frac{2}{3}\frac{a_{ik}}{\alpha_k}\frac{D\alpha_k}{Dt}}_{Volume\ change} + \underbrace{\sum_j \psi_{kj}^{intergroup}}_{Intergroup\ sources} + \underbrace{\sum_j \psi_{kj}^{internal}}_{Internal\ sources} . \tag{2.44}$$

A particular case of the solution can be obtained if we consider two groups of bubbles. For example, experimentally a limit can be observed between quasi-spherical and distorted bubbles. Then we can separate the distribution of those groups into 2 distinct distributions.

From the Boltzman transport equation of the distribution function $f_d(X_d, \xi_d, t)$, with external parameters X_d, internal variables χ_d and S_d source term:

$$\frac{\partial f_d}{\partial t} + \nabla(f_d\frac{dX_d}{dt}) + \frac{\partial}{\partial \xi_d}(f_d\frac{d\xi_d}{dt}) = S(X_d, \xi_d, t). \tag{2.45}$$

Then we multiply the surface area of the particle A_i, intergrate over the volume of all particles between $Vmin$ and $Vmax$. Then by switching integrals and derivative in the left hand of the equation we get for the group k of velocity U :

$$\int_{Vmin}^{Vmax}(\frac{\partial f_d}{\partial t} + \nabla(f_d\frac{dX_d}{dt}) + \frac{\partial}{\partial \xi_d}(f\frac{d\xi_d}{dt}))A_i d\xi_d = \frac{\partial a_{ik}}{\partial t} + \nabla(a_{ik}U_k) + \int_{Vmin}^{Vmax}\frac{\partial}{\partial \xi_d}(f_d\frac{d\xi_d}{dt})A_i d\xi_d. \tag{2.46}$$

In order to simplify the formulation, we can assume that the time rate of change in the relative particle volume is independent of its volume, then :

$$\int_{Vmin}^{Vmax} \frac{\partial}{\partial \xi_d}(f_d \frac{d\xi_d}{dt}) A_i d\xi_d = \frac{1}{V}\frac{dV}{dt}\int_{Vmin}^{Vmax} \frac{\partial f_d \xi_d}{\partial \xi_d} A_i d\xi_d = \frac{1}{V}\frac{dV}{dt}(f_{dmax}A_{max}V_{max} - f_{dmin}A_{min}V_{min} - \int_{Vmin}^{Vmax} f_d V dA_i). \tag{2.47}$$

By assuming the distribution large enough we can neglect the min contribution for the first group and the max contribution for the second group. The term $\frac{1}{V}\frac{dV}{dt}$ is simply the dilatation of volume and can be express thanks to the mass conservation in isothermal configurations by :

$$\frac{1}{V}\frac{dV}{dt} = \frac{1}{\alpha}\frac{D\alpha}{Dt}. \tag{2.48}$$

By reminding that $a_i = \int f A_i dV$, $V = \frac{\pi D^3}{6}$ and $A_i = \pi D^2$ then :

$$\int f_d V dA_i = \int f_d A_i \frac{D}{6} dA_i = \int f_d A_i \frac{D}{6}\frac{4}{D} dV = \frac{2}{3} a_i. \tag{2.49}$$

Then [52] proposed to model the intermediate (up range for the first group and down range of the second group) range between the two groups as:

$$A_{ic} f_{dc} V_c = \chi_d a_{i1} (\frac{D_{smc}}{D_{sm1}})^2. \tag{2.50}$$

Finally, for the first group we get

$$\frac{\partial a_{i1}}{\partial t} + \underbrace{\nabla(a_{i1}\mathbf{U}_{g1})}_{Transport} = \underbrace{\frac{2}{3}\frac{a_{i1}}{\alpha_{g1}}\frac{D\alpha_{g1}}{Dt}}_{Volume\ change} \underbrace{-\chi_d(\frac{D_{smc}}{D_{sm1}})^2 \frac{a_{i1}}{\alpha_{g1}}\frac{D\alpha_{g1}}{Dt}}_{D_{smc}\ group\ shift} + \underbrace{\sum_j \psi_{1j}^{intergroup}}_{Intergroup\ sources} + \underbrace{\sum_j \psi_{1j}^{internal}}_{Internal\ sources}. \tag{2.51}$$

And for the second group, we get :

$$\frac{\partial a_{i2}}{\partial t} + \underbrace{\nabla(a_{i2}\mathbf{U}_{g2})}_{Transport} = \underbrace{\frac{2}{3}\frac{a_{i2}}{\alpha_{g2}}\frac{D\alpha_{g2}}{Dt}}_{Volume\ change} \underbrace{+\chi_d(\frac{D_{smc}}{D_{sm1}})^2 \frac{a_{i1}}{\alpha_{g1}}\frac{D\alpha_{g1}}{Dt}}_{D_{smc}\ group\ shift} + \underbrace{\sum_j \psi_{2j}^{intergroup}}_{Intergroup\ sources} + \underbrace{\sum_j \psi_{2j}^{internal}}_{Internal\ sources}. \tag{2.52}$$

The intergroup mass transfer is obtained by a similar way with intergroup mass source terms η^{inter} but by modeling the transfer of volume in the intermediate range as $\chi_d a_{i1}(\frac{D_{smc}}{D_{sm1}})^3$:

$$\Gamma_{g1-g2} = \rho_g(\underbrace{\sum_j \eta_j^{inter}}_{Intergroup\ sources} \underbrace{+\chi_d(\frac{D_{smc}}{D_{sm1}})^3 \frac{a_{i1}}{\alpha_{g1}}\frac{D\alpha_{g1}}{Dt}}_{D_{smc}\ group\ shift}). \tag{2.53}$$

χ_d is equal to 1 for a uniform distribution profile. Indeed, because there is no prior determination of the form of the solution of the distribution, the easiest from to consider is a uniform distribution. However, the intermediate sliding between the distribution is not the dominant term. Then the complexity is assumed to arise from source terms. Although a modified form of this term was proposed in [11], it is not suitable for implementation in our model due to the constraint $1 - \chi_d(\frac{D_{smc}}{D_{sm1}})^3 > 0$ incompatible with $\chi_d = 1$.
An accurate state of the art of the progress of the IATE model for one-group [143, 34, 52, 103,

92, 112] and for the two-group model [35, 28, 123, 125, 48, 37] among the last decades was proposed by Kim et al.[53]. We notice that formulations based on the Drift-flux approach was proposed for the one-group[129] and the two-groups [4] models.
During the averaging process proposed in [51] , two new terms emerged from the instantaneous equation: a diffusion term and a lift term. For example, the diffusion term can be implemented as :

$$K\sqrt{u'^2}D_{sm}\nabla a_i = K\sqrt{\frac{2k}{3}}D_{sm}\nabla a_i, \tag{2.54}$$

with K a constant equal to 1/3.
However, it is essential to note that these terms have not yet been fully validated in various configurations [97], leading to the decision not to include them initially in the analysis.

An significant part of those models is the sources terms. The principle to get them is to first model the interactions based on simple assumptions and mechanistic phenomena [124, 42, 120, 88, 107, 114, 138]. Then the model constants are calibrated and tested on a large variety of experiments [45, 91, 23, 21]. The following section is dedicated to those source terms.

2.2.3 Source terms

Source terms are essential to reproduce bubble mechanism. All source term models are based on five categories of mechanism: the Random Collisions (RC), the Wake Entrainment (WE), the Turbulent Impacts (TI), the Shearing-off (SO) and the Surface Instability (SI). The RC is a bubble coalescence phenomenon where 2 bubbles collide and merge because of a turbulent eddy of comparable size. The WE happens when one smaller bubble is in the wake of a bigger one, accelerates and collides it. The TI is due to turbulent eddies that break-up bubbles. The SO is a break-up phenomenon that source from the shearing-off of cap bubbles. The SI is due to the break-up of large bubbles due to their surface instability.
The number of processes and the dimensionless coefficient can strongly differ from one model to another. This work focuses on 5 models that are commonly used or available in CFD codes:

- The Sun and al. model [124] was developed for a 2 group configuration with a 200 × 10 mm^2 confined rectangular channel data [126]. The effect of the wall is then very significant. It was performed for liquid superficial velocity between $0,32$ and $2,84$ m/s and gas velocity between $0,39$ and $2,01$ m/s. It deals with cap-bubbly and churn-turbulent flows.

- The Smith and al. [120] model was developed for a 2 group configuration with 0.102 mm and $0,152$ mm diameter pipes. It deals with bubbly, cap-bubbly and churn-turbulent flows[121] (see also [28, 22]).

- The Schlegel and al. model [107] was developed for a 2 group configuration with large diameter channels [106]. It deals with bubbly and cap-bubbly flows. Several constitutive relations and correlations were used to tune this model.

- The Kuidjo model [83] was developed for a 2 group configuration to compute real fluid dynamics in channel flows. It uses Smith model with Sun model's dimensionless coefficients (see appendices A.2).

- The Ruyer-Seiler model [100] is a MoM model for 1 group configurations. It uses a quadratic law for the distribution, inspired by experimental data.

The source terms used in this thesis are Kuidjo's terms. An example of dynamics is presented in the following figure 2.11.

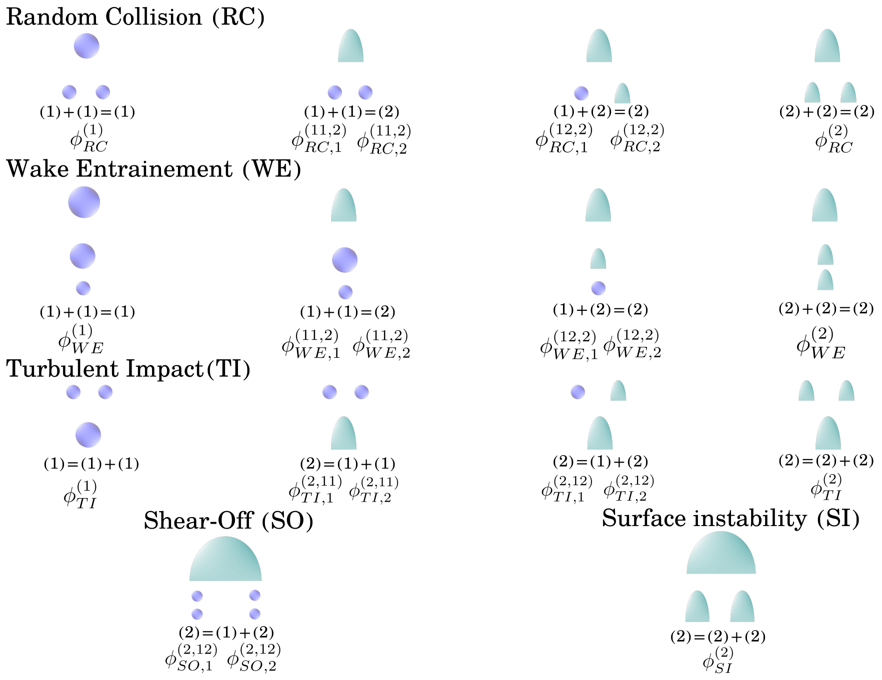

Figure 2.11: Representation of 2 group bubble mechanism.

The primary mechanism for coalescence is random collisions between bubbles caused by turbulent eddies. Binary collisions are modeled to simplify the expression for the source terms. The model is based on turbulent variables and activation-like models.
The second major mechanism is the entrainment of bubbles in the wake of preceding bubbles. The acceleration due to the wake may lead to collisions. The model is based on relative velocities and probability of meeting.
As a mirror mechanism to random collision coalescence, the primary mechanism for break-up is turbulent impacts due to turbulent eddies. The eddies that can lead to break-up are assumed to have a comparable size to the bubble. Larger eddies can carry smaller bubbles without causing break-up, and smaller eddies do not carry enough energy to induce break-up. The models are based on turbulent variables and efficiency models that depend on the critical Weber number to determine their stability with respect to break-up.
Another break-up mechanism is the shearing-off of Group 1 bubbles at the base of large cap bubbles. In highly viscous flows, cap bubbles can get thinner around their base, giving birth to small bubbles being sheared off. The model is based on the balance between surface tension and interfacial shear force. It includes surface tension variables and efficiency based on Weber numbers.
The last break-up mechanism modeled is surface instability. When coalescence leads to a bubble larger than the maximum stable bubble limit, the induced bubble is unstable and disintegrates.

The accurate prediction of turbulent quantities is crucial for determining both the forces and source terms of the IATE. Consequently, it becomes necessary to handle an appropriate modeling approach for the turbulent stresses. This modeling is discussed in detail in the following section.

2.3 Modeling of the turbulent stress

2.3.1 Fundamentals of single-phase turbulence models

The turbulent stress term is derived from the process of averaging the momentum equation of the Navier-Stokes equations. While the turbulence tends to expand the range of length scale, the averaged approach tends to erase the smallest scales. The Reynolds Averaged Navier-Stokes (RANS) simulates only the macroscopic scale and models the other scales. It is the cheapest approach in terms of computational power, but it needs a high proportion of model to get complex behaviors.
For simplicity, we will focus on a single-phase, incompressible problem without any external sources. The momentum equation for this example can be expressed as follows:

$$\frac{\partial v_i}{\partial t} + \underbrace{v_i \frac{\partial v_i}{\partial x_k}}_{Advection} = \underbrace{-\frac{1}{\rho}\frac{\partial P}{\partial x_i}}_{Pressure} + \underbrace{\nu \frac{\partial^2 v_i}{\partial x_k \partial x_k}}_{Viscosity} . \tag{2.55}$$

In order to apprehend the averaging, we stand that the quantities v_i and P can be decomposed into a mean value U_i, $\bar{P}$ and a fluctuation u_i, p value so that $v_i = U_i + u_i$.
By applying the mean to the previous equation we get :

$$\frac{\partial U_i}{\partial t} + \underbrace{U_i \frac{\partial U_i}{\partial x_k}}_{Advection} + \underbrace{\frac{\partial \overline{u_i u_k}}{\partial x_k}}_{Turbulent\ stress} = \underbrace{-\frac{1}{\rho}\frac{\partial \bar{P}}{\partial x_i}}_{Pressure} + \underbrace{\nu \frac{\partial^2 U_i}{\partial x_k \partial x_k}}_{Viscosity} . \tag{2.56}$$

The operating average filter preserves the fundamental structure of the instantaneous equation, with one notable exception: the emergence of the turbulent stress term, also called Reynolds stress, represented as $\overline{u_i u_j}$. This term captures the effects of turbulent fluctuations that occur within the flow. Thus, it becomes crucial to compute this term to properly account for these fluctuations.
If we subtract the previous equation to the first one, we can get the equation Eq_i of the fluctuating velocity u_i. The Reynolds stress equation can be obtained by performing the operation $\overline{u_j Eq_i + u_i Eq_j}$:

$$\begin{aligned} \frac{\partial \overline{u_i u_j}}{\partial t} + \underbrace{U_i \frac{\partial \overline{u_i u_j}}{\partial x_k}}_{Advection} + \underbrace{\overline{u_i u_k}\frac{\partial \bar{U}_j}{\partial x_k} + \overline{u_j u_k}\frac{\partial U_i}{\partial x_k}}_{Exchange\ mean-fluctuations} + \underbrace{\frac{\partial \overline{u_i u_j u_k}}{\partial x_k}}_{Triple\ correlation\ transport} \\ = \underbrace{\frac{1}{\rho}\overline{p(\frac{\partial u_i}{\partial x_j} + \frac{\partial u_j}{\partial x_i})}}_{Pressure\ redistribution} \underbrace{-\frac{1}{\rho}\frac{\partial}{\partial x_k}(\overline{u_i p}\delta_{jk} + \overline{u_j p}\delta_{ik})}_{Pressure\ diffusion} - \underbrace{2\nu \overline{\frac{\partial u_i}{\partial x_k}\frac{\partial u_j}{\partial x_k}}}_{Pseudo-dissipation} + \underbrace{\nu \frac{\partial^2 \overline{u_i u_j}}{\partial x_k \partial x_k}}_{Molecular\ dissipation} . \end{aligned} \tag{2.57}$$

This expression is an analytical equation for the Reynolds stress. However, 4 non-linear terms need models because they cannot be computed because they are not directly depending on the Reynolds stress or the mean flow. We then have 6 equations with 34 new unknowns. In order to get rid of some terms, one idea is to consider the turbulent kinetic energy $k = \frac{1}{2}\overline{u_i u_i}$. The equation then becomes :

$$\begin{aligned}\frac{\partial k}{\partial t} + \underbrace{U_i\frac{\partial k}{\partial x_k}}_{Advection} + \underbrace{\overline{u_iu_k}\frac{\partial U_i}{\partial x_k}}_{Exchange\ mean-fluctuations} + \underbrace{\frac{\partial\frac{1}{2}\overline{u_iu_iu_k}}{\partial x_k}}_{Triple\ correlation\ transport} \\ = -\underbrace{\frac{1}{\rho}\frac{\partial}{\partial x_k}\overline{u_kp}}_{Pressure\ diffusion} - \underbrace{\nu\overline{\frac{\partial u_i}{\partial x_k}\frac{\partial u_i}{\partial x_k}}}_{Dissipation} + \underbrace{\nu\frac{\partial^2 k}{\partial x_k\partial x_k}}_{Molecular\ dissipation} .\end{aligned} \tag{2.58}$$

Three fundamental quantities can be notified from those equations and are presented in table 2.5. In this example, the instantaneous pressure also depends on the mean flow and the fluctuations. The Poisson equation gives the instantaneous value for the pressure. With incompressible hypothesis and without external forces, the equation is as follows:

Quantity	Symbol	Expression
Turbulent kinetic energy	k	$\frac{1}{2}\overline{u_iu_i}$
Dissipation	ε	$\nu\overline{\frac{\partial u_i}{\partial x_k}\frac{\partial u_i}{\partial x_k}}$
Anisotropy	b_{ij}	$\frac{\overline{u_iu_j}}{2k} - 1/3\delta_{ij}$

Table 2.5: Table of the fundamental turbulent quantities.

$$\frac{1}{\rho}\frac{\partial^2 P}{\partial x_i\partial x_i} = -\frac{\partial v_i}{\partial x_j}\frac{\partial v_j}{\partial x_i} = \underbrace{-S_{ij}S_{ji}}_{Pure\ deformation\ sink\ term} + \underbrace{\frac{\Omega^2}{2}}_{Rotation\ source\ term} , \tag{2.59}$$

with $S_{ij} = \frac{1}{2}(\frac{\partial v_j}{\partial x_i} + \frac{\partial v_i}{\partial x_j})$ and $\Omega = \nabla \times \mathbf{v}$

By applying the mean to the previous equation we get :

$$\frac{1}{\rho}\frac{\partial^2 \bar{P}}{\partial x_i\partial x_i} = \underbrace{-\bar{S}_{ij}\bar{S}_{ji} + \frac{\bar{\Omega}^2}{2}}_{Mean\ contribution} \underbrace{-\bar{s}_{ij}\bar{s}_{ji} + \frac{\bar{\omega}^2}{2}}_{Fluctuating\ contribution} , \tag{2.60}$$

with s_{ij} the pure deformation from the fluctuating velocity and ω_{ij} the rotational of the fluctuating velocity.

As for the velocity, the operating average filter preserves the fundamental structure of the instantaneous equation, with one notable exception: the emergence of the fluctuating pressure. Then by subtracting this equation to the instantaneous Poisson equation, we get :

$$\frac{1}{\rho}\frac{\partial^2 p}{\partial x_i\partial x_i} = \underbrace{-2\frac{\partial^2 u_iU_j}{\partial x_i\partial x_j}}_{Slow\ linear\ term} - \underbrace{\frac{\partial^2(u_iu_j - \overline{u_iu_j})}{\partial x_i\partial x_j}}_{Fast\ quadratic\ term} . \tag{2.61}$$

The equation reveals a fundamental propriety: both the mean and fluctuating pressures depend on the velocity field's values at any given point and time. It emphasizes the relevance of investigating pressure effects to fully capture the proprieties of turbulence.

For industrial purposes 2 type of models are commonly used based on the previous equations. The first type is the first-order models, which aim to estimate turbulence by computing the equations for the scalars k and ε. They are often referred as the $k-\varepsilon$ models and follow a classical formulation, with N a model :

$$\frac{\partial k}{\partial t}+U_i\frac{\partial k}{\partial x_i}=N^{Diffusion}+N^{Production}-N^{Dissipation}+\nu\frac{\partial^2 k}{\partial x_k\partial x_k}. \tag{2.62}$$

To close the problem the idea is to use a propriety of turbulence : creating strong inertial flows. From this observation, an isotropic homogeneous turbulence could be seen as a strong diffusive phenomenon with a viscosity ν_t. The so-called Boussinesq relation that rely on this hypothesis gives then :

$$R_{ij}=-2\nu_t S_{ij}+\frac{2}{3}k\delta_{ij}, \tag{2.63}$$

with $S_{ij}=\frac{1}{2}(\frac{\partial U_i}{\partial x_j}+\frac{\partial U_j}{\partial x_i})$ and $k=\frac{1}{2}\overline{u_i u_i}$.
The turbulent viscosity is then evaluated by :

$$\nu_t=C_\mu\frac{k^2}{\varepsilon}, \tag{2.64}$$

with C_μ a constant often taken as equal to 0.09.
The classical formulation of the $k-\varepsilon$ model available in industrial codes is given in the appendices A.1.

The advantage of this model is its reduced reliance on differential equations compared to second-order models, resulting in lower CPU costs. It offers ease of computation and excellent stability. It accurately predicts shear stress in free sheared flows and free flows with strong turbulence, addressing well-documented errors. However, due to its linear behavior, this model cannot effectively capture the interaction between a wake and a mix layer, flows with pronounced curvature, and boundary layers. Additionally, a significant drawback of this model is the inherent positivity of the production term, leading to the well-known issue of overestimating turbulent kinetic energy in boundary layers prior to a stagnation point.

The second type of model is known as the second-order model or Reynolds Stress Model (RSM). These models directly incorporate equations for the Reynolds tensor and the dissipation rate. One key advantage of the RSM is its ability to accurately capture nonlinear phenomena and avoid stagnation point anomalies, thanks to an analytical production term. This term plays a crucial role in various turbulent phenomena. For instance, in turbulent flows around a cylinder, it induces the redistribution of velocities from turbulence to the mean flow. However, the RSM has some limitations compared to the linear model. It is numerically less robust, meaning it may encounter stability issues during computations. Calibration of the RSM is also more challenging due to its nonlinear behavior, requiring more intricate adjustments and fine-tuning. The general equation of the model is given by : :

$$\begin{aligned}\frac{\partial}{\partial t}R_{ij}+U_k\frac{\partial R_{ij}}{\partial x_k}&=-R_{ik}\frac{\partial U_j}{\partial x_k}-R_{jk}\frac{\partial U_i}{\partial x_k}+N^{Pressure\ redistribution}\\&\quad-N^{Dissipation}+\nu\frac{\partial^2 R_{ij}}{\partial x_k\partial x_k}-N^{Triple\ correlation\ transport}.\end{aligned} \tag{2.65}$$

In the simulation of turbulent flows, the near-wall region is a crucial area that raises challenges for modeling. In this region, turbulence is weaker compared to viscosity, involving standard turbulent models failure. To address this issue, two approaches are commonly used: near-wall laws and near-wall damping effects.

The first approach involves implementing a law that describes the behavior of velocity in the near-wall region. It assumes the presence of a viscous boundary layer with a thickness denoted as δ for the dimensionless distance to the wall, $y^+ = \frac{y}{\delta}$. Typically, it is recommended to ensure that the first cell size in the near-wall region satisfies the condition of $30 < y^+ < 100$, as the model cannot be directly integrated all the way to the wall. These models are typically referred to as High-Reynolds models. However, a significant challenge associated with this approach is the constraint it imposes on the fluid's behavior near the wall, and the question of its universality for all flow configurations is still a topic of debate.

The second solution involves introducing a damping function or a new term that becomes active near the wall to dampen the turbulence in that region. This approach allows achieving $y^+ \approx 1$, enabling the models to be integrated closer to the wall. Models that can be integrated all the way to the wall are typically referred to as Low-Reynolds models.

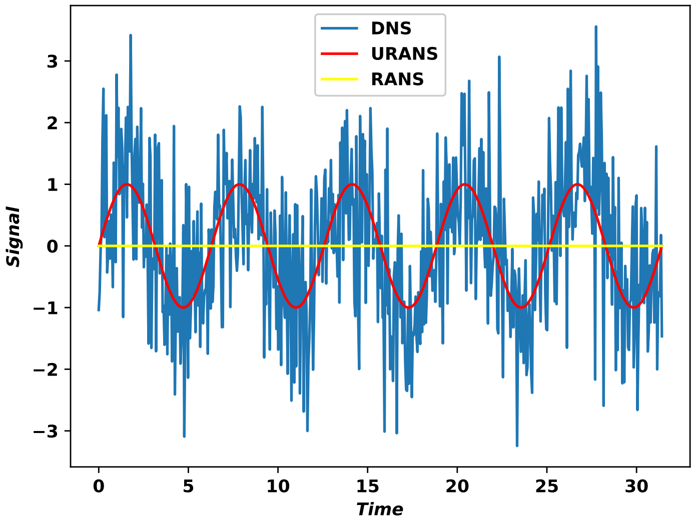

Figure 2.12: Visualization of RANS and URANS treatments from DNS.

When considering the equations of turbulence, a crucial aspect to address is the treatment of temporal changes. The operation of averaging raises a question about the interpretation of temporal changes when the fluctuations are subjected to averaging. This particular aspect of turbulence modeling is commonly referred to as Unsteady Reynolds-Averaged Navier-Stokes (URANS) models, and it remains a subject of ongoing debate and discussion within the scientific community. This approach tries to solve the instantaneous averaged Navier-Stokes equations. The idea is that the statistical treatment could separate scales of low frequencies and macroscopic effects from real turbulence. In turbulent flows, it is essential to acknowledge the possibility of disequilibrium and interactions with other phases that exist outside the traditional range of frequencies associated with real turbulence. This consideration becomes relevant when attempting to reproduce low-frequency phenomena, as depicted in Figure 2.12. Consequently, the ergodicity hypothesis, which states that ensemble average and temporal average are equal, is no longer

valid when computing URANS models at any given time. To address this issue, averaging over time is required to restore the validity of the ergodicity hypothesis. By averaging the results obtained from URANS simulations over a longer time period, a more representative and consistent estimation of the flow behavior can be achieved.
URANS can be interpreted as the application of an implicit filter, able to separate real random fluctuations from coherent structures. The main problem comes with the use of first order models. Indeed, they are based on equilibrium hypothesis and calibrated for stationary flows. Coherent structures can be broken by the fixed equilibrium. Furthermore, those models tend to overestimate the turbulent viscosity, blurring unsteadiness. Several solutions are possible: trying to artificially reduce the turbulent viscosity (OES, that takes $C_\mu = 0.02$), to use non-linear models that can take into account non-equilibrium (thanks to the production term) or even to use hybrid RANS/LES approaches.

Based on those general concepts of turbulence, we can describe the model chosen for this work : the EBRSM [77]. A description of this model proposed on the following section.

2.3.2 The Elliptic Blending - Reynolds Stress Model

One fundamental phenomena that must be modeled is the dissipation ε. However, the equation of ε that can be derived from its analytical formula is way too complex and the physical interpretation of all the terms is difficult. Furthermore, no term is experimentally accessible only numerical simulation can access it. For example, in the $k-\varepsilon$ model [47] the dissipation equation is a standard equation with source, sink terms and a diffusion term. The other noticeable example is the SSG [9] that try to model the influence of the anisotropy. Indeed, their work try to use a linear algebraic equation from the degeneration of the transport of the pseudo-dissipation in case of energetic equilibrium and $2D$ homogeneous velocity gradient. This way they get a non-linear relation with the mean velocity gradient. So that it can reproduce global shear phenomenon but not real anisotropy.
The main model of the dissipation used in this thesis is :

$$\frac{D\varepsilon}{Dt} = \underbrace{\frac{C'_{\varepsilon 1}P}{T}}_{Production\ term} - \underbrace{\frac{C_{\varepsilon 2}\varepsilon}{T}}_{Destruction\ term} + \underbrace{\frac{\partial}{\partial x_l}\left(\frac{C_s}{\sigma_\varepsilon}R_{lm}T\frac{\partial \varepsilon}{\partial x_m}\right)}_{Diffusion\ term} + \nu\underbrace{\frac{\partial^2 \varepsilon}{\partial x_k \partial x_k}}_{Viscous\ term}, \tag{2.66}$$

with $C'_{\varepsilon 1} = C_{\varepsilon 1}(1 + A_1(1-\beta^3)\frac{P}{\varepsilon})$, $A_1 = 0.065$, $C_{\varepsilon 1} = 1.44$, $C_{\varepsilon 2} = 1.85$, $C_s = 0.22, \sigma_\varepsilon = 1.22, T = max(\frac{k}{\varepsilon}, 6(\frac{\nu}{\varepsilon})^{\frac{1}{2}})$ and $P = \frac{1}{2}trace(P_{ij})$ and β the blending variable from the elliptic blending (cf next part).

Unlike dissipation, the triple correlation is experimentally accessible by measuring the fluctuating velocity. Its weight is significant when the turbulence is intensifying the mix. It is the reason why gradient models are likely to use to capture the phenomenon. The main difficulty is to preserve the tensor's symmetry. Few errors come from the model of this term, but few amelioration can be made when it is the case. The most popular model -used for the EBRSM - was proposed in [19] :

$$\overline{u_i u_j u_k} = -C_s \frac{k}{\varepsilon}\overline{u_k u_l}\frac{\partial \overline{u_i u_j}}{\partial x_l}, \tag{2.67}$$

with $C_s \approx 0.22$.

The equation of the Reynolds stress model used in the EBRSM is :

$$\begin{aligned}\frac{\partial}{\partial t}R_{ij} + \underbrace{U_k\frac{\partial R_{ij}}{\partial x_k}}_{\textit{Advection}} = \underbrace{-R_{ik}\frac{\partial U_j}{\partial x_k} - R_{jk}\frac{\partial U_i}{\partial x_k}}_{\textit{Production}} + \underbrace{(1-\beta^3)\phi^w_{ij} + \beta^3\phi^h_{ij}}_{\textit{Redistribution by pressure}} \\ \underbrace{-(1-\beta^3)\frac{R_{ij}\varepsilon}{k} + \frac{2}{3}\beta^3\varepsilon\delta_{ij}}_{\textit{Dissipation}} + \underbrace{\nu\frac{\partial^2 R_{ij}}{\partial x_k\partial x_k}}_{\textit{Viscosity}} + \underbrace{\frac{\partial}{\partial x_l}(\frac{C_s}{\sigma_k}R_{lm}T\frac{\partial R_{ij}}{\partial x_m})}_{\textit{Triple correlation Transport}} \quad ,\end{aligned} \tag{2.68}$$

with ϕ^h_{ij} is the model from SSG (cf appendices A.1), ϕ^w_{ij} is the asymptotic model described hereafter in the next part, $\sigma_k = 1.0$.

The SSG model is widely used to address fluctuating pressure redistribution in turbulence. It originated from theoretical research on the pressure-strain correlation term ϕ_{ij}, accounting for turbulence redistribution due to pressure fluctuations. This term incorporates crucial directional information for the Reynolds stress tensor's off-diagonal components. The model's development involved invariant theory, asymptotic analysis, and calibration to establish desirable behavior based on the anisotropy tensor. By introducing additional macroscopic variables, it enables simulation of anisotropy and ensures realistic Reynolds stress tensor predictions. The SSG model effectively predicts various phenomena like secondary flows and blockage effects. However, it exhibits discrepancies in certain cases, such as non-physical phenomena near walls, leading to its denoted term ϕ^h_{ij}.

Durbin [25] identified that the near-wall issues associated with second-order turbulence models are due to the assumptions of locality and quasi-homogeneity. Near the wall, non-viscous and non-local phenomena, such as the "wall echo" effect and the blocking effect, significantly affect the flow. To address this, Durbin proposed introducing non-locality artificially by assuming an exponential decrease in correlations between points. This modification aims to capture the influence of significant small-scale fluctuations on the flow. By incorporating this non-local behavior, Durbin aims to improve the accuracy of turbulence models near the wall and better account for the complexities of near-wall flows. This hypothesis then leads to the elliptic relaxation equation :

$$\underbrace{\phi_{ij}}_{\textit{Redistribution by pressure}} \underbrace{-L^2\nabla^2\phi_{ij}}_{\textit{Blending}} = \underbrace{\phi^h_{ij}}_{\textit{Quasi-homogeneous model}} \quad , \tag{2.69}$$

with ϕ^h a quasi-homogeneous valid model and L representing a correlation length.

In the near-wall region, certain terms such as viscous diffusion, dissipation ε, and velocity-pressure gradient correlation ϕ play dominant roles. However, these terms require further modeling for accurate representation. Regarding the velocity-pressure gradient correlation, Manceau [78] proposed to establish a transition between an asymptotically valid model, denoted as ϕ^w, based on invariant theory, and a quasi-homogeneous valid model, denoted as ϕ^h, which incorporates an algebraic expression and a one-component differential equation inspired by the elliptic relaxation from R. Manceau's thesis. This transition is designed to ensure the appropriate behavior of the velocity-pressure gradient correlation. To address the issue of singularity at the wall and improve the behavior of dissipation ε, a new equation was proposed. The objective was to significantly reduce the number of additional equations, enhance numerical stability, and maintain the desirable properties of the elliptic relaxation approach. Subsequently, the EBRSM (Elliptic Blending Reynolds Stress Model) [77] was further developed based on theoretical arguments from invariant theory and extensive comparison with DNS data. The near-wall behavior is then computed as:

$$\begin{aligned}
\phi_{ij} &= (1-\beta^3)\phi_{ij}^w + \beta^3\phi_{ij}^h \\
\varepsilon_{ij} &= (1-\beta^3)R_{ij}\frac{\varepsilon}{k} + \frac{2}{3}\beta^3\varepsilon\delta_{ij} \\
\beta - L^2\nabla^2\beta &= 1,
\end{aligned} \tag{2.70}$$

with the dissipation tensor $\underline{\underline{\varepsilon}}$, $L = 0.133max(\frac{k^{3/2}}{\varepsilon}, 80\frac{\nu^{3/4}}{\varepsilon^{1/4}})$, $\phi_{ij}^w = -5\frac{\varepsilon}{k}(R_{ik}n_jn_k + R_{jk}n_in_k - \frac{1}{2}R_{kl}n_kn_l(n_in_j + \delta_{ij}))$ and n is the wall normal.
The wall boundary conditions are then : $U_i = 0, R_{ij} = 0 \; and \; \beta = 0$. One of the strength of this model is also to constrain the behavior of the dissipation to the wall to get the right behavior : $\varepsilon = 2\nu \lim_{y \to 0} \frac{k}{y^2}$.

The choice of EBRSM is motivated by its demonstrated performance in handling complex flow configurations and accurately predicting near-wall phenomena. Indeed, traditional models like the SSG model are insufficient in reproducing the dynamics near the wall, often resulting in non-physical velocities in that region [30]. This limitation is commonly observed in High-Reynolds models.
In single-phase flows, the EBRSM model has been demonstrated to perform well for bundle geometries, as shown by Benhamadouche et al. [1]. This model effectively captures the near-wall behavior, pressure losses, mean velocity, and velocity fluctuations (r.m.s. levels). The study also highlighted the limitations of other Reynolds-Averaged Navier-Stokes (RANS) models in developing unsteadiness, which was attributed to an overestimation of diffusion in the wake region. In comparison, the EBRSM model exhibited promising results, with some configurations showing comparable performance to Large Eddy Simulation (LES). This suggests that the EBRSM has potential for studying fluid-structure interaction, making it a valuable tool in such analyses. The validation of the EBRSM in two-phase flows was carried out by Colombo et al. [15] against various air-water flows using both a monodispersed model and a pseudo-turbulence model. The validation database included upward and downward pipe flows, large diameter pipes, and square duct flows with void fractions up to 0.15%. The results demonstrated a good agreement between the EBRSM predictions and experimental data. Notably, the accuracy of near-wall pressure gradients obtained using elliptic blending eliminated the need for wall-lubrication techniques. However, the observations regarding wall-lubrication should be further examined in the context of polydispersion and tubes to confirm their applicability in a broader range of configurations.

The EBRSM is a single phase turbulent model. However, in a two-phase flow, the intermittence of bubbles in the liquid phase induces fluctuations that are not reproduced in the single-phase turbulent model. The next section is then about the model of two-phase turbulence induced by bubbles.

2.3.3 Two-phase pseudo-turbulence

Although there is no universally optimal approach for every single-phase configuration, extensive research conducted over the years has yielded well-known models that are recognized for their strengths and weaknesses, along with established best practices for their application. However, when it comes to two-phase flows, the situation is more complex. Purely two-phase turbulence models have been found to perform poorly in terms of validation and have even generated significant controversy. In reality, due to the difference in density between gas and water, the turbulence induced by the presence of gas is typically insignificant in the majority of industrial test cases. Consequently, it is often disregarded. However, the fluctuations caused by the bubbles in the liquid phase cannot be overlooked or neglected. These fluctuations play a crucial role in the behavior of two-phase flows and require careful consideration in modeling and analysis. For example, in a single phase channel flow the intensity is often between 5% and 8%. However, in two-phase flows the intensity can be much higher [154, 116]. Indeed for void fraction between 0 and 0.2 (i.e. bubbly flows), the intensity can go from 5% to around 10%. For transitional flows of void fraction between 0.2 and 0.3, the intensity can go from 10% to 17%. For intermittent flows of void fraction between 0.3 and 0.6, the intensity at the center is around 17% and near the wall can go from 20% to more than 60% du to the high intermittency of churn bubbles. An interesting experimental description of what are the agitation, mixing, and transfers induced by bubbles was proposed by Risso [98] and is suggested for deeper understanding of the phenomena. According to Lucas and al. [72], the effects of bubble induced turbulence has nothing to do with real turbulence. The fluctuations induced by bubble wakes and relative velocity can not be related to turbulence. It is why it is often called pseudo-turbulence. Actually, the "additional" level of energy due to these phenomena is supposed to be taken into account by the hydrodynamic forces previously introduced. However, it is interesting to mention that it exists some work about models for Bubble Induced Turbulence (BIT) combined with Shear Induced Turbulence (SIT). It supposes that the total turbulent shear stress is the superposition of classical turbulent shear-stress and bubble induced turbulence. The phenomena that are supposed to be simulated had been identified by Lance and al [62]:

- The turbulent kinetic energy increase due to the relative motion of liquid and gas
- The shear induced turbulence due to the wake of the bubbles
- The turbulence damping due to the deformation of bubbles

For example with a $k - \varepsilon$ model the total turbulent kinetic energy is the sum of the classical one and $k_{BI} = \frac{1}{2}\alpha C_{VM} U_r^2$ - with C_{VM} a dimensionless coefficient and U_r the relative velocity between the phases. A work of comparison had been made by Rzehak and Krepper [101] about BIT. A scale up attempt from DNS results had also been done by Du Cluzeau [12] for a decomposition of BIT into Wake Induced Fluctuations (WIF) and Wake Induced Turbulence (WIT) in order to justify the use of this approach. While the WIF takes into account "laminar" fluctuating effects due to a relative velocity change around a bubble, the WIT try to take into account the fluctuating effects due to the wake of bubbles. However, those approaches still lack of diverse cases of validation and adapted/established near-wall methods for two-phase near-wall regions. Furthermore, a criticism can be made about the "laminar" part that is diagonal, only adding energy in the flow but introducing no redistribution by the fluctuation. Then the frontier between this part and the drag force seems to blur. Nonetheless, several attempts of combining turbulence and pseudo-turbulence were proposed for multiple test cases [15, 13, 14, 74, 75] among the last years. However, the pure contribution of pseudo-turbulence is not clearly demonstrated.

The model used in this work was developed by [81] and is called the Large Inclusions model (LI). It adds a production term linked to the bubble drag in the Reynolds tensor equation and a source term in the dissipation's equation as given hereafter :

$$In\ R_{ij}\ equation\ :\ \frac{2}{3}\mathbf{F}_D\mathbf{U}_r(br_{ij}+\delta_{ij}), \tag{2.71}$$

$$In\ \varepsilon\ equation\ :\ \frac{\mathbf{F}_D \mathbf{U}_r}{\tau_b} \frac{min(\alpha, 0.5)}{\alpha}, \tag{2.72}$$

with F_D the drag force, C_D the drag coefficient, $br_{ij} = \frac{Ur_i Ur_j}{2k_B} - \frac{1}{3}\delta_{ij}$, $k_B = \frac{U_r^2}{2}$ and $\tau_b = \max\left(\left(\frac{D_{sm}^2}{\varepsilon}\right)^{\frac{1}{3}}, \frac{k}{1.83\varepsilon}\right)$.
The main advantage of this model is that it follows the streamwise direction and so needs no rotation step. It is noticeable that it is still proportional to the drag force and the drift velocity.

2.4 Simulations before modifications

In the literature, various configurations of channel flows have been investigated using the models previously introduced [24, 26, 59, 145, 140, 87, 41, 96, 149, 141, 40, 10, 11, 38]. Notably, in the context of vertical upward two-phase flows, an insightful review of CFD models and corresponding experiments was conducted in [10]. In order to apprehend briefly the singular effect of the interfacial transport, the BIT, the turbulence and the presence of an obstacle, we propose in Table 2.6 some of the most recent significant CFD studies conducted for bubbly flows.

Reference	Configuration	Interfacial transport	Turbulence	BIT
Colombo et al. [15]	Channel flows	Constant diameter	EBRSM	yes
Tas-Koehler et al. [127]	Pipe flow with obstacle	MUSIG	SST	yes
Liao et al. [151]	Pipe flow	Constant diameter	SST	yes
Sharma et al. [109, 108]	Pipe flow	IATE-2grps	$k-\varepsilon$	yes
Wang et al. [141]	Pipe flow	IATE-2grps	$k-\varepsilon$	no

Table 2.6: Table of significant CFD work on upward two-phase channel flows.

Despite the extensive research in the field of upward two-phase flow, the literature reveals a notable absence of significant CFD studies using an 'all regimes' model or even models handling IATE or MUSIG for flows around a cylinder. Some applications of two-phase models around obstacles are available in [142] but lacks of experimental confrontation. This lack of relevant investigations highlights a crucial research gap, indicating the need for further exploration and application of such advanced CFD approaches in the context of two-phase flow phenomena around cylinders.

2.4.1 Description of the experiment and numerical model

A platform hosted at CEA is dedicated to the study of two-phase flows around a unique cylinder. The loop pump is able to deliver 5 to 300 L/s of water and an air compressor able to deliver up to 3000 m^3/h at an absolute pressure of 8 bar. The loop can thus function in water flow, air flow or water-to-air flow. It allows reproducing regimes similar to the ones encountered in the SG and DIVA. The experimental setup is composed of an upward channel of $0.18 \times 0.3\ m^2$ rectangular section in which can be set an horizontal tube of diameter $0.03\ m$ as presented in Figure 2.13.

The Power Spectral Density (PSD) of the fluid force (drag and lift directions) acting on the tube is measured for various volume flow rates of air and water. The nature of the forces exerted on the tube can be identified by the balance equations and summing for any phase and over the cylinder surface. Then, according to the equations, the force $\mathbf{F}$ is due to the distribution of pressure P around the tube of oriented surface $\mathbf{ds}$, to the distribution of the viscous stress $\underline{\underline{\tau}}$, as follows:

$$\mathbf{F} = - \oint_S P\,\mathbf{ds} + \oint_S \underline{\underline{\tau}}\,\mathbf{ds}. \tag{2.73}$$

Regarding the spectral analysis, because the simulation and the experiment signals are temporally discrete a special treatment must be used. A random signal can yield different results depending on the analysis intervals. In order to characterize the random force signal, it is essential to get the frequency range occupied by the signal. To understand the force spectra, we need to remind the definition of the cross-correlation $\overline{s_2 s_2}$ between two signals, denoted as s_1 and s_2, of delay τ, over time T:

$$\overline{s_2 s_2}(\tau) = \lim_{T \to +\infty} \frac{1}{T} \int_0^{\tau} s_1(t) s2(t-\tau) dt \tag{2.74}$$

Then, the cross-spectrum is the Fourier transform of the cross-correlation with f the frequency :

$$< s_1, s_2 > (f) = \int_{-\infty}^{\infty} \overline{s_1 s_2}(\tau) e^{-i2\pi f \tau} d\tau \tag{2.75}$$

The auto-spectrum $< s, s >$ is also known as the Power Spectral Density (PSD) of the signal s. It allows us to measure the distribution of power along the frequency axis.
To ensure meaningful data comparison, it is essential that the simulated signal and the experimental signal share identical temporal discretization, along with consistent post-processing methods. This is crucial because spectral analysis is highly sensitive to both the temporal time step and signal post-processing techniques.

One crucial aspect of the simulation involves creating a mesh that is specifically designed to address the problem. This is particularly crucial in the case of Neptune_CFD, which specifically uses hexahedral meshes for stability reasons and to accurately model systems that are sensitive to volume distortion. SALOME [128], an open-source software that provides a generic pre- and post-processing platform for numerical simulation, was used to generate the different meshes. To achieve this, it is recommended to handle a mesh strategy that incorporates the following features presented in Figure 2.13. The mesh should incorporate a boundary layer that expands rapidly. This expansion is limited in space to ensure accurate representation of the boundary layer phenomenon. The boundary layer region of the cylinder needs to be refined extensively. This is because the boundary layer plays a significant role in generating the mixing layer and Von Karman instabilities, which are important phenomena to capture accurately in the simulation.

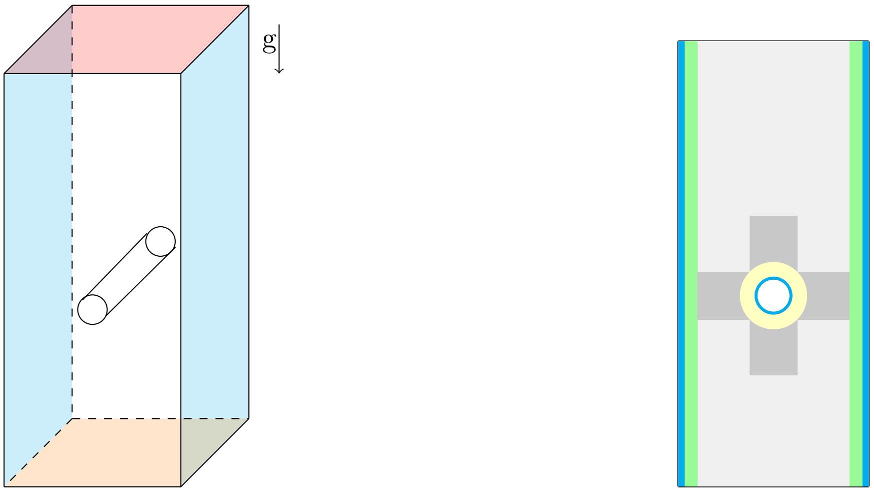

Figure 2.13: Scheme (left) and mesh strategy (right) of the single tube configuration.
Scheme legend (Left) : 🟧 Inlet 🟥Outlet 🟦 Wall.
Mesh strategy legend (Right): 🟦 Boundary layer (1D expansion), 🟩 Junction (expansion 1D), 🟨 Boundary layer junction, ▩ Curvature junction, ⬜ Squared.

The simulation involves solving a system of 22 scalar ordinary differential equations with non-linear source terms. Those equations are distributed across the different phases as presented in table 2.7.

Phase	Conservation of	Unknown	Number of scalars
Liquid	Mass	α_l	1
Liquid	Momentum	$\mathbf{U}_l$	3
Liquid	Reynold stress	R_{ij}	6
Liquid	Dissipation	ε	1
Liquid	Blending	β	1
1st gas group	Mass	α_{g1}	1
1st gas group	Momentum	$\mathbf{U}_{g1}$	3
1st gas group	Interfacial area concentration	a_{i1}	1
2nd gas group	Mass	α_{g2}	1
2nd gas group	Momentum	$\mathbf{U}_{g2}$	3
2nd gas group	Interfacial area concentration	a_{i2}	1
Total			22

Table 2.7: Table of the system of differential equations.

As a reminder, the equations governing the motion between the phases are those of mass conservation :

$$\frac{\partial\left(\alpha_{g1}\rho_g\right)}{\partial t}+\nabla\cdot\left(\alpha_{g1}\rho_g\mathbf{U}_{g1}\right)=-\Gamma_{g1\to g2}, \tag{2.76}$$

$$\frac{\partial\left(\alpha_{g2}\rho_g\right)}{\partial t}+\nabla\cdot\left(\alpha_{g2}\rho_g\mathbf{U}_{g2}\right)=\Gamma_{g1\to g2}, \tag{2.77}$$

$$\frac{\partial\left(\alpha_l \rho_l\right)}{\partial t}+\nabla \cdot\left(\alpha_l \rho_l \mathbf{U}_l\right)=0, \tag{2.78}$$

and the equations for the conservation of momentum :

$$\frac{\partial}{\partial t}\left(\alpha_{g1} \rho_g \mathbf{U}_{g1}\right)+\nabla \cdot\left(\alpha_{g1} \rho_g \mathbf{U}_{g1} \mathbf{U}_{g1}\right)=-\nabla(\alpha_{g1} P)+\nabla \cdot\left(\alpha_{g2} \underline{\underline{\tau}}_{g1}\right)+\alpha_{g1} \rho_g \mathbf{g}+\mathbf{F}_{l \rightarrow g1}, \tag{2.79}$$

$$\frac{\partial}{\partial t}\left(\alpha_{g2} \rho_g \mathbf{U}_{g2}\right)+\nabla \cdot\left(\alpha_{g2} \rho_g \mathbf{U}_{g2} \mathbf{U}_{g2}\right)=-\nabla(\alpha_{g2} P)+\nabla \cdot\left(\alpha_{g2} \underline{\underline{\tau}}_{g2}\right)+\alpha_{g2} \rho_g \mathbf{g}+\mathbf{F}_{l \rightarrow g2}, \tag{2.80}$$

$$\frac{\partial}{\partial t}\left(\alpha_l \rho_l \mathbf{U}_l\right)+\nabla \cdot\left(\alpha_l \rho_l \mathbf{U}_l \mathbf{U}_l\right)=-\nabla(\alpha_l P)+\nabla \cdot\left[\alpha_l\left(\underline{\underline{\tau_l}}+\underline{\underline{\tau}}^T\right)\right]+\alpha_l \rho_l \mathbf{g}-\mathbf{F}_{l \rightarrow g1}-\mathbf{F}_{l \rightarrow g2}, \tag{2.81}$$

with $\underline{\underline{\tau}}^T$ the turbulent stress tensor.

In this section, we aim to highlight the challenges encountered in modeling a case involving a single cylinder, which is representative of the difficulties associated with the presence of an obstacle. Our goal is to demonstrate the results of a two-phase model without modifications, as it existed prior to the start of this thesis. Despite the model's validation in various channel configurations, we wish to emphasize that the presence of the obstacle introduces a unique flow topology, thus questioning the accuracy of its reproduction in this context compared to the validation in a channel. We also aim to demonstrate that the need to use slightly different models helps to identify problems within the models more easily, particularly within TRITON.

2.4.2 Results and analysis

In order to apprehend and understand the TRITON model, we chose to study a bubbly flow test case. The operating conditions are defined by a liquid superficial velocity $j_l = 0,25$ m/s and a gas superficial velocity $j_g = 0.082$ m/s. The flow is then characterized by a void fraction $\alpha_g = 0.247$ and a liquid Reynolds $Re_l = 7500$. A mesh convergence study was performed on several meshes and a satisfying convergence was obtained with a general mesh size of 0.066 mm and a first wall cell satisfying $y^+ \approx 0,8$. The forces selected for this study are unchanged Ishii's Drag, Tomiyama's lift, Zuber's added mass, Lavieville's dispersion and Tomiyama's wall lubrication. The EBRSM is used without adding bubbles induced turbulence.

By computing the previous system of equations with TRITON model, some quantities exhibited divergence, while others displayed non-physical behavior, such as an excessive increase in velocity near the cylinder. Upon analyzing the calculations, the source of the problem seemed not to lie in numerical aspects but rather in the modeling itself.
Close to the cylinder, numerous areas exhibit a void fraction that is on average 2 to 4 times higher than in the upstream region. This phenomenon is a direct result of the interaction and modeling between the fluid and the structure. These specific regions can be characterized as dynamic, primarily because the behavior of the bubbles in those areas is spatially uncorrelated from the bubbles present in the main flow, as depicted in Figure 2.14.

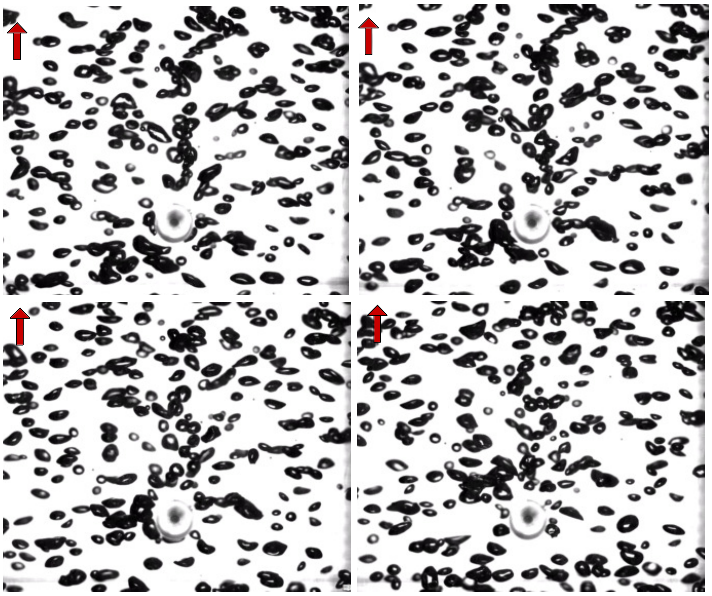

Figure 2.14: Extract of a video of bubble trapping in a cylinder wake from the Heat Transfer and Multiphase Flow Lab of Penn State University. Accesible at https://www.raulab.psu.edu/cylinder-wake-modification-in-bubbly-flow/.

Indeed comparing with Figure 2.14, it becomes obvious that the presence of the cylinder in the flow induces a slowdown of the bubbles upstream, as compared to the bubbles within the main flow. This behavior subsequently leads to an increase in the averaged local void fraction as modeled in the simulation. Additionally, the wake region created by the cylinder induces a bubble trapping region, causing them to remain in that area for an extended period, resulting in a significantly higher void fraction. These areas of high void fraction, as observed in the simulation, have a physical basis directly attributed to the presence of the cylinder. Importantly, such areas do not occur in channel flows, highlighting the incompatibility of the basic model developed for channels in capturing this phenomenon. Therefore, modifications of the model are necessary, particularly to account for these high void fraction regions.

In order to gain a partial understanding of the root causes of these issues, another model already available in NEPTUNE_CFD was examined. In this case, the forces and turbulence model were retained, but the transitional aspect was removed, and the IATE equation was replaced. Consequently, only one group remained, connected to a transport equation developed by Ruyer-Seiler. Multiple simulations were conducted by varying injection diameters to further explore this case.

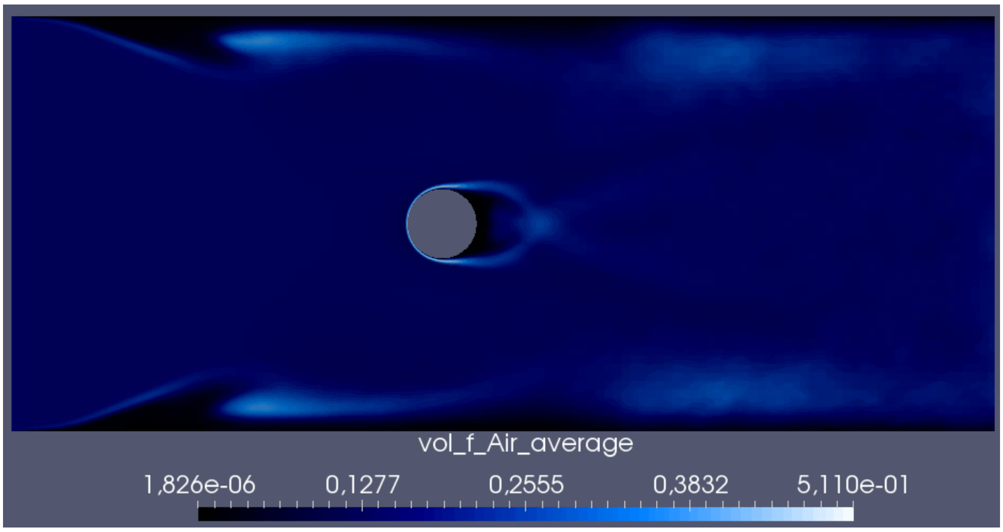

Figure 2.15: Time-averaged void fraction color map from the simulation of two-phase flow around a cylinder with Ruyer-Seiler for $D_{sm1} = 6$ mm.

Figure 2.15 illustrates the color map of the time-averaged void fraction of group 1 obtained from the numerical simulation, with an injected diameter of 6 mm. Notably, a homogeneous region can be observed in the upstream region, away from the cylinder, with a void fraction approximately around 0.12. Close to the cylinder, several areas exhibit an averaged void fraction that is 4 times higher than the upstream void fraction, as observed in [44] and previously illustrated.
It should be noted that qualitative information alone is insufficient to accurately determine the fidelity of the model and comprehend its successes or limitations. Therefore, it becomes imperative to investigate the spectrum of forces exerted on the cylinder to gain a deeper understanding of the phenomena and assess the model's performance at a more detailed level.

Figure 2.16 depicts the power spectral densities (PSD) of drag and lift exerted on the cylinder for various injection diameters (1 mm, 4.5 mm, and 6 mm), which are compared with experimental data. Both 1 mm and 4.5 mm depict almost no noticeable fluctuation for the drag and the lift until 2 Hz, then some harmonics seem to be captured with a negative slop lower than in the experimental graphs. For the 6 mm case, the lift and the drag depict an almost flat curve with one fluctuation around 3.4 Hz for the lift and some fluctuations close to the experimental ones for the drag. The results show significant disparities in the drag and lift behaviors as a function of the injection diameter. The drag spectra obtained for injection diameters of 1 mm and 4.5 mm exhibit more significant deviations from the experimental results, displaying only a characteristic frequency at $St = 0.18$ and its corresponding echoes. In contrast, the drag spectrum for the 6 mm diameter closely resembles the experimental graph. This discrepancy can be attributed to the excessive coalescence observed in the first two cases compared to the 6 mm case. For instance, in the 4.5 mm case, the predicted average diameter at the rear reaches approximately 6.5 mm, representing an increase of over 40%, while for the 6 mm case, it is only 11%. This overestimated coalescence leads to pronounced variations in the drag model for the bubbles, which subsequently amplifies a specific frequency observed in the lift graph. While there is optimism regarding the model's ability to reproduce the fluctuations for the drag, none of the considered injection diameters successfully capture the experimental fluctuations observed for the lift. Only the fluctuation of the wake can be observed. In one case, the bubbles belonging to the first group experience shearing forces from the liquid close to the wall. In the other case, the bubbles cluster slightly further away from the cylinder before being sheared. This difference in behavior arises from the interplay between the low pressure caused by bubble clustering and the low pressure resulting from the Von Kármán alley. When the pressure behind the cylinder exceeds the pressure resulting from bubble clustering, the clusters of bubbles move away from the cylinder wall.

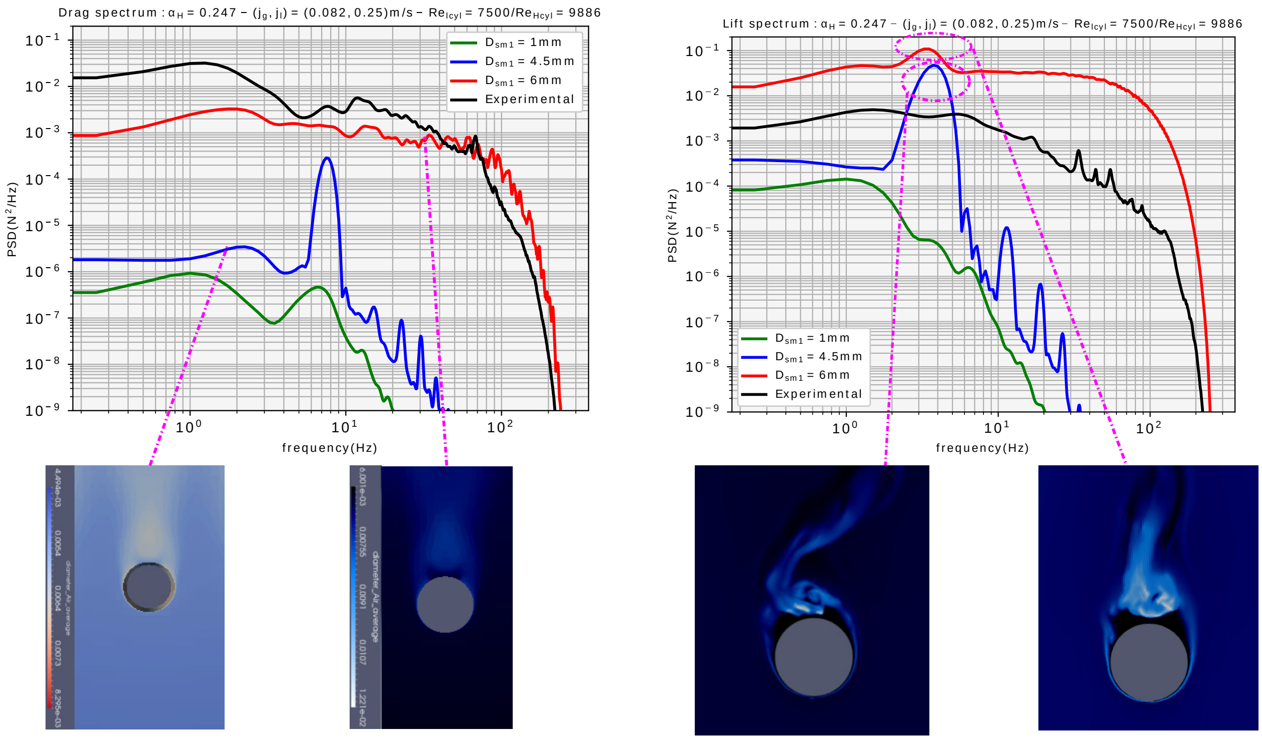

Figure 2.16: PSD of the drag and lift exerted on tube from simulation and experimental data. The simulations are performed with different inlet 1st group diameters.

Due to the poor performance of the Ruyer-Seiler model in reproducing the observed fluctuations and TRITON to reproduce a flow with an obstacle, it becomes necessary to introduce modifications in order to improve the spectrum and the simulations. Modifications are necessary to achieve a more precise representation of the force spectrum and of the flow. To pursue further improvements, the next section of the study focuses on investigating enhancements in a less complex configuration: channel flows. As key parts of the model, the IATE, the turbulence coupling, the dispersion and the transition must be studied to prevent the emergence of problems and quantify the performances of the model.

Chapter 3

New modeling and modifications based on channel flow investigations

Summary

This chapter aims to address the modeling challenges proposed in this thesis associated with the presence of the cylinder and the uncertainties related to turbulence.

The first part discusses the use of turbulence models in channels by comparing two-phase turbulent simulations with experimental data. The initial section focuses on turbulence in a narrow rectangular channel, while the second part examines turbulence in a large square channel.

The second part deals with the modifications introduced in the model to correct problems related to high void fraction due to the presence of the cylinder or due to the regime (high proportion of group 2). This part is divided into four sections. The first one suggests modifications to the modeling of the forces, particularly regarding turbulent dispersion forces. The second part proposes adjustments to some source terms to mitigate local issues in predicting interfacial area. The third part proposes modifications to the pseudo-turbulence model to align it with existing literature. The final part deals with modeling the dynamics of large bubble group 2 and gas pockets. It presents various approaches used to address the simulation challenges associated with this group.

3.1 On the coupling with a turbulence model

3.1.1 A paradigm shift

The original concept of the model proposed in [60] is to provide a criterion for the maximum void fraction α_{gmax}, a maximum diameter $10D_{smc}$ and another one based on the mesh size Δx for transitioning from the dispersed to the continuous model. The last criterion is widely used in literature, although its sophistication may vary. Figure 3.1 illustrates the difference in paradigm between all-regimes models from the literature and our model. Indeed, in models found in the literature, the confusion between dispersed modeling (the area concentration per unit of volume $A_i = \pi D^2$, see equation 2.43) and dispersed vision regarding a mesh of sensors introduces the reconstruction of interfaces when they are larger than the numerical grid size [102]. The use of smoothing techniques between models becomes necessary when transitioning from dispersed modeling to continuous interface reconstruction. In our approach, modeling is grounded in physical considerations. Initially, we assume that the coalescence of small bubbles from Group 1 gives rise to bubbles in Group 2. Subsequently, deformed bubbles from Group 2 can emerge as large gas pockets and extensive interfaces. This perspective arises from the natural growth of interfaces, shifting from one category and thus, one modeling approach (Group 1 to Group 2) and finally to a continuous field. This transition occurs when the equivalent diameter becomes too large, creating a large interface, or when the void fraction becomes too high, as large bubbles have a shape that limits their arrangement, leading to the presence of an annular regime.

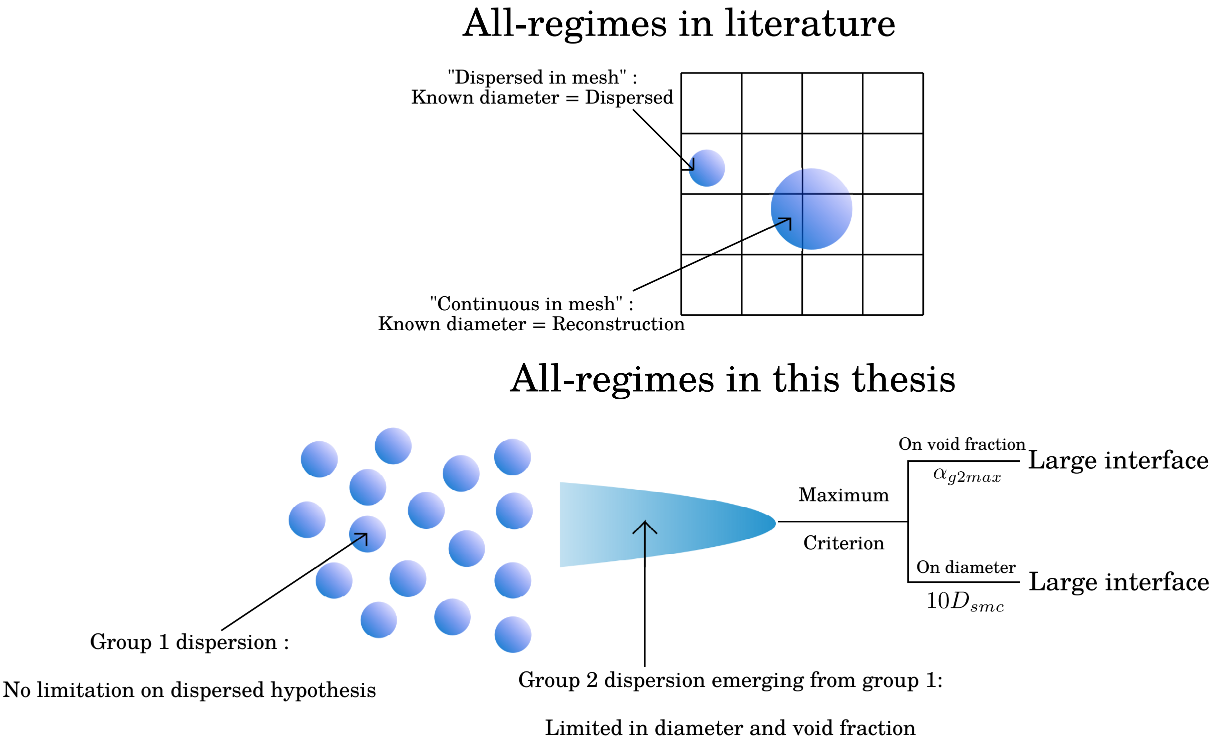

Figure 3.1: All-regimes model paradigm comparison between all-regimes in the literature and our modeling.

Furthermore, this latter criterion should be avoided, especially when investigating complex flow phenomena around a cylinder.
First, if we were able to create a homogeneous mesh, this criterion imposes limitations on possible injection velocities. For instance, in the case of a roughly converged mesh in RANS, the

near-wall first cell size Δx_0 should be such that $\Delta x_0 \approx \frac{60\nu_l}{0.05U_l}$ for High-Re turbulence models, with U_l the mean liquid velocity and ν_l the liquid kinematic viscosity. Kuidjo's criterion states that the mesh step Δx is so that $4\Delta x \geq D_{sm}$, which implies that for bubbles of the order of a millimeter, we have $U_l < \frac{800\nu_l}{0.05D_{sm}} \approx 1.2$ m/s. For a Low-Re mesh configuration like that of EBRSM, this translates to $U_l < \frac{8\nu_l}{0.05D_{sm}} \approx 0.16$ m/s. However, in the case of the DIVA configuration (tube bundle), the presence of tubes increases the flow gap velocity by a factor of three, due to the pitch ratio, resulting in allowable injection velocities of 0.4 m/s and 0.053 m/s, respectively. It would mean that the LIM is activated everywhere. This makes the EBRSM incompatible with this criterion for a homogeneous mesh if we want to test the IATE even for low void fractions.

Secondly, the presence of the bundle makes it nearly impossible to use a perfectly homogeneous mesh, as the curvature of the tubes demands cells of varying sizes. This is particularly obvious given that NEPTUNE _CFD uses hexahedral meshes. Consequently, the dispersed-to-continuous transitions could potentially become non-physical due to mesh-induced effects. This make the physical interpretation of the model difficult.

Thirdly, the first criterion based on a maximum void fraction relies on predicting the void fraction, which depends on mesh accuracy. Hence, there is a risk of missing out on physical phenomena if the mesh is too coarse.

Lastly, this criterion makes the interpretation of simulations, particularly in terms of simulation error - a critical factor in the nuclear field - almost impossible. Actually, the physical interpretation of a simulation relies on distinguishing between discretization error from the mesh and the intrinsic error of the model itself. However, if the criterion depends on the mesh, then the intrinsic error of the model also becomes mesh-dependent. As a reminder, the mesh is a spatial discretization that aims to approximate our continuous differential equations; it is tied to mathematical concepts, it is not a grid of sensors. Consequently, without a tool to estimate cross-correlated error, we are unable to conclude whether the error arises from the approximation of our balance equations or from the balance equations themselves, thus, implicating an error in the modeling. Similarly, even after optimizing parameters and mesh based on numerous experimental comparisons, if the model is used in a scenario lacking experimental comparison, the results remain subject to no physical interpretation. This makes the model non-predictive.

To conclude, the TRITON model no longer handle the criterion based on mesh size but focuses only on the void fraction criterion. Section 3.2.4 of this chapter is actually dedicated to understanding the origin of this criterion and attributing it a physically interpretable value. This chapter is dedicated to understanding, adapting, and validating the modeling by focusing on addressing potential challenges arising from turbulence and the modeling of both gas groups.

An area of potential concern lies in the interaction between the two-phase model and single-phase turbulence. Consequently, our initial focus is directed towards investigating and understanding this coupling phenomenon, specifically for two distinct configurations. We aim to assess the sensitivity of the two-phase modeling approach through the use of three distinct turbulence models: $k-\varepsilon$, SSG, and $EBRSM$. Additionally, we seek to evaluate the contribution of the bubble induced turbulence model (denoted as LI) in enhancing predictive accuracy. Our focus is centered on air-water flows in vertical channels. Rather than primarily focusing on fine-tuning model parameters to achieve optimal predictions, our study lies in investigating the development of a well-established quasi-steady solution within an elongated channel. To ease this analysis, we undertake numerical simulations and compare their outcomes with experimental data from two sources: [126], which is a rectangular section channel (see Figure 3.2), and [122], which deals with a square section channel (see to Figure 3.5). The simulations are performed in three dimensions using the NEPTUNE_CFD software, including gravity.

3.1.2 Air-water flow in a rectangular section channel

The experimental setup, detailed in [126], encompasses a vertical channel with a height of 2.95 m and a rectangular cross-section measuring 200 × 10 mm^2, as visually represented in Figure 3.2. In this setup, the test case is characterized by superficial velocities of $j_l = 0.63$ m/s for the liquid phase and $j_g = 0.42$ m/s for the gas phase. Various local parameters, including the void fraction (α_{g1}), gas velocity (magnitude of U_{g1}), interfacial area concentration (ai_{g1}), and Sauter mean diameter (D_{sm1}), are measured. These measurements are conducted using probes positioned on a quarter cross-section. For clarity, Figure 3.2 provides insight into the specific (x, y) coordinates of the probes. The y-averaged values are subsequently calculated through summations across the data collected from these probes.

For numerical simulations, specific boundary conditions are applied at the inlet. Notably, the void fractions are set to $\alpha_{g1} = 0.344$ and $\alpha_{g2} = 0.077$. Additionally, axial velocities are specified as $U_l = 1.25$ m/s for the liquid phase, and $U_{g_1} = U_{g_2} = 1.389$ m/s for both gas phases. Furthermore, Sauter mean diameters are initialized at $D_{sm1} = 3$ mm for the first group and $D_{sm2} = 17$ mm for the second group.

To perform these simulations, a mesh comprising 440,000 individual elements is used. This mesh was determined through a comprehensive mesh sensitivity analysis that encompassed different meshes, including 80,000, 440,000, and 1,170,000 cells. The results of this analysis conclusively indicated that numerical predictions of α_{g1} converged effectively with the mesh containing 440,000 cells.

Figure 3.3a illustrates the evolution of $\langle a_{ig1} \rangle$, which represents the time-averaged and y-averaged interfacial area concentration of the first gas group, at a specific height of $z = 2.7$ m. The plot is presented in terms of the dimensionless distance x/w. Notably, all turbulence models successfully capture the experimentally observed variations in $\langle a_{ig1} \rangle$. The behavior of $\langle a_{ig1} \rangle$ demonstrates a distinct pattern: it initially rises in the near-wall region ($x/w \to 0$), reaches a peak close to $x/w \approx D_{sm1}/w$, and subsequently decreases to nearly constant values as $x/w \to 0.5$ (which corresponds to the center of the channel). Comparing the numerical predictions with experimental data, the $k-\varepsilon$ turbulence model exhibits the least deviation, with discrepancies amounting to a maximum of approximately 13%. On the other hand, the EBRSM turbulence model shows the highest level of deviation. This can be attributed to the gradual dissipation of turbulent kinetic energy in the EBRSM model, leading to the breakup of bubbles and subsequent reduction in their diameters. This phenomenon is addressed more effectively by the SSG and $k-\varepsilon$ turbulence models, which maintain higher turbulence intensity along the channel and consequently experience minimal bubble breakup. Particularly noteworthy is the performance of the EBRSM+LI turbulence model, which successfully mitigates this challenge by preserving elevated turbulence intensity throughout the channel.

Figure 3.3b presents the evolution of $\langle \alpha_{g_1} \rangle$, which represents the time-averaged and y-averaged void fraction of the first gas group, as a function of the dimensionless distance x/w at a specific height $z = 2.7$ m. All turbulence models correctly replicate the experimentally observed variations in $\langle \alpha_{g_1} \rangle$. The behavior of $\langle \alpha_{g_1} \rangle$ follows a distinct pattern: it initially increases in the near-wall region ($x/w \to D_{sm1}/w$), attains a peak in proximity to $x/w \approx 0$, and subsequently stabilizes at nearly constant values as $x/w \to 0.5$ (which corresponds to the center of the channel). Comparing the numerical predictions with experimental data, the $k-\varepsilon$ turbulence model demonstrates the least deviation, with discrepancies reaching a maximum of approximately 6%. In contrast, the EBRSM+LI turbulence model exhibits the highest deviation. This can be at-

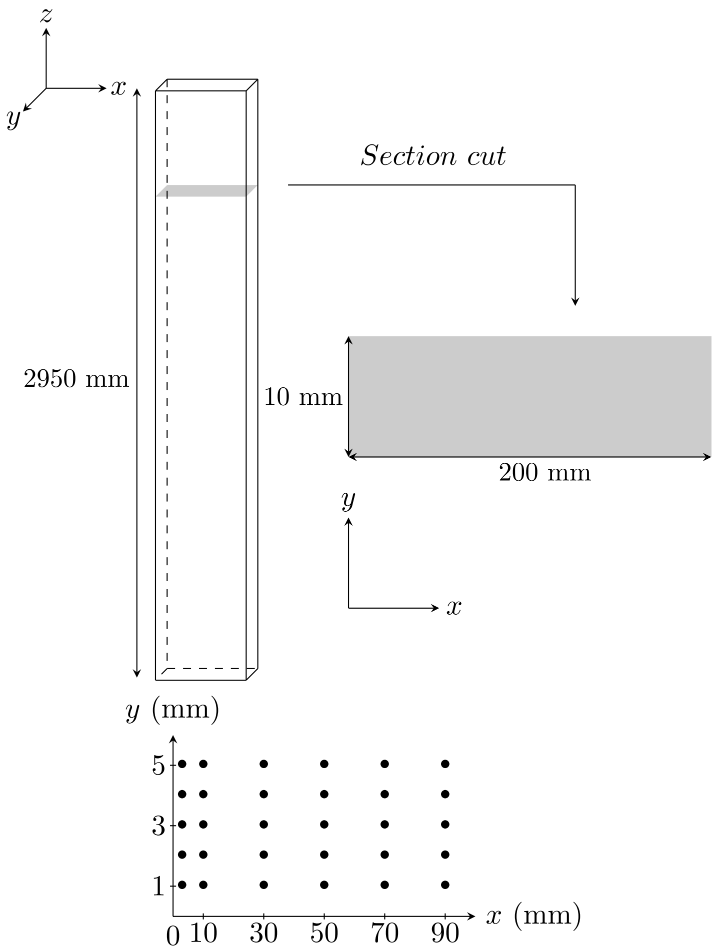

Figure 3.2: Scheme of the experimental setup of [126].

tributed to the EBRSM+LI model's robust generation of turbulent kinetic energy, resulting in notable liquid velocities and restricted void fraction drift. However, the void fraction prediction is influenced by the drag model, which does not encompass turbulence effects. To mitigate this limitation, potential corrections based on factors like turbulent intensity or adjusted inlet velocities could be implemented. It is notable that the current shortage of experimental data in the near-wall region limits precise determination of the maximum value and location of $\langle \alpha_{g_1} \rangle$ in terms of x/w.

Figure 3.4 depicts the evolution of $\langle |\mathbf{v}_{g_1}| \rangle$, which represents the time-averaged and y-averaged magnitude of gas velocity for the first gas group. This evolution is plotted against the dimensionless distance x/w at a specific height of $z = 2.7$ m. All turbulence models effectively capture the experimentally observed variations in $\langle |\mathbf{v}_{g_1}| \rangle$. Specifically, $\langle |\mathbf{v}_{g_1}| \rangle$ exhibits a rapid increase within the near-wall region ($x/w \to D_{sm1}/w$) and subsequently saturates as it approaches the central region ($x/w \to 0.5$). Despite the qualitative agreement for the variations, notable deviations arise between numerical predictions and experimental measurements, particularly in the near-wall region. The EBRSM+LI model demonstrates a deviation of approximately 14%, while the EBRSM model exhibits a larger deviation of around 25%. It is notable that both the EBRSM+LI and EBRSM models are the only ones capable of predicting low values of $\langle |\mathbf{v}_{g_1}| \rangle$ as $x/w \to 0$ due to the absence of wall laws in their formulation.

In this section, we conducted a comprehensive comparison between numerical predictions

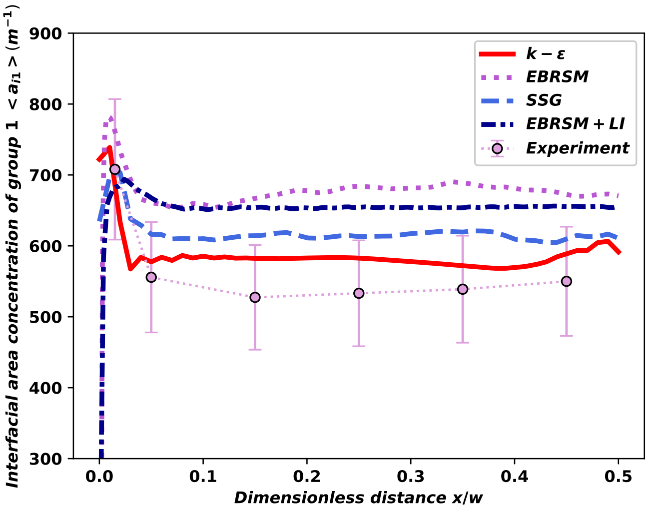

(a) Interfacial area concentration $\langle a_{ig1} \rangle$.

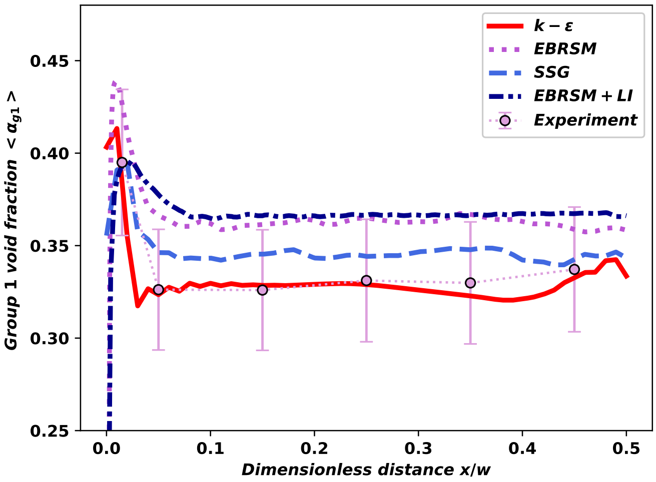

(b) Void fraction $\langle \alpha_{g_1} \rangle$.

Figure 3.3: First gas group time-averaged and y-averaged quantities ($z = 2.7$ m) vs. dimensionless distance x/w with $w = 200$ mm. Lines are numerical predictions from simulations carried out with different turbulence models. Points are experimental results extracted from [126].

and experimental measurements conducted by [126]. Our analysis encompassed various turbulence models, revealing that these models yield similar outcomes. However, determining the optimal model for simulating air-water flows in vertical rectangular channels remains inconclusive. We established that all turbulence models successfully capture the variations of $\langle a_{ig1} \rangle$, $\langle \alpha_{g_1} \rangle$, and $\langle |\mathbf{v}_{g_1}| \rangle$ along a specific direction (x/w) within a designated cross-section ($z = 2.7$ m). The deviations between numerical predictions and experimental measurements remain within satisfactory limits, particularly beyond the region near to the channel walls. In the subsequent section, our assessment extends to the evaluation of turbulence models within the context of a square section channel configuration.

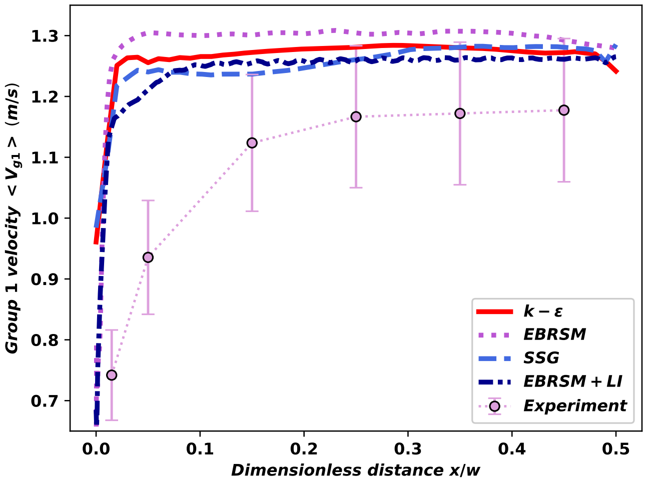

Figure 3.4: Magnitude of gas velocity of first gas group, $\langle|\mathbf{v}_{g_1}|\rangle$ (time-averaged, y-averaged, $z = 2.7$ m) vs. dimensionless distance x/w with $w = 200$ mm. Lines are numerical predictions from simulations carried out with different turbulence models. Points are experimental results extracted from [126].

3.1.3 Air-water flow in a square section channel

The experimental configuration detailed in [122] involves a vertical channel with a height of 2.95 m and a square cross-section measuring 136×136 mm^2, as depicted in Figure 3.5. In this setup, the test case is characterized by superficial velocities of $j_l = 0.50$ m/s for the liquid phase and $j_g = 0.09$ m/s for the gas phase. Various local parameters, including the void fraction (α_{g1}), gas velocity (magnitude of U_{g1}), interfacial area concentration (ai_{g1}), and Sauter mean diameter (D_{sm1}), are measured. Probes are positioned along three lines within a quarter cross-section, as illustrated in Figure 3.5. It is crucial to note that the experimental study does not provide a localized estimation of experimental error. Consequently, global errors are utilized in the subsequent presentation of results to approximate the experimental error. Furthermore, the experiment conducted by [122] provides a mean to evaluate the turbulent kinetic energy (k), enabling the validation of the turbulence modelling.

Regrading the numerical simulations, specific boundary conditions are imposed at the inlet. For void fractions, these conditions are set as $\alpha_{g_1} = 0.152$ and $\alpha_{g_2} = 0.00$. Axial velocities are prescribed as $v_l = 0.59$ m/s for the liquid phase, and $v_{g_1} = v_{g_2} = 0.59$ m/s for both gas phases. Additionally, Sauter mean diameters are initialized at $D_{sm_1} = 4$ mm for the first group and $D_{sm_2} = 11$ mm for the second group.

To perform these simulations, a mesh comprising 676,000 individual elements is used. This mesh was determined through a comprehensive mesh sensitivity analysis that encompassed different meshes, including 130,000, 676,000, and 3,256,000 cells. The results of this analysis conclusively indicated that numerical predictions of α_{g1} converged effectively with the mesh containing 676,000 cells.

Figure 3.6 presents the evolution along the diagonal line of $\langle\alpha_{g1}\rangle$ (time-averaged void fraction of the first gas group) and $\langle v_l\rangle$ (time-averaged axial liquid velocity) as a function of the dimensionless distance x/w at a specific height of $z = 2.2$ m. All turbulence models accurately reproduce the observed variations. Specifically, $\langle\alpha_{g1}\rangle$ increases within the near-wall region ($x/c \rightarrow 1$),

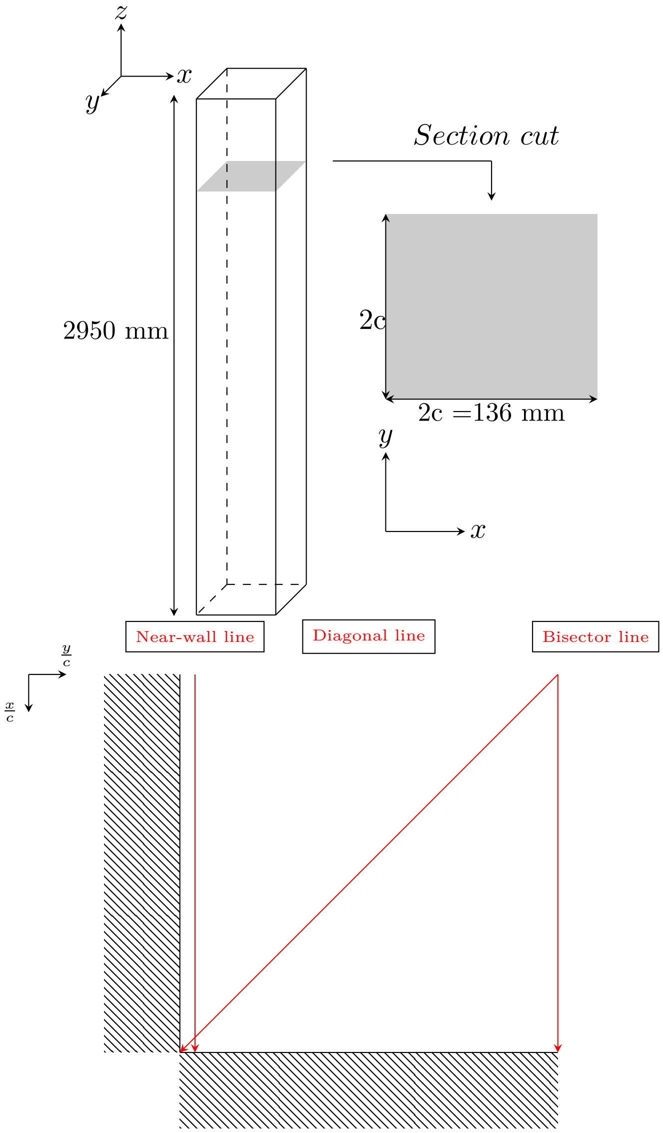

Figure 3.5: Scheme of the experimental setup of [122].

reaches a peak close to $x/c \approx 1 - D_{sm1}/c$, and subsequently stabilizes as $x/c \to 0$ (center of the channel). The oscillatory behavior observed in most models, excluding EBRSM+LI, arises from weak turbulent dispersion and pronounced deviating phenomena near the wall region. Where the models differ significantly is in the prediction of the void fraction peak within the near-wall region. The SSG model exhibits the largest disparity, with the peak positioned approximately 60% further from the wall. Consequently, the void fraction prediction for the probe closest to the wall is over 10 times smaller than the experimental data. This discrepancy can be attributed to the SSG model's tendency to predict increased turbulent energy in the near-wall region (as observed in Figure 3.9), leading to greater bubble growth and an additional peak closer to the wall. On the contrary, the EBRSM+LI model displays the smallest overall deviation, with a maximum local error of 16%. This model's performance is notable for its improved prediction accuracy in capturing the void fraction peak, further enhancing its reliability in this context.
For $\langle v_l \rangle$, all models consistently fall within the range of error bars. However, it is the EBRSM+LI model that accurately reproduces the observed variations of $\langle v_l \rangle$ in the experimental data. This includes the pattern where $\langle v_l \rangle$ increases as $x/c \to 1$ within the near-wall region and subse-

quently decreases as $x/c \rightarrow 0$ toward the center of the channel. In contrast, among the other models, the $k-\varepsilon$ model predicts an increment of $\langle v_l \rangle$ as $x/c \rightarrow 1$, followed by a tendency toward a near-constant value as $x/c \rightarrow 0$ exhibiting a non-physical wall acceleration. The EBRSM model displays an opposite trend in the center of the channel ($x/c \rightarrow 0$), while correctly predicting the behavior in the near-wall region ($x/c \rightarrow 1$). The SSG model, due to the position of the void fraction peak, depicts a notable decrease in axial velocity within the near-wall region ($x/c \rightarrow 1$), leveling off to an almost constant value as $x/c \rightarrow 0$. In terms of overall performance, the EBRSM+LI model emerges as the most accurate and consistent, boasting the smallest overall discrepancy in comparison to the experimental data.

Figure 3.7 illustrates the evolution along the bisector line of $\langle \alpha_{g1} \rangle$ (time-averaged void fraction of the first gas group) and $\langle v_l \rangle$ (time-averaged axial liquid velocity) as functions of the dimensionless distance x/w at a specific height of $z = 2.2$ m. Focusing on $\langle \alpha_{g1} \rangle$, all turbulence models, excluding the $k-\varepsilon$ model, faithfully reproduce the observed variations. This includes the behavior where $\langle \alpha_{g1} \rangle$ increases within the near-wall region ($x/c \rightarrow 1$), reaches a peak near $x/c \approx 1 - D_{sm1}/c$, and subsequently stabilizes toward an almost constant value as $x/c \rightarrow 0$ (center of the channel). Among the models, the EBRSM turbulence model exhibits the largest deviation, reaching approximately 23%. This discrepancy is most prominent in the misplaced void fraction wall peak, as observed in the diagonal line assessment. It is notable that the SSG model also displays a similar issue of a misplaced void fraction wall peak in the bisector line assessment.
Regarding $\langle v_l \rangle$, all models consistently fall within the range of error bars. However, only the SSG and EBRSM models accurately reproduce the observed variations of the experimental data. This variation displays an increase in $\langle v_l \rangle$ within the near-wall region ($x/c \rightarrow 1$), followed by an almost constant value as $x/c \rightarrow 0$, corresponding to the center of the channel. In contrast, the $k-\varepsilon$ model predicts an increase in $\langle v_l \rangle$ as $x/c \rightarrow 1$, and approaches an almost constant value as $x/c \rightarrow 0$, a behavior that seems to hide the specific wall law used. This discrepancy stems from the non-physical wall acceleration attributed to the intricate interplay between gas forces and wall laws, which strongly interact with the liquid field within the initial cells. The EBRSM+LI model accurately reproduces the behavior observed for $\langle v_l \rangle$: an increase within the near-wall region ($x/c \rightarrow 1$) followed by a decrease as $x/c \rightarrow 0$ toward the center of the channel. This robust consistency further underscores the reliability of the EBRSM+LI model in capturing the flow dynamics.

Figure 3.8 shows the near-wall line evolution of $\langle \alpha_{g1} \rangle$ (time-averaged void fraction of the first gas group) and $\langle v_l \rangle$ (time-averaged axial liquid velocity) as functions of the dimensionless distance x/w at a specific height of $z = 2.2$ m. For $\langle \alpha_{g1} \rangle$, all turbulence models accurately reproduce the observed variations. As previously discussed, $\langle \alpha_{g1} \rangle$ exhibits an increase within the near-wall region ($x/c \rightarrow 1$), peaks near $x/c \approx 1 - D_{sm1}/c$, and subsequently stabilizes toward an almost constant value as $x/c \rightarrow 0$ (center of the channel). However, a constant discrepancy emerges for all models around the center of the channel ($x/c \rightarrow 0$), with the SSG model demonstrating the highest deviation of approximately 30%. This emphasizes the potential for enhancement and modelling in accurately capturing near-wall behaviors. The conclusions drawn from the diagonal and bisector line analyses hold parallels within this near-wall line assessment, further affirming the trends observed in various regions of the channel.

Figure 3.9 illustrates the bisector line evolution of the fluctuating kinetic energy k across the dimensionless distance x/w at a specific height of $z = 2.2$ m. This selection of the bisector line is deliberate, as the isotropic assumption used to derive these experimental values is

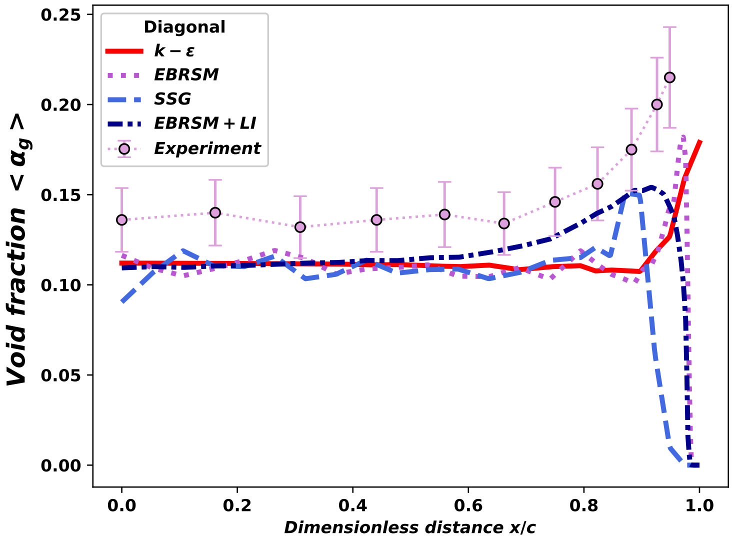

(a) Void fraction $\langle \alpha_{g_1} \rangle$.

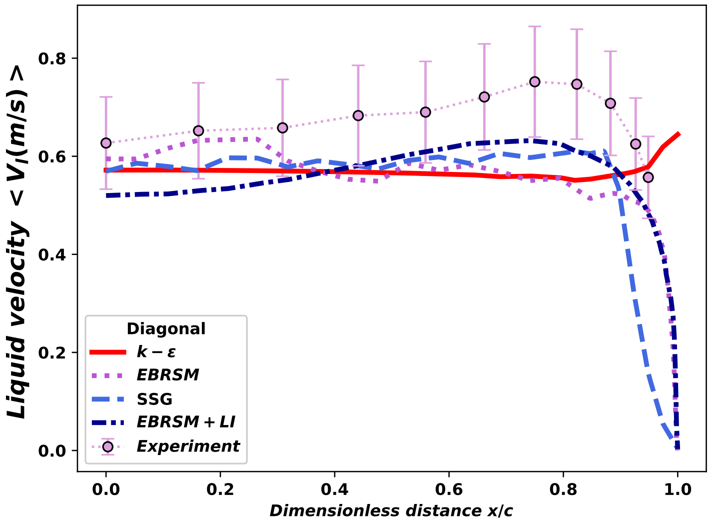

(b) Axial liquid velocity $\langle v_l \rangle$.

Figure 3.6: Diagonal line evolution of time-averaged quantities of the first gas group vs. dimensionless distance x/c with $c = 68$ mm, at height $z = 2.2$ m. Lines are numerical predictions from simulations carried out with different turbulence models. Points are experimental results extracted from [122].

notably accurate within this region of geometric symmetry. Among the models, it is only the EBRSM+LI model that accurately captures the variations of k as observed in the experimental data. Specifically, k increases within the near-wall region ($x/c \to 1$), reaches a maximum, and then gradually decreases as $x/c \to 0$ toward the center of the channel. Conversely, all other models predict an initial increase of k in the near-wall region ($x/c \to 1$), followed by a peak near $x/c \approx 1 - D_{sm1}/c$, a rapid decline, and finally a slow increase toward a nearly constant value as $x/c \to 0$ at the center of the channel. Notably, a substantial gap in fluctuating energy exists between the experimental data and the predictions of the classical EBRSM, $k - \varepsilon$, and SSG

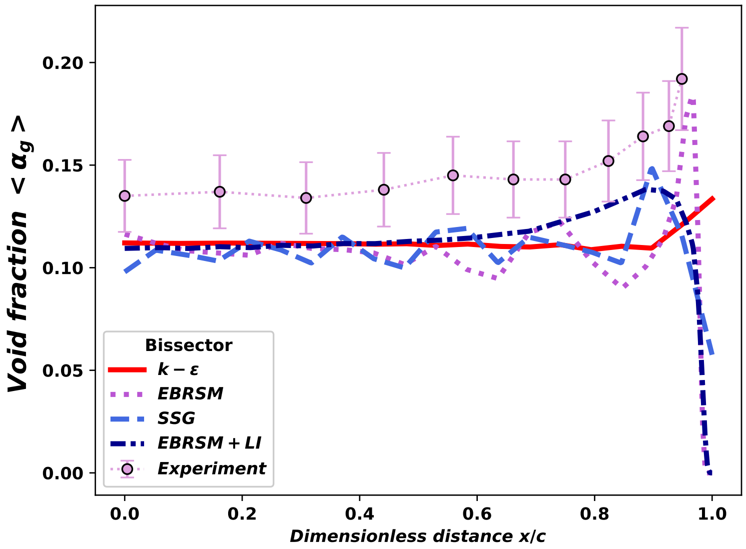

(a) Void fraction $\langle \alpha_{g_1} \rangle$.

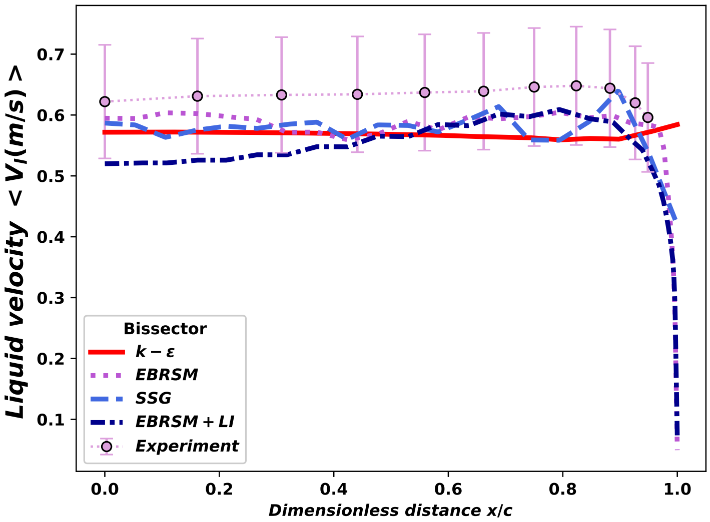

(b) Axial liquid velocity $\langle v_l \rangle$.

Figure 3.7: Bissector line evolution of time-averaged quantities of the first gas group vs. dimensionless distance x/c with $c = 68$ mm, at height $z = 2.2$ m. Lines are numerical predictions from simulations carried out with different turbulence models. Points are experimental results extracted from [122].

models, which amounts to approximately 60%, 70%, and 70%, respectively, at the center of the channel. The disparities among the latter three models are primarily localized in the near-wall region, where a significant increase coincides with the position of the void fraction wall peak. The capability of the EBRSM+LI model to reproduce both the turbulence trend and intensity is attributed to the use of BIT. Unlike the other models, which only account for single-phase turbulent kinetic energy, the EBRSM+LI model introduces fluctuations owing to drag forces. It is crucial to highlight that the pure turbulent intensity remains relatively low, indicative of a process of turbulence reduction due to the localized reduction in the volumetric presence of the

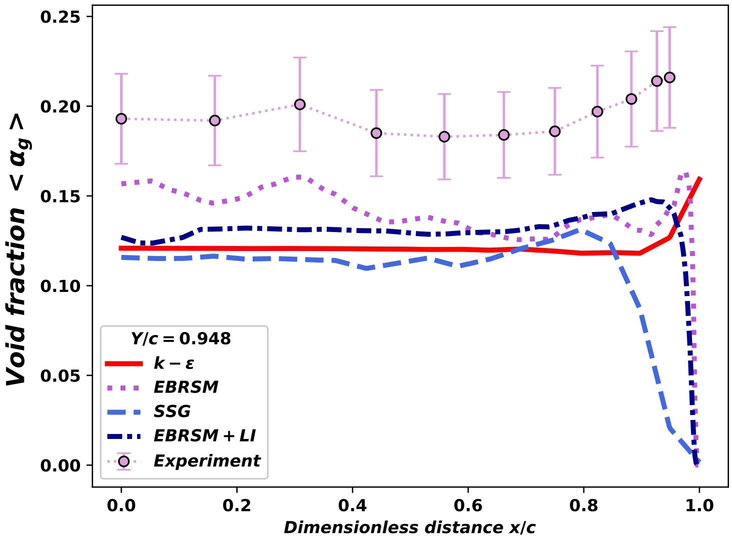

(a) Void fraction $\langle \alpha_{g_1} \rangle$.

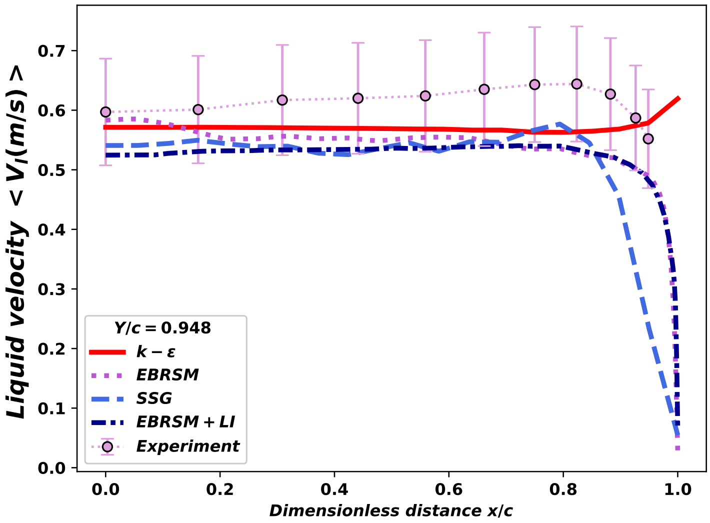

(b) Axial liquid velocity $\langle v_l \rangle$.

Figure 3.8: Near wall line evolution of time-averaged quantities of the first gas group vs. dimensionless distance x/c with $c = 68$ mm, at height $z = 2.2$ m. Lines are numerical predictions from simulations carried out with different turbulence models. Points are experimental results extracted from [122].

liquid phase, linked to the presence of bubbles. Although a noticeable deviation in fluctuating energy intensity exists between the experimental data and the EBRSM+LI model's prediction, it still leads to a favorable prediction and trend for the liquid velocity, further underlining the model's competence in capturing the complex flow dynamics.

Consequently, the comprehensive prediction of the EBRSM+LI model emerges as notably interesting. This model demonstrates a reduced level of deviation and successfully captures the correct trends for variables such as void fraction, liquid velocity, and turbulent kinetic energy.

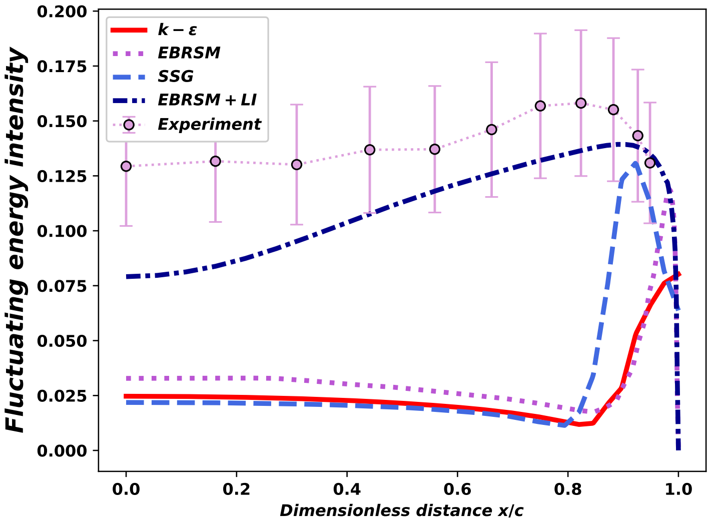

Figure 3.9: Comparison of the diagonal predictions of the fluctuating kinetic energy among the different models at height of 2.2 m.

Despite these strengths, it is crucial to note that when compared to the experimental data, both the void fraction and liquid velocity exhibit a trend to be under-predicted by the EBRSM+LI model.

The combination of TRITON modeling and turbulence appears to yield profiles with similar trends to the experimental data for the EBRSM and EBRSM+LI models in terms of velocity and near-wall void fraction, although the void fraction is generally underestimated compared to the experimental results. This observation may be attributed to a potential problem with the drag force in the simulation. Another explanation could also stem from the experimental measurements. In fact, it appears that the experimenter measured a local void fraction of $<\alpha_g>= 0.139$ at the center and considered this value as a measurement for the entire cross-section. If we use the calculation from the next section, $<U_r>=<Ub>(1-<\alpha_g>)^{1/2}$, we obtain $<U_r>\approx 0.213$ m/s, which corresponds to a gas velocity of $U_g \approx 0.803$ m/s, and thus, a local void fraction of $\alpha_g \approx 0.11$. This result aligns with the simulation by measuring at the center of the channel. Now, if we perform a reverse calculation to obtain the experimental values measured at the center, we can use the following equations:

$$<U_g>\approx<U_l>+<U_b>(1-<\alpha_g>)^{1/2}, \tag{3.1}$$

$$<\alpha_g>=\frac{j_g}{<U_g>}. \tag{3.2}$$

Then, we get :

$$j_g \approx <\alpha_g>(<U_l>+<U_b>(1-<\alpha_g>)^{1/2}). \tag{3.3}$$

The experimental measurements yield $<U_l>\approx 0.68$ m/s and $<\alpha_g>= 0.139$. The experimentalist then calculated $j_g=<\alpha_g><U_l>\approx 0.09$ m/s using local measurements. However, according to the calculation, we obtain $j_g = 0.124$ m/s, which is greater than 0.09 m/s, resulting in a cross-sectionnal void fraction of $<\alpha_g>= 0.182$. This value is more consistent with a central void fraction of 0.139 and a wall void fraction of 0.2. To accurately compute this case, the following injection parameters should be used: $j_g = 0.124$ m/s, $j_l = 0.556$ m/s, and $<\alpha_g>= 0.182$.

Beyond confirming the coupling between turbulence and TRITON, it appears that a different modeling approach is still required to account for effects specific to the presence of the obstacle. Particularly, there are issues related to modeling small bubbles, including concerns about forces, source terms, and turbulence. The next section, therefore, addresses the challenges encountered in TRITON modeling from the perspective of the dispersed bubbles groups.

3.2 On the modeling of the two groups of bubbles

An aspect that need careful consideration is the modeling of the bubbles under conditions of high void fraction. As illustrated in the previous section, there exists a possibility that the issue might be attributed to the models of hydrodynamical forces, of the source terms within the IATE, or of the bubble induced turbulence. As a mean to address this potential concern, we suggest conducting an investigation into all these aforementioned models. Indeed, most models have been developed and validated for moderate void fractions. Thus, non-physical divergence issues due to high void fractions have not been addressed in the literature.

3.2.1 Modifying and adapting forces

The hydrodynamical closure models are fundamental components of the momentum equation, crucial for accurately predicting the velocities of both gas and liquid phases and their respective void fractions. Despite numerous studies available in the literature, most of these models have been validated primarily for scenarios involving low to moderate void fractions and are not always coupled with turbulence. When attempting to apply these closure models to more complex configurations, their performance becomes uncertain. The lack of a widely accepted universal combination of forces adds difficulties. Incorporating additional complexity into a specific model can introduce numerical issues when combined with other models. Thus, the issue of divergence and poor performance can partially be attributed to the dispersed forces. Notably, these hydrodynamical closure models have not been adequately validated for flows around a cylinder, indicating a significant gap in their applicability when dealing with such geometries.
As a reminder, the interfacial momentum exchange term is modeled by hydrodynamical forces as follow :

$$\mathbf{I}_{l->g} = \underbrace{\mathbf{F}^{D}_{l->g}}_{Drag} + \underbrace{\mathbf{F}^{L}_{l->g}}_{Lift} + \underbrace{\mathbf{F}^{AM}_{l->g}}_{Added\ mass} + \underbrace{\mathbf{F}^{WL}_{l->g}}_{Wall\ Lubrication} + \underbrace{\mathbf{F}^{T}_{l->g}}_{Turbulent\ dispersion} . \tag{3.4}$$

The primary challenge in simulating flow around a cylinder lies in accurately predicting a high void fraction near the cylinder. To address this issue, it becomes crucial to investigate forces that non-linearly depend on the void fraction. Such forces include the drag force $\mathbf{F}^{D}_{l->g}$, added mass force $\mathbf{F}^{AM}_{l->g}$, and turbulent dispersion $\mathbf{F}^{T}_{l->g}$.

Drag force

The first force to investigate is the drag force $\mathbf{F}^{D}_{l->g}$. Consider an upward adiabatic free bubbly flow - only 1st group bubbles - in a rectangular channel, without wall, we neglect the turbulence, the bubbles interactions and the viscous shear. In this scenario, we can assume a homogeneous dispersed flow with bubbles. Assuming that the flow is statistically steady, it becomes obvious that only the drag force significantly influences the flow dynamics. Other forces can be disregarded due to the idealized conditions. From equation 2.79, we derive the following $1D$ balance equation in the direction of the relative velocity, denoted as U_r, with respect to the gas phase, with P the pressure field :

$$\alpha_g \nabla P = F^D_{l->g} - \alpha_g \rho_g g. \tag{3.5}$$

Similarly, we also derive from equation 2.81 the following $1D$ balance equation for the relative velocity, with respect to the liquid phase, by neglecting liquid velocity changes :

$$(1-\alpha_g)\nabla P = -F^D_{l->g} - (1-\alpha_g)\rho_l g. \tag{3.6}$$

By considering the equations for the relative velocity in both the gas and liquid phases, and taking into account that the pressure is uniform and equal for both fields, we deduce from equations 3.5 and 3.6 the following:

$$\nabla P = -((1-\alpha_g)\rho_l + \alpha_g \rho_g)g. \tag{3.7}$$

By considering the classical drag force, equation 3.5 can be rewritten as :

$$\frac{3}{4}\alpha_g \rho_l \frac{C_D}{Dsm} U_r^2 = \alpha_g \Delta\rho g(1-\alpha_g). \tag{3.8}$$

We finally get :

$$U_r^2 = \frac{4}{3}\frac{Dsm}{C_D \rho_l}\Delta\rho g(1-\alpha_g) = Ub^2(1-\alpha_g), \tag{3.9}$$

with $Ub^2 = \frac{4}{3}\frac{Dsm}{C_D\rho_l}\Delta\rho g$ and C_D the drag coefficient. For example, with $C_D = \frac{2}{3}\frac{D_{sm}}{La}$, $Ub \approx 0.230$ m/s.
However, with C_D =min($C_{Dellipse}, C_{Dcap}$) (see equations 2.18 and 2.19), whatever the diameter, when the void fraction tends to 1 the C_{Dcap} model is selected. With the previous equation, we have :

$$U_r^2 = Ub^2_{cap}\frac{1}{1-\alpha_g}, \tag{3.10}$$

with $Ub^2_{cap} = Ub^2(C_D = 8/3)$.
The analysis reveals that as the void fraction approaches 1, the relative velocity U_r tends towards infinity. However, the liquid velocity remains continuous and finite, implying that the gas velocity approaches infinity. To maintain model accuracy, physical consistency, and continuity for the first group of bubbles, the most elegant approach is to introduce a new drag coefficient. This new coefficient will appropriately modify the drag force model, allowing for better predictions of the behavior of the gas phase without sacrificing the model's overall performance :

$$C_{Dg1} = \max(C_{Dlow}, \min(C_{Dellipse}, \max(C_{Dcap}, C_{Dellipse}(\alpha_g = 0)))). \tag{3.11}$$

Added mass force

The next force to be explored is the added mass force $\mathbf{F}^{AM}_{l->g}$. This force comes into play in accelerating bubbly flows as a result of the surrounding fluid's influence on the acceleration of bubbles within the flow. The added mass force becomes especially significant in flows around a cylinder due to the deviation induced around the cylinder. As a reminder, the Zuber's added mass coefficient[90] is proportional to $\frac{1+2\alpha_g}{1-\alpha_g}$. It becomes obvious that when $\alpha_g \to 1$ this expression tends toward infinity, which is not physical. To overcome this issue and ensure a valid model even at high void fractions, a modified version is required. The expression proposed by Cai and Wallis [6] presents an interesting approach as it provides an averaged model that yields a finite value when the void fraction approaches 1. Moreover, the model used can be viewed as a special case of the model used, when the density ratio between the liquid and gas is infinite, and the void fraction remains at moderate levels. The expression of the force is then as follows :

$$\mathbf{F}^{AM}_{l->g} = -\alpha_g \frac{(1+2\alpha_g)\gamma + 1 - \alpha_g}{2\gamma(1-\alpha_g) + 2 + \alpha_g} \rho_l \left(\frac{D\mathbf{U}_g}{Dt} - \frac{D\mathbf{U}_l}{Dt} \right), \tag{3.12}$$

with $\gamma = \frac{1}{2}\frac{\rho_l}{\rho_g}$.

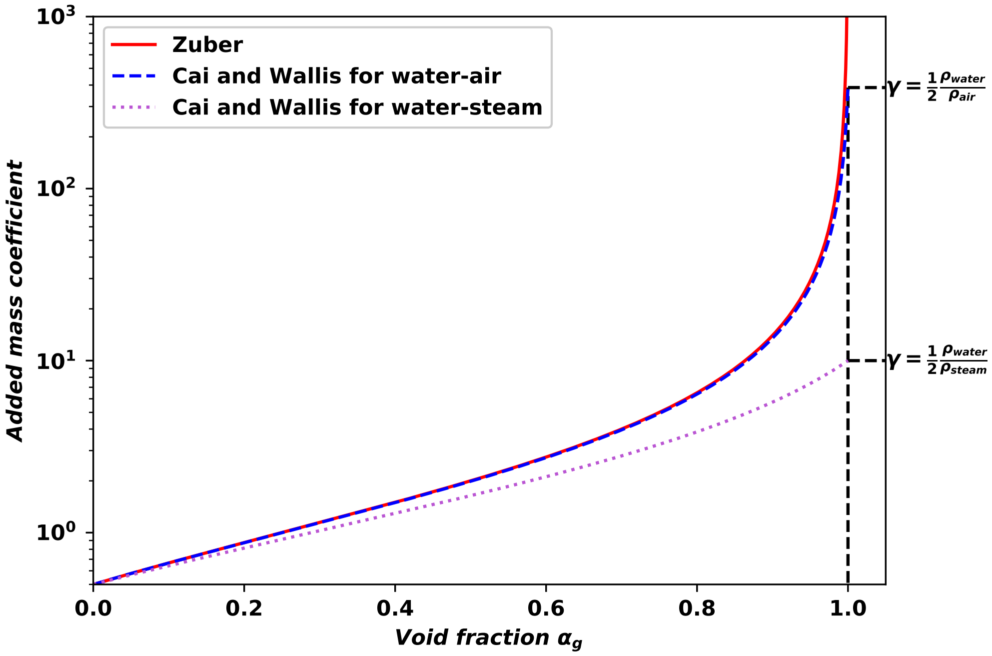

Figure 3.10: Added mass coefficient according to the value of α_g with Zuber's model[90] and Cai and Wallis' model [6] for water-air and water-steam cases.

Figure 3.10 compares the evolution of the added mass coefficient according to the value of α_g for with Zuber's model and Cai and Wallis' model [6] for water-air and water-steam cases. For air-water, it highlights the very small difference between the models until $\alpha_g \approx 0.8$. Then, while Zuber coefficient tends to infinity, Cai and Wallis' tends toward γ for any case.

Turbulent dispersion force

The last force to investigate is the turbulent dispersion force $\mathbf{F}^{T}_{l->g}$. This force allows redistribution of the void fraction by the flow fluctuations. The original expression of the force suffers from being overly isotropic, leading to excessive dispersion behind cylinders. This dispersion has a detrimental effect on dynamical structures, particularly on bubble clusters, which are crucial for accurately representing real physical processes. By substituting the turbulent kinetic energy with the Reynolds stress in the force expression, the model promotes non-isotropic dispersion. To extend this force, we can refer to the work presented in [64]. The expression proposed in [64] is primarily focused on the drag and added mass forces, with the possibility of easily incorporating additional terms from their final equation. By disregarding the lift force, if we examine the final balance equation as presented in [64], we can express it as follows:

$$\frac{\partial}{\partial t}\alpha_g\rho_g U_{gi} + \underbrace{U_{gi}\frac{\partial}{\partial x_j}\alpha_g\rho_g U_{gj}}_{\text{Transport}} + \underbrace{\frac{\partial}{\partial x_j}\alpha_g\rho_g R^g_{ij}}_{\text{Gas turbulence}} = \underbrace{-\alpha_g\rho_g\frac{\partial}{\partial x_i}P}_{\text{Pressure}} \underbrace{-\alpha_g\rho_l\frac{D_{ri}}{\tau^t_{lg}}}_{\text{Drift contribution}} \underbrace{-\alpha_g\rho_l f^D(U_{ri}-D_{ri})}_{\text{Drag force}} \underbrace{-\rho_l C_{AM}\left(\alpha_g\frac{\partial}{\partial t}U_{ri}+\frac{\partial}{\partial x_j}\alpha_g(R^g_{ij}-R^{lg}_{ij})\right)}_{\text{Added mass force}}, \tag{3.13}$$

with R^k_{ij} is the components of the Reynolds stress tensor in cartesian coordinates of phase k, R^{lg}_{ij} is the liquid-gas cross-correlation, C_{AM} the added mass coefficient of the distribution of bubbles, $\mathbf{D_r}$ the drift velocity between the phases. It is assumed in [64] that :

$$D_{ri} = -\tau^t_{lg}\left(\frac{1}{\alpha_g\rho_g}\frac{\partial}{\partial x_j}\alpha_g\rho_g R^{lg}_{ij} - \frac{1}{\alpha_l\rho_l}\frac{\partial}{\partial x_j}\alpha_l\rho_l R^l_{ij}\right). \tag{3.14}$$

Upon rearranging the terms, while omitting the derivatives of ρ_g as well as the one of the various Reynolds stress and cross-correlation tensors, and considering $\alpha_l = 1-\alpha_g$, the equation 3.13 is as follows: :

$$\frac{\partial}{\partial t}\alpha_g\rho_g U_{gi} + \underbrace{U_{gi}\frac{\partial}{\partial x_j}\alpha_g\rho_g U_{gj}}_{\text{Transport}} = \underbrace{-\alpha_g\rho_g\frac{\partial}{\partial x_i}P}_{\text{Pressure}} - \underbrace{\alpha_g\rho_l f^D U_{ri}}_{\text{Averaged drag force}} - \underbrace{\rho_l C_{AM}\alpha_g\frac{\partial}{\partial t}U_{ri}}_{\text{Averaged added mass force}} - \frac{\partial}{\partial x_i}\alpha_g\left(\underbrace{\rho_g R^g_{ii}}_{\text{Gas turbulence}} + \underbrace{\rho_l(R^g_{ii}-R^{lg}_{ii})C_{AM}}_{\text{Added mass fluctuations}} + \underbrace{\rho_l(f^D\tau^t_{lg}-1)(R^{lg}_{ii}+\frac{\alpha_g}{1-\alpha_g}R^l_{ii})}_{\text{Drag and drift fluctuations}}\right). \tag{3.15}$$

From [64], we also have :

$$R^{lg}_{ii} = \frac{b+\eta_r}{1+\eta_r}R^l_{ii}, \tag{3.16}$$

$$R^g_{ii} = \frac{b^2+\eta_r}{1+\eta_r}R^l_{ii}, \tag{3.17}$$

we then get a new formulation for the GTD by using $\rho_l R^l_{ii}\frac{\partial}{\partial x_i}\alpha_g$ as a common factor, so that $\mathbf{F}^T_{l->g} = -GTD\rho_l R^l_{ii}\frac{\partial}{\partial x_i}\alpha_g$, with previous $GTD = (f^D\tau^t_{lg}-1)\frac{b+\eta_r}{1+\eta_r} + C_{AM}\frac{b^2+\eta_r}{1+\eta_r}$ from [64] :

$$GTD = \underbrace{\frac{\rho_g}{\rho_l}\frac{b^2+\eta_r}{1+\eta_r}}_{\text{Gas turbulence}} + \underbrace{C_{AM}\frac{b^2-b}{1+\eta_r}}_{\text{Added mass contribution}} + \underbrace{\left(f^D\tau^t_{lg}-1\right)\left(\frac{b+\eta_r}{1+\eta_r}+\frac{\alpha_g}{1-\alpha_g}\right)}_{\text{Drag and drift contribution}}. \tag{3.18}$$

This expression is remarkable because we get a physics based "constant" instead of just an adjustable constant, but we still have too many variables to understand its behavior easily. The idea is not to propose new physics but to reorganize the terms in order to study them and suggest a slightly different approach for some terms. Our idea is to remind that $\tau^F_{lg}f^D = \frac{\rho_g}{\rho_l} + C_{AM}$ and

$\eta_r = \frac{\tau_{lg}^t}{\tau_{lg}^F}$, to get the final expression :

$$GTD = \underbrace{C_{AM}}_{Added\ mass} \left(\underbrace{\frac{b^2 - b}{1+\eta_r}}_{Dragging\ effect} + \eta_r \underbrace{\left(\frac{b+\eta_r}{1+\eta_r} + \frac{\alpha_g}{1-\alpha_g} \right)}_{Cross-correlation} \right) + \underbrace{\frac{\rho_g}{\rho_l}}_{Mass\ ratio} \left(\underbrace{\frac{b^2+\eta_r}{1+\eta_r}}_{Dispersed\ velocity\ fluctuations} + \eta_r \underbrace{\left(\frac{b+\eta_r}{1+\eta_r} + \frac{\alpha_g}{1-\alpha_g} \right)}_{Cross-correlation} \right) - \underbrace{\left(\frac{b+\eta_r}{1+\eta_r} + \frac{\alpha_g}{1-\alpha_g} \right)}_{Cross-correlation\ destruction} . \tag{3.19}$$

Figure 3.11 illustrates the behavior of the GTD according to α_g and η_r, assuming that they are independent variables, regarding a spherical bubble, using Cai and Wallis added mass force [6]. Notably, the graph exhibits a divergence towards infinity as α_g approaches 1. This divergence arises due to the void fraction becoming excessively high. However, in such scenarios, the dispersion force should not increase as the spatial fluctuations caused by the liquid turbulence decrease.

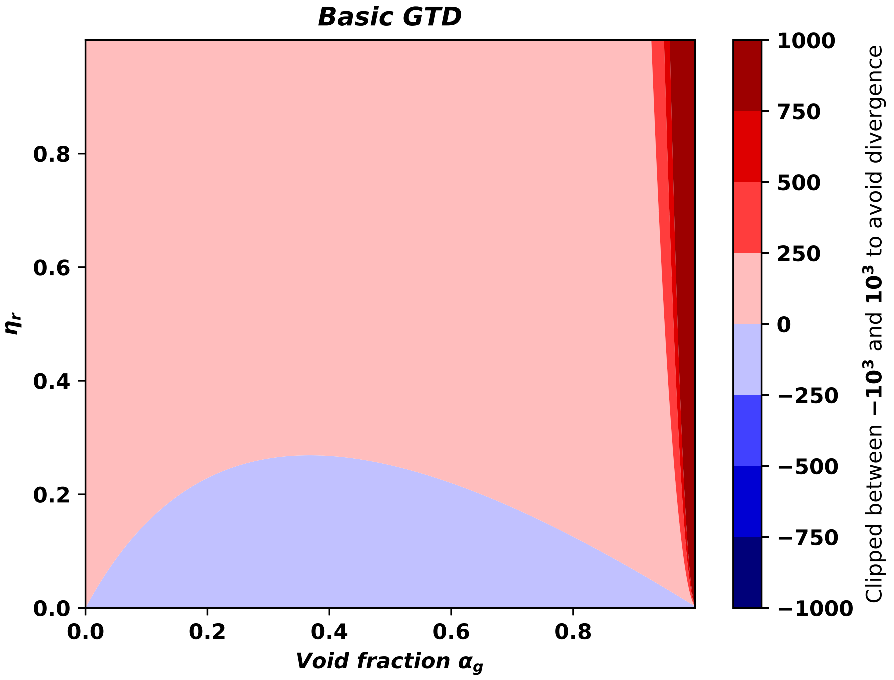

Figure 3.11: Basic GTD coefficient from equation 3.19 according to the value of η_r and α_g, assuming that they are independent variables, regarding a spherical bubble, using Cai an Wallis added mass force [6]. The values are clipped between -10^3 and 10^3 in order to avoid divergence.

To account for this phenomenon, we can observe that the term $\frac{b+\eta_r}{1+\eta_r} + \frac{\alpha_g}{1-\alpha_g}$ plays a significant role in predicting GTD behavior. This term in the model reflects the variance of liquid fluctuations encountered along the trajectory of a bubble. It is broken down into two components. The first component represents the correlation of liquid fluctuations associated with gas fluctuations, while the second component represents the correlation arising from the spatial distribution of gas. To account for areas with high void fractions caused by the spatial decorrelation of the gas distribution, like around cylinders, there needs to be a limitation on the void fraction related to this decorrelation. To better grasp this phenomenon, we consider a simplified scenario where the density ratio is assumed to be infinite, allowing us to use the Zuber model and neglect the density ratio in $b = \frac{1+C_{AM}}{C_{AM}}$:

$$GTD = \underbrace{C_{AM}}_{Added\ mass} \left(\underbrace{\frac{b^2-b}{1+\eta_r}}_{Dragging\ effect} + \underbrace{\eta_r \left(\frac{b+\eta_r}{1+\eta_r} + \frac{\alpha_g}{1-\alpha_g} \right)}_{Cross-correlation} \right) - \underbrace{\left(\frac{b+\eta_r}{1+\eta_r} + \frac{\alpha_g}{1-\alpha_g} \right)}_{Cross-correlation\ destruction} . \tag{3.20}$$

Figure 3.12 illustrates the behavior of the two components of the term with respect to the void fraction. The first component $\frac{b+\eta_r}{1+\eta_r}$ exhibits a decreasing trend as the void fraction increases. This is because at low void fractions, there is a strong correlation between gas and liquid fluctuations, primarily influenced by the bubble whose trajectory we are following. However, as the void fraction rises and more bubbles appear, the correlation between gas and liquid fluctuations weakens, as the influence of the leading bubble weakens. This behavior is logically consistent with the physical understanding of the system. Conversely, the second component $\frac{\alpha_g}{1-\alpha_g}$ shows an increasing trend with increasing void fraction. When the void fraction is low, there is limited correlation between fluctuations along the bubble trajectory and the bubbles away from the trajectory. However, as the void fraction increases, the coherence between these fluctuations grows rapidly due to the flow's inherent symmetry. This behavior is also in line with our understanding. It is crucial to note that this component diverges as the void fraction approaches 1. This divergence indicates that the model or approach used in the analysis becomes inadequate near complete gas phase, and additional considerations or modifications may be necessary to account for such conditions.

Figure 3.13 represents the evolution of the full term as a function of α_g for different η_r. Notably, regardless of the value of η_r, the term tends toward infinity when α_g tends toward 1. This behavior is primarily due to the ratio of the gas fraction to that of the liquid. To better understand how to address this issue, we can consider two ideal cases.

As a reminder, η_r represents the ratio between the characteristic time of turbulence along the trajectory of the bubble and the characteristic time of the bubble. The first case is when $\eta_r = 0$, as depicted in Figure 3.13. It means that the turbulence is instantaneous with respect to the bubble trajectory. In this situation, the bubbles move in a turbulent field that remains undisturbed. Consequently, the maximum variance of fluctuations experienced by the distribution of bubbles is when there is no bubble in the turbulent field, which occurs when $\alpha_g = 0$.

The second case, represented in Figure 3.13, is when $\eta_r \to \infty$. It means that the bubble path is instantaneous with respect to the time of turbulent structures. In this scenario, turbulence completely disperses the bubbles, and the liquid fluctuations encountered along their trajectory are only due to the fluctuations of the liquid flow. As a result, the correlation tends toward 1, which again corresponds to the case when $\alpha_g = 0$, i.e., when bubbles are absent. Therefore, in the general case, the maximum deviation of liquid fluctuations encountered on a bubble trajectory occurs when there is no bubble. In other words, the presence of bubbles does not lead to an increase in the deviation of liquid fluctuations along their path compared to the fluctuations generated in the liquid itself (this effect is taken into account in the turbulent time in η_r). The wake of the bubbles remains a source of fluctuations, but it cannot introduce wider liquid fluctuations than what is already present in the liquid turbulence. This observation gives rise to

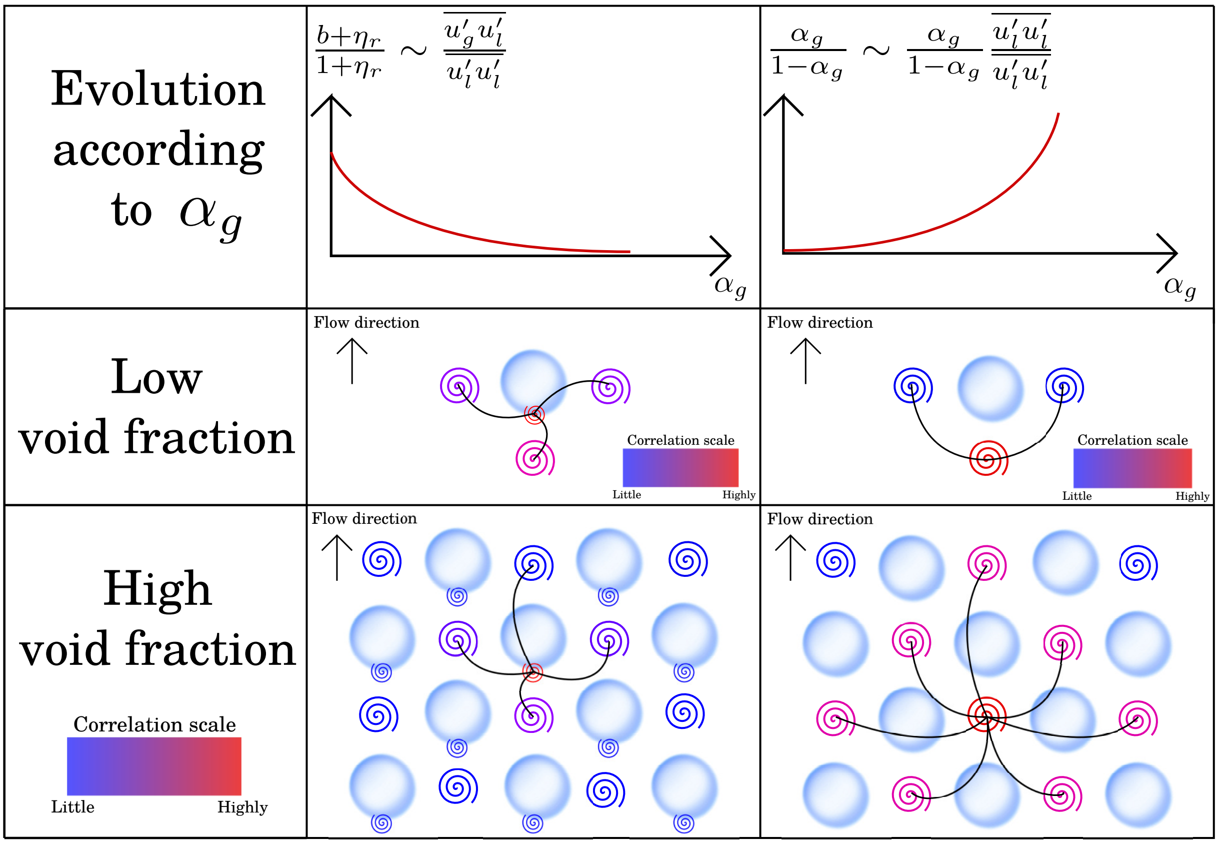

Figure 3.12: Evolution of $\frac{b+\eta_r}{1+\eta_r}$ and $\frac{\alpha_g}{1-\alpha_g}$ with the void fraction with η_r seen as a constant (top). Those two terms represent the gas-liquid and liquid-liquid correlation rates along bubble trajectories, respectively. The diagrams illustrate the interactions between the red swirls, representing the reference swirl, and distant swirls whose color indicates their correlation level, in the case of low void fraction (middle) and high void fraction (bottom).

the following equation :

$$\frac{b+\eta_r}{1+\eta_r} + \frac{\alpha_g}{1-\alpha_g} = \frac{b(\alpha_g = 0)+\eta_r}{1+\eta_r}, \tag{3.21}$$

with $b(\alpha_g = 0) = \frac{1+\frac{1}{2}}{\frac{1}{2}} = 3$. The solution of this equation gives the dispersion limit α_{gmax}, that depends on η_r :

$$\alpha_{gmax} = \frac{5-\eta_r}{2(\eta_r+4)}. \tag{3.22}$$

Notably, when $\eta_r = 0$, α_{gmax} reaches $\frac{5}{8} = 0.625$. This value is similar to the commonly used value for a random stack of solid spheres 0.62 and is also consistent with the limits of compactness observed in the bubbly regime. Indeed, the origin of this value is somewhat underdiscussed from a theoretical point of view in the literature, as it stems from experimental data. [85] offers an explanation based on the difference between the added mass of a bubble distribution (Zuber model) and the one derived from a potential calculation ($C_{AM} = 5 \times \frac{2}{3}$). However, contrary to what is indicated, the calculation actually yields $\alpha_g = \frac{17}{26} \approx 0.654$. However, this idea has forged the basis for most of the considerations presented in this thesis regarding the added mass.

The Figure 3.13 also illustrates the minimum value α_{gmin}, solution of $b + \frac{\alpha_g}{1-\alpha_g} = b(\alpha_g = 0)$, occurring when $\alpha_g = 4 - \frac{3}{2}\sqrt{6} \approx 0.3257$. This value is similar to the one used as limit for the

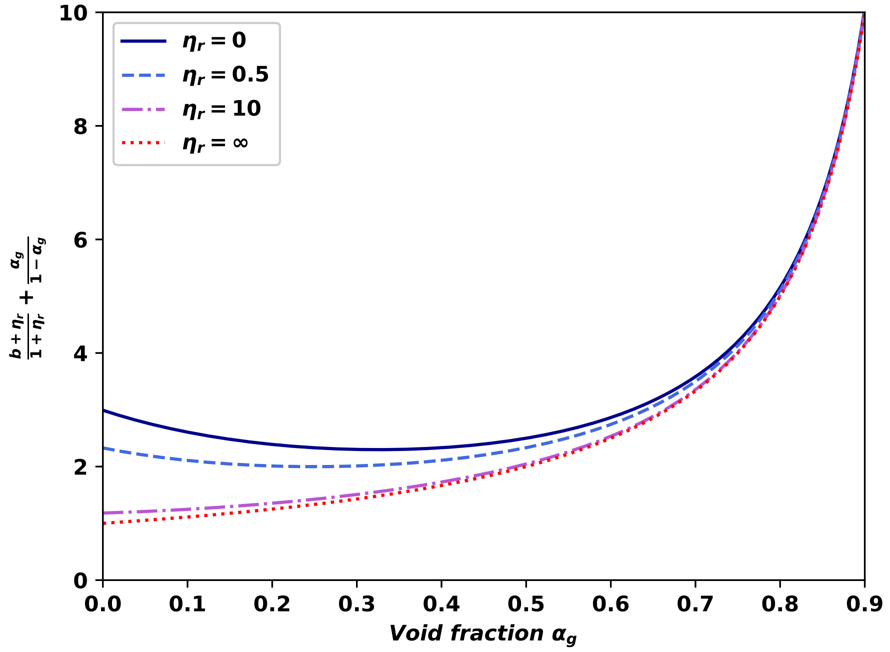

Figure 3.13: Evolution of the quantity $\frac{b+\eta_r}{1+\eta_r} + \frac{\alpha_g}{1-\alpha_g}$ according to the void fraction for different η_r .

bubbly regime. An interesting observation can be made when $\eta_r > 5$: $\alpha_{gmax} = 0$. In this case, the turbulence is so strong that void fraction effects are cancelled.
A similar analysis can be performed solving equation 3.21 using Cai and Wallis' model [6] (modifying b), with $\eta_r = 0$ and $\gamma = \frac{1}{2}\frac{\rho_l}{\rho_g}$. The solutions, depicted in Figure 3.14, are :

$$\alpha_{gmax} = \frac{10\gamma^3 - 18\gamma^2 - 3\gamma - 2}{(2\gamma - 1)^2(4\gamma + 1)}, \tag{3.23}$$

$$\begin{aligned}\alpha_{gmin} = & \frac{1}{8\gamma^4 + 24\gamma^3 - 2\gamma^2 + 6\gamma - 1}\Big(32\gamma^4 + 40\gamma^3 + 16\gamma^2 + 10\gamma + 2 - \\ & \sqrt{6}\sqrt{144\gamma^8 + 336\gamma^7 + 436\gamma^6 + 388\gamma^5 + 232\gamma^4 + 112\gamma^3 + 33\gamma^2 + 9\gamma}\Big)\end{aligned}. \tag{3.24}$$

For air-water flow, $\alpha_{gmax} \approx 0.623$ and $\alpha_{gmin} \approx 0.3250$. It appears that Zuber model [90] is satisfying for the modeling of dispersion in the current system.

The dispersion coefficient is ultimately constrained by α_{gmax} from equation 3.22. Figure 3.16 shows the evolution of new GTD concerning α_g and η_r with its new expression from 3.19 and 3.22. It highlights that the coefficient's order of magnitude is now more accurate. However, in certain areas, GTD could be negative according to this new formulation. A negative GTD coefficient would imply that the model might require further modifications to account for physical phenomena or could lead to the formation of bubble clustering. This observation highlights the potential for enhancing the model to better represent clustering phenomena.

In the general case, when $C_{AM}(\alpha_g = 0)$ is unknown we have :

$$\alpha_{gmax} = \frac{3 - C_{AM}(\alpha_g = 0)(1 + \eta_r)}{3 + 2C_{AM}(\alpha_g = 0)(1 + \eta_r)}. \tag{3.25}$$

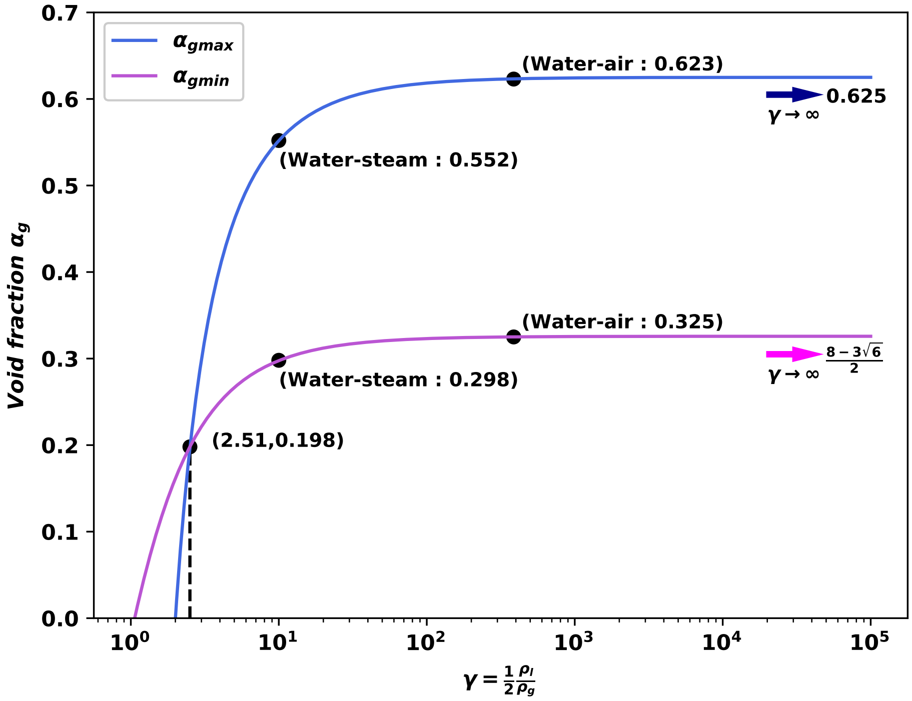

Figure 3.14: Evolution of α_{gmax} and α_{gmin} as a function of γ, computed with Cai and Wallis' model [6] and for $\eta_r = 0$.

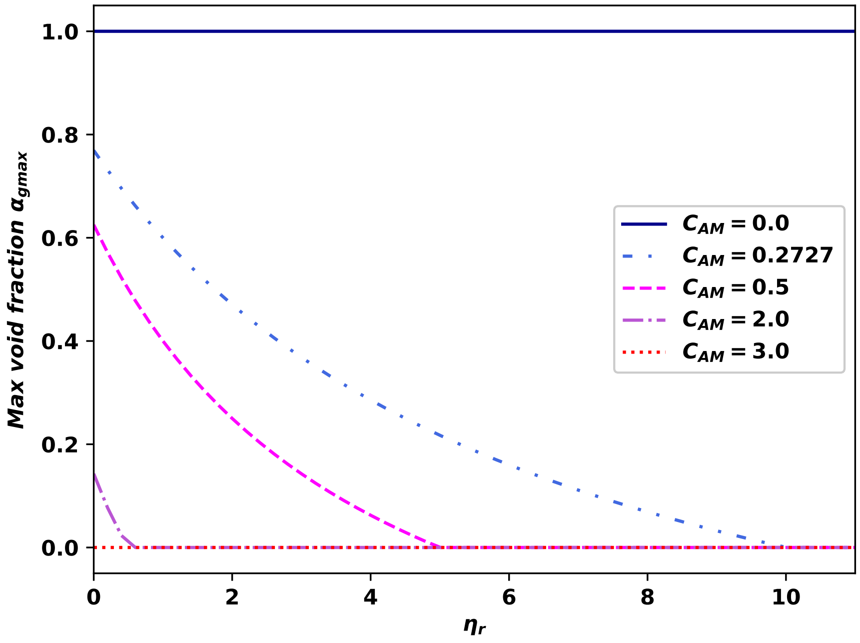

Figure 3.15: Evolution of α_{gmax} according to η_r for several values of $C_{AM}(\alpha_g = 0)$.

Figure 3.15 illustrates the evolution of α_{gmax} according to η_r for several value of $C_{AM}(\alpha_g = 0)$. It shows that the value of the added mass has strong effect on the prediction of α_{gmax}. When η_r,

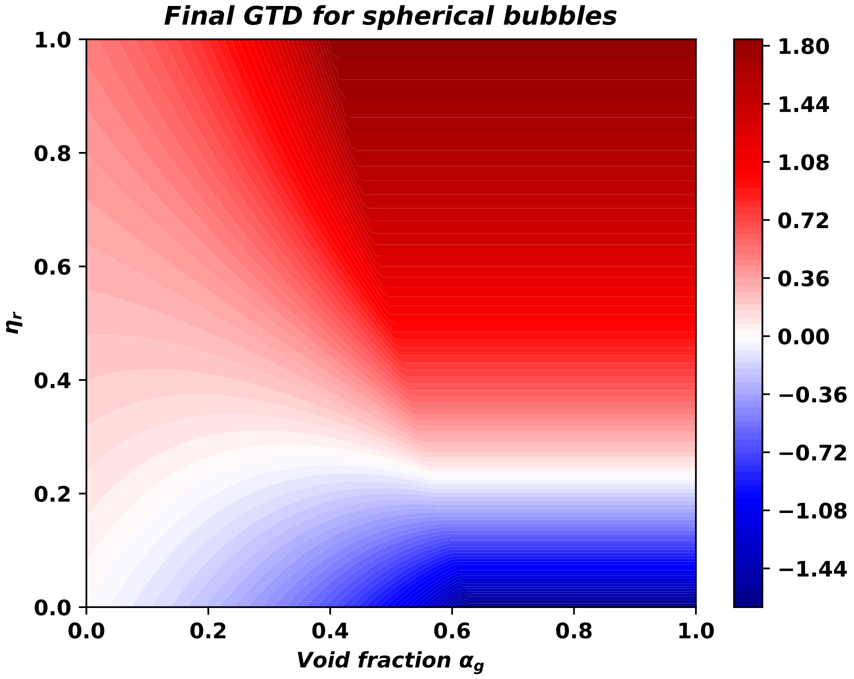

Figure 3.16: Final GTD coefficient for a spherical bubble according to the value of η_r and α_g.

α_{gmax} tends toward $\frac{3-C_{AM}(\alpha_g=0)}{3+2C_{AM}(\alpha_g=0)}$, making $\alpha_{gmax} = 0$ for any value of η_r for $C_{AM}(\alpha_g = 0) \geq 3$. It means either that 3 is a limit for the added mass coefficient or that when $C_{AM}(\alpha_g = 0)$ is more than 3, no void fraction effect should be taken into account.
Finally, we use the expression of GTD from equation 3.19 constrained by $\alpha_g = \min(\alpha_g, \alpha_{gmax})$, with α_{gmax} from equation 3.25.

The prediction of forces depends not only on the void fraction but also on the mean Sauter diameter. Predicting this diameter relies significantly on the prediction of the interfacial area and, consequently, the IATE. The source terms in the IATE equations are crucial for replicating bubble mechanisms. However, they are based on considerations regarding forces and the values of predicted fields, which are then adjusted to experimental values through their evolution in cross-sections. To use them accurately, particularly for high void fractions, it is necessary to study them locally. This is the focus of the next section.

3.2.2 Modifying and adapting the source terms

The challenges in TRITON's interfacial area modeling arise from the need to accurately represent the complex interactions of coalescence and break-up between bubbles (see section 2.2.3). Source terms are introduced in the equations that describe these interactions between bubbles. These source terms are essentially simplified mathematical representations of the underlying physical mechanisms governing coalescence and break-up. To validate and optimize these models, researchers typically compute a $1D$ version of the equations (in the cross-section), which allows for easier analysis and comparison with experimental data. While the equations themselves have been successfully computed in $3D$ CFD simulations, the models have mostly been confronted to bubbly flows without obstacle. As a result, there are concerns about the suitability and accuracy of some of these models due to their reliance on simplistic assumptions and theoretical considerations. The main issue lies in the emergence of regions with a high void fraction. Those areas are manifesting when obstacles, such as cylinders, are present within the fluid domain. As a reminder, the source terms are based on the five following categories : RC, WE, TI, SO and SI (see section 2.2.3).

The first source terms that may cause issues are RC terms. Indeed, almost all models are proportional to the following three functions h_1, h_2, h_3 (see appendices A.2), with $C_{RC1} = 3.0$:

$$h_1(\alpha_{g1}) = \frac{\alpha_{g1}^{8/3}}{\alpha_{g1max}^{1/3} - \alpha_{g1}^{1/3}} \left(1 - \exp\left(-C_{RC1}\frac{\alpha_{g1}^{1/3}\alpha_{g1max}^{1/3}}{\alpha_{g1max}^{1/3} - \alpha_{g1}^{1/3}}\right)\right), \tag{3.26}$$

$$h_2(\alpha_{g1}) = \alpha_{g1}^{8/3}\left(1 - \exp\left(-C_{RC1}\frac{\alpha_{g1}^{1/3}\alpha_{g1max}^{1/3}}{\alpha_{g1max}^{1/3} - \alpha_{g1}^{1/3}}\right)\right), \tag{3.27}$$

$$h_3(\alpha_{g1}) = \alpha_{g1}^{5/3}\left(1 - \exp\left(-C_{RC1}\frac{\alpha_{g1}^{1/3}\alpha_{g1max}^{1/3}}{\alpha_{g1max}^{1/3} - \alpha_{g1}^{1/3}}\right)\right). \tag{3.28}$$

Figure 3.17 depicts the evolution of the functions h_1, h_2, and h_3 derived from the IATE source terms with respect to the void fraction of group 1. Notably, all three functions exhibit a pronounced discontinuity at $\alpha_{g1max} = 0.62$ and take large positive values for h_1 and large negative values for h_2 and h_3 when $\alpha_{g1} > 0.62$. This discontinuity is particularly concerning as it leads to a divergence in coalescence around this void fraction value. Moreover, the plot reveals that the issue arises at an earlier stage for the function h_1 compared to h_2 and h_3.

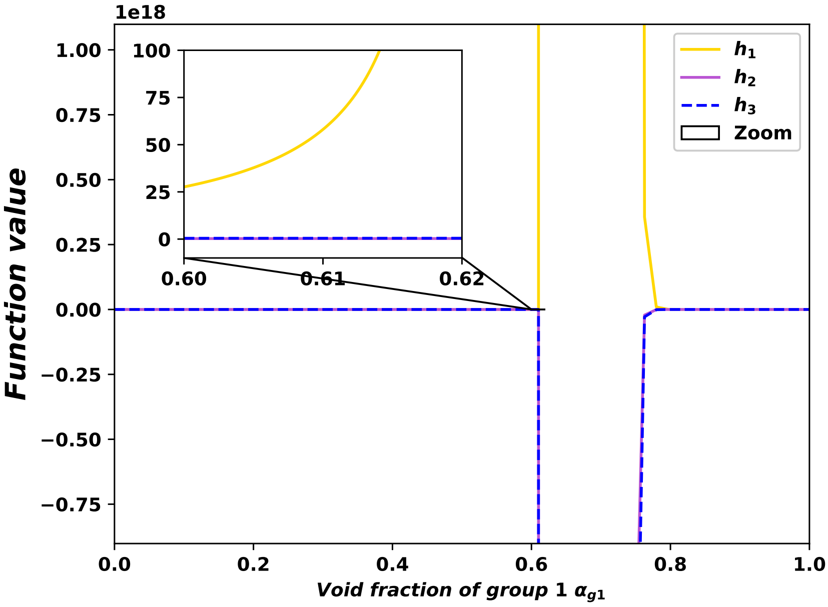

Figure 3.17: Graph of the evolution of different function h_1, h_2, h_3 from IATE source terms [120] according to the void fraction of the group 1.

The source term from the IATE that carries the most significant weight is $\phi_{RC}^{(1)}$ (see [83]) because it is proportional to the function h_1. This term is defined by :

$$\phi^{(1)}_{RC} = -0.17 C^{(1)}_{RC} \lambda^{(1)}_{RC} \frac{\varepsilon^{1/3} \alpha_{g1} ai^{5/3}}{\alpha_{gmax}^{1/3} (\alpha_{gmax}^{1/3} - \alpha_{g1}^{1/3})} \left(1 - exp\left(-C_{RC1} \frac{\alpha_{g1}^{1/3} \alpha_{gmax}^{1/3}}{\alpha_{gmax}^{1/3} - \alpha_{g1}^{1/3}}\right)\right). \tag{3.29}$$

Discrepancy issues are addressed when α_g approaches α_{gmax}. This can be done by writing $\phi^{(1)}_{RC}(\alpha)$ as the product of a term $\phi^0_{RC} = -0.17 C^{(1)}_{RC} \lambda^{(1)}_{RC} \varepsilon^{1/3} (\frac{6}{Dsm})^{5/3} \frac{1}{\alpha_{gmax}^{1/3}}$, independent of α_{g1} and a function depending on α_{g1} and α_{gmax}. We get :

$$h_1(\alpha_{g1}) = \frac{\phi^{(1)}_{RC}}{\phi^0_{RC}} = \frac{\alpha_{g1}^{8/3}}{(\alpha_{gmax}^{1/3} - \alpha_{g1}^{1/3})} \left(1 - exp\left(-C_{RC1} \frac{\alpha_{g1}^{1/3} \alpha_{gmax}^{1/3}}{\alpha_{gmax}^{1/3} - \alpha_{g1}^{1/3}}\right)\right). \tag{3.30}$$

Figure 3.18 illustrates the graph of function h_1 with respect to the void fraction. The observation made from the graph is that as the void fraction approaches α_{gmax}, there is a divergence of the source term, leading to an infinite coalescence. The modification is based on two key principles: continuity of the source term and independence of random collisions from the presence of an individual bubble once it becomes uncorrelated from the mean flow. The selected solution involves saturating the source term, constraining its value to be constant when $\alpha_g > 0.509$. This means that when the void fraction equals or surpasses 0.509, the source term will be capped at this threshold, thereby preventing its divergence toward infinity. Notably, the function value of h_1 is ten times higher than the previously established value of 0.325, which was identified as a cross-sectional limit for bubbly flow. Moreover, both 0.509 and 0.325 are close to the values in [104], used for predictions in TRACE (Transient Reactor Analysis Code), the american counterpart of the french CATHARE (Code for Analysis of THermalhydraulics during Accident of

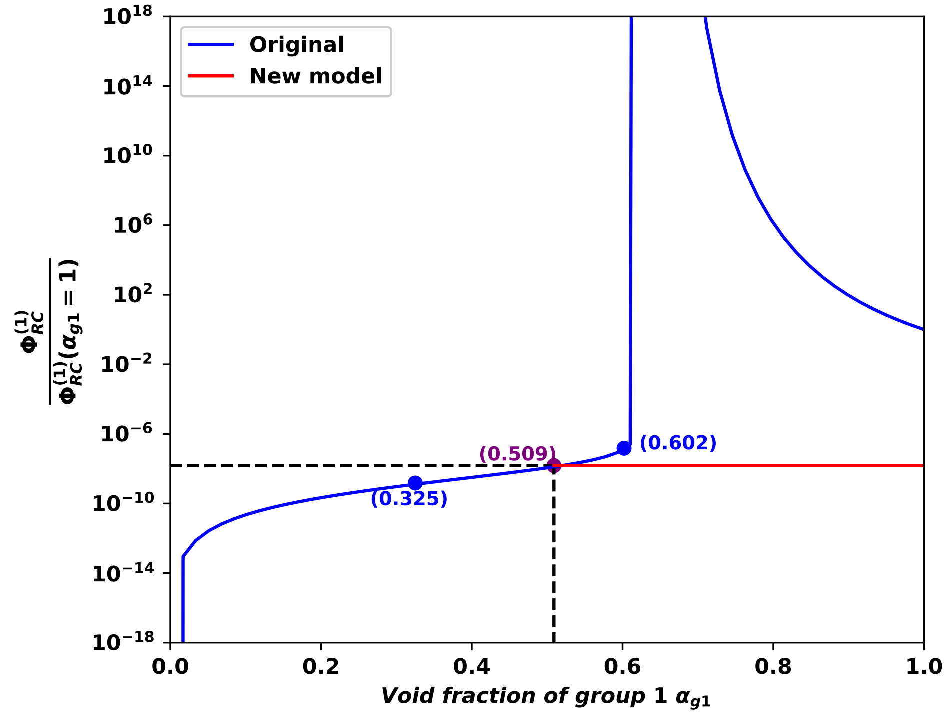

Figure 3.18: Graph of the evolution of the function $\frac{\phi^{(1)}_{RC}}{\phi^{(1)}_{RC}(\alpha_{g1}=1))}$ according to the void fraction.

Reactor and safety Evaluation) developed at CEA. Specifically, 0.602 gives a function value of h_1 ten times the one of 0.509. However, upon examining these cases, it becomes obvious that a void fraction of 0.509 yields the most appropriate coalescence behavior, given that the original value of 0.602 still induces excessive coalescence phenomena.

Another significant challenge arises from the WE sources (see appendices A.2). These sources directly depend on the velocity fields of the gas and liquid phases, making them highly sensitive to changes in velocity, particularly around the cylinder. One challenge stands in the source term of the bubbles of the first group $\phi^{(1)}_{WE}$. This term is defined by :

$$\phi^{(1)}_{WE} = -0.17 C^{(1)}_{WE} C^{1/3}_{D1} U_r a_i^2, \tag{3.31}$$

with $C_{D1} = \frac{2Dsm}{3}\sqrt{\frac{g\Delta\rho}{\sigma}}\left(\frac{1+17.67(1-\alpha_g)^{9/7}}{18.67(1-\alpha_g)^{3/2}}\right)^2$. However, U_r also depends on C_D, so it is crucial to have a good modeling of this term for large void fractions. Figure 3.19 shows the evolution of C_{D1} bubbly for different bubble diameters in the order of a millimeter. In particular, when the void fraction approaches 1, C_{D1} tends towards infinity. It can therefore no longer be used in modelling. One way to solve this problem, proposed by Tomiyama [132] is to consider for the high void fraction $C_{D2} = \frac{8}{3}(1-\alpha_g)^2$. We then take $C_D = min(C_{D1}, C_{D2})$.

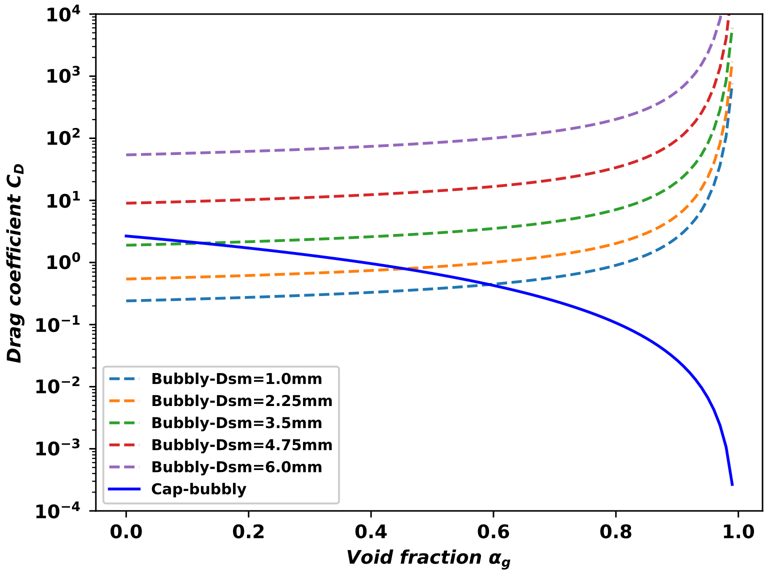

Figure 3.19: Graph of the evolution of drag coefficients for so-called bubbly and cap-bubbly regimes as a function of the void fraction.

Figure 3.19 also shows the behavior of C_{D2} cap-bubbly according to the void fraction. Note this time that C_{D2} tends to 0 when α_g tends to 1. However, U_r is inversely proportional to C_D, so if C_{D2} tends to 0 then U_r tends to infinity, which is not physically acceptable. To solve this, the idea is to remember that there is a quasi-static limit for void fraction. There is therefore a limit for the average bubble drag coefficients compared to that of a single bubble. We therefore choose for high void fraction, corresponding to a "single" bubble dynamic, to use the drag coefficient of a single bubble. We thus obtain $C_D = min(C_{D1}, max(C_{D2}, C_{D1}(\alpha_g = 0)))$. Depending on the chosen diameter we thus obtain 2 cases :

- Either the diameter is too large (around 4 mm) and no swarm effect is considered and the drag coefficient of a single bubble is used.

- Either the diameter is small enough and we obtain 3 velocities : a swarm velocity, a limit velocity and in between a dynamic (quasi-static) velocity.

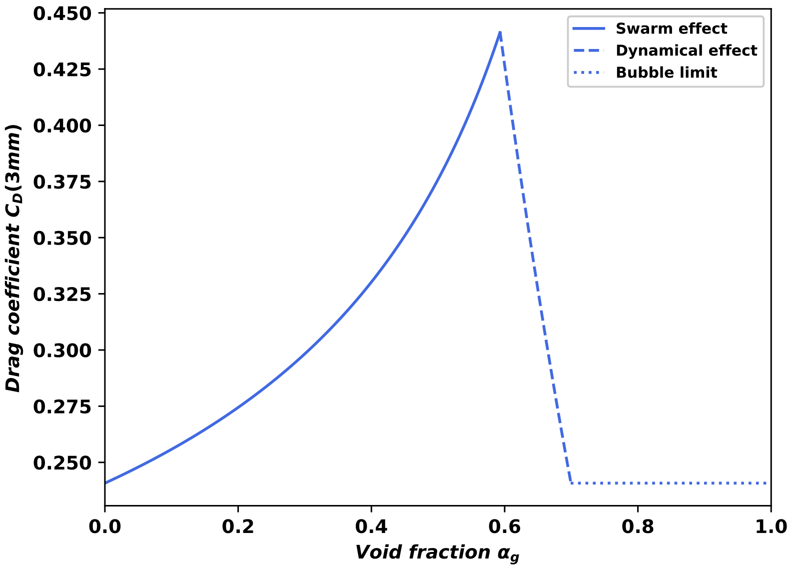

Figure 3.20: Graph of the evolution of the new drag coefficient as a function of the void fraction for a bubble of 3 mm.

Figure 3.20 shows the evolution of the new drag coefficient as a function of void fraction for a bubble of 3 mm, corresponding to the 2nd case previously mentioned.

Additionally, within the source terms, there is a modeling that corresponds to the relative velocity of the bubbles from group 1 within the wake of the bubbles from the second group. This velocity, denoted as U_{w12}, depends on the relative velocities of the two groups of bubbles and the modeling of a wake velocity, denoted as $U_{rw2} = 0.94 U_{r2} C_{Dcap}^{1/3}$:

$$U_{w12} = U_{rw2} + U_{r1} - U_{r2}. \tag{3.32}$$

Three source terms are then directly proportional to this velocity. However, it is highly sensitive to the prediction of the different fields and can lead to a significant mass transfer between gas fields, resulting in acceleration and possibly even changing the sign of the source term. To better apprehend the issue, we can use the solution derived in the section (3.2.1) to obtain $U_{r1} = U_b(1-\alpha_{gtot})^{1/2}$ and $U_{r2} = U_b\sqrt{\frac{D_{sm2}}{La}\frac{1-\alpha_{gtot}}{1-\alpha_{g2}}}$, with $La = \sqrt{\frac{\sigma}{g\Delta\rho}}$ and $\alpha_{gtot} = \alpha_{g1} + \alpha_{g2}$. The problem occurs in the near-wall region causing U_{r1} to become very small compared to U_{r2}. In this situation, $U_{w12} \propto 0.94(\frac{8}{3}(1-\alpha_{g2})^2)^{1/3} - 1$, which becomes negative when $\alpha_{g2} \approx 0.328$ for any value of the mean Sauter diameter. Consequently, the term is null whereas there is no physical explanation of it.

As previously discussed, using the Ishii drag coefficient [84] leads to its divergence when α_{g1}

tends toward 1. Therefore, we neglect the effects of void fraction on the calculation of the drag coefficient for group 1. In the general case with the aforementioned expressions, we obtain the following h_4 function so that $U_{w12} = U_{r1} h_4$:

$$h_4(\alpha_{g2}) = 1 - \frac{\sqrt{\frac{D_{sm2}}{4La}}}{1-\alpha_{g2}} \left(1 - 0.94\left(\frac{8}{3}(1-\alpha_{g2})^2\right)^{1/3}\right). \tag{3.33}$$

This function, illustrated in Figure 3.21, also changes its sign based on the predicted diameter

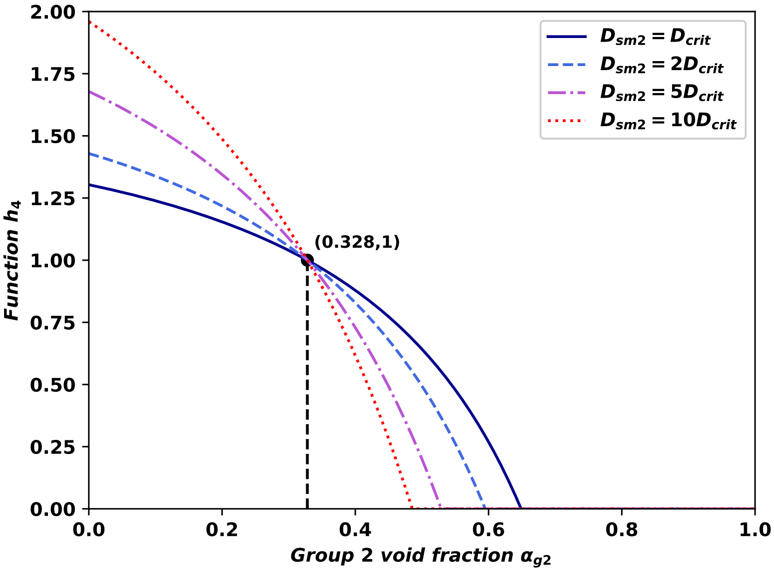

Figure 3.21: Evolution of $h4$ according to the void fraction of the second group α_{g2} for several values of D_{sm2}.

and so is damped to 0. For instance, considering the critical diameter value yields a maximum void fraction of approximately 0.65, near the close packing limit of the first group. Indeed, for $D_{sm2} = D_{crit}$ the bubbles behavior must be similar to the one of the first group. However, for $D_{sm2} = 10D_{crit}$ its value is approximately 0.485, it could correspond to too short wakes from group 2, compared to group 1 path, that can not entrain the bubbles of the first group until meeting. Notably, a point of intersection appears for $\alpha_{g2} \approx 0.328$ regardless of the diameter of group 2. Although, group 2 and group 1 void fraction phenomena are different, those values appearing in this model seem to be close to group 1 void fraction phenomena. This expression allows keeping the physics on which this expression is based while avoiding issues of divergence and rapid changes near the wall. Indeed, the model does not take into account near-wall effects.

Another issue with the source terms of the RC and TI model is related to the use of the turbulent dissipation ε (see appendices A.2). Even in single-phase flows, this variable is known for its difficulty in quantification and its varying orders of magnitude, making it less reliable in source terms. Furthermore, in the EBRSM model, ε can take very large values, especially near walls. However, in the RC and TI models, ε is used to quantify the turbulent eddies. Moreover, the dissipation near the wall is not only related to local eddies. Indeed, the EBRSM model tries to model the real dissipation near the wall that is not only related to eddies. Thus, the dissipation used in the coalescence/break-up source terms $\varepsilon^{source\ terms}$ must be changed, not to take into account the wall effect. If we use the equation 2.70, we have $L = 0.133max(\frac{k^{3/2}}{\varepsilon}, 80\frac{\nu^{3/4}}{\varepsilon^{1/4}})$. For homogeneous isotropic turbulence we have $\varepsilon = 15\nu\overline{(\frac{\partial u'}{\partial x})^2} \approx 15\nu\frac{\frac{2}{3}k}{L^2}$. By combining those two expressions we can express the new $\varepsilon^{source\ terms}$, as a function of the dissipation computed by the EBRSM ε^{EBRSM} :

$$\varepsilon^{source\ terms} = min\left(\frac{\frac{2}{3}15k\varepsilon^{EBRSM\ 1/2}}{0.133^2 80^2 \nu^{1/2}}, \varepsilon^{EBRSM}\right), \tag{3.34}$$

with k is the turbulent kinetic energy and ν is the kinematic viscosity. By limiting ε in this way, the model accounts for the isotropic behavior and aligns better with the assumptions made in the RC modeling approach. This modification helps to improve the accuracy and reliability of the RC model, especially in regions near walls where non-local effects can significantly impact the turbulence characteristics.

As previously discussed, it is crucial to accurately predict turbulent quantities such as dissipation and turbulent kinetic energy to compute the source terms, the coupling forces, and even the mean liquid velocity field. Pseudo-turbulence remains an area with more open questions than answers, and in the following section, we modestly propose to address some discrepancies between models for our specific application.

3.2.3 Modifying and adapting two-phase turbulence

While bubble-induced turbulence appears effective in a channel, its application around a cylinder gives rise to certain issues. The only available experiment in the literature that investigates two-phase flow around a cylinder, specifically addressing the fluctuations induced by bubbles, is [65]. Although this study handle a cylinder diameter of 30 mm, bubble velocities on the order of 0.3 m/s, and bubble diameters ranging from 3.4 mm to 4 mm – which are comparable to the experiment conducted at CEA – the experiment only covers void fractions below 2%. Consequently, direct comparison is available only with CFD studies in order to account for bubble-induced fluctuations and its interaction with a cylinder.

The primary problem is an overestimation of dissipation, which leads to the almost complete dissipation of turbulence. This issue arises from the challenge of selecting an appropriate relaxation time for the bubbles. In the basic model, the scale chosen is denoted as $\tau_b = (\frac{D_{sm}^2}{\varepsilon})^{1/3}$. However, in the EBRSM model, as the flow approaches the cylinder, dissipation shows a significant increase. Consequently, this mechanism causes a sharp reduction in the τ_b scale. As the dissipation linked to bubbles is inversely proportional to this characteristic time, it results in a substantial dissipation source. The dissipation becomes so intense that it effectively eliminates all turbulent structures. To address this challenge, two solutions can be considered: to reduce the influence of bubbles near the wall, or/and, to modify the scale of this relaxation process.

Due to the asymptotic behavior of the EBRSM, a solution arises. The EBRSM relies on a relaxation equation between two pressure redistribution models: a local and a non-local one. The transition between these models is identified by the variable β. Bubble fluctuations occur due to local pressure changes as bubbles pass through. Therefore, the solution involves modulating the BIT using the same scale β. To switch from the local model to the non-local model, all BIT-related sources should be multiplied by β^3. The second solution involves a simple adjustment of the timescale τ_b. In recent literature, two other scales are preferred: $\frac{D_b}{U_r}$ and $\frac{D_b}{\sqrt{k}}$. The first scale yields slightly better results in the center of the channels, while the second provides better results close to the walls - see [75]. To avoid the characteristic time becoming almost zero, one can consider the following expression :

$$\tau_b = max\left(\frac{D_b}{U_r}, \frac{D_b}{\sqrt{k}}\right). \tag{3.35}$$

Another aspect of this modeling, which has not been adequately addressed in the literature, regard the derivation of the coefficients used in the model. Currently, there is no justification provided for these coefficients. Therefore, it becomes crucial to compare this model, which depends on the direction of U_r, with existing literature. One straightforward approach is to compare it with the Colombo model. To derive the Colombo solution, one needs to reorganize the terms considering a single direction of bubble movement. Upon performing the calculations in our case, we obtain coefficients of 10/9 in the direction of flow and 4/9 in the transverse directions. On the other hand, Colombo's model yields coefficients of 1 in the direction of flow and 0.5 in the transverse directions. While the values are close, they are different. However, no justification has been provided for this discrepancy. The proposed idea is to reevaluate the model using the Colombo coefficients. The recalculated model yields the following results:

$$In\ R_{ij}\ equation\ :\ \frac{2}{3}\mathbf{F}_D\mathbf{U}_r\left(\frac{3}{4}br_{ij} + \delta_{ij}\right), \tag{3.36}$$

$$In\ \varepsilon\ equation\ :\ \frac{\mathbf{F}_D\mathbf{U}_r}{\tau}. \tag{3.37}$$

Case	Unmodified	Modified
1 component	$\begin{pmatrix} 10/9 & 0 & 0 \\ 0 & 4/9 & 0 \\ 0 & 0 & 4/9 \end{pmatrix}$	$\begin{pmatrix} 1 & 0 & 0 \\ 0 & 1/2 & 0 \\ 0 & 0 & 1/2 \end{pmatrix}$
2 components	$\begin{pmatrix} 7/9 & 0 & 0 \\ 0 & 7/9 & 0 \\ 0 & 0 & 4/9 \end{pmatrix}$	$\begin{pmatrix} 3/4 & 0 & 0 \\ 0 & 3/4 & 0 \\ 0 & 0 & 1/2 \end{pmatrix}$
3 components	$\begin{pmatrix} 2/3 & 0 & 0 \\ 0 & 2/3 & 0 \\ 0 & 0 & 2/3 \end{pmatrix}$	$\begin{pmatrix} 2/3 & 0 & 0 \\ 0 & 2/3 & 0 \\ 0 & 0 & 2/3 \end{pmatrix}$

Table 3.1: Table of the matrix of the modified and unmodified models in the principal directions for the cases : 1 component, 2 component isotropic and 3 components isotropic.

It is then interesting to investigate the behavior of the model in three idealized scenarios: the one-component case, the two-component isotropic case, and the three-component isotropic case. The outcomes of this analysis are summarized in Table 3.1. The study reveals that the energy level of the two models is identical, but there are slight differences in the redistribution process. Notably, the modified version aligns more closely with the findings reported in the existing literature.

In this section, we focused on modeling bubbles from Group 1. Despite a fairly extensive literature on modeling quasi-spherical bubbles, modifications were needed concerning the forces, IATE source terms, and pseudo-turbulence to properly account for the unique topology of a flow with obstacles. The other group also exhibited modeling challenges but had relatively limited literature available. Consequently, we had to take a new perspective and develop a different model to ease the calculations. The following section specifically deals with the modeling of the deformed bubble group and provides a comparison with an experimental case.

3.2.4 On the impact of the added mass of the second group

During the case study involving a majority of bubbles from the second group and high void fractions, several significant issues arose. The activation zones of the LIM (interface reconstruction method) were very wide due to strong void fraction gradients, particularly near the walls and upstream of the cylinder. Several causes have been identified:

- From group 2 diameter field: unexpected jumps appeared in the field representing the diameter of the second group of bubbles, leading to significant variations in forces and resulting in void fraction gradients. This could be indicative of improper formulation or numerical implementation of equations, or it might be related to an incompatibility with other fields sharing information.
- From the turbulent dispersion force: the turbulent dispersion force could also play a role in this problem, especially if the coefficient associated turned out to be negative, which would be unsuitable in this context.
- From the LIM (interface reconstruction method) activation criterion: another possible factor is an issue related to the activation criterion of the LIM. This criterion determines when large interfaces are present and choosing an inappropriate criterion could lead to excessive activation in inappropriate zones.

The most obvious issue is the presence of a negative dispersion zones. There are two forces that can be looked at in an attempt to modify the dispersion coefficient: the drag force and the added mass force. The drag force directly influences the characteristic time of the bubbles, while the added mass force influences the weight of different mechanisms. The drag force already provides consistent results in other configurations in the literature and in various simulations carried out. Therefore, the idea is to focus on the added mass force.
The coefficient $C_{AM} = \frac{1}{2}$ is suitable for spherical or almost spherical bubbles. However, the 2nd group of bubbles is made of deformed bubbles that have way more resistance to its motion. The added mass coefficient is then underestimated and must be computed. However, no general computation is available for any type of bubble of the second group. Then, we choose the model used by Shen and Hibiki [113] for the second group. As depicted in Figure 3.22 We consider a cap bubble, of small axis h_w and half of the longer axis a_w, with a wake angle θ_w of 50° - typically the angle found in experiments. Then, its aspect ratio :

$$\mu_w = \frac{h_w}{2a_w} = \frac{h_w}{2a_w} = \frac{1}{2}\frac{1-cos(\theta_w)}{sin\theta_w} \approx 0.233. \tag{3.38}$$

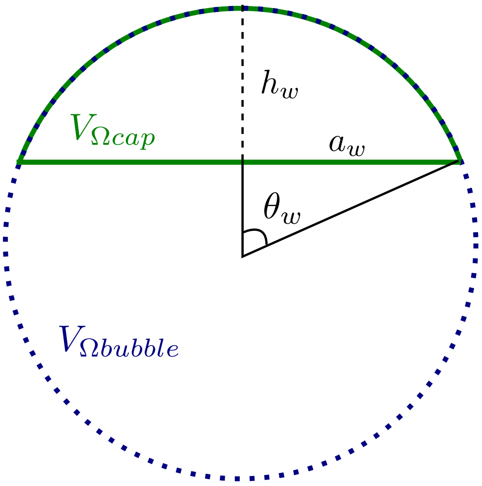

Figure 3.22: Scheme of a cap bubble

We then have the volume of the cap $V_{\Omega cap} = \frac{\pi a_w^3 \mu_w (3+4\mu_w^2)}{3}$ and its surface $S_{cap} = 2\pi a_w^2(1+2\mu_w^2)$. We have then :

$$\frac{V_{\Omega cap}}{S_{cap}} = \frac{D_{sm}}{6} = \frac{a_w \mu_w}{6} \frac{3+4\mu_w^2}{1+2\mu_w^2}. \tag{3.39}$$

Then we have $\frac{D_{sm}}{a_w} = \mu_w \frac{3+4\mu_w^2}{1+2\mu_w^2}$. If we use Simcik and et al.[117] formula for the shape factor f_{shape} :

$$f_{shape} = \frac{V_{\Omega cap}}{V_{\Omega bubble}} = \frac{1}{4} sin^3(\theta_w)\mu_w(3+4\mu_w^2) \approx 0.0842. \tag{3.40}$$

Then according to the value found by Simcik an al. [117], we have :

$$C_{AM} = 1.01 f_{shape}^{-0.416} \approx 2.83, \tag{3.41}$$

for rigid cap bubbles and :

$$C_{AM} = 1.13\times10^{-5}(180° - \theta_w)^3 - 3.4\times10^{-3}(180° - \theta_w)^2 + 0.356(180° - \theta_w) - 11.9 \approx 1.75, \tag{3.42}$$

for deformable cap bubbles. We chose to use the last one because the first result is too high.

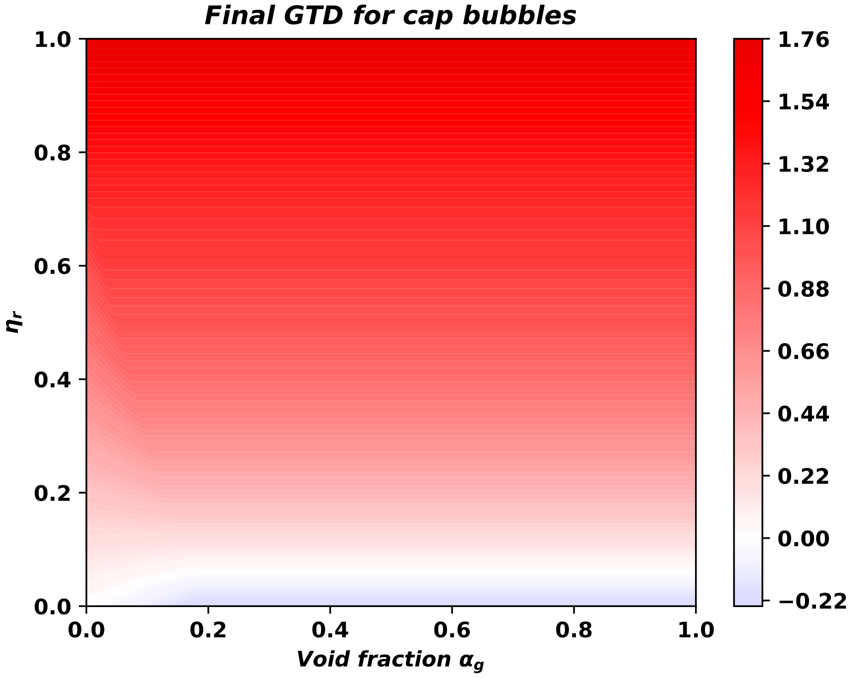

Figure 3.23: Final GTD coefficient for a cap bubble according to the value of η_r and α_g.

The figure B.10 shows the evolution of GTD according α_g and η_r with its new expression for a cap bubble, with $C_{AM} = 1.75$. It can be noticed the area of negative GTD is way smaller and that in general the GTD for the cap bubble is close to the one for the spherical bubbles. For $C_{AM} = 1.75$ and $\eta_r = 0$, $\alpha_{gmax} \approx 0.192$ close to the maximum packing limit of $\alpha_{gmax} \approx 0.2$ used in [49] for squeezed cap bubbles in order to deduce a flow regime transition criteria for two-phase flow in vertical annulus. In the case one would like to use 0.2 exactly as cap-bubble packing limit, the added mass coefficient should be $\frac{12}{7} \approx 1.71$ and so $\theta_w \approx 50.82°$.

To repair the appearance of diameter jumps due to strong dynamics, it is crucial to have a repair and smoothing method. Indeed, we strongly constrain the diameter of group 2 to prevent its field from reaching values outside the permissible range i.e. the range of group 1. The idea to avoid excessive constraints is to introduce diffusion in the diameter fields. The original idea from [51] is to add diffusion terms related to the average of the near-interface transport term in the equation for a_i.
In NEPTUNE _CFD, it is not a_i that is solved, but rather $X_g = \frac{a_i}{\rho_g \alpha_g}$. Therefore, we need to modify this term to adapt to our resolution:

$$\frac{D_{a_i}}{\alpha_g}\nabla a_i = \frac{\rho_g D_{a_i}}{\alpha_g}(X_g \nabla \alpha_g + \alpha_g \nabla X_g) = \rho_g D_{a_i}(X_g \nabla ln(\alpha_g) + \nabla X_g). \tag{3.43}$$

We obtain two terms, one dependent on α_g and the other on X_g. The first term presents a divergence issue when $\alpha_g = 0$ and becomes dependent on the logarithm of the void fraction for other cases. To address this, we choose to set its diffusion coefficient to 0 and neglect this term in our equation. Consequently, we obtain a term identical to the one proposed by [51]. However, this gives rise to the issue of modeling the diffusion term. It is suggested that $D_{a_i} = K D_{sm}|v'_l|$, with $K = \frac{1}{3}$. While this coefficient K is known to match experimental observations for bubbly cases, it lacks sufficient justification for straightforward application to group 2.

Therefore, our objective is to understand its likely origin. The diffusion coefficient in the equation should quantify the bubble's ability to transfer its energy to fluctuating structures. Thus, a commonly used scale arises naturally, inspired by [24] for the turbulent diffusion, the time scale τ_b for energy transfer from bubbles to the liquid :

$$\tau_b = \frac{\frac{1}{2}(\rho_g + C_{AM}\rho_l)\alpha_g U_r^2}{\frac{3}{4}\rho_l C_D U_r^3 \frac{\alpha_g}{D_{sm}}} \approx \frac{2}{3}\frac{C_{AM}D_{sm}}{C_D U_r}. \tag{3.44}$$

We now have a velocity scale for energy transfers, $C_D U_r$, and a spatial scale of $\frac{2}{3}C_{AM}D_{sm}$. If we revisit the definition of the diffusion coefficient, it can be expressed as the velocity fluctuations multiplied by the characteristic scale of energy transfers, which yields:

$$D_{ai} = \frac{2}{3}C_{AM}D_{sm}|v_l'|. \tag{3.45}$$

We have $K = \frac{2}{3}C_{AM}$ in this case. For a spherical bubble, $C_{AM} = \frac{1}{2}$, thus yielding $K = \frac{1}{3}$ for spherical bubbles. For bubbles in group 2, we have $K = \frac{2}{3} \times 1.75 \approx 1.167$.

The final issue concerns the criterion of the maximum allowable void fraction to transition from dispersed to continuous modeling. This criterion is not yet based on any physical phenomenon. Additionally, [60] demonstrated that the results did not provide insight into the true influence of this parameter, and thus, no criterion exists to optimize it. Therefore, it is necessary to identify the origin of this limit in order to assign a coherent value to it in the modeling process. An aspect that appears to be gaining importance in the case of group 2 is the added mass effect. To be more precise, the additional mass resulting from the presence of group 2 bubbles seems to exert significant influence. In fact, [85] suggested an added mass effect in the transition from dispersed bubbles to slugs and their stability due to strong added mass force. Therefore, investigating this effect is pertinent since gas pockets are similar to slugs. For this purpose, we can study an ideal scenario using the LIM perspective (interface reconstruction method). We suppose a vertical one-dimensional dynamic channel to focus only on these 3 cells, neglecting wall effects, turbulence and density ratio. We therefore want the transition from LIM in the interface from a maximum value α_{gcd} to retain the fluid impulse of an idealized gas pocket, taken from [85]. In other words, we want point out when the dispersed point of view is equal to a mean cross-sectionnal point of view. This value should depend on the presence of gas both groups. α_{gcd} will then be the void fraction before the LIM activation. α_{g2}' gives the void fraction of the second group in the central cell. α_{gtot} gives the total void fraction of gas in the central cell. By continuity with the LIM we want continuity of the impulse in the cross-area :

$$\underbrace{C_{AM}^{Disp}\frac{D\frac{1}{2}U_r^2}{Dt}}_{\textit{Dispersed bubble perspective}} = \underbrace{C_{AM}^{Ideal\ gas\ pocket}\frac{D\frac{1}{2}U_b^2}{Dt}}_{\textit{Average gas inclusion perspective}} . \tag{3.46}$$

However, at equilibrium $U_r^2 = Ub^2(1-\alpha_{gtot})$ and by neglecting the time derivative of α_g, we get :

$$C_{AM}^{Disp}(1-\alpha_{gtot}) = C_{AM}^{Ideal\ gas\ pocket}. \tag{3.47}$$

In order to simplify the equation, we use the Zuber model and Ishii model for the added mass, giving $C_{AM}^{Disp} = C_{AM0}\frac{1+2\alpha_{g2cd}}{1-\alpha_{g2cd}}$ and $C_{AM}^{Ideal\ gas\ pocket} = \frac{2}{3}\frac{1}{1-\alpha_{g2}'}$. We have by conservation of the gas in the three cells:

$$\alpha_{g2}' = \frac{2\alpha_{g2} + \alpha_{g1} - 1}{1-\alpha_{g1}}. \tag{3.48}$$

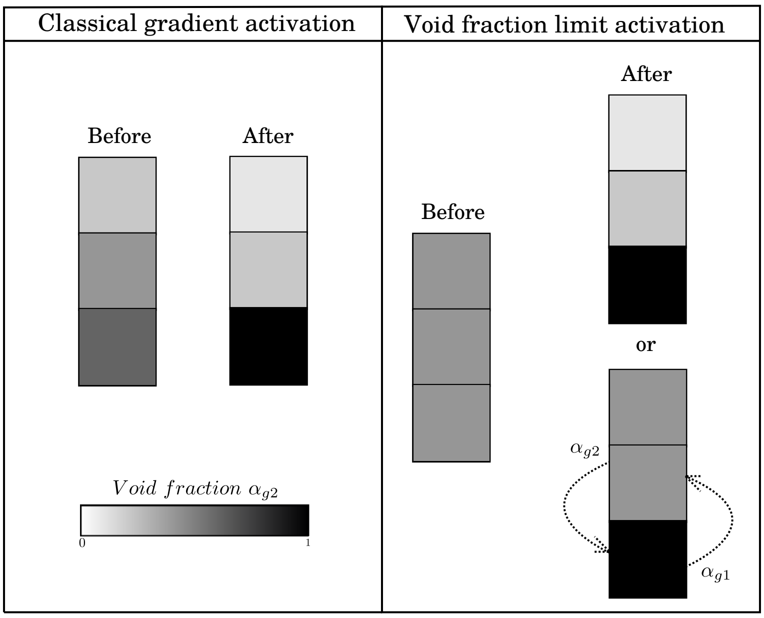

Figure 3.24: Scheme of the different activation of the continuous phases from the LIM point of view.

Figure 3.24 illustrates the two principles of continuous model activation from the perspective of the LIM. The conventional activation occurs through the void fraction gradient of Group 2. However, this criterion alone is insufficient to localize the activation zones of the continuous field. In fact, a maximum void fraction limit is also necessary. We can distinguish between two cases. The first case involves the emergence of large interfaces due to the average void fraction within the section. This can be linked to the appearance of annular flow within the section. The second case involves the appearance of significant interfaces concealed by the presence of Group 1. The first case is easily interpretable but more challenging to study since it is not directly linked to any particular phenomenon that could be used to compute the limit. In contrary, the second case may be associated with dynamics related to added mass. Therefore, this phenomenon must manifest when the LIM fails to detect the gradient due to it being hidden within the void fractions. Thus, we must consider that $\alpha'_{g2} = \alpha_{g2cd}$. We then have :

$$\alpha_{g1} = \frac{1-\alpha_{g2cd}}{1+\alpha_{g2cd}}. \tag{3.49}$$

This limit will be strongly affected by the value of C_{AM0}. However, it can vary from 0 to 3 depending on the shape of the churn bubble according to the dispersion force. We choose to use the maximum limit of 3. The equation is then :

$$3\frac{1+2\alpha_{g2cd}}{1-\alpha_{g2cd}}(1-\alpha_{gtot}) = \frac{1}{3}\frac{1-\alpha_{g1}}{1-\alpha_{gtot}}. \tag{3.50}$$

Then by considering $\alpha'_{g2} = \alpha_{g2cd}$ not to activate the reconstruction, we have :

$$\frac{1+2\alpha_{g2cd}}{1-\alpha_{g2cd}}\left(1-\alpha_{g2cd}-\frac{1-\alpha_{g2cd}}{1+\alpha_{g2cd}}\right)^2 = \frac{1}{9}\left(1-\frac{1-\alpha_{g2cd}}{1+\alpha_{g2cd}}\right). \tag{3.51}$$

This equation has 2 interesting solutions, a maximum $\alpha_{g2cdmax}$ and a minimum $\alpha_{g2cdmin}$. The solutions are way too complex to be implemented in a code because it supposes the simplification of a complex number but are real numbers. Indeed, their analytical expression are - with i denoting the complex number so that $i^2 = -1$:

$$\alpha_{g2cdmax} = \frac{1}{6}\left(1 + \frac{\sqrt[3]{-36 + i\sqrt{13443}}}{3^{2/3}} + \frac{17}{\sqrt[3]{3\Big(-36 + i\sqrt{13443}\Big)}}\right) \approx 0.810, \qquad (3.52)$$

$$\alpha_{g2cdmin} = \frac{1}{6} - \frac{(1 + i\sqrt{3})\sqrt[3]{-36 + i\sqrt{13443}}}{12 \times 3^{2/3}} - \frac{17(1 - i\sqrt{3})}{12\sqrt[3]{3\Big(-36 + i\sqrt{13443}\Big)}} \approx 0.246. \qquad (3.53)$$

This behavior is intriguing because according to Ishii and Hibiki [85] slug bubbles appear with a void fraction around 0.8. It means that the model can handle the dynamical behavior of a slug with the LIM model. The second value seems to be difficult to interpret because it can not be found in the literature. However, an explanation of its origins is given in the chapter on the DIVA experiment and simulations by looking at data.

The same computation can be done by taking into account the density ratio within the added mass coefficient (from equation 3.12) and balance equation, so that equation 3.46 becomes :

$$\underbrace{\frac{\rho_g}{\rho_l}\frac{D\frac{1}{2}U_r^2}{Dt} + C_{AM}^{Disp}\frac{D\frac{1}{2}U_r^2}{Dt}}_{\textit{Dispersed bubble perspective}} = \underbrace{\frac{\rho_g}{\rho_l}\frac{D\frac{1}{2}U_b^2}{Dt} + C_{AM}^{Ideal\ gas\ pocket}\frac{D\frac{1}{2}U_b^2}{Dt}}_{\textit{Average gas inclusion perspective}}. \qquad (3.54)$$

There is no simple general form for the solution. For water-air, we get for the upper limit $\alpha_{g2cdmax} \approx 0.806$ and for the lower limit $\alpha_{g2cdmin} \approx 0.247$. It is then a good approximation to use the previous correlation as it is the result of a simpler equation. However, for a SG mix $\gamma \approx 10$, the upper limit is $\alpha_{g2cdmax} \approx 0.668$ and for the lower limit $\alpha_{g2cdmin} \approx 0.290$. It means that in this case, the upper limit should be modified to take into account the density ratio.

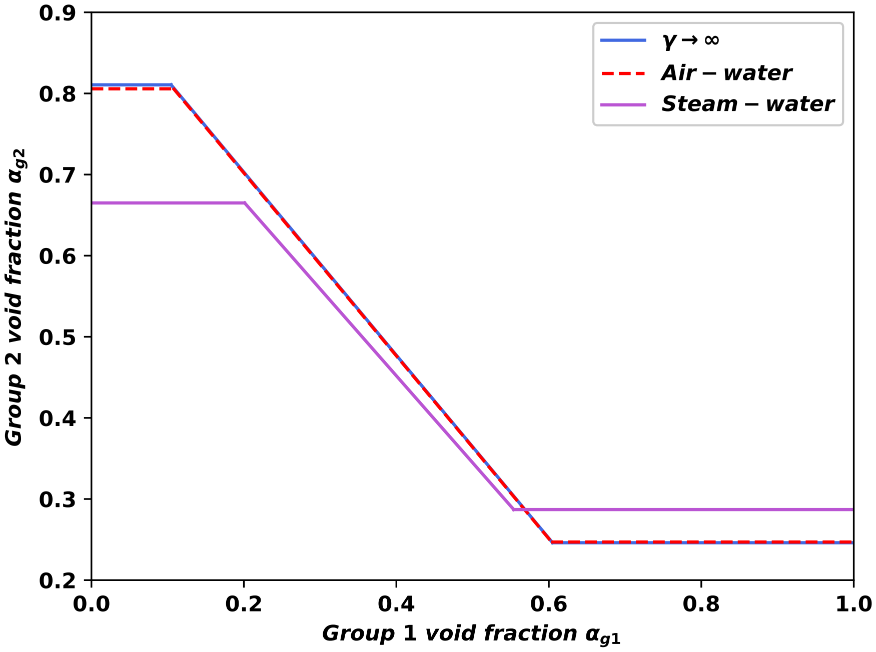

Figure 3.25: Linear approximation of the void fraction limit of the 2nd group from dispersed to continuous according to the void fraction of the first group for different $\gamma = \frac{1}{2}\frac{\rho_l}{\rho_g}$. Air-water : $\gamma = 387$, Steam-water in SG : $\gamma = 10$.

Figure 3.25 shows the difference of a linear approximation of the void fraction limit of the 2nd group from dispersed to continuous according to the void fraction of the first group for different $\gamma = \frac{1}{2}\frac{\rho_l}{\rho_g}$. It highlights that the correlation for air-water ($\gamma = 387$) is very close to the one on infinite density ratio whereas for steam-water in a SG ($\gamma = 10$) the correlation is very different and suppose a different behavior of the model in this area. For our application, $\alpha_{g2cdmax} \approx 0.806$ is set to be the next limit for the activation of the continuous model. Furthermore, the linear approximation of the 2nd group is inserted in the IATE in order to get more balance between the 2 groups in the source terms so that :

$$\alpha_{g1}^{source\ term} = min\Big(\alpha_{g1}, 0.623\Big), \tag{3.55}$$

$$\alpha_{g2}^{source\ term} = min\Bigg(\alpha_{g2}, min\Big(0.81, max(-1.181 \times \alpha_{g1} + 0.9285, 0.246)\Big)\Bigg). \tag{3.56}$$

In this chapter, we focused on the foundational modeling used to replicate two-phase flows in the presence of an obstacle. In the initial part, we highlighted the contribution and significance of turbulence models in relation to TRITON modeling. Notably, we emphasized their good performance in reproducing observed trends in void fraction and averaged liquid velocity, particularly with the EBRSM and EBRSM+LI models.

The next part dealt with the modification necessary for the modeling. We identified issues arising from the presence of the obstacle, such as increased void fraction, affecting various aspects of the modeling. Proposed modifications included adjustments to the drag and added mass coefficients, the turbulent dispersion force, some source terms in the transport of interfacial area concentration, and the modeling of pseudo-turbulence. The last part focused on a distinct modeling approach for the deformed bubbles in group 2, motivated by poor numerical results. We presented considerations regarding the added mass coefficient, introducing a significant difference in dynamics for added mass and turbulent dispersion forces, for the source terms of interfacial area concentration, and the transition criterion to shift to annular or churn regimes, where statistical dispersed modeling is no longer able to represent more chaotic interfaces effectively.

Now that modifications have been introduced to address the primary modeling challenges, it is necessary to return to a configuration with an obstacle to check if the model is able to reproduce two-phase flows around a cylinder before moving on to the DIVA configuration. This is the focus of the next chapter.

Chapter 4

Simulations of two-phase flows around a cylinder

Summary

This chapter focuses on simulations carried out with a single cylinder.

The first part deals with sensitivity of the model via force spectra. Initially, a section demonstrates the sensitivity of force spectra to the mesh in single-phase simulations to check the relevance of our approach. The following part studies the sensitivity of the force spectra to injection conditions in a bubbly test case, aiming to understand the physical phenomena that can be extracted from the spectra.

The second part investigates experimental results and simulations to understand the key parameters of the fluid-tube interaction and what physical phenomena can be extracted from the simulations. The first section briefly presents the experimental results and highlights the key parameters for the simulations. The following section presents simulations in the bubbly regime, while the subsequent section covers cap-bubbly/churn test cases.

4.1 Sensitivity of the TRITON model

4.1.1 Numerical tools

NEPTUNE_CFD is a software platform for advanced two-phase flows simulation involving the CEA, EDF, IRSN and Framatome. The extension used is the two-fluid model [85] with one unique pressure field for the two-phases. Among else, it can deal with unsteady turbulent bubbly flows[119].
The numerical approach is based on a finite-volume co-located cell-centered approach and a "alpha-pressure-energy cycle" solver at first order in time based on a pressure correction fractional step method with an iterative coupling between energy and mass balance equations that ensures the conservation of mass and energy. A complete description of NEPTUNE_CFD's numerical methods is proposed by E.Kuidjo Kuidjo in [60]. A short version of the algorithm is proposed after from a step n to the step n+1 with a criterion on the convergence j_{max}:

- U_k^{n+1} semi-implicit and P explicit to initialize the mass efflux.
- The variables point to the n+1 step.
- Initialization of the criteria j.
- Start of the iteration : update the enthalpy, update the density with state equation, update the void fraction, pressure correction, mass flux correction from pressure correction, update of velocities.
- End of cycle if j_{max} reached or axiom of continuity get minor value otherwise $j = j + 1$.

An upwind second-order scheme is used for the convective schemes of every variable, except when the LIM is activated we must use a first order because the higher order can damage the prediction of the interface.
Inlets are computed with flat profiles of constant speed, volume fraction, turbulent intensity and Sauter Mean Diameter(D_{sm}). Outlets are computed with no back-flow conditions and imposed pressure condition. For 2D calculation, symmetric conditions can be imposed on some boundaries. For walls, a weak no-slip condition is imposed to allow the determination of the velocity gradient with the turbulent variables. The Van Driest analysis is used to obtain the velocity gradient for the high Reynolds turbulence models :

$$U^+ = \int_0^{y^+} \frac{2d\xi}{1+\sqrt{1+4\kappa^2(1-exp(-\xi/A))^2\xi^2}}, \tag{4.1}$$

with $\kappa = 0.42$ and $A = 25.6$.
For two-phase flows with interface reconstruction, we advise not to use tetrahedral meshes in general.

The simulations computed in chapters 4 and 5 using the new TRITON model handle the modifications presented in chapter 3. As a reminder for the following sections, the LIM [16, 17, 18] is an interface reconstruction method, activated when $\alpha_{g2} > 0.81$ or $D_{sm2} > 108$ mm,that can be summarized in three steps:

- Recognition of interface through void fraction prediction and its gradient.

- Interface reconstruction through void fraction gradient.
- Frictional force applied at the interface.

Post-processing for the spectra requires retrieving pressure and viscous shear information at each of the calculated time steps. The calculations are performed using an unsteady solver with adaptive time stepping. However, for the purpose of measuring forces, the experiment is conducted at a fixed time step of 0.0019531 seconds. The method for obtaining force spectra requires a constant time step and is sensitive to it. As a result, each of the simulated signals, which has a time step always smaller than that of the experiment, is re-sampled at the experimental time step using quadratic interpolation. Additionally, force spectra are sensitive to the simulation duration and the options used. To address the first issue, the analysis can be performed over different durations to ensure statistical convergence. Empirically, it is necessary to have at least $10,000$ experimental time steps and 100 time steps characteristic of the studied dynamics, excluding the "transient" period. To overcome post-processing issues, the raw experimental signal undergoes the same post-processing as the simulated signal.

4.1.2 On the mesh sensitivity in single phase flow

The prospects of obtaining meaningful quantitative results regarding the force spectra reproduction on the central cylinder of the tube bundle rely on the outcomes presented in [130]. Indeed, simulations employing various URANS approaches and hybrid URANS-LES approaches were conducted in a single-phase scenario on the DIVA configuration. The results reveal that the shapes of the power spectral densities from the numerical simulation and the experiment are quite similar. Although energy levels are occasionally slightly over or underestimated, the rates of energy decay are of the same order of magnitude. It has also been highlighted that the predictions from two-dimensional simulations are relatively accurate. However, an essential aspect we aim to verify in this section is if the meshing strategy is suitable for the numerical model and to justify the interpretability of graphs concerning $2D$ mesh convergence, as well as the contribution of $3D$ in a single-phase scenario.

This thesis exclusively focuses on pseudo $2D$ cases (a single cell in the tube direction) with tubes, rather than encompassing scenarios that take into account $3D$ effects. First, there exists no means to ensure the accuracy of the physics in this direction, as there is a lack of experimental investigation on this aspect for two-phase flows. Secondly, DIVA supposes using wall boundary conditions on each side of the tube, making it challenging to quantify the actual influence of these boundaries. Additionally, even when considering a segment of the experiment and imposing symmetry conditions, it remains difficult to conclude on the true symmetries of the flow and assess the impact of symmetry on the $3D$ structures. Furthermore, the continuous interface reconstruction method (LIM) has undergone limited testing in complex $3D$ cases involving tubes, raising doubts about its efficiency in replicating $3D$ structures along the tube's direction. In addition, an assessment of the mesh count necessary for a coarse $3D$ calculation, conducted through tests on one-third of the geometry (approximately 3 tube diameters), has underscored the requirement for a mesh containing at least three billion elements. Consequently, the benefits of performing $3D$ simulations in terms of computational time and energy consumption for the intended application is limited.

We now focus on a channel geometry with a single tube with diameter D of 0.03 m, of depth $10D$, length $6D$, and height $16D$ enclosed by walls. In the $2D$ configuration, there is only one mesh layer in the depth because NEPTUNE_CFD is a 3D code, whereas the $3D$ configuration covers $7D$ in the depth. We set a boundary condition at the inlet with a velocity plateau of $U_l = 0.74$ m/s, corresponding to a Reynolds number of 22200. We tested six different meshes, three for the $2D$ case ($20,000$, $70,000$ and $150,000$ cells), and three for the $3D$ (under-resolved) case ($350,000$, $700,000$ and $1,400,000$ cells), categorized as Coarse, Medium, and Fine. The complete TRITON model is used with $\alpha_{g1} = 0$, $\alpha_{g2} = 0$, $D_{sm1} = 10^{-6}$ m, and $D_{sm2} = 10.8 \times 10^{-3}$ m.

Case	St	Error (%)	C'_D	Error (%)	C'_L	Error (%)
Experiment	0.22	–	0.063	–	0.176	96
$2D$ *Coarse*	0.16	27	0.0066	89	0.0074	89
$2D$ *Medium*	0.26	18	0.029	54	0.66	89
$2D$ *Fine*	0.28	27	0.076	21	0.899	420
$3D$ *Coarse*	0.18	18	0.01	84	0.001	100
$3D$ *Medium*	0.25	14	0.023	63	0.107	39
$3D$ *Fine*	0.24	9	0.028	55	0.165	6

Table 4.1: Table of the results of the Strouhal number St and the standard deviation of the drag C'_D and the lift C'_L forces exerted on the tube from the mesh convergence study of TRITON simulation in single phase flow. Errors are computed as : Error= $\frac{Simulated\ value\ -\ Experimental\ value}{Experimental\ value}$

Table 4.1 compiles the results of TRITON simulations in single-phase flow for increasingly finer 2D and 3D meshes regarding the Strouhal number St and the standard deviation of the drag C'_D and the lift C'_L forces exerted on the tube. Regarding the Strouhal number, all cases have an error above 9%. None of the simulations yield an exact result, but they provide a good estimation. This is because the confinement effects can be significant in numerical simulations compared to experiments, inducing an overestimation of the increase of velocity and so shifting the frequency. However the error in the frequency is acceptable for all cases. Regarding the standard deviations of drag C'_D, all cases have an error above 20%, with a minimum for the 2D fine case. Regarding the standard deviations of lift C'_L, the error is minimum (6%) for the $3D$ fine case and maximum (420%) for the $2D$ fine case. As for the standard deviations, the 2D simulations seem to perform better for drag, while the $3D$ simulations tend to underestimate it. Conversely, the error in the standard deviation of lift C'_L is much better for the $3D$ case. This is because obtaining an accurate lift standard deviation is challenging due to the confinement effect, which is mitigated in $3D$. However, obtaining a good standard deviation value for drag C'_D and lift C'_L forces is not a guarantee of accurately replicating the physical phenomenon. A straightforward way to verify this is by examining the force spectra to identify the frequency content of the random forces.

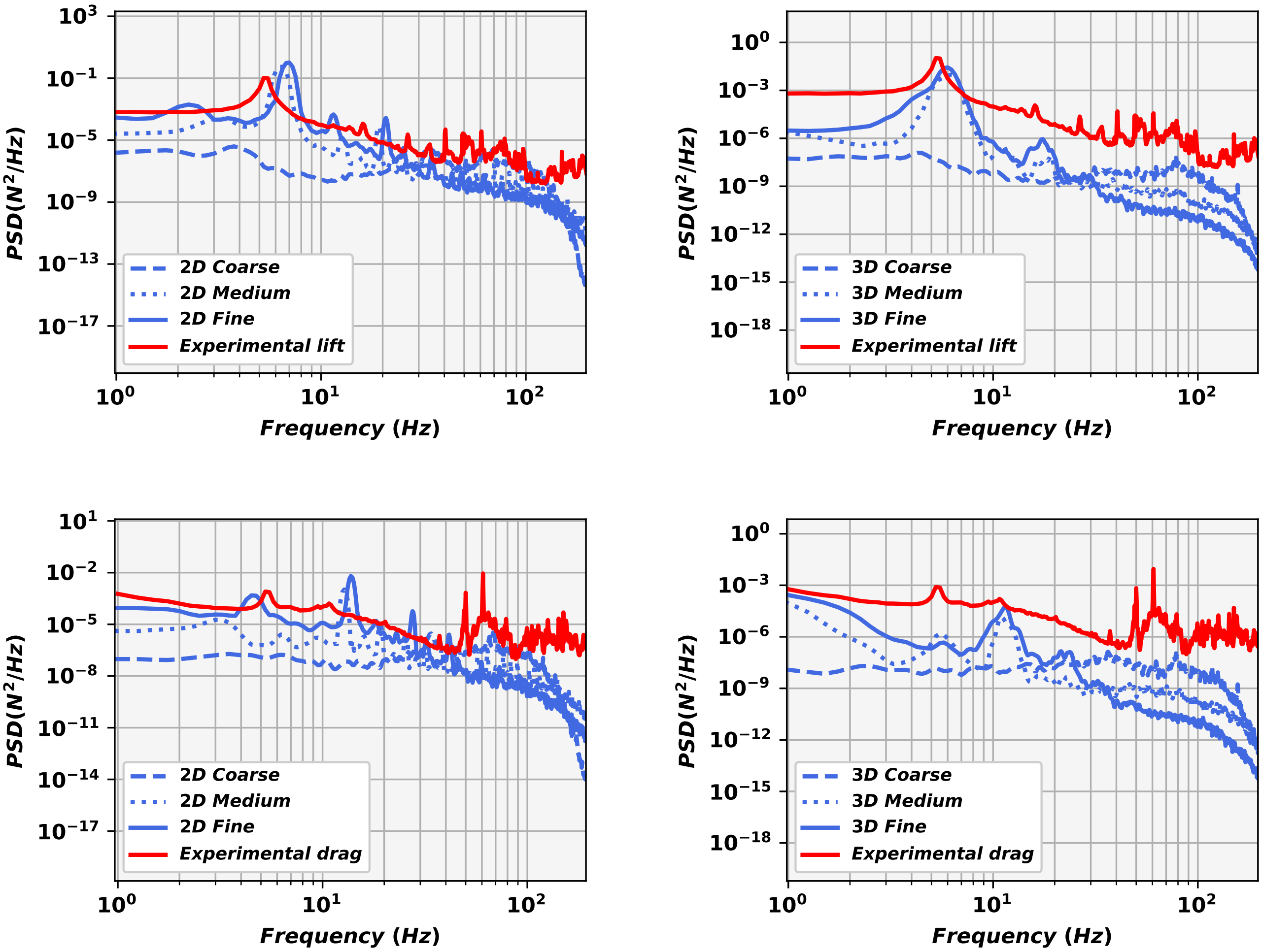

Figure 4.1: Lift (top) and drag (bottom) forces spectra from the mesh convergence study in $2D$ (left) and $3D$ (right) compared to experimental data (red) according to the frequency. Simulated with TRITON model.

Figures 4.1 depicts the lift (top) and drag (bottom) force spectra exerted on the cylinder for both $2D$ (left) and $3D$ (right) meshes compared to experimental data (red) according to the frequency. According to the graphs, the experimental lift spectrum (top) exhibits a sharp increase between 2.5 Hz and 5.4 Hz, featuring a characteristic peak indicative of Von Karman alleys (Strouhal number of $St = \frac{fD}{U_l} = 0.22$). It then decreases significantly until around 7.4 Hz, with a slight peak at 16.3 Hz (Strouhal number of $0.66 = 3 * 0.22$), followed by a steady decline up to 40 Hz. Getting $St = 0.22$ and the third harmonic is a charateristic of the lift spectrum with Von Karman alleys for single cylinder configuration. On the other hand, the experimental drag spectrum (bottom), initially remains relatively constant between 2.5 Hz and 10 Hz, with a peak at 5.2 Hz ($St = 0.21$). It then maintains near-constant behavior until around 10.9 Hz ($St = 0.44$), after it decreases up to 45 Hz. Getting $St = 0.22$ and the second harmonic is a carateristic of the drag spectrum with Von Karman alleys for single cylinder configuration.
In the $2D$ lift graph (top-left), we observe a convergence of spectra with finer mesh resolution. There is also a frequency shift, as previously noted in the table 4.1. Focusing on the fine mesh, we notice substantial growth between 2.7 Hz and 6.9 Hz ($St = 0.28$), followed by a steep decline until around 200 Hz, after which it decreases with two peaks at 11 Hz ($St = 0.44$) and 20.9 Hz

($St = 0.85 \approx 0.28 * 3$). Even though noticeable differences exist compared to the experimental data, it is interesting to note that we achieve a behavior similar to the experimental results.
Regarding the $3D$ lift graph (top-right), we can observe a more difficult convergence of spectra with the mesh resolution. However, there is a less significant frequency shift compared to the 2D case. This phenomenon is likely due to the $3D$ effects that mitigate accelerations. Focusing on the fine mesh spectrum, we notice a very strong peak spanning three orders of magnitude, extending from 2.5 Hz to 14 Hz, with a maximum around 5.9 Hz ($St = 0.24$). A second peak is observed around 17 Hz ($St = 0.69 \approx 0.24{*}3$), with a very steep decline. It becomes obvious that the 3D behavior is quite different from the experimental behavior. Indeed, turbulence models like EBRSM are not able to adequately accounting for $3D$ effects, which is obvious from this graph. The 2D calculation, despite its sensitivity to confinement accelerations, is more interesting from a physics point of view than the 3D calculation.
In the $2D$ drag graph (bottom-left), we observe a convergence of spectra with finer mesh resolution. There is also a frequency shift, as previously noted in the table. Focusing on the fine mesh spectrum, we notice substantial growth between 3.8 Hz and 5.4 Hz, with a maximum at 4.7 Hz ($St = 0.19$), followed by a steep decline until around 10 Hz, after which it decreases gradually with a peak at 14 Hz ($St = 0.56$). Even though noticeable differences exist compared to the experimental data, it is interesting to note that we achieve a behavior similar to the experimental results.
Looking at the $3D$ drag graph, we can also observe a convergence of spectra with the mesh resolution. However, there is a less significant frequency shift compared to the 2D case. This phenomenon is likely due to the $3D$ effects that mitigate accelerations. Focusing on the fine mesh spectrum, we notice a sharp decline between 2 Hz and 7 Hz, followed by a very strong peak spanning two orders of magnitude, extending from 8 Hz to 14 Hz, with a maximum around 11.5 Hz ($St = 0.47$). Afterward, there is a very steep decline. As with lift, it becomes evident that the 3D behavior of drag is quite different from the experimental behavior.

Although the spectra do not completely overlap, a similar frequency distribution is clearly discernible. Additionally, despite different standard deviations, the distributions of frequency in $2D$ and experiments are quite similar. Therefore, the contribution of the $3D$ simulations appears to be somewhat redundant. Indeed, reproducing $3D$ effects like separation is challenging, and despite an overestimation in the lift standard deviation, the $2D$ simulations yield interesting results.
To summarize, TRITON model may not be the best URANS model, however, it still gives appealing results concerning the force spectra, without adjustable parameters. The next step is to understand the sensitivity of the spectra to the injection conditions. These conditions tend to lead to a specific flow topology that subsequently influences the graphs. This is the focus of the following section.

4.1.3 On the effect of injection conditions on the force spectra

In order to analyze and understand the predictive capabilities of the model, the difficulty of obtaining good results and to be able to draw clear conclusions, we are interested in the sensitivity of the model response to the conditions of operating injection. We are interested in a classic bubbly test case in single tube configuration. As a reminder, the experimental setup is composed of an upward channel of 0.18×0.3 m^2 rectangular section in which can be set a horizontal tube of diameter 0.03 m. The operating conditions are defined by a liquid superficial velocity $j_l = 0.25$ m/s and a gas superficial velocity $j_g = 0.082$ m/s. The flow is then characterized by a void fraction $\alpha_g = 0.247$ and a liquid Reynolds $Re_l = 7500$. A mesh convergence study was performed on several meshes and a satisfying convergence was obtained with a general mesh size

of 0.066 mm and a first wall cell satisfying $y^+ \approx 0.8$.
The investigation focuses on the sensitivity of the injected void fraction for group 1 and mean Sauter diameter. The sensitivity analysis was performed with injected diameters, but because it draws the same conclusions we focus only on 2 different ones. Here, we decide to choose 5 cases representative of the sensitivity of the spectra. Consequently, we look at simulations with $\alpha_{g1} \in \{0.247, 0.183, 0.072\}$ and first group diameter $D_{sm1} \in \{2, 4\}$ mm. The operating conditions of this study are summarized in Table 4.2.

α_{g1}	D_{sm1} (mm)	α_{g2}	D_{sm2} (mm)
0.247	4	0.	10.8
0.183	4	0.064	10.8
0.072	4	0.175	10.8
0.183	2	0.064	10.8
0.072	2	0.175	10.8

Table 4.2: Table of the conditions of the study of α_{g1} without BIT.

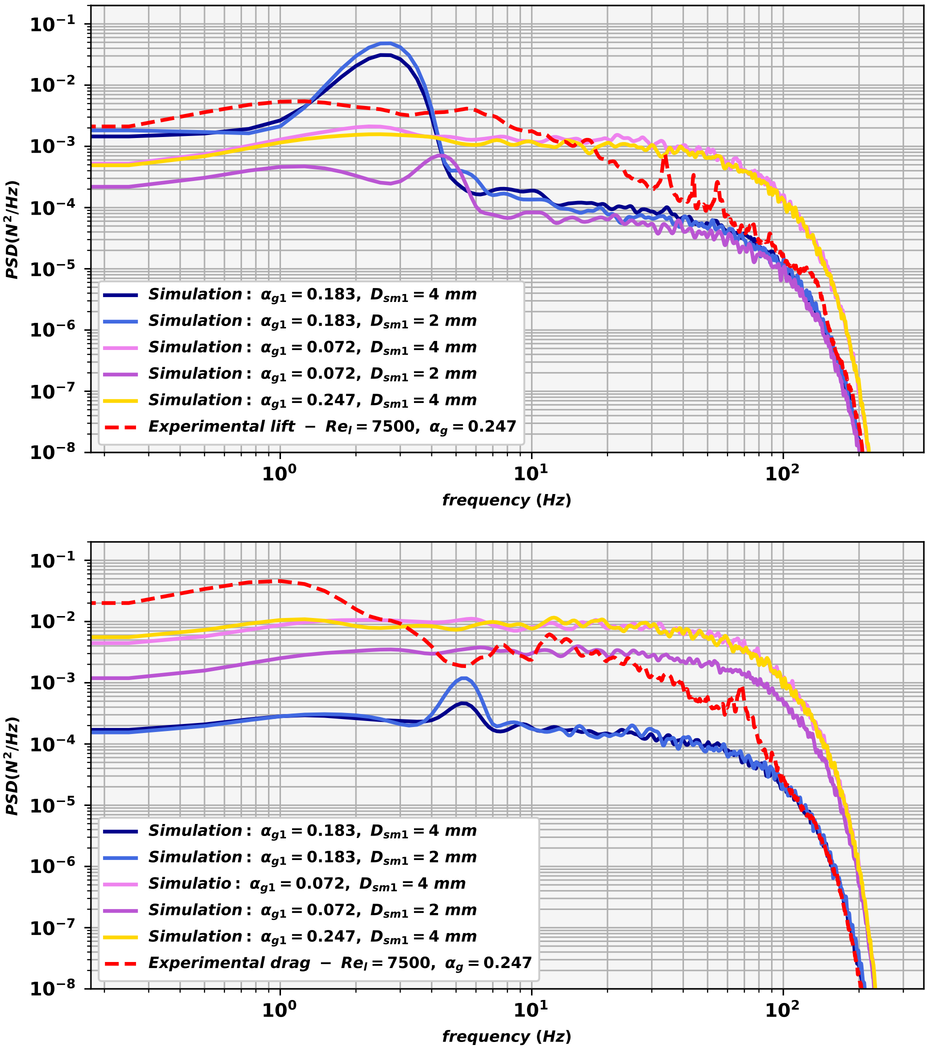

Figure 4.2: Lift (top) and drag (bottom) spectra from the sensitivity study of the distribution of the void fraction between the two groups and change of first group diameter for a liquid Reynolds number of 7500 and a homogeneous void fraction of 0.247. Simulations with new TRITON model.

Figures 4.2 shows the lift (top) and drag (bottom) spectra, respectively, from the sensitivity study of the distribution of the void fraction between the two groups for a liquid Reynolds number of 7500 and a homogeneous void fraction of 0.247.

According to Figure 4.2, the experimental lift spectrum exhibits a nearly plateau-like behavior between 1 Hz and 6 Hz, followed by a decrease towards the cutoff frequency. The two spectra with group 1 void fractions of 0.247 and 0.072 and a first group diameter of 4 mm also exhibit a plateau-like trend between 1 Hz and 30 Hz, with then a slight decline until the cutoff frequency. However, the spectra corresponding to $\alpha_{g1} = 0.183$ sharply increase between 1 Hz and 2.6 Hz before steeply decreasing to 6 Hz, indicating shear close to the cylinder. They continue to decrease until the cutoff frequency. The case with $\alpha_{g1} = 0.072$ and $D_{sm1} = 2$ mm, exhibits a nearly plateau-like behavior between 1 Hz and 5 Hz with two peaks around 1 Hz and 4.1 Hz,

it slightly decreases until 6 Hz and is then almost constant until the cutoff frequency. None of these simulations appear to accurately replicate the experimental lift.
According to Figure 4.2, the experimental drag spectrum exhibits a sharp decrease between 1 Hz and 5 Hz, followed by a slight upward trend just after 10 Hz, before ultimately declining until the cutoff frequency. The two spectra with Group 1 void fractions of 0.247 and 0.072 and $D_{sm1} = 4$ mm both display a plateau-like trend between 1 Hz, with a slight decline starting around 30 Hz until the cutoff frequency. The spectra corresponding to $\alpha_{g1} = 0.183$ show a similar trend, except for a slight bump around 5 Hz, while the trend of the case with $\alpha_{g1} = 0.072$ and $D_{sm1} = 2$ mm has the same trend. None of these simulations appear to accurately replicate the experimental drag.

Indeed, among all the simulations conducted, none have accurately reproduced the force spectra, even when modifying furthermore various parts of the all-regime model. From the simulations presented in the introduction, it becomes obvious that the spectra are highly sensitive to the flow topology around the cylinder, particularly the shear that affects the position and shape of the cluster at the rear of the cylinder. Consequently, single-phase turbulence plays a crucial role in replicating the spectra. However, it is important to note that the proposed model is far less sensitive to injection conditions than the basic model. Notably, we obtain reasonable orders of magnitude for the fluctuations. To assess the influence of turbulence, it is possible to activate pseudo-turbulence (LI) in the case with only one group i.e. $\alpha_{g1} = 0.247$. The results of the fluctuations are summarized in the following table.

Fluctuating force	Experimental	Without LI	With LI
Drag (N)	0.43	0.76	6.27
Lift (N)	0.23	0.27	2.99

Table 4.3: Table of the standard deviations of the lift and drag forces for the experiment, for the simulations with and without pseudo-turbulence (LI).

Table 4.3 gives the standard deviations of the lift and drag forces for the experiment, for the simulations with and without pseudo-turbulence (LI). The use of pseudo-turbulence (LI) has significantly altered the magnitude of fluctuations. It completely changes the flow topology by introducing turbulent intensity, particularly around the stagnation point. This effect tends to create very strong turbulence and unsteady void fraction gradients. Therefore, it is advisable not to use this option, as it appears to be incompatible with the presence of an obstacle. Further investigations are necessary to account for those effects. Hence, it becomes crucial to understand what truly influences the experimental and numerical force spectra. To achieve this, the next section focuses on experimental spectra to identify the influencing parameters of the spectra. Subsequent studies will examine cases with different flow topologies based on Reynolds number and flow regime to understand what influences the numerical spectra.

4.2 On the effect of the liquid Reynolds number

In this section, we focus on the study of drag and lift force spectra in a single cylinder. The goal is to identify the primary factors influencing these force spectra. Initially, we analyze experimental results to draw initial conclusions, followed by simulations using the model to verify if similar observations can be obtained.

4.2.1 In experiments

A study of a single-cylinder cross two-phase flow case can be found in [94]. The study was conducted on the lift force with a diameter of 0.01215 m - as opposed to 0.03 m in this study - and for homogeneous void fractions ranging from 30% to 95% and liquid Reynolds numbers ranging from 3.5×10^4 to 2.8×10^6. Their study notably showed that the low-frequency components increase with void fraction, while the decay slopes decrease more rapidly. It demonstrates that for local void fractions between 11% and 20%, the spectra increases with void fraction, and the graphs appear to collapse for local void fractions above 40% - no measurements were taken between 20% and 40%.

Since the single-tube experiment was conducted before DIVA, we don't have access to the method - described in section 5.1.1 - for identifying the flow regime. However, since the single-tube experiment and DIVA share identical characteristics, comparing the injection maps allows us to predict a map of regimes for classifying the spectra. The greatest uncertainty arises in the identification of cap-bubbly regimes compared to churn because they exhibit similar spectra. However, as annular and bubbly regimes are easily identifiable, we can have greater confidence in their identification.

Figures 4.3 and 4.4 depict force spectra – drag (bottom) and lift (top) - for liquid Reynolds numbers of 7500 and 15000 respectively with regime identification from section 5.1.1. Regarding the lift spectra (top), it is obvious that all the graphs exhibit a decreasing trend between 10 Hz and 200 Hz, which becomes more pronounced after 20 Hz for $Re_l = 7500$. Notably, there is a clear collapse of curves for cap-bubbly and churn regimes, while bubbly regimes appear to be more spread out. It is noticeable that the curves mainly align with increasing void fraction, except for the annular case. This trend can be explained by the quasi-absence of liquid. In this scenario, predominantly gas-phase behavior is likely observed. Therefore, it appears that the lift spectra depend on the Reynolds number as well as the flow regime, whether it is bubbly, cap-bubbly/churn, or annular. The increase in fluctuations with void fraction in the bubbly regime, followed by its stagnation in the cap-bubbly/churn regime, suggests that the overall level of fluctuations likely depends primarily on the small bubble dynamics and by changing of regime on the presence of larger structures. The balance introduced by the presence of larger structures such as cap bubbles or gas pockets tends to dampen fluctuations until the system becomes predominantly gaseous. Consequently, achieving accurate results in the bubbly regime is challenging, as it relies on bubble fluctuation phenomena that are not modeled, unlike in the cap-bubbly/churn regime where the presence of large structures stabilizes the flow, making it less sensitive to small bubble fluctuations.

Regarding the drag spectra, there is a consistent decreasing trend starting at around 20 Hz, with a change in slope occurring around 70 Hz. In contrast to the lift, there is no observable spectrum collapse at a specific void fraction, but rather an increase in amplitude with increasing void fraction. Additionally, it appears that the decay slopes also increase with void fraction. Although the curves between Reynolds numbers are quite similar, it seems that drag is less sensitive to liquid Reynolds number variations than lift. However, the limited dataset does not allow for broader conclusions across all Reynolds numbers. Nevertheless, there is a significant variability in spectrum with respect to void fraction. It will likely be more challenging to obtain accurate results for drag force spectra as void fraction appears to be the most influential parameter. However, it is noticeable that the Reynolds number has a more significant impact

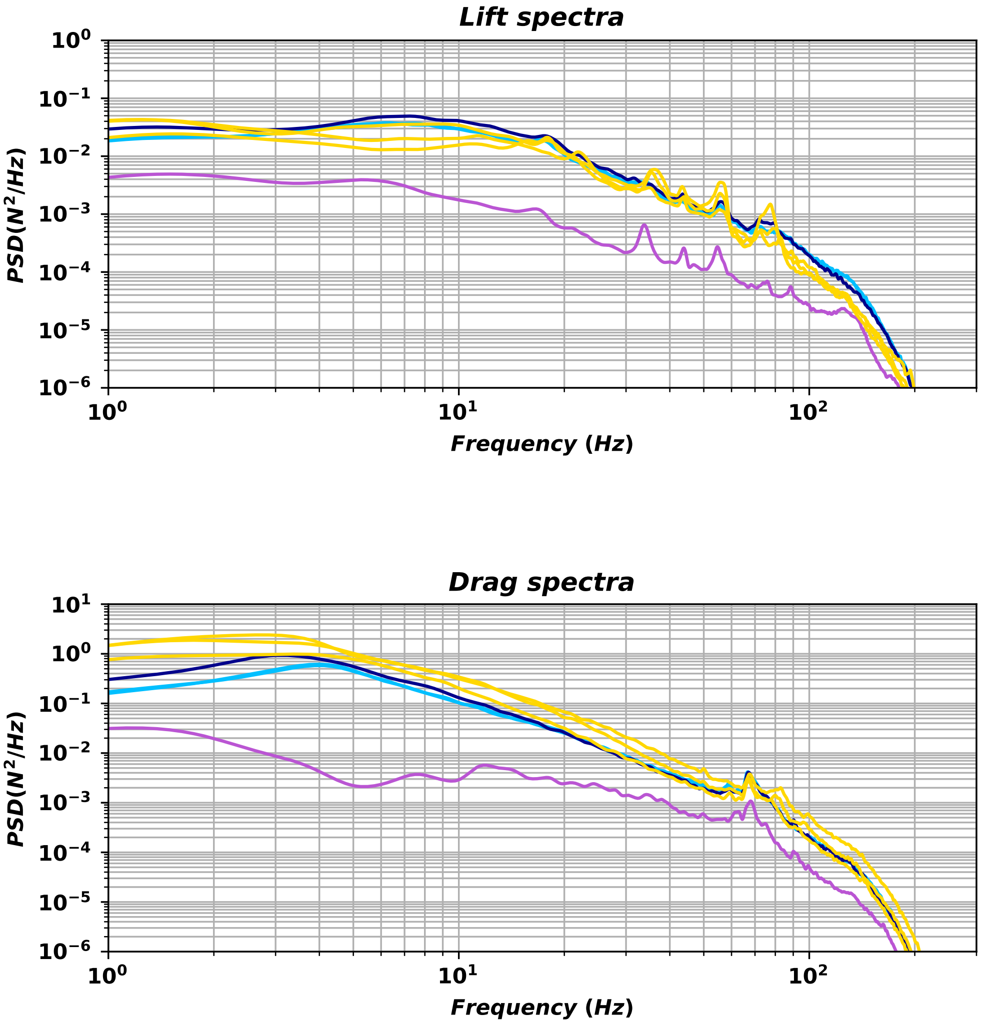

Figure 4.3: Experimental force spectra with a liquid Reynolds $Re_l = 7500$ with increasing void fraction according to the frequency. Legend : 🟪 Bubbly regime, 🟦 Cap-bubbly regime, 🟦 Churn regime, 🟨 Annular regime. Regime identification from section 5.1.1.

on the bubbly regime than on other regimes. Achieving this variability in our simulations seems more complex. Therefore, obtaining good results in the cap-bubbly/churn regime might be easier than in the bubbly regime.

It appears, therefore, that the variability of the graphs depends on the liquid Reynolds number and the void fraction, particularly in relation to the flow regimes. It appears that the bubbly regime is more sensitive to the liquid Reynolds number and void fraction than other regimes. Obtaining accurate results in the bubbly regime might be more challenging. This could be explained by a greater influence of bubble-related fluctuations in the bubbly case, which are then mitigated by the presence of large structures within the flow and the lower proportion of water. To test this hypothesis numerically, the next sections will focus on the bubbly and cap-bubbly/churn cases.

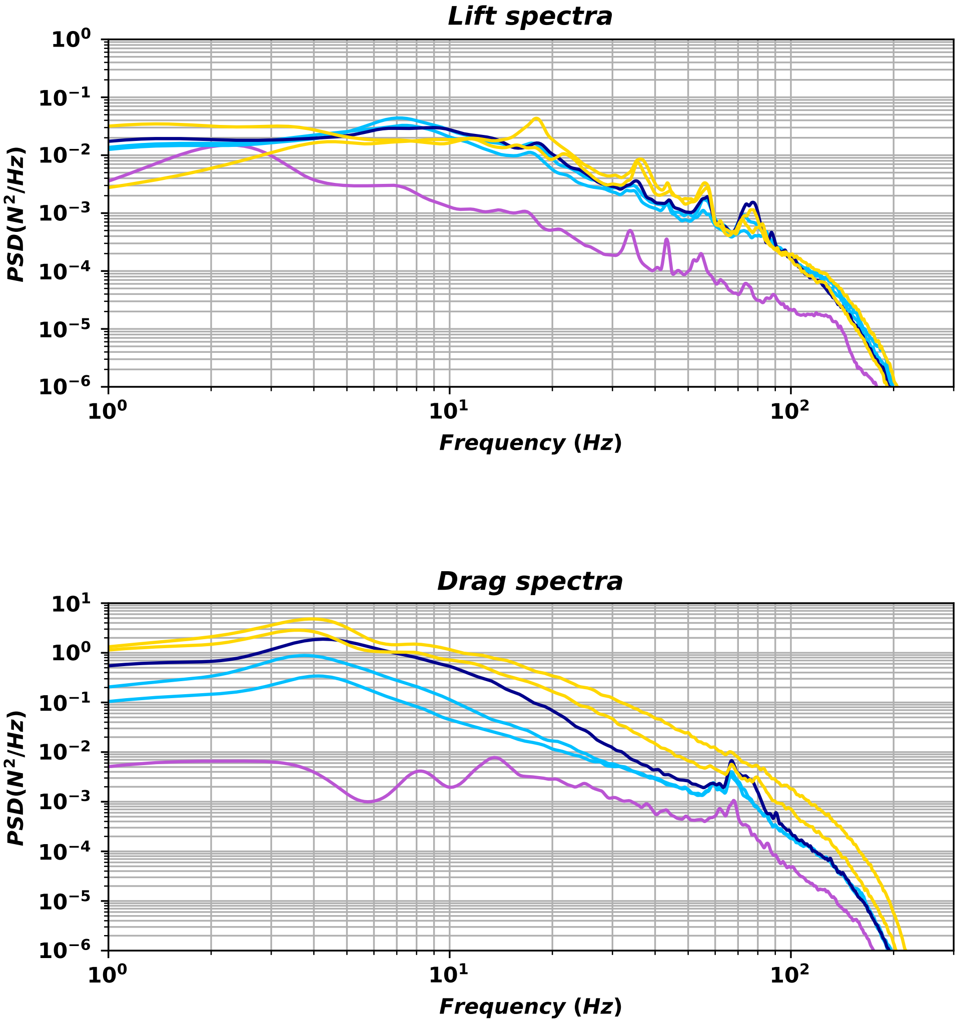

Figure 4.4: Experimental force spectra with a liquid Reynolds $Re_l = 15000$ with increasing void fraction according to the frequency. Legend : 🟪 Bubbly regime, 🟦 Cap-bubbly regime, ■ Churn regime, 🟨 Annular regime. Regime identification from section 5.1.1.

4.2.2 Bubbly flows simulations

Comparative data involving a single cylinder is relatively rare. Moreover, merely aligning with a specific experiment is not sufficient to establish that the model, even if it accurately predicts all configurations, is able to capture the underlying physics. Particularly, our focus lies in the qualitative observations given by Inoue et al.[44]. Indeed, a problem arose regarding the reproduction of single-cylinder bubbly flows. The CEA experiment allows comparison of the forces spectra experienced by the cylinder, but no local data within the flow is available. In contrast, [44] provides qualitative and quantitative data on the flow without having the spectra. However, the experiments conducted at CEA are limited. We have data from experiments conducted with comparable liquid Reynolds numbers but often very different void fractions. However, it has been observed that force spectra are primarily sensitive to the liquid Reynolds number and less to the void fraction (the overall spectrum shifts slightly upwards with the void fraction). Therefore, we can still use experimental data on the spectra as a reference to compare, at a lower cost, the experiments conducted at CEA and those of [44] with our simulations. An essential aspect of validation is the model's response to the liquid Reynolds number, aiming to replicate the various structures observed in the experimental setup. Thus, we intend to undertake a qualitative comparison between the experimental setup and the simulation results, subsequently extracting more quantitative insights. The operational conditions for this study are summarized in the Table 4.4.

Re_{lsimu}	Re_{lexp}	j_{lsimu} (m/s)	j_{gsimu} (m/s)	α_{gsimu}
9940	9000	0.25	0.082	0.247
19880	18000	0.5	0.164	0.247
39760	38000	1.	0.328	0.247

Table 4.4: Table of the conditions of the study of single cylinder configuration in bubbly regime.

As a reminder, Inoue et al.[44] observed that the area near the separation point produces high local void fraction 3 to 4 times the homogeneous volume fraction. A high void fraction area is located behind the cylinder. As the liquid velocity increases, its void fraction peak increases and its position comes closer to the cylinder. A liquid layer where bubbles can hardly penetrate can be produced in the front and in the rear of the cylinder due to the static pressure gradient. Its thickness respectively increases and decreases in the front and in the rear with increasing flow velocity.

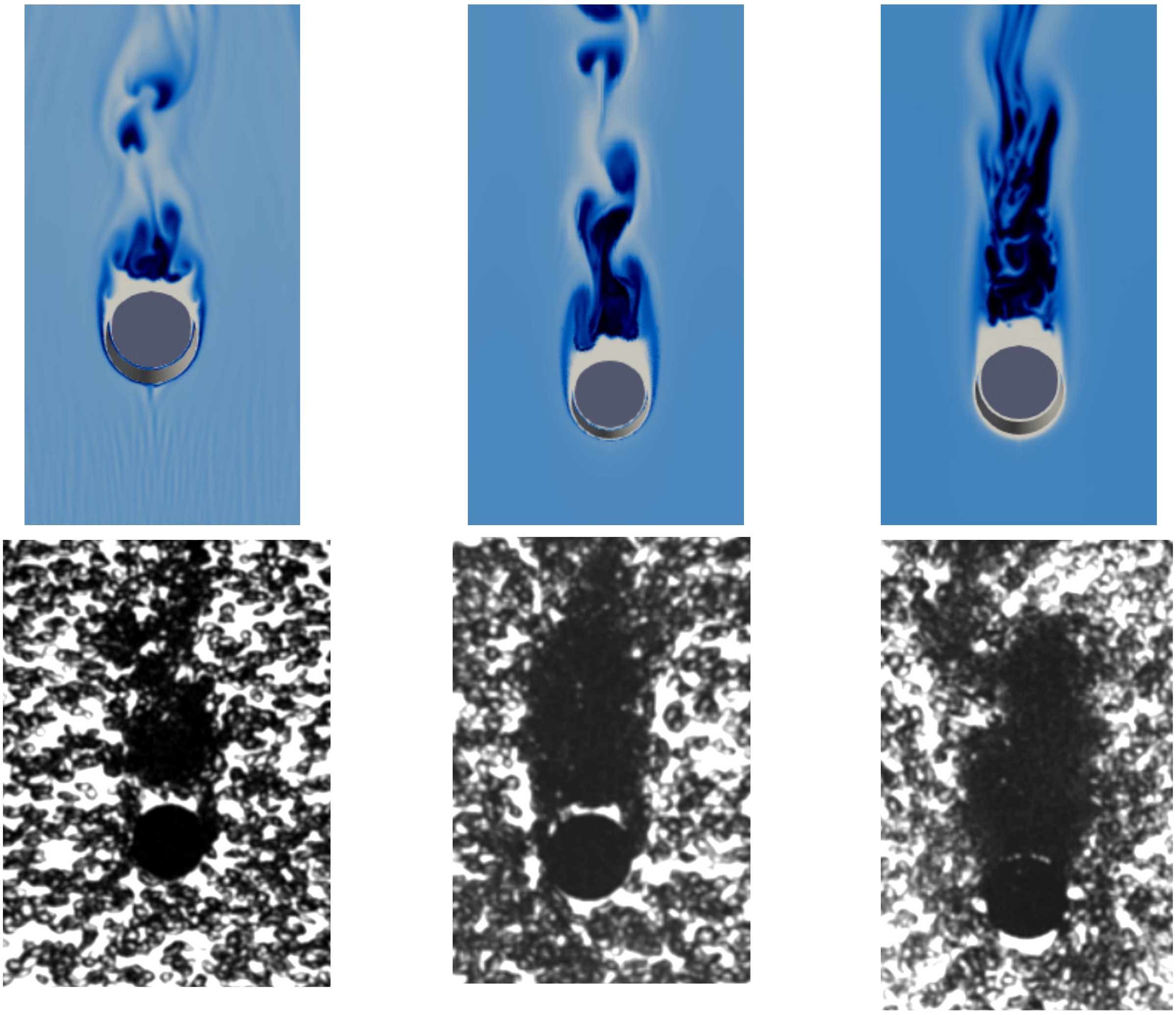

Figure 4.5: Qualitative comparison between simulations (top, instantaneous void fraction), with $D = 30$ mm and [44] (bottom), with $D = 20$ mm, with increasing Reynolds number from left to right. The conditions are summarized in the Table 4.4.

Figure 4.5 displays images of the flow from Inoue et al.[44] (bottom) and simulation results of the experiment (top, instantaneous void fraction) with increasing Reynolds number from left to right. The conditions are summarized in the Table 4.4. Clear observations can be made from Inoue et al.'s photos. There is a region close to the cylinder where bubbles concentrate, causing an increase in void fraction. For the lowest Reynolds number (bottom-left), a cluster of bubbles can be seen at the rear, which is later sheared, and an area where bubbles cannot pass through. As the liquid velocity increases (bottom-middle), the cluster spreads out, the shearing occurs farther from the cylinder, and the upstream region near the stagnation point appears to start pushing the bubbles back. With further increases in velocity (bottom-right), the cluster continues to spread and is sheared even farther away. The upstream region pushing the bubbles becomes more evident, while the cluster moves closer to the cylinder.
Now, looking at the simulations, for the lowest Reynolds number (top-left), we see the presence of a clustered zone being sheared close to the cylinder. A high void fraction zone can also be observed around the cylinder, associated with lubrication forces and pressure that is not strong enough to repel the gas phase. As we increase the liquid velocity, we obtain a larger clustered zone that is sheared farther away from the cylinder. We also notice the disappearance of the high

void fraction zone close to the wall in favor of the pressure, which begins to dominate and push the gas phase away. Subsequently, with a further increase in liquid Reynolds number, we observe the presence of a region where there is no gas upstream of the cylinder due to the pressure around the stagnation point. There is also the presence of an elongated tail of the cluster, which is sheared farther away. Thus, we qualitatively obtain zones where the void fraction increases significantly around the cylinder, clusters whose positions change with velocity upstream and downstream in a manner consistent with the experiment.

It appears that the liquid Reynolds number is a key parameter influencing the flow topology around the cylinder in simulations with TRITON. Therefore, one can expect that the position of the cluster and the distribution of void fraction around the cylinder will have a significant impact on the prediction of drag and lift forces.

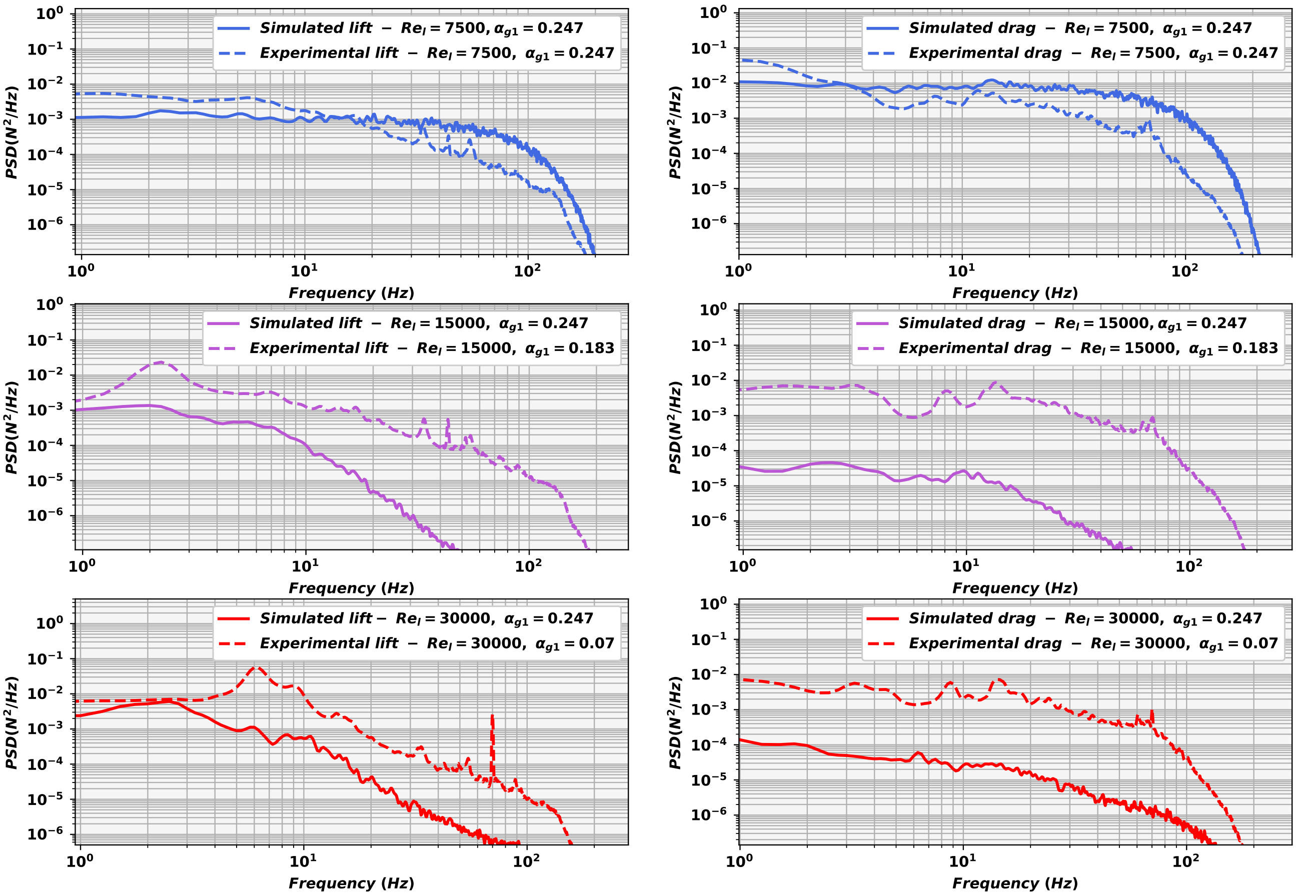

Figure 4.6: Lift (left) and drag (right) forces spectra of the simulations with injected void fraction of 0.247 and Reynolds of 9940 (top), 19880 (middle) and 39760 (bottom) compared to experimental data with same Reynolds, but different injected void fraction. Simulations with new TRITON model.

Figure 4.6 shows the spectra of drag forces (left) and lift forces (right) for simulations with Reynolds numbers of 9940 (top), 19880 (middle), and 39760 (bottom), compared to our experimental data with the same Reynolds numbers, but with different injected void fractions.

Looking at the lift graph for the Reynolds number of 9940 (top-left), the experimental spectrum exhibits a low-amplitude bump between 1 Hz and 3 Hz, followed by a second bump between 3

Hz and 10 Hz, and then a decrease towards the cutoff frequency. In contrast, the simulation shows a slight increase between 3 Hz and 5 Hz, followed by a mainly flat response up to the cutoff frequency, with a small bump between 1.3 Hz and 3.1 Hz. This frequency appears to be related to the inability of the lubrication force to push back the gas phase due to insufficient pressure. Examining the corresponding drag spectrum (top-right), the experimental data reveal a decrease up to 5 Hz, then a relatively constant behavior, with two bumps at 7.6 Hz and 11 Hz, before decreasing again towards 20 Hz. The frequency of 11 Hz could stem from the natural frequency of the flow ($\frac{j_l+j_g}{D} = 0.332/0.03 \approx 11$ Hz). In contrast, the simulated graph remains mainly constant up to the cutoff frequency. Consequently, this simulation has not accurately reproduced the random force spectra. Notably, the presence of this plateau and the absence of high-frequency decrease seem to originate from the artificially created region near the wall due to the lubrication force. The modeling of lubrication for a single cylinder appears to be potentially detrimental, as it can induce a particular flow topology around the cylinder. Thus, the flow topology near the wall seems to have a significant influence on the prediction of the spectrum. To get deeper understanding, we can explore spectra at higher Reynolds numbers, which exhibit very different flow topologies.

Looking at the lift graph for the Reynolds number of 19880 (middle-left), the experimental spectrum shows a sharp increase between 1 Hz and 2 Hz, followed by a decrease to 7 Hz, and then a change in slope before gradually decreasing with a constant slope up to the cutoff frequency. Considering the natural frequency of the flow ($f^{flow} = \frac{j_g+j_l}{D} = 22$ Hz), it appears that 2 Hz is related to the formation of structures around the cylinder. In contrast, the simulation exhibits a slight increase between 1 Hz and 2 Hz, followed by a decrease to 7 Hz, and then a decrease with a significant change in slope. This demonstrates a qualitatively similar behavior to the experimental data. However, the standard deviation of the lift (area under the curve) is lower than in the experimental results. Indeed, it was observed experimentally that an increase in void fraction leads to an elevation of the spectra. Thus, its low position indicates an underestimated value. Turning to the experimental drag spectrum (middle-right), we observe growth between 1 Hz and 3 Hz, followed by a decrease to 5.2 Hz. Subsequently, it increases with the presence of two peaks at 8 Hz and 11 Hz before decreasing again towards the cutoff frequency. Those frequencies are comparable to bubble frequencies, but not to the frequency of the mean flow itself (f^{flow}). The simulated spectrum exhibits two broad peaks in the range of 1 Hz to 5 Hz, with one peak at 2.1 Hz, due to the structures behind the tube. It then presents two peaks of comparable amplitudes at 6 Hz and 10 Hz before decreasing towards the cutoff frequency. Similar to the lift, we qualitatively obtain a similar frequency distribution, but at a much lower level. This behavior can be attributed to the pressure zone pushing back the gas phase and the cluster at the rear of the cylinder being too distant. In this case, we would obtain lower standard deviations that affect the overall spectrum level without significantly altering the frequency distribution of random forces. To confirm this, we can study the highest Reynolds number.

If we look at the experimental lift spectrum for the Reynolds number of 30000 (bottom-left), we observe a plateau until 4 Hz and a peak at 6 Hz (maybe linked to structures behind the tube), ranging from 3 Hz to 11 Hz, before gradually decreasing with a constant slope up to the cutoff frequency. In contrast, the simulated spectrum increases between 1 Hz and 2.4 Hz, then decreases to 10 Hz with a peak at 6 Hz, due to the structures behind the tube, before gradually decreasing with a constant slope. We can clearly see a similar behavior, but with a spectrum level that is too low. Similarly, if we look at the experimental drag spectrum (bottom-right), we observe a mainly flat level between 2 Hz and 20 Hz, with three peaks at 3 Hz, 9 Hz, and 11

Hz. These last two frequencies are related to bubble frequencies, not to the mean flow (with a natural frequency of 44 Hz). The simulated graph shows a decreasing trend between 1 Hz and 10 Hz, with peaks at 1.9 Hz and 6 Hz, before gradually decreasing with a constant slope. We find drag spectra with similarities, but at a much lower level.

As a reminder, increasing the void fraction only raises the overall force spectra. The difference in void fraction between the experiment and the simulation does not explain the discrepancy in the spectra or could solve the problem. Therefore, we can conclude that the upstream area near the cylinder, potentially having a single-phase region, as well as the distance of the cluster from the cylinder, are topological factors of significance in accurately reproducing the force spectra. It also appears that the frequencies related to bubble passage are not captured. This is not surprising since their presence is given as an average, and the fluctuations due to their intermittency are not reproduced in the model. However, these areas are sensitive to:

1. The injection diameter, which identifies if repulsion occurs via lubrication and also constrains the velocity field through near-wall drag.
2. The velocity profile, which establishes the balance between the phases and the shearing at the rear of the cylinder. This velocity is also influenced by the walls that confine the flow.
3. Turbulence, which affects the flow topology around the cylinder as well as fluctuations and did not yield perfect results in single-phase simulations.

These factors collectively contribute to the complexity of the problem and the challenges involved in accurately simulating the force spectra.
The basic model from NEPTUNE_CFD yielded results that were highly sensitive to inlet conditions, often diverging significantly from experimental data, making it unreliable for predictions. While our model does not provide perfect results, it is less sensitive to input conditions and more reliable in reproducing the trends observed in force spectra. However, these spectra tend to underestimate the overall magnitude compared to experimental data. This aspect is intriguing considering the various assumptions and models that are not perfect even in academic cases. We also notice variability in standard deviations and results, which appears to stem from deficiencies in modeling and/or balancing the regions near the stagnation point and shear. Nevertheless, the confined nature of the experiment does not make it easy to perfectly replicate experimental topologies. However, these results offer hope for improving models. Additionally, these critical areas will be locally constrained by the cylinders in DIVA. This will enable us to identify whether the issues primarily stem from modeling, as the clusters and upstream and downstream recirculation lengths will be constrained by the upstream and downstream cylinders, or if they mainly result from the difficulty in obtaining the correct topologies and distances upstream and downstream of the cylinder. Another aspect to verify is the improvement of the spectra with more group 2 bubbles because the experimental spectra seem to show less sensitivity to the liquid Reynolds number in the cap-bubbly/churn regimes. Therefore, in the next section, we focus on cap-bubbly/churn simulations.

4.2.3 Cap-bubbly and churn flows simulations

In this section, we focus on examining the influence of the Reynolds number for cap-bubbly and churn regimes. Indeed, experimental comparisons can be conducted using the gathered data. We want to verify the experimental observations. We investigate three liquid Reynolds number cases: 7500, 15000, and 30000 for approximately homogeneous void fractions of about 0.64.

Table 4.5 summarizes the conditions of the test cases studied.

Re_l	j_l (m/s)	j_g (m/s)	α_g
7500	0.25	0.447	0.636
15000	0.5	0.896	0.642
30000	1.	1.83	0.646

Table 4.5: Table of the conditions of the study with single cylinder in cap-bubbly/churn flow regime.

Table 4.6 provides the results of direct measurements of the Sauter diameter and local void fraction.

$D_{sm}^{measured}$ (mm)	$\alpha_g^{measured}$
6	0.34
6.3	0.496
4.9	0.574

Table 4.6: Table of the operating conditions of the study with single cylinder in cap-bubbly/churn flow regime.

Regarding the single-tube experiment, only average local void fraction and the average Sauter diameter have been measured. These data fall short when dealing with cap, churn, or even annular flow regimes. In contrast, the DIVA experiment was conducted across a wide range of velocities and void fractions, featuring a more extensive set of measurement that can help to establish accurate inlet conditions. Furthermore, DIVA's experimental setup is identical to the single tube configuration, providing additional justification for its relevance in determining inlet conditions. The methodology used to derive these inlet conditions for DIVA is accessible in the subsequent chapter 5. Analyzing experimental data for conditions similar to the proposed ones has given data for the inlet conditions. Assuming this similarity, specific inlet conditions were derived and are presented in Table 4.7.

$\alpha_{g1}^{computed}$	$\alpha_{g2}^{computed}$	$D_{sm1}^{computed}$ (mm)	$D_{sm2}^{computed}$ (mm)
0.279	0.357	3.9	19
0.117	0.525	4.0	21
0.569	0.077	3.1	17

Table 4.7: Table of the operating conditions of the study at the inlet of the domain, in single cylinder configuration and in cap-bubbly/churn flow regime.

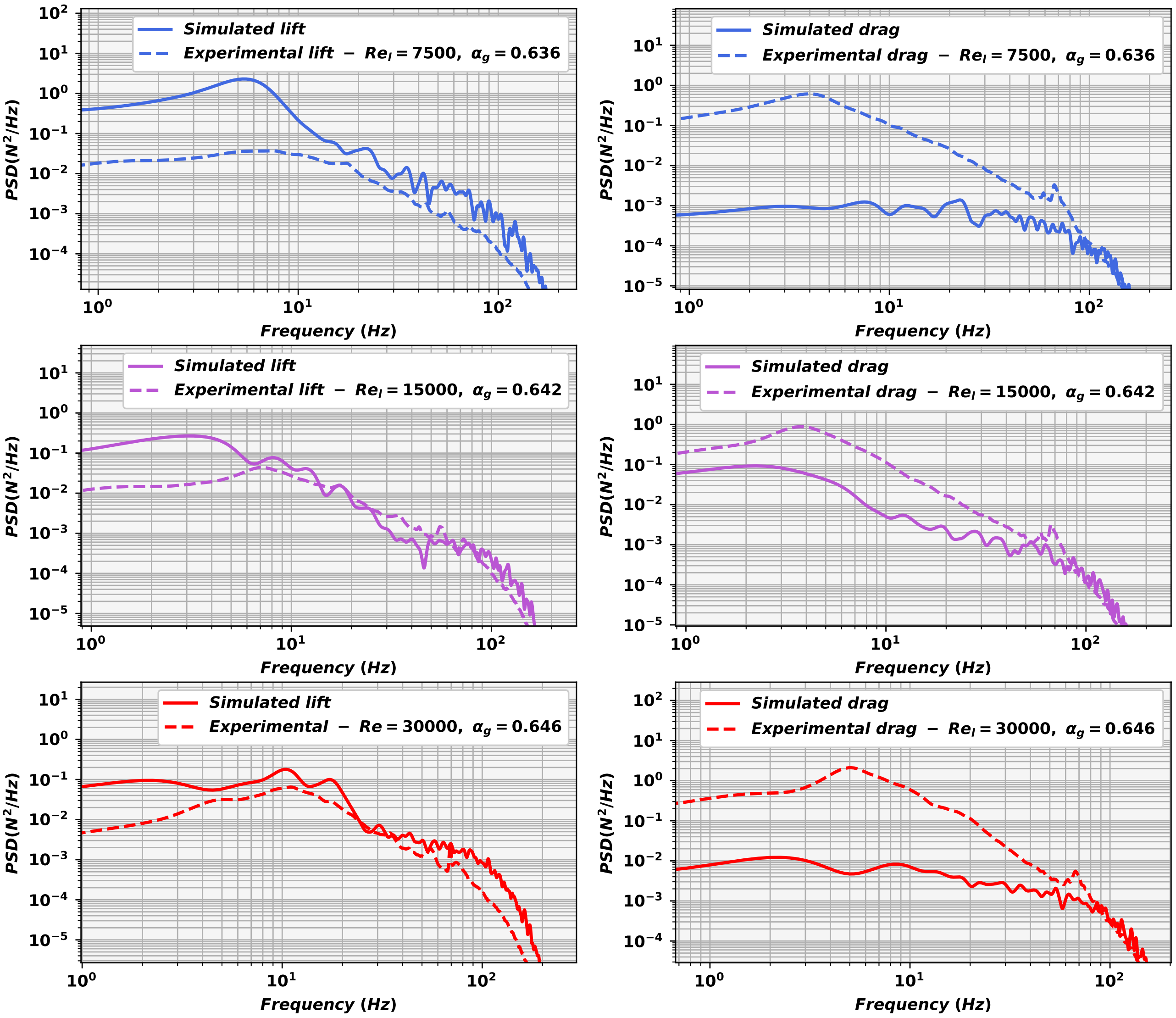

Figure 4.7: Lift (left) and drag (right) forces spectra of the simulations with injected void fraction of around 0.64 and liquid Reynolds number of 7500 (top), 15000 (middle) and 30000 (bottom) compared to experimental data. Simulations with new TRITON model.

Figure 4.7 shows the spectra of drag forces (right) and lift forces (left) for simulations with liquid Reynolds numbers of 7500 (top), 15000 (middle), and 30000 (bottom), compared to experimental data.

Looking at the Lift graph for the Reynolds number of 7500 (top-left), the experimental spectrum exhibits a plateau like behavior between 0.2 Hz and 10 Hz with two low-amplitude bumps at 1 Hz and 6 Hz, followed by a decrease towards the cutoff frequency. In contrast, the simulation shows a slight increase between 1 Hz and 5.1 Hz (due to the injection of group 2 bubbles), followed by a decrease up to the cutoff frequency, with a small bump at 20 Hz. Examining the corresponding drag spectrum (top-right), the experimental data reveal an increase between 1 Hz and 4 Hz, followed by a decrease up to the cutoff frequency. This frequency around 4 Hz, visible for all Reynolds numbers in both simulations and experiments, appears to be characteristic of this regime and thus indicative of the presence of large gas structures. In contrast, the simulated graph increases between 1 Hz and 4 Hz, then decreases to 11 Hz, with a bump at 10 Hz before remaining mainly constant up to the cutoff frequency. Consequently, this simulation has better reproduced the random force spectra than in bubbly flow. However, the lift standard deviation seems to be over-predicted. This behavior can be caused by the acceleration due to the confinement and by the velocity field of group 2 impacting the cylinder. It seems that the second group has a beneficial effect on the prediction of the force spectra.

Looking at the lift graph for the Reynolds number of 15000 (middle-left), the experimental spectrum shows a plateau-like behavior between 1 Hz and 4 Hz, followed by a bump at 7 Hz and then decreases with a constant slope up to the cutoff frequency, with a bump at 18 Hz. In contrast, the simulation exhibits an increase between 1 Hz and 4 Hz, followed by a decrease to 7 Hz, then has a plateau-like behavior until 11 Hz followed by a decrease at 18 Hz before decreasing with a significant change in slope. This demonstrates a qualitatively similar behavior to the experimental data. However, the standard deviation of the lift (area under the curve) is higher than in the experimental results. Regarding the experimental drag spectrum (middle-right), we observe growth between 1 Hz and 4 Hz, followed by a decrease towards the cutoff frequency. The simulated spectrum exhibits an increase between 1 Hz and 2 Hz, followed by a first decrease until 13 Hz before changing of slope with a bump at 19 Hz. Similar to the lift, we do not obtain a perfect simulated graph, but we qualitatively obtain a similar frequency distribution, but at a much lower level. This behavior could be attributed to a better reproduction of the topology around the cylinder. This case has the highest void fraction for group 2 and appears to have the best results regarding the force spectra, aligning with experimental observations.

If we look at the experimental lift spectrum for the Reynolds number of 30000 (bottom-left), we observe an increase between 1 Hz and 10 Hz, with a bump at 5 Hz, followed by a decrease with a constant slope up to the cutoff frequency. In contrast, the simulated spectrum increases between 1 Hz and 10 Hz, with a bump at 2 Hz, then exhibits a bump at 18 Hz then has a decreasing trend up to 27 Hz before gradually decreasing with a constant slope. We can clearly have a different behavior, but not any behavior. It seems that we can get parts of the distribution. Similarly, if we look at the experimental drag spectrum (bottom-right), we observe growth between 1 Hz and 5 Hz, followed by a decreasing trend up to the cutoff frequency. The simulated graph shows a slightly increasing trend between 1 Hz and 10 Hz, with a bump at 2 Hz before gradually decreasing up to the cutoff frequency. We find drag spectra is far away from the experimental one. An intriguing observation is that the simulation with a higher proportion of group 1 bubbles exhibits the most divergent behavior compared to the experimental results. This suggests that the presence of the second group of bubbles has a significant positive impact on the accuracy of the simulation and that there is room for improvement for the first group of bubbles. Since the inlet conditions were extrapolated from the DIVA configuration, it is likely that they do not correspond accurately to the reality of the single-cylinder setup. Examining the injection conditions reveals a very low void fraction for group 2. This case is close to a bubbly regime, which could explain the simulated drag spectrum. However, we can note that the simulations yield promising results and are not entirely different from the experimental spectra, which was not initially expected considering the modeling and the principles of URANS. We also confirm that this regime yields better results as it is less sensitive to the liquid Reynolds number, mainly due to the presence of large structures. To attempt to understand the changes in the topology that lead to better results, we can look at the void fraction distribution within the flow.

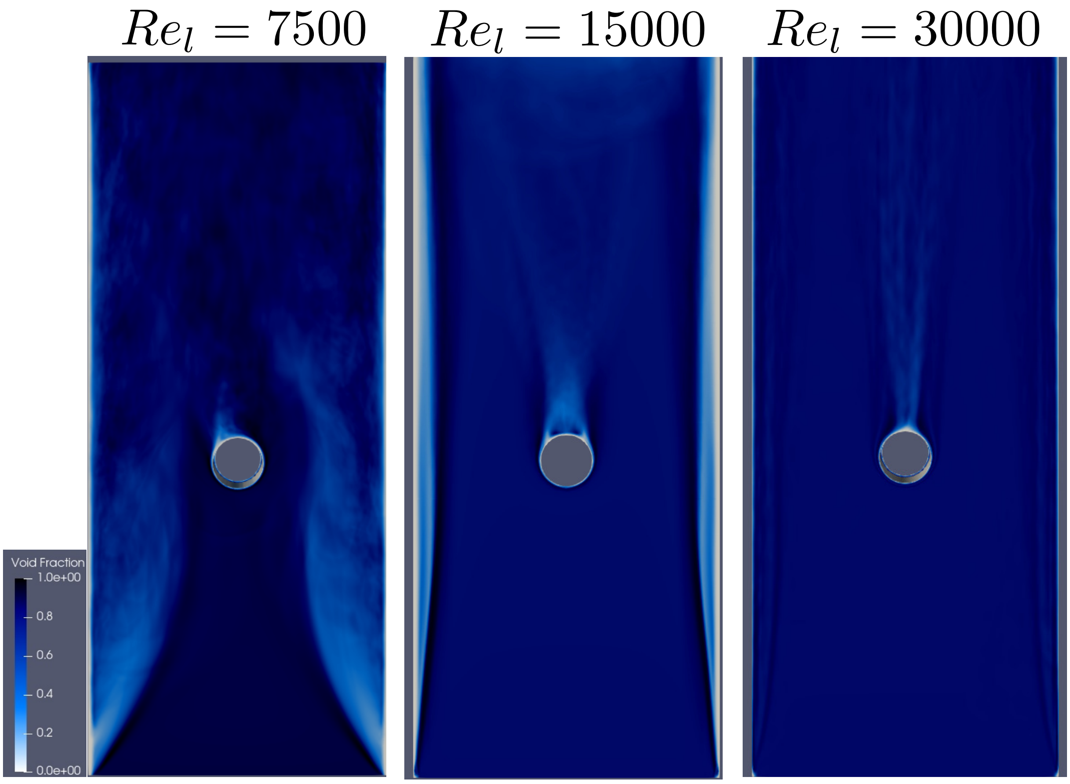

Figure 4.8: Colormap of the averaged void fraction in simulated cap/churn single-tube experiment for $Re_l = 7500$ (left), $Re_l = 15000$ (middle) and $Re_l = 30000$ (right). Simulations with new TRITON model.

Figure 4.8 depicts the averaged void fraction in a simulated cap/churn single-tube experiment for three different Reynolds numbers: $Re_l = 7500$ (left), $Re_l = 15000$ (middle), and $Re_l = 30000$ (right). In the case of the lowest Reynolds number (left), we observe detachment at the channel inlet due to the presence of group 2 bubbles. Additionally, the simulation exhibits a lack of symmetry. This asymmetry is partly due to the averaging process, which is conducted over a short time interval of a few seconds, with a time step of 0.1 seconds. However, this phenomenon is also indicative of the challenges in the modeling process. Ultimately, the prediction of both groups of bubbles has limited interaction because it occurs through the liquid phase. Consequently, the balance between the gas phases can be fragile. This can lead to wall detachments that result in significant flow asymmetry, destabilizing the flow and causing a deviation in the jet, ultimately leading to a stable state without intermittency around the cylinder. This issue is particularly pronounced at low superficial velocities. Therefore, there may be a need for improved modeling of momentum exchange between the bubbles, especially in cases with low Reynolds numbers, to further stabilize the jets. This deviation of the jet is a key factor contributing to the increase in the lift standard deviation.

In the case of the intermediate Reynolds number (middle), we also notice a slight deviation in the jet behind the cylinder. In this scenario, this effect is primarily attributed to the averaging time step (which differs from the measurement time step around the cylinder) being somewhat large and the total averaging time (which is not the same as the total simulation time) possibly being a bit short. However, it is worth noting that the simulation is symmetric and appears well-balanced. We observe a larger wall gradient compared to the bubbly flow due to the presence of group 2 bubbles.

In the case of the highest Reynolds number (right), we also observe a slight asymmetry at the rear of the cylinder for the same reasons mentioned earlier. However, this time, we see weaker near-wall gradients because group 2 is significantly less dominant. Consequently, we encounter a topology closer to that of a purely bubbly flow scenario.

We observe a significant characteristic of this regime: the void fraction is distributed more isotropic on average than in the bubbly regime. To better understand the mean changes, it is essential to investigate the unsteady fields, which are, however, more challenging to interpret since one needs to capture the meaning behind this unsteadiness. To help to understand, the void fraction can be interpreted as the probability of finding gas at a specific point at a given moment.

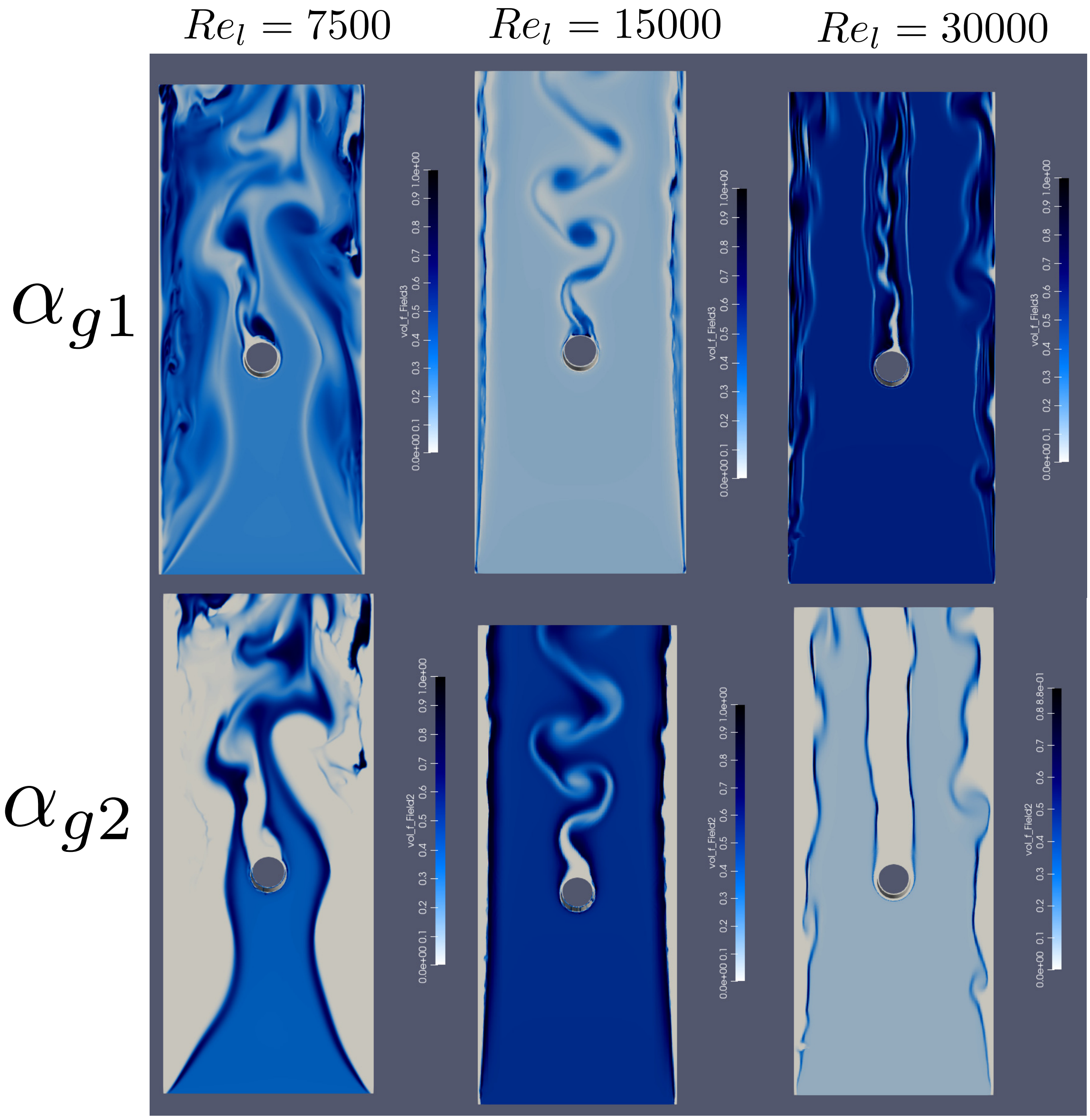

Figure 4.9: Colormap of typical instantaneous void fraction fields, of group 1 α_{g1} and group 2 α_{g2}, from simulated cap-bubbly/churn single-tube experiment for $Re_l = 7500$ (left), $Re_l = 15000$ (middle) and $Re_l = 30000$ (right). Simulations with new TRITON model.

Figure 4.8 illustrates the instantaneous void fraction of group 1 (top) and group 2 (bottom) in simulated cap-bubbly/churn single-tube experiment for $Re_l = 7500$ (left), $Re_l = 15000$ (middle) and $Re_l = 30000$ (right). In the case of the lowest Reynolds number (left), we can visually observe the jet deviation to the left. For group 1 (top-left), we see many dynamic structures near the wall, primarily due to the presence of group 2 bubbles and the low injection velocity. This could be attributed to a lack of communication between the two gas fields and/or an over-prediction on the lift force in the motion equations. Notably, there is no direct influence of the void fraction on the lift force, and no experiments exist to verify its significance at very high void fractions. Additionally, we observe the absence of clusters behind the cylinder, but the presence of a highly sheared dynamic zone, likely responsible for the peak in the lift spectrum. As for the gas field 2 of bigger bubbles (bottom-left), we notice a narrowing of the jet from the channel inlet. We also partially observe the activation of the LIM during the jet shearing after the cylinder, followed by partial dispersion. This indicates a transition from dispersed to LIM and from LIM to dispersed, which appears to be functioning correctly. There is no cluster zone observed behind the cylinder because the 'larger bubbles' are too inert and are sheared further away than the smaller bubbles. This behavior seems qualitatively reasonable. We also observe near-wall zones where the LIM is activated, but it doesn't necessarily yield qualitatively meaningful results. Indeed, the LIM lacks modeling and validation regarding its interaction with the wall and some problems of back flow from LIM-outlet interaction can arise. One of the challenges encountered is that if the LIM is not adequately pushed away from the wall, it can stagnate in very near-wall cells, hindering proper convergence of the calculations. Therefore, a more detailed examination of the interaction between the large interface and the wall with the LIM would be necessary.

When considering the intermediate Reynolds number and the void fraction field of group 1 (middle-top), we observe a topology that is somewhat similar to what is seen in bubbly flow, with a slight cluster behind the cylinder and a thin single-phase zone upstream of the cylinder. However, we do notice dynamic zones along the vertical walls, primarily due to the presence of the group 2 field. If we look at the group 2 field of bigger bubbles (middle-bottom), we see a region behind the cylinder where there are no bubbles, owing to the high presence of small bubbles. Nevertheless, there is significant shear around the field of group 1 bubbles. We also observe that the LIM does not activate around the cylinder, but rather near the vertical walls, adopting an annular field behavior in this region. This behavior is qualitatively consistent, but underscores the need for further validation of the LIM when it interacts with the wall. This topology, with fewer bubbles from the first group, seems to promote a more balanced behavior, which could explain the better results in the force spectra. It is possible that the drag force needs improvement to account for more slip, achieving a less precarious balance between the phases. To explore this, we can examine the test case with a majority of group 1 bubbles and a higher Reynolds number.

In the case of the higher Reynolds test case, particularly in the group 1 field (top-right), we observe dynamic zones near the vertical walls due to the presence of group 2 bubbles. Interestingly, there is neither a purely single-phase zone nor a clustering around the cylinder. However, a single-phase zone is observed at the center of the bubble shear, which appears surprising. This phenomenon is a result of the narrowing of the sheared zone due to the presence of group 2 bubbles and likely an imbalance between the two phases. Examining the gas field of group 2 bubbles, we notice that these bubbles are not entrained in the wake of the cylinder, creating a wake constraint that influences the shape of the group 1 field. Activation of the LIM is almost non-existent because the presence of group 2 is significantly less dominant. Near the wall, we observe strong vortices due to lift forces. This raises questions about whether the lift force is correctly modeled for group 2 bubbles. The distinct topology observed behind the cylinder, different from other cases, is likely the cause of the poor drag force results. As for lift, the narrowing of the zone due to the presence of group 2 causes acceleration and thus a slightly different standard deviation compared to the experimental data, which may explain the deviation from the experimental results.

In summary, the force spectra obtained are consistent with the simulated topology, and we observe some favorable trends compared to the experimental data. It is worth recalling that even in bubbly flow, achieving spectra close to experimental results was challenging. However, it is noteworthy that the presence of group 2 bubbles did not significantly degrade the predictive capability of the model. It appears that group 2 imposes a favorable topology similar to that observed in experiments. It seems that it is likely easier to obtain good spectra compared to experimental data for these regimes. While improvements are required, the results obtained are not arbitrary; they are rather encouraging. Through this study, we have identified areas for improvement:

- The lift force appears to have too significant an influence compared to the drag force in the modeling. It is particularly important to thoroughly investigate the effect of void fraction on lift. Additionally, it seems that improvements are needed for modeling lift forces for group 2 bubbles.

- A force or a new drag coefficient that could promote a better balance between the two groups of bubbles seems necessary when dealing with dynamic zones, especially when the injection velocity is low or when the presence of group 2 is significantly less dominant. Indeed, these less responsive bubbles tend to disrupt the dynamics when they are in the minority or when the flow rate is low.

- An improvement of the lubrication force to better account for near-wall effects, particularly addressing issues related to the stagnation point in dispersed phases.

We have seen that liquid Reynolds number and homogeneous void fraction were the most influential parameters, giving rise to different flow regimes. It was observed that obtaining force spectra corresponding to the bubbly regime was the most challenging due to its sensitivity to liquid fluctuations, the topology around the cylinder, and the acceleration caused by confinement. This was confirmed by comparing experimental and numerical observations. However, for the DIVA configuration, the cylinders upstream and downstream of the central cylinder are expected to constrain the flow topology around it, bringing it closer to the experimental setup. Additionally, velocities at the rear and front of the central cylinder should be more moderate, reducing the influence of liquid fluctuations and potentially leading to a better reproduction of the experimental flow. Hence, we are hopeful of achieving relatively good results. Moreover, we have demonstrated that cap-bubbly/churn regimes are more resilient to liquid fluctuations and void fraction variations. We aim to obtain qualitatively good results, showcasing the potential of our modeling approach.

Chapter 5

Simulations of two-phase flows in a square tube bundle configuration

Summary

This chapter presents the two-phase simulations of a square tube bundle (DIVA) configuration.

The first part studies the experimental results and analyze them before conducting several simulations. The initial section focuses on how to estimate the operational conditions of the experimental loop to correctly simulate with our model. In particular, a method is discussed for estimating the injection conditions between the two groups and justifying the model's relevance concerning the experiment. The following part deals with the experimental spectra of drag and lift forces for some experimental tests, aiming to highlight the key parameters for selecting and justifying the simulations performed.

The second part addresses the DIVA test cases in this thesis. The first section investigates the effect of the liquid Reynolds number in the bubbly case, while the second section explores the effect of the Reynolds number in cap-bubbly and churn cases.

5.1 On studying experimental results for simulations

5.1.1 Estimation of the operational conditions for the simulations

As a reminder, the experimental DIVA setup hosted at CEA, as depicted in Figure 1.15, is dedicated to the study of square-pitch bundle vibrations. The loop is set with a pump able to deliver water at a flow rate ranging from 5 to 300 L/s and an air compressor able to supply up to 3000 m^3/h at an absolute pressure of 8 bar. This loop can operate with a water flow, an air flow, or an air-water flow. The experimental configuration is an ascending channel with a rectangular cross-section measuring 0.18 m × 0.3 m, within which a square tube bundle, made of rigid tubes with dimensions of 5 × 3, and a pitch ratio of 1.5, can be placed, as presented in [95] and in Figure 1.15.

Flow measurements at the inlet and outlet of the channel allow for the precise measurement of the operational air and water flow rates for each of the tests, and consequently, the superficial velocities of the liquid j_l and the gas j_g. Measurements of interfacial velocities have also been conducted to obtain a measurement of the mean Sauter diameter D_{sm}. Two optical probes positioned midway between the central tube and the downstream tube, on either side of the centerline, enable the measurement of the local void fraction α_g within the setup. Therefore, for each of the tests, we have the following information: α_g, D_{sm}, j_l, and j_g. However, to faithfully reproduce the operating conditions of DIVA with TRITON, it is necessary to prescribe the following information at the inlet: α_{g1}, α_{g2}, D_{sm1}, D_{sm2}, j_l, and j_g. Hence, we need to find a way to estimate these quantities in order to initialize simulations.

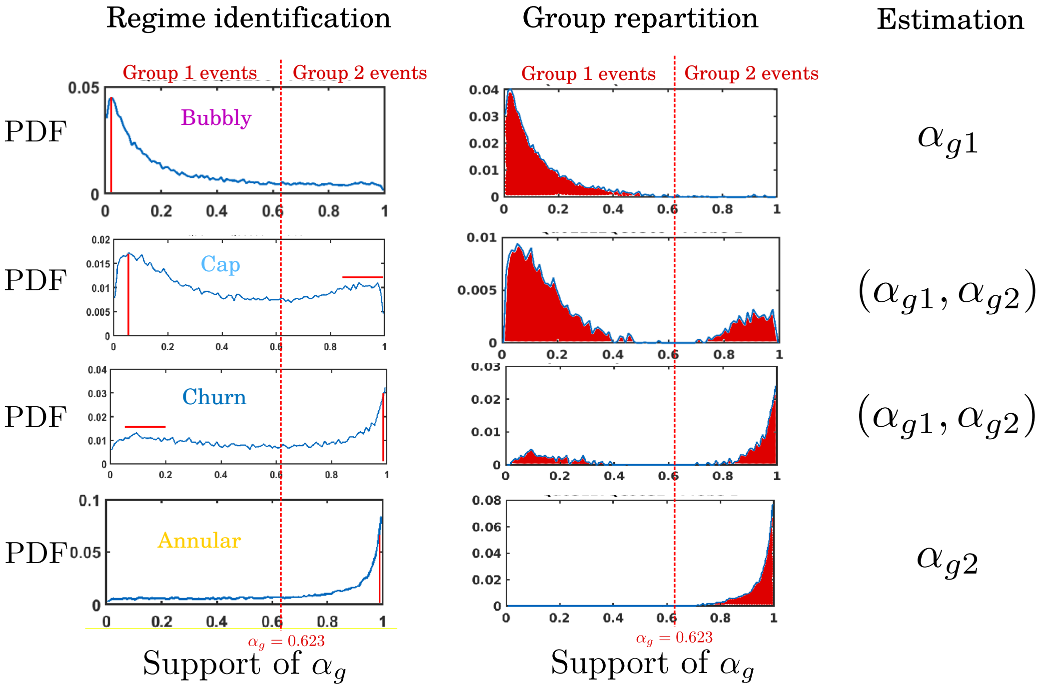

Figure 5.1: Measuring method of α_{g1} and α_{g2} from support of void fraction measurement PDF. Legend : 🟪 Bubbly regime, 🟦 Cap-bubbly regime, 🟦 Churn regime, 🟨 Annular regime.

Figure 5.1 illustrates the methods used to identify flow regimes and void fraction distribution between the two groups of bubbles. The left graph, titled "Regime Identification," shows how different experimental flow regimes are identified using the Probability Density Function (PDF) of the local void fraction. The bubbly regime is characterized by a single peak between 0 and

0.2, while the annular regime is characterized by a single peak between 0.9 and 1. The cap-bubbly regime is characterized by a peak between 0 and 0.2 extending into higher void fractions, while the churn regime is characterized by a peak between 0.9 and 1 extending into lower void fractions. Since regime transitions are not entirely abrupt, some judgment must be exercised in some cases. However, the regime identification and the next calculation were performed independently.

The central graph illustrates the method for assessing the distribution of void fraction between the two groups of bubbles. The void fraction PDF graphs from all experimental trials exhibit a dip around $\alpha_g \approx 0.6$, which consistently falls within a region of decreasing probability density function for both bubbly and annular regimes. This phenomenon is similar to the distribution of mean Sauter diameters between the two groups. This observation led to the differentiation of events between the two groups around the calculated value of chapter 3 for water-air, $\alpha_{g1max} \approx 0.623$. Consequently, this method enables the discrimination of two event areas corresponding to the two groups of bubbles. We thus estimate the mean local void fractions of the two bubble groups by measuring the respective area under the curve f from both sides of α_{g1max}, so that:

$$\alpha_{g1} = \frac{\int_0^{\alpha_{g1max}} f(\alpha_g)\, d\alpha_g}{\int_0^1 f(\alpha_g)\, d\alpha_g}\alpha_g, \;\; \alpha_{g2} = \frac{\int_{\alpha_{g1max}}^1 f(\alpha_g)\, d\alpha_g}{\int_0^1 f(\alpha_g)\, d\alpha_g}\alpha_g. \tag{5.1}$$

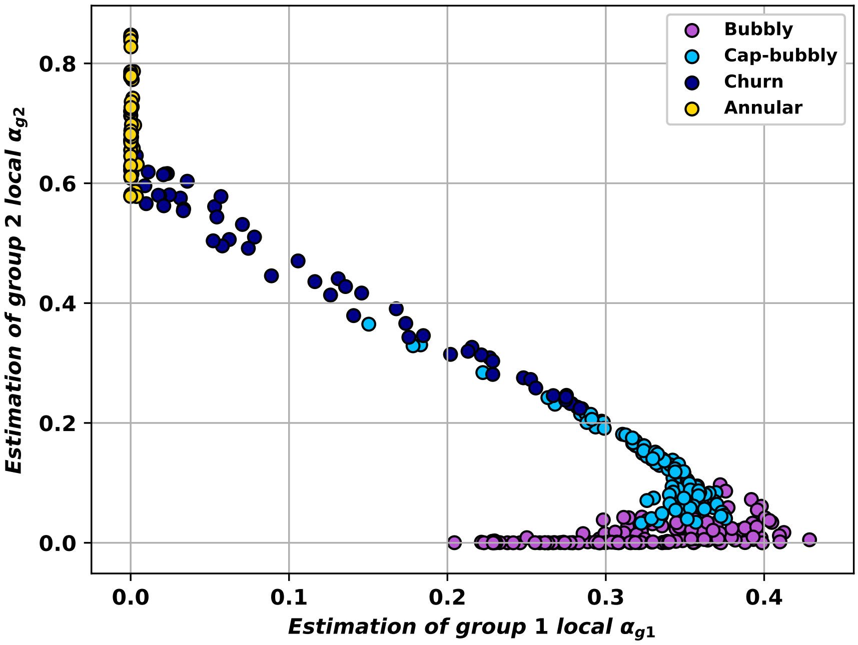

Figure 5.2: Graph of the distribution of the local void fraction between the 2 gas groups, estimated from the support of the local void fraction. Legend : 🟪 Bubbly regime, 🟦 Cap-bubbly regime, 🟦 Churn regime, 🟨 Annular regime.

Figure 5.2 displays the distribution of the local void fraction between the two gas groups using the previous method. It can be observed that the points corresponding to the bubbly regime are spread in the region primarily occupied by group 1, and this distribution subsequently converges towards the distribution of the cap-bubbly regime. This observation aligns with our expectations. The points corresponding to the cap-bubbly regime initially cluster in an area around $\alpha_{g1} = 0.35$ and $\alpha_{g2} = 0.07$, then appear to follow a line with a slope of 1.47, common to the churn regime. The line ends at the annular regime, where only group 2 is present.

This local measurement does not allow for the direct estimation of the void fraction distribution to be injected due to the slip between phases. To achieve this, it is necessary to estimate the void fraction in the section and then obtain the void fraction to be injected. We can rely on the characteristics of the two groups. The proportion of the void fraction in group 1 is mainly due to phase slip, as it composed of many bubbles. To do this, we can first estimate the void fraction in the section as $<\alpha_{g1}>_S$ by:

$$<\alpha_{g1}>_S \approx \frac{\alpha_{g1}\Big((j_l+j_g)+U_b\sqrt{1-\alpha_{gH}}\Big)}{jg}, \tag{5.2}$$

with $\alpha_{gH} = \frac{j_g}{j_g+j_l}$, the homogeneous void fraction.
For group 2, since the bubbles are very large and rather 'lonely,' they completely pass in front of the probe. Therefore, the locally measured path time is indeed representative in the section, and thus:

$$<\alpha_{g2}>_S = \frac{jg_2}{j_l+j_g} = \frac{j_g-jg_1}{j_l+j_g} \approx max\Big(\alpha_{gH} - <\alpha_{g1}>_S, 0\Big). \tag{5.3}$$

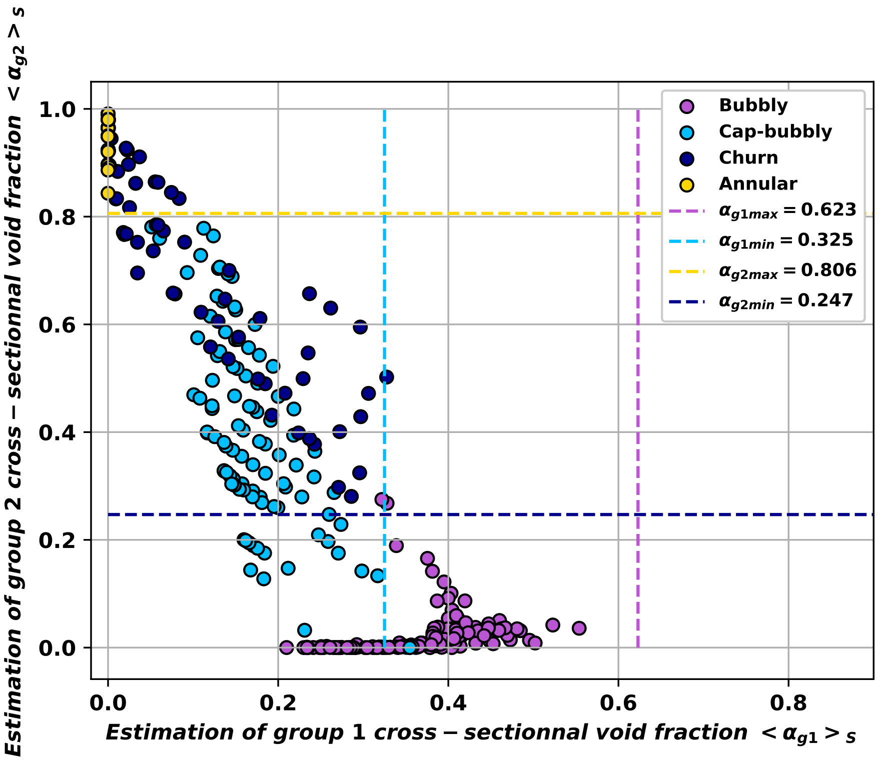

Figure 5.3: Graph of the distribution of the cross-sectionnal void fraction between the 2 gas groups, estimated from the support of the local void fraction. Legend : 🟪 Bubbly regime, 🟦 Cap-bubbly regime, 🟦 Churn regime, 🟨 Annular regime.

Figure 5.3 illustrates the distribution of the void fraction within the section between the two groups of bubbles. As expected, we observe that the bubbly regime is primarily characterized

by a high proportion of group 1 bubbles in the section. We can observe a cap-churn point in the middle of bubbly flow regime points, it means that this one may not be well identified and belongs to bubbly regime or that the computation was not accurate. The cap-bubbly and churn regimes, on the other hand, are characterized by an increase in the proportion of group 2 compared to group 1, as anticipated. Ultimately, the increase in group 2 tends to reduce the presence of group 1, leading to an annular regime where only group 2 is represented. This estimation of the gas distribution within the section naturally includes a significant uncertainty due to the assumptions made to obtain these results. However, it is also important to note the presence of computed limitations related to the void fraction, introduced in chapter 3.
The first one is the packing limit for group 1, $\alpha_{g1max} = 0.623$, used in the estimation. It is obvious that the bubbles of group 1 do not exceed this limit. However, it may be necessary to conduct more experiments with higher superficial velocities to approach this limit. We also get that in the cross-section, the void fraction is rarely above 0.51, value already discussed in chapter 3 and often observed experimentally. The second limit, associated with group 1, $\alpha_{g1min} = 0.325$, which corresponds to the minimum of liquid fluctuations observed by the bubbles, aligns well with the experimental limit for the bubbly regime of group 1, as seen in the literature. The third limit, related to the second group of bubbles, $\alpha_{g2max} = 0.806$, corresponding to the limit for the presence of large structures computed in chapter 3 and supported by the literature, is indeed respected. More surprisingly, the limit $\alpha_{g2min} = 0.247$, derived from the same calculation as α_{g2max}, is difficult to interpret since it does not correspond to anything in the literature, but seems to be a good estimate of the limit for the churn regime. These observations support the idea that this estimation in our case is fairly accurate.

However, since we do not know the velocity profile, we are required to inject uniformly with flat velocity and void fraction profiles at the inlet of the domain of computations. Therefore, it is necessary to estimate the homogeneous void fraction to be injected into the section. To do this, we assume that the distribution in the section is identical to what needs to be injected. Indeed, the average gas velocities of the two groups are often very close, so we can assume that distribution of the void fractions of the two groups in the section is the one injected due to the conservation of the flow rates of the two groups. We then have that the void fractions to be injected, $< \alpha_{g1}^{inj} >_S$ and $< \alpha_{g2}^{inj} >_S$, respectively for group 1 and group 2, are:

$$< \alpha_{g1}^{inj} >_S = \frac{\alpha_{g1}}{\alpha_{g1} + \alpha_{g2}} \alpha_{gH}, \tag{5.4}$$

$$< \alpha_{g2}^{inj} >_S = \alpha_{gH} - < \alpha_{g1}^{inj} >_S . \tag{5.5}$$

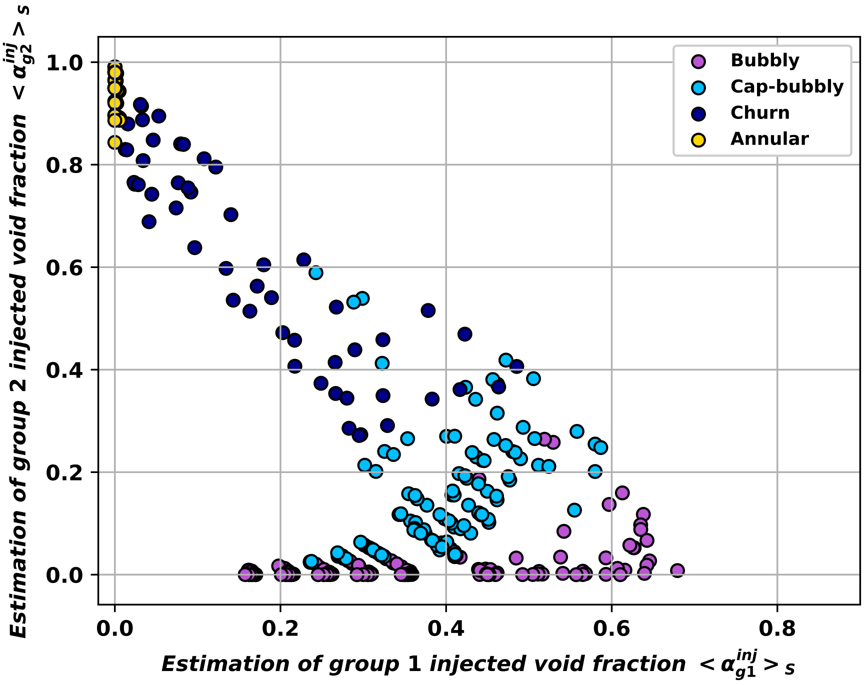

Figure 5.4: Graph of the distribution of the cross-sectionnal void fraction between the 2 gas groups to be injected, estimated from the support of the local void fraction. Legend : 🟪 Bubbly regime, 🟦 Cap-bubbly regime, 🟦 Churn regime, 🟨 Annular regime.

Figure 5.4 illustrates the distribution of the void fraction to be injected into the simulations for the two groups of bubbles. We can clearly see clusters of simulations with homogeneous void fractions for the bubbly cases, which is consistent with the experimental tests. The distribution remains identical to the one described earlier, with values shifted due to the slip of gas relative to the liquid. These values are then used for simulating the flows in DIVA.

However, there is a missing estimation of the diameters of the two groups to inject properly into the simulations. Measuring Sauter diameters without a distribution is very challenging. By conserving the total interfacial area $a_i = \frac{6\alpha_g}{D_{sm}} = a_{i1} + a_{i2} = \frac{6\alpha_{g1}}{D_{sm1}} + \frac{6\alpha_{g2}}{D_{sm2}}$, we have :

$$\frac{\alpha_g}{D_{sm}} = \frac{\alpha_{g1}}{D_{sm1}} + \frac{\alpha_{g2}}{D_{sm2}} \tag{5.6}$$

By reminding the axiom of continuity, $\alpha_{g1} = \alpha_g - \alpha_{g2}$ we have:

$$\frac{\alpha_{g2}}{\alpha_g} = \frac{\frac{1}{D_{sm}} - \frac{1}{D_{sm1}}}{\frac{1}{D_{sm2}} - \frac{1}{D_{sm1}}}. \tag{5.7}$$

However, we do not have the information of D_{sm1}. Nevertheless, we can attempt a rough estimation by assuming that the probe primarily measures the interfacial area of group 1 since it is an order of magnitude larger in most cases. Since the calculation is based on interfacial velocities, a first approximation is to assume that the measured diameter is simply the diameter of the first group D_{sm1} visually enlarged by the presence of bubbles from the second group. The enlargement is due to the time of presence of group 2 t_{g2} compared to the total gas time t_g, as follows:

$$D_{sm1} = \frac{D_{sm}}{1 + \frac{t_{g2}}{t_g}} = \frac{D_{sm}}{1 + \frac{\alpha_{g2}}{\alpha_g}}, \tag{5.8}$$

with $\alpha_g = \alpha_{g1} + \alpha_{g2}$. We then assume that the results are within the interval $[D_{crit}, 10D_{crit}]$.

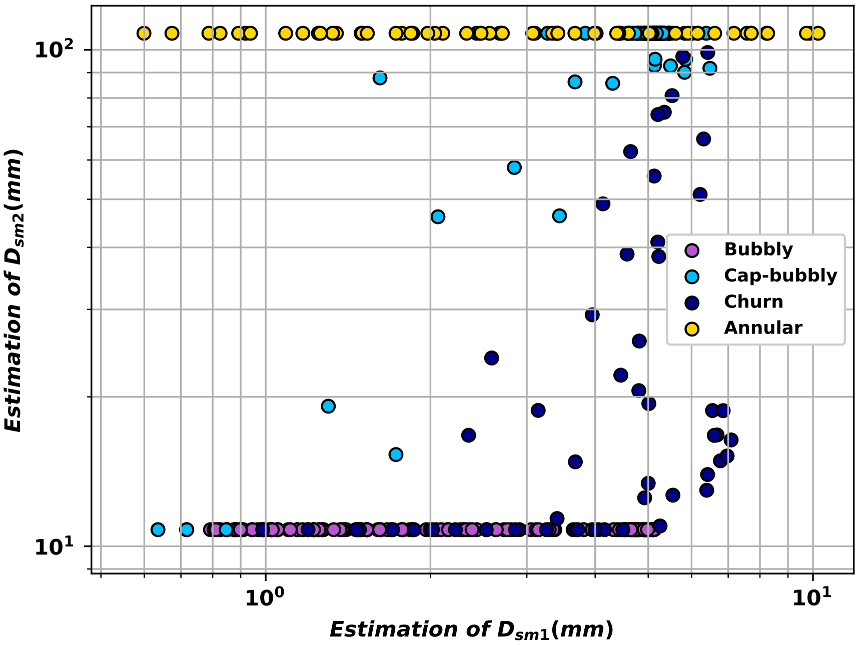

Figure 5.5: Graph of the estimation of the mean Sauter diameters of the 2 gas groups to be injected, estimated from the support of the local void fraction. Legend : ■ Bubbly regime, ■ Cap-bubbly regime, ■ Churn regime, ■ Annular regime.

Figure 5.5 illustrates the estimation of the mean Sauter diameter for the two groups of bubbles. This method appears to provide consistent values for group 1 and values for the second group in a limited number of cases. However, it is important to note that this method relies on highly simplified and debatable assumptions. Fortunately, the prediction of spectra should not be very sensitive to the value of the diameter if it correctly handles the dynamics, as long as it remains reasonably physical. Additionally, the interfacial area of group 2 is often too small to be measured by a single probe, and measuring and characterizing the large interfaces can be complex. Therefore, we will use these measurements for the cases to be simulated only when it gives coherent values.

5.1.2 Identification of key parameters for forces spectra

It is essential to identify the key parameters that influence the changes in experimental force spectra in order to wisely choose some test cases. Figures 5.6 and 5.7 depict the drag and lift force spectra acting on the central tube of DIVA as a function of the liquid reduced frequency $f_r = \frac{fD}{j_l}$ for liquid Reynolds numbers (based on liquid injection) of 8275 and 45514, for various injected void fractions.

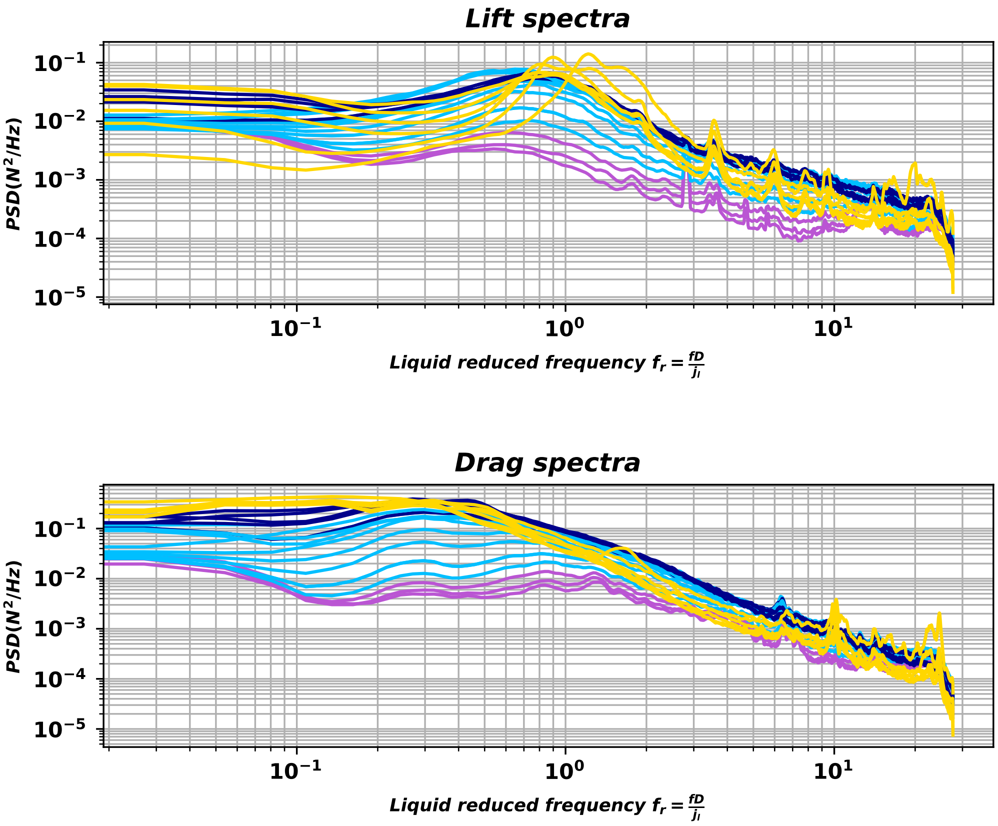

Figure 5.6: Experimental lift (top) and drag (bottom) forces spectra for $Re_l = 8275$ with increasing void fraction according to the liquid reduced frequency $f_r = \frac{fD}{j_l}$. Colors are the one chosen to represent the different regimes. Legend : 🟪 Bubbly regime, 🟦 Cap-bubbly regime, 🟦 Churn regime, 🟨 Annular regime.

Figure 5.6 encompasses all four identified regimes. The drag spectrum (bottom) consistently exhibits an increasing trend between $f_r = 0.1$ and $f_r = 0.5$, followed by a decreasing trend starting at $f_r = 2$. The behavior between $f_r = 0.5$ and $f_r = 2$ depends on the injected void fraction. The lift spectrum (top) displays a similar behavior. A similar but shifted behavior in terms of f_r is obvious in Figure 5.7. There is a general uplift in the spectra with respect to the void fraction, with no significant effect from the regimes, except for the annular case in the lift spectrum. While the drag spectrum appears to be well bounded between purely liquid and purely gas cases, the lift spectrum seems to be bounded between the purely liquid and churn regimes. Indeed, the annular regime appears to exhibit a distinct behavior, likely due to the extremely low presence of liquid. This behavior is also observable in Figure 5.7.

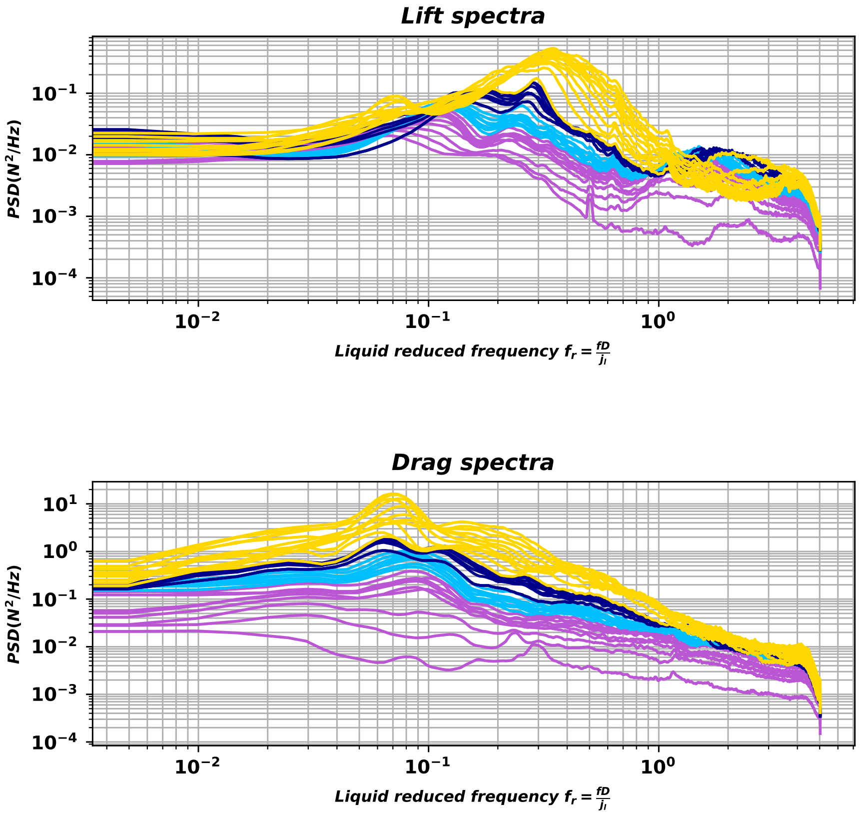

Figure 5.7: Experimental forces spectra for $Re_l = 45514$ with increasing void fraction according to the liquid reduced frequency $f_r = \frac{fD}{j_l}$. Colors are the one chosen to represent the different regimes. Legend : ■ Bubbly regime, ■ Cap-bubbly regime, ■ Churn regime, ■ Annular regime.

Different behaviors are noticeable among the various Reynolds numbers, but an increase in the void fraction tends to rise the graphs, enhance the slopes of the decay, and broaden the frequency peaks. Based on these observations, it appears that the force spectra primarily depend on the liquid Reynolds number and the injection void fraction, and thus, on the parameter pair (j_l, j_g) at first order in our simulations. No effect of injected diameter is visible on those spectra. Unlike the case with a single cylinder, there is no cluster between the spectra of the cap-bubbly and churn regimes. The « linearity » in the evolution of spectra with void fraction indicates that the spectra are not very sensitive to bubble diameters within the flow. Based on observations made in a single cylinder, it can be inferred that this phenomenon arises from the specific bundle configuration that forces the flow to have a certain topology. The distinctive behavior of lift spectra in the annular regime suggests that the liquid almost no longer influences the spectra, but the large structures present in the annular flow are of paramount importance, especially concerning passages between the cylinders, which impose a certain topology. It appears, therefore, that it is necessary for the modeling of the continuous gas phase to carefully consider the interaction with the cylinders to obtain accurate results.

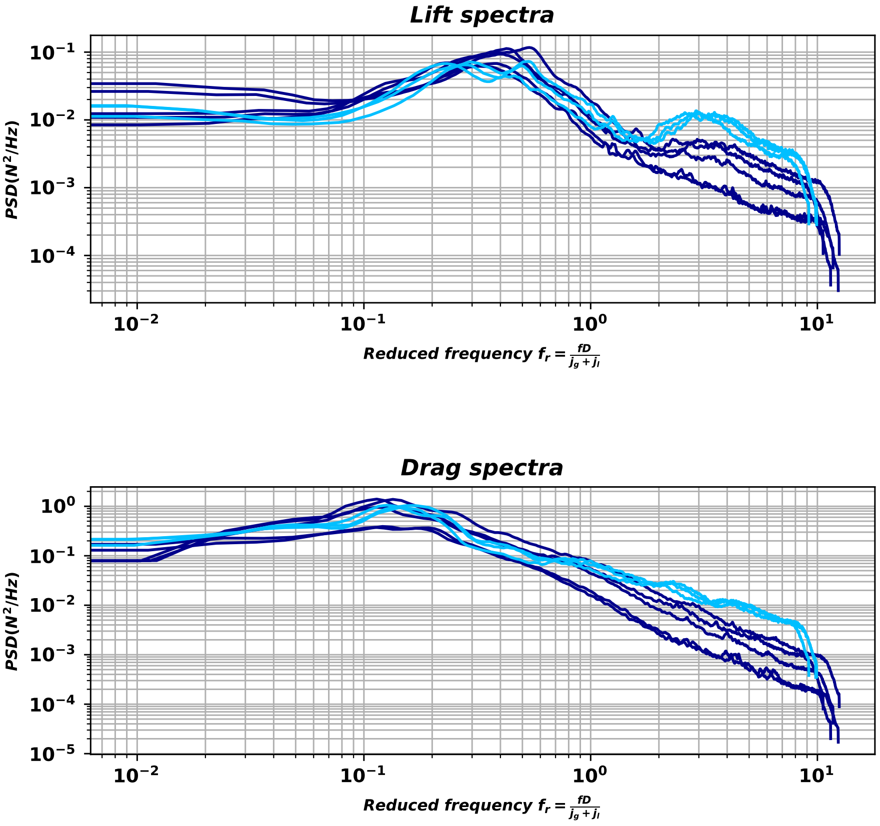

Figure 5.8: Experimental graph of the force spectra of the drag and lift spectra as a function of the reduced frequency $f_r = \frac{fD}{j_l + j_g}$ for void fractions ranging from $\alpha_{gH} = 0.62$ to $\alpha_{gH} = 0.93$ and Reynolds numbers ranging from 55000 to 75000. Legend : 🟪 Bubbly regime, 🟦 Cap-bubbly regime, 🟦 Churn regime, 🟨 Annular regime.

Figure 5.8 displays the drag and lift spectra as a function of the reduced frequency $f_r = \frac{fD}{j_l + j_g}$ for void fractions ranging from $\alpha_{gH} = 0.62$ to $\alpha_{gH} = 0.93$ and Reynolds numbers ranging from $55,000$ to $75,000$. On the drag spectra (bottom), a similar pattern is observed for every case with a slope increase between 0.7 and 1 up to approximately $f_r \approx 0.2$, followed by a slope decrease of 1.95 for the churn regime and from $f_r = 0.6$ for the cap-bubbly regime. This behavior can be explained by the difference in Reynolds number, indeed all cap-bubbly flow regimes are those with higher Reynolds number. The lift spectra (top) also exhibit a similar pattern with an increase around $f_r \approx 0.5$, followed by a slope decrease of 1.2 up to $f_r \approx 1.7$, and then a change in slope for the churn regime and a jump followed by a slope change for the cap-bubbly regime, both with a slope of 1.95. The slightly different behavior of the cap-bubbly regime may also be explained by difference of the Reynolds numbers. Indeed, according to Figures 5.6 and 5.7 this effect depends on the Reynolds number. Thus, it appears that Re_l and α_g are the parameters of paramount influence for the behavior of the spectra at the first order in this case.

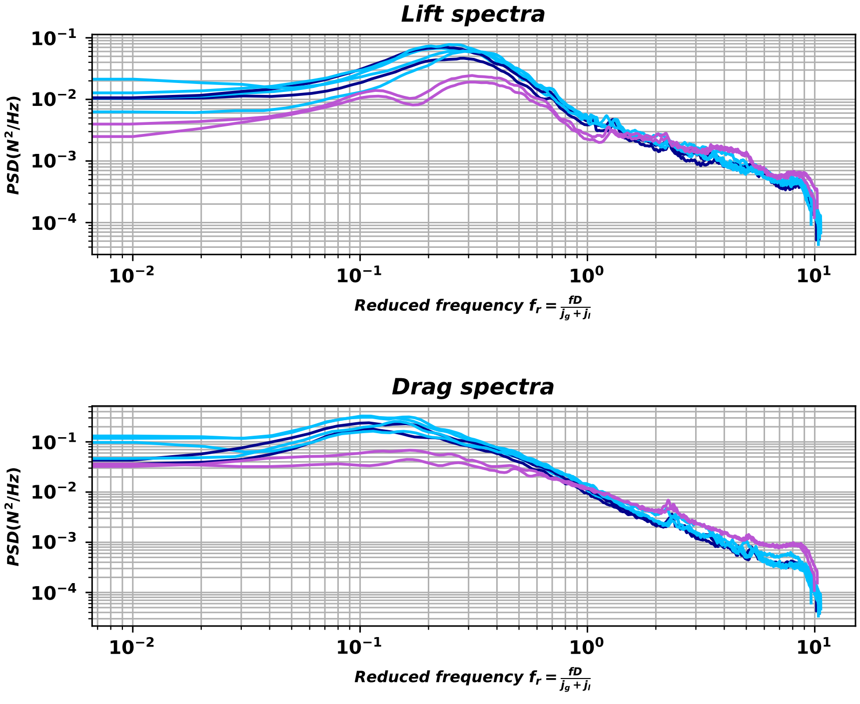

Figure 5.9: Experimental graph of the force spectra of the drag and lift spectra as a function of the reduced frequency $f_r = \frac{fD}{j_l + j_g}$ for void fractions ranging from $\alpha_{gH} = 0.46$ to $\alpha_{gH} = 0.89$ and Reynolds numbers ranging from 9800 to 11000. Legend : 🟪 Bubbly regime, 🟦 Cap-bubbly regime, 🟦 Churn regime, 🟨 Annular regime.

Figure 5.9 depicts the drag and lift spectra as a function of the reduced frequency $f_r = \frac{fD}{j_l + j_g}$ for void fractions ranging from $\alpha_{gH} = 0.46$ to $\alpha_{gH} = 0.89$ and Reynolds numbers ranging from 9800 to 11000. Similar observations to those made previously for the churn and cap-bubbly cases are noticeable. In the bubbly regime, the lift spectrum exhibits a similar appearance, whereas the drag spectrum is rather flat or even decreasing. This behavior appears to be characteristic of high Reynolds number bubbly flows with void fractions below $0.5 - 0.6$.
As a reminder, we first concluded on the effect of (j_l, j_g) at first order. However, we did not know if it was the effect of liquid Reynolds (with j_l) and void fraction (with $\frac{j_g}{j_l + j_g}$) or if it was due to the liquid mean cross-sectionnal velocity (with $j_g + j_l$) at first order and regime dependency at second order. Hence, with the previous observations it becomes obvious that $j_g + j_l$ and the flow regime have the most significant influence on the force spectra.

The spectra are sensitive to $j_g + j_l$ and the flow regime with little influence from the diameter at the first order. It can be noted that the bubbly and annular regimes exhibit distinct behaviors concerning drag and lift spectra, respectively. Obtaining accurate drag spectra for bubbly regimes and high Reynolds numbers seems somewhat more complicated. This can be explained by the strong depression at the back of the cylinder and lower velocities in these areas compared to the spaces between the cylinders. Conversely, lift spectra in the annular regime have a unique behavior, possibly due to the presence of large gas structures between the tubes, where there is little liquid, and horizontal movements between the cylinders. To verify these hypotheses based on experimental data and the methods used to calculate inlet conditions, it is necessary to study numerical simulations.

5.2 Simulations of the DIVA experiment

5.2.1 Meshing strategy

A particular work had to be carried out on the meshing of the DIVA configuration. Indeed, it is necessary to mesh the entire configuration with hexahedral elements that are not too deformed. Furthermore, the boundary layer zone around the cylinders already has particularly compressed elements, so it is preferable to avoid a non-uniform grid in the tangential direction to the cylinder. To achieve this, the strategy is first to constrain the grid to cover 10% of the cylinder's size, making it as homogeneous as possible. Then, the idea is to avoid stretching the elements too much in all directions and too abruptly. The meshing challenge then lay in correctly accounting for the boundary layer on the flat wall and the one around the cylinder. The goal is to have a mesh that does not cause abrupt changes due to strong variations in mesh volume, especially near the wall. Finally, after studying several configurations with bubbly test cases, a meshing strategy was developed and is presented in Figure 5.10.

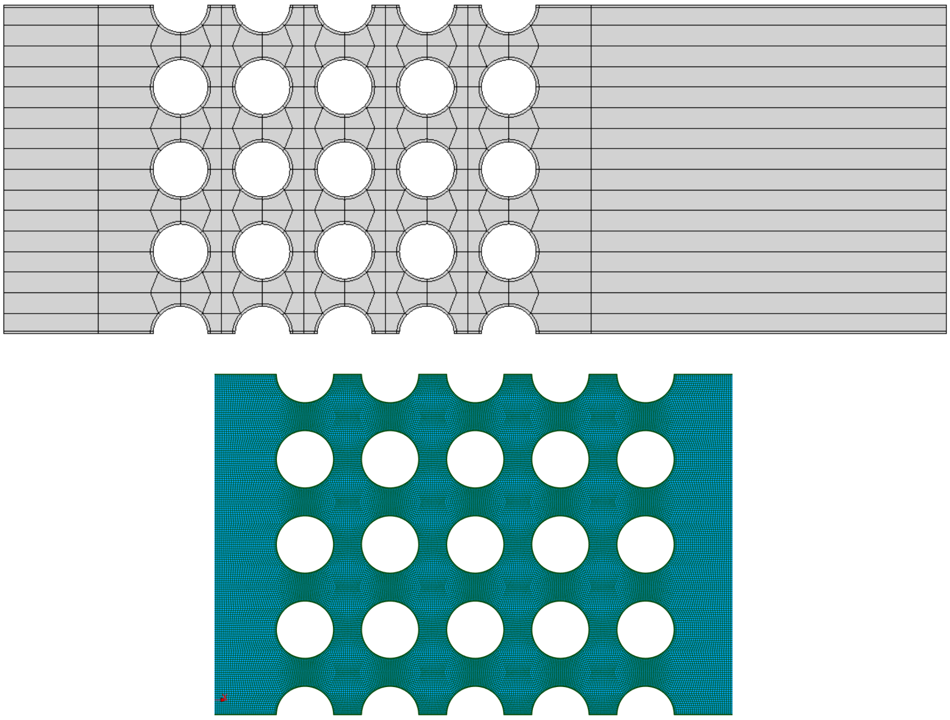

Figure 5.10: Mesh building strategy (top) and example of coarse mesh (bottom) for DIVA simulations.

Figure 5.10 shows an example of a coarse mesh for the DIVA configuration. The strength of these meshes is that they exhibit few severe distortions near the walls, mesh convergence is straightforward to interpret because the elements maintain their aspect ratio, and as the mesh becomes finer, the distortions become less significant for the flow. Regarding mesh convergence, the model is sensitive to the mesh and typically converges less easily than a mesh for a purely single-phase flow. For the studied velocities, the maximum boundary layer thicknesses δ_{max} are compiled in the following table 5.1.

	First case	Second case	Third case
Bubbly: $2\delta_{max}$ (mm)	0.2	0.07	0.06
Cap/churn : $2\delta_{max}$ (mm)	0.03	0.026	0.024

Table 5.1: Table of the maximum boundary layers δ_{max} for all the DIVA test cases. The first mesh size must be around $2\delta_{max}$.

To ease the study of mesh convergence and the design of different meshes, we used the mesh convergence of the highest Reynolds number from the bubbly case as our reference. Therefore, we have the Coarse, Medium, and Fine meshes, corresponding to general mesh sizes of 1 mm, 0.6 mm, and 0.1 mm. For the fine mesh of the bubbly case, the near-wall mesh had to be divided by 2. Convergence is verified for all meshes in comparison to the time-averaged void fraction profile in the middle between the inlet and the first cylinders. All simulations presented here are done using the Medium meshes. Thus, the mesh for the bubbly case with the lowest Reynolds number is finer than necessary, but that of the churn cases is guaranteed to converge for the large interfaces.

We have verified that the solution was sufficiently converged to obtain interpretable results. Therefore, our initial focus is on bubbly simulations and their sensitivity to validate experimental observations.

5.2.2 Bubbly flow simulations

The previous section helped identify the liquid Reynolds number and the void fraction as important parameters influencing force spectra. Therefore, in this section, we aim to replicate the Reynolds number effect in bubbly test cases. Indeed, experimental comparisons can be conducted using the collected data and the estimated inlet conditions presented in the previous section. We investigate three liquid Reynolds number cases: 5516, 8275, and 15171, for approximately homogeneous void fractions of about 0.2. Table 5.2 summarizes the conditions of the test cases studied.

Re_l	j_l (m/s)	j_g (m/s)	α_{gH}	$D_{sm1}^{measured}$ (mm)
5516	0.185	0.05	0.213	4.8
8275	0.277	0.067	0.194	4.6
15171	0.509	0.15	0.227	3.3

Table 5.2: Table of the conditions of the study of DIVA simulation in bubbly flow regime.

To understand the challenge of obtaining accurate force spectra and to demonstrate the contribution of our modeling, we first analyze the same model as in the last part of the introduction : the native NEPTUNE_CFD model with Ruyer-Seiler polydispersion. For this purpose, we focus on the first case with $Re_l = 5516$.

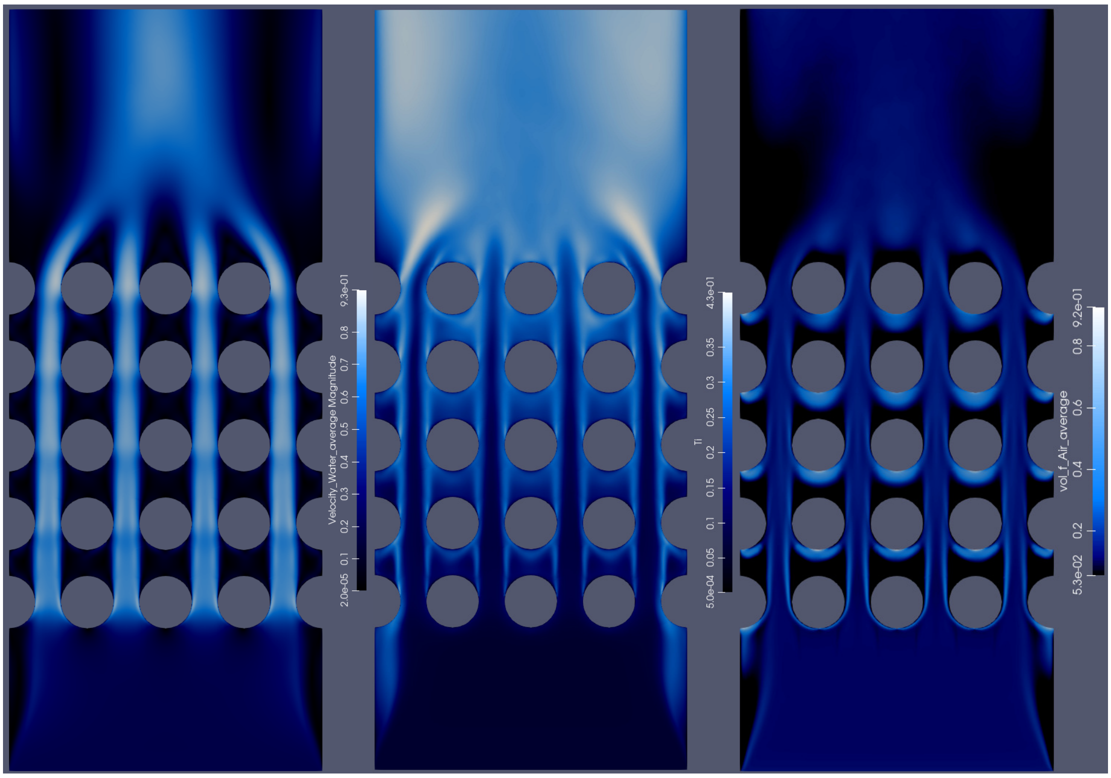

Figure 5.11: Colormap of the time-averaged void fraction (right) , turbulent intensity (midlle) and time-averaged liquid velocity (left) for $Re_l = 5516$ by computing with the model before modifications and Ruyer-Seiler model.

Figure 5.11 illustrates the temporal averages of liquid velocity (left), turbulent intensity (middle), and void fraction (right). It quickly becomes visible that the colormap representations are symmetric, indicating a correct resolution. In the velocity graph (left), there is an acceleration between the cylinders and the forks at the end of the bundle, which results from turbulence. This appears consistent with a single-phase perspective. The graph of turbulent intensity (middle) shows that it increases around the cylinders, with a turbulence intensity of 40%, which is a reasonable order of magnitude compared to single-phase flows in the literature, although there is no direct comparison available for this two-phase case. Regarding the void fraction graph (right), there is an increase in void fraction upstream of the cylinders, similar to the case with a single cylinder. It is also visible that the region corresponding to the cluster observed in the single-cylinder case is constrained by the downstream cylinder. At the outlet of the bundle, the void fraction spreads out, with a preferred zone toward the center of the channel. These observations align with the expected flow topology. However, this is not enough; it is now essential to analyze the force spectra, which serve as our indicators of fluctuating forces.

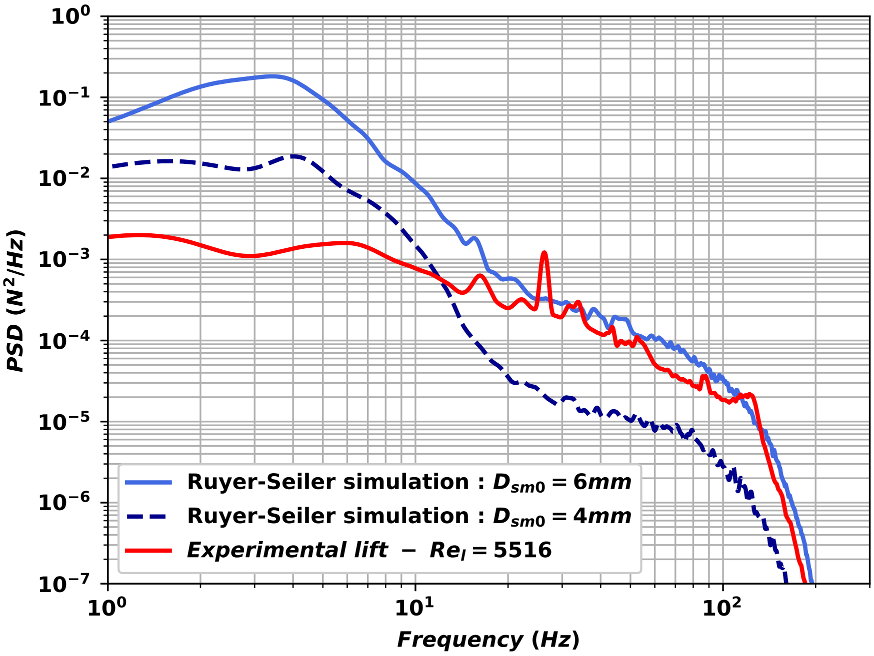

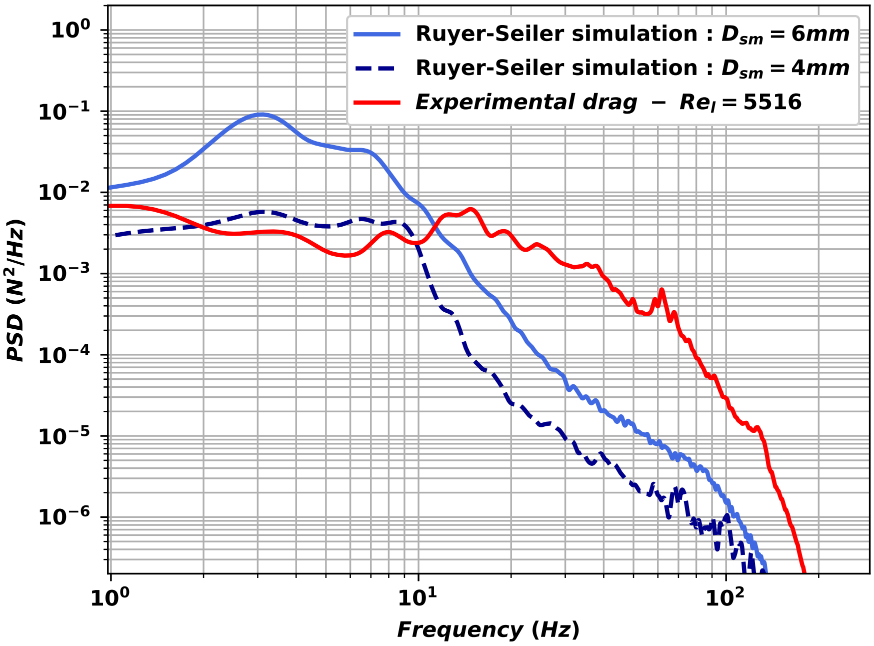

Figure 5.12: Lift (top) and drag (bottom) forces spectra of simulated DIVA for $Re_l = 5516$ with native NEPTUNE_CFD model compared to experimental data.

Figure 5.12 shows the lift and drag force spectra from DIVA experiment and simulations for a liquid Reynolds number of 5516, using the native NEPTUNE_CFD model with injected diameters of 6 mm and 4 mm, in comparison with the experimental data. Looking at the experimental lift spectrum (top), there is a relatively flat distribution between 3 Hz and 10 Hz with two peaks at 1 Hz and 6 Hz, followed by a decrease with a constant slope up to the cutoff frequency. The

two simulated lift spectra have a similar trend with a sharp increase with a bump between 1 Hz and 6 Hz, followed by a decrease up to 20 Hz and a change in slope, continuing to decrease at a constant rate. Thus, they deviate significantly from the experimental lift behavior. Regarding the drag spectrum, the experimental data shows a decrease between 1 Hz and 6 Hz, followed by an increase up to 16 Hz with two peaks at 8 Hz and 16 Hz, then gradually decreasing to 40 Hz before reaching the cutoff frequency. The two simulated drag spectra also exhibit a similar trend with an increase between 1 Hz and 3 Hz, followed by a plateau up to 7 Hz for $D_{sm} = 6$ mm and 9 Hz for $D_{sm} = 4$ mm, before rapidly decreasing to the cutoff frequency. Therefore, these spectra also differ substantially from the experimental ones.
The basic modeling approach does not appear to capture the correct trends of the experimental force spectra. This is one of the reasons that motivated the use and development of a new model.

Now that we have seen that we can qualitatively obtain good results regarding averaged quantities, but that the spectra can be quite different from the experimental spectra, we can return to the study presented in the beginning of the section. This will allow us to quantify the contribution of our modeling compared to what can be obtained by default. To compare with the native model, we first analyze the time-averaged void fraction and liquid velocity fields and see the changes.

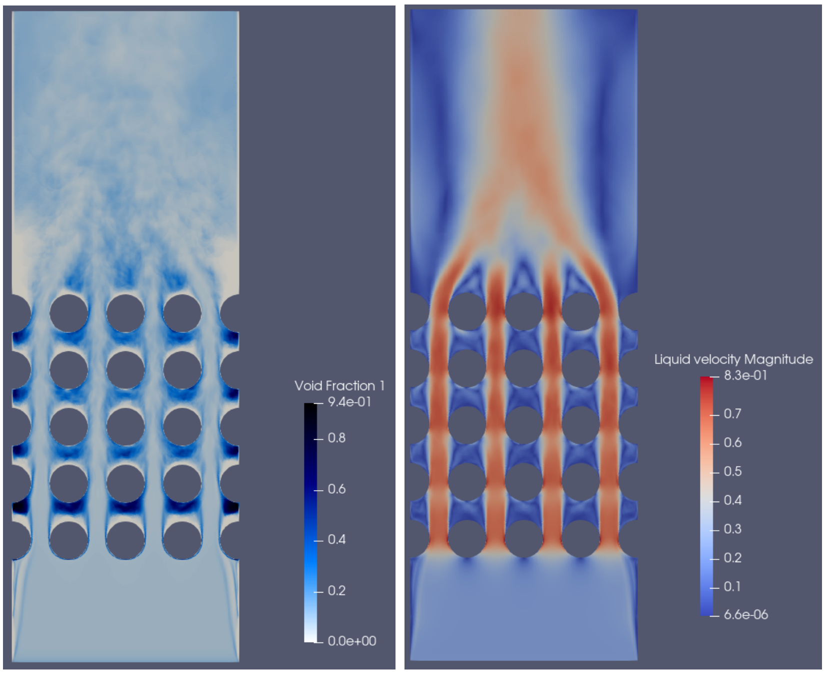

Figure 5.13: Colormap of the time-averaged void fraction (left) and time-averaged magnitude of liquid velocity field (right) for $Re_l = 5516$. Simulation with new TRITON model.

Figure 5.13 shows the colormaps of the time-averaged void fraction (left) and time-averaged magnitude of liquid velocity field (right) for $Re_l = 5516$. It is immediately noticeable that both fields are mostly symmetrical. Looking at the time-averaged void fraction field (left), we can observe nearly the same aspect compared to Figure 5.11 and an increase in void fraction near the walls. However, we can see that the regions behind the cylinders are more spread out and less conforming to the cylinder's shape. There are also remnants of fluctuations related to turbulence. This effect is mainly due to the anisotropy of the turbulent dispersion force, resulting in more fluctuations and a different topology. Now, if we look at the liquid velocity field (right), we can qualitatively see few differences in velocities compared to the basic model, except for wider velocity dispersion between the tubes in our model. So, we have qualitatively similar results, but it appears to take into account more fluctuations. To understand the effect of these fluctuations, we can analyze the force spectra for different liquid Reynolds numbers.

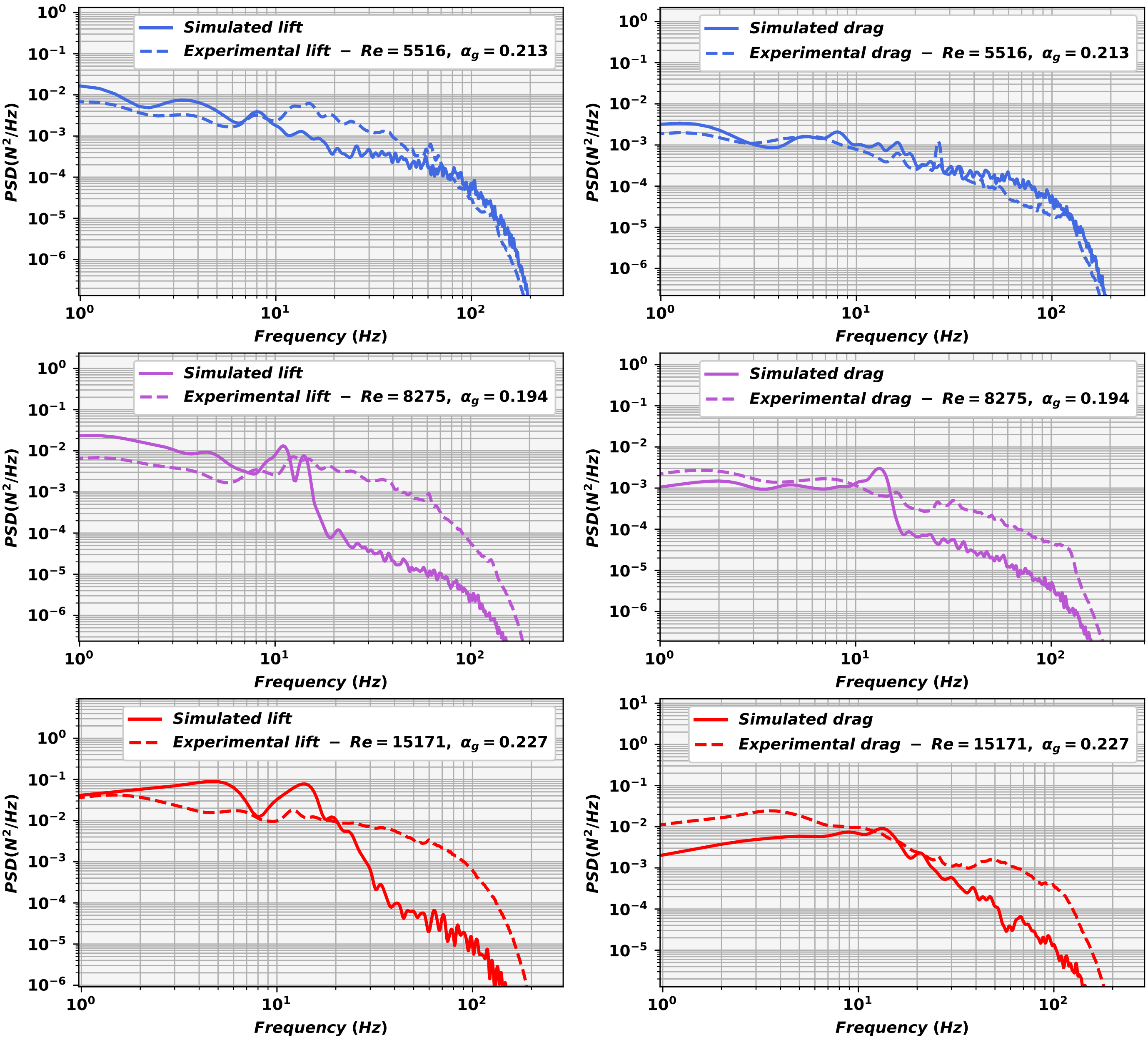

Figure 5.14: Lift (left) and drag (right) force spectra of simulated DIVA for $Re_l = 5516$ (top), $Re_l = 8275$ (middle) and $Re_l = 15171$ (bottom) compared to experimental data. Simulations with new TRITON model.

As a reminder, we concluded in section 5.1.2 that the forces spectra depend on the average liquid velocity in the section at first order. Therefore, it is maybe possible to connect the two-phase simulations with frequencies already observed in the single-phase DIVA cases. To recall, single-phase DIVA simulations were presented in [130]. The author demonstrates the presence of specific reduced inter-tube frequencies $f_r^{inter} = \frac{fD}{3j_l}$ (3 due to restricted area made by the presence of tube) in the simulated force spectra:

- A frequency corresponding to Von Karman phenomena in the drag spectrum at $f_r^{inter} \approx 0.23$.
- A frequency corresponding to confinement between tubes in both spectra at $f_r^{inter} \approx 0.33$.
- A frequency corresponding to mixing phenomena at $f_r^{inter} \approx 0.75$.

Figure 5.14 displays the lift (top) and drag (bottom) spectra of the forces exerted on the central cylinder by the fluid for Reynolds numbers of 5516 (left), 8275 (middle), and 15171 (right), compared to experimental spectra.
Focusing on the lift spectrum for the $Re_l = 5516$ case (top-left), the experimental data decreases between 1 Hz and 10 Hz with three bumps at 1 Hz, 3.1 Hz, and 8 Hz. Since the natural inter-tube frequency is 23.5 Hz, it appears that these two frequencies (3.1 Hz and 8 Hz) could correspond to Von Karman and confinement phenomena. It then shows a new bump between 10 Hz and 20 Hz before gradually decreasing towards the cutoff frequency. The frequency around 10 Hz could correspond to fluctuations related to bubbles since it is not visible in the simulated spectrum. The simulated spectrum exhibits a rather decreasing trend between 1 Hz and 20 Hz with three bumps at 1 Hz, 3.2 Hz, and 8 Hz. This reinforces the hypothesis of Von Karman and confinement, as observed in the simulation. It is mainly flat between 10 Hz and 20 Hz before decreasing towards the cutoff frequency. Therefore, the simulated spectrum closely matches the experimental one, unlike the results obtained with the native model. We had anticipated this behavior by observing the experimental results from DIVA and the simulations with a single cylinder.
To further confirm the validity of the results, it is also important to look at the drag spectrum (top-right). The experimental spectrum is mainly flat between 1 Hz and 10 Hz, with a bumps at 6 Hz, followed by a consistent slope before the cutoff frequency. The simulated spectrum also exhibits a similar flat behavior between 1 Hz and 10 Hz, with two bumps at 6 Hz and 8 Hz. It then decreases with a constant slope before the cutoff frequency. Thus, there is an overall similarity between the simulated behavior and the experimental observations. It appears that, in this case, the modeling has significantly improved the force spectrum acting on the central cylinder.

If we look at the lift spectrum for the $Re_l = 8275$ case (middle-left), the experimental data initially decreases between 1 Hz and 8 Hz. It then increases up to 12 Hz before decreasing towards the cutoff frequency. The simulated spectrum exhibits a decrease between 1 Hz and 8 Hz. Then, two additional bumps can be seen at 10 Hz and 12 Hz before declining towards 20 Hz and decreasing to the cutoff frequency. These frequencies are related to the confinement. Therefore, the simulated spectrum is similar to the experimental one up to 11 Hz. The lack of power in these frequencies likely stems from the turbulence model, which may not account for these scales, or from the URANS aspect, which could admits cutoffs.
To check whether it is indeed a scale cutoff phenomenon and not a modeling deficiency, we can look at the drag spectrum (middle-right). The experimental spectrum is mainly flat between 1

Hz and 10 Hz, with a bump between 7 Hz and 8 Hz. It then decreases with a typically constant slope before the cutoff frequency. The simulated spectrum also displays a relatively flat behavior between 1 Hz and 10 Hz. It then has a peak at 11 Hz (confinement) before rapidly declining to 17 Hz and then decreasing to the cutoff frequency. Again, we observe a behavior similar to the experimental. It seems that, in this case, the modeling is not sufficient to account for fluctuations above 11 Hz to accurately reproduce the lift spectrum or that certain frequencies are favored over others. To conclude on some issues, we can study the higher Reynolds number case.

If we look at the lift spectrum for the $Re_l = 15171$ case (bottom-left), the experimental data mainly decreases towards the cutoff frequency. The simulated spectrum shows an overall flat behavior between 1 Hz and 20 Hz, with two bumps at 4.9 Hz and 14 Hz. It then rapidly declines to 40 Hz before decreasing to the cutoff frequency. Thus, the simulated spectrum closely matches the experimental one up to 20 Hz. While the simulated spectrum is qualitatively comparable to the experimental one, there is a decrease in amplitude towards higher frequencies. This result suggests that lower frequencies are favored by the modeling. Moreover, in this simulation, the effects of confinement, horizontal movements, and Von Karman are amplified, tending to reduce the contribution of smaller scales.
To gain a better understanding of this phenomenon, we can look at the drag spectra (bottom-right). The experimental spectrum is almost flat between 1 Hz and 10 Hz, with a bump at 4 Hz, then decreases with a typically constant slope up to 40 Hz, followed by a peak at 50 Hz before the cutoff frequency. The simulated spectrum increases between 1 Hz and 11 Hz and then decreases up to the cutoff frequency. Except for the peak at 50 Hz, it appears that the simulated spectrum is fairly accurate. It seems reasonable if it is indeed a mixing phenomenon related to bubbles. Therefore, we are missing high-frequency phenomena that likely arise from the modeling, particularly turbulence for the drag.

We observed that in the bubbly regime, similar frequencies to the single-phase case were found, including confinement and Von Karman effects, but we missed phenomena related to fluctuations generated by the bubbles. It would be interesting to model them correctly to verify this. However, we can obtain spectra closer to the experimental one than those in a single cylinder, as anticipated in Chapter 4. To understand where the attenuation of high frequencies in lift and drag comes from, we can study the instantaneous void fraction profiles to understand the differences between Reynolds numbers and the variations in fluctuations.

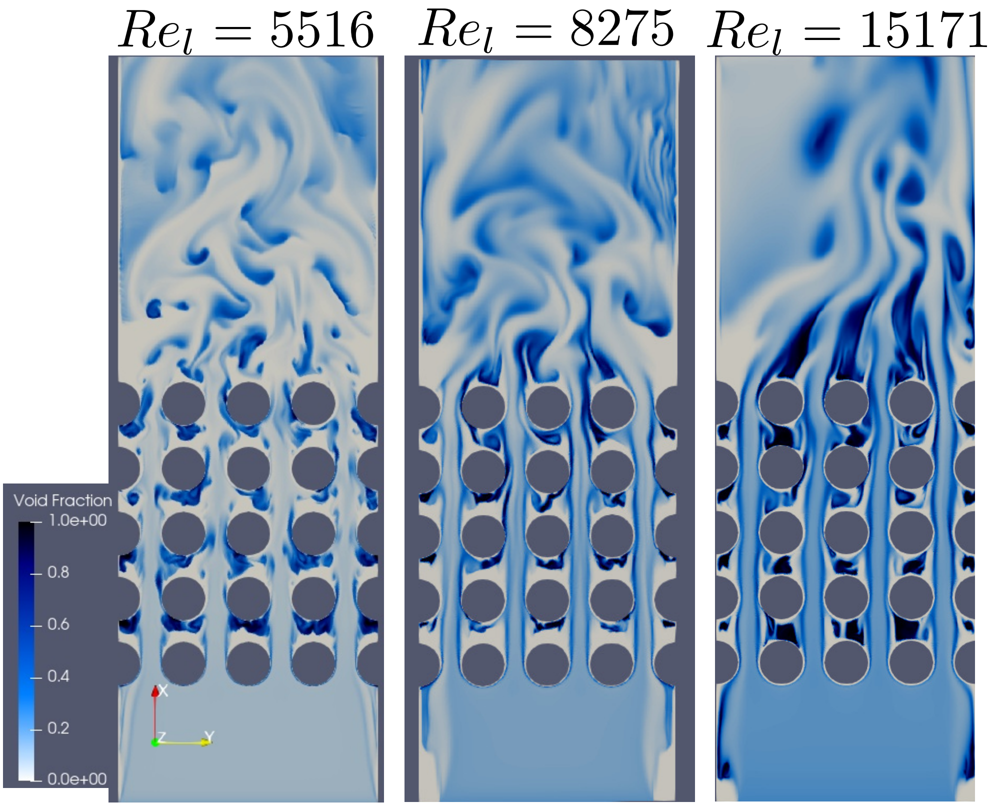

Figure 5.15: Colormap of a typical instantaneous void fraction field in simulated DIVA for $Re_l = 5516$ (left), $Re_l = 8275$ (middle) and $Re_l = 15171$ (right). Simulations with new TRITON model.

Figure 5.15 shows color maps of the instantaneous void fraction for DIVA bubbly simulations at Reynolds numbers of 5516 (left), 8275 (middle), and 15171 (right). Looking at the overall appearance of the simulations, we can observe regions with high void fraction, single-phase regions where gas has difficulty penetrating, and fluctuations. Focusing on the lowest Reynolds number (left), we notice areas of high void fraction at the rear of the cylinders, which can be interpreted as regions where bubbles reside for a longer duration. In this case, the local void fraction is relatively low, around 11%, which tends to emphasize the void fraction fluctuations, potentially resulting in less smoothed fluctuations. There are also phenomena of bubbles passing between rows of tubes and from the rear of one cylinder to another. The fluctuations at the exit of the bundle are relatively dispersed compared to the regions around the cylinders.

If we look at the intermediate Reynolds number (middle), we notice a less pronounced slip between phases because the local void fraction is higher due to the higher velocity. This results in fluctuations that have less impact, especially during the transitions between the cylinders. We also observe less void fraction at the rear of the cylinders compared to the other Reynolds number, which can explain the lower high-frequency components in the drag, as they are weaker, and the lift is smoothed by the smaller void fraction variation. At the exit of the bundle, we can see more concentrated regions at the rear, indicating turbulent shear and less slip.

If we look at the case of the highest Reynolds number (right), we observe even less slip between the phases, resulting in a local void fraction close to 20%. This leads to even more concentrated areas. There is a protective zone around the cylinder due to wall lubrication force but not causing damage to forces spectra. Additionally, there is a highly spread high void fraction zone at the rear of the cylinders, which induces strong lift fluctuations during horizontal void fraction variations, leading to more intense lift peaks. Furthermore, the high void fraction zones, which do not have fluctuations associated with the gas phase, may explain the lack of high frequencies, as the fluctuations are smoothed out by the strong presence of gas. At the exit of the bundle, there is a very strong presence of gas, including a deviation of the jet due to the horizontal movement of bubbles, causing instability in random directions.

We can conclude that the modeling is relatively accurate in partially reproducing the force spectra acting on the central tube. Especially compared to the model before modifications, and with Ruyer-Seiler model, we have significantly improved the simulated spectra. However, there is room for improvement to better account for certain effects that are either too smoothed out or overly emphasized in our case. One area for improvement could involve better management of slip effects, especially when slip is relatively low at high velocities. With more slip, there would be a greater influence of void fraction fluctuations relative to the local mean field. Furthermore, a more accurate modeling of bubble-induced turbulence, especially around the cylinders, could help capture fluctuations related to the gas phase more effectively, like mixing phenomena. As shown in the previous chapter, the current modeling of bubble-induced turbulence is too intense, creating areas of high fluctuations around the stagnation point and excessive smoothing in regions where turbulence should be present due to its overly high level.

Since regions with high void fractions tend to smooth out fluctuations, we are interested in test cases where large bubbles and gas pockets are present. Additionally, due to our limited estimates of bubble diameters, we can only focus on a limited number of test cases. Therefore, in the following section, we aim to study the topology created by our second gas field and the spectra it induces in cap-bubbly and churn flow cases.

5.2.3 Cap-bubbly and churn flow simulations

The previous section helped identify the liquid Reynolds number and the void fraction as important parameters influencing force spectra. Therefore, in this section, we aim to replicate the Reynolds number effect in bubbly cases. Indeed, experimental comparisons can be conducted using the collected data and the estimated inlet conditions presented in the previous section. We investigate three Reynolds number cases: 2758, 5516, and 8275, for approximately homogeneous void fractions of around $0.65-0.68$. Table 5.3 summarizes the conditions of the test cases studied.

Re_l	j_l (m/s)	j_g (m/s)	α_{gH}
2758	0.0926	0.184	0.665
5516	0.185	0.409	0.688
8275	0.278	0.528	0.655

Table 5.3: Table of the conditions of the study.

Table 5.4 provides the results of direct measurements of the Sauter diameter and local void fraction, along with an estimation of the local void fraction for Group 1. Table 5.5 presents the calculated injection conditions using the method outlined in the previous section.

$D_{sm}^{measured}$ (mm)	$\alpha_g^{measured}$	$\alpha_{g1}^{estimated}$
6.97	0.345	0.196
7.58	0.463	0.279
7.8	0.538	0.284

Table 5.4: Table of the operating conditions of the study.

$\alpha_{g1inj}^{computed}$	$\alpha_{g2inj}^{computed}$	$D_{sm1inj}^{computed}$ (mm)	$D_{sm2inj}^{computed}$ (mm)
0.437	0.228	4.8	39
0.339	0.349	5.4	49
0.25	0.415	5.3	35

Table 5.5: Table of the operating conditions of the study.

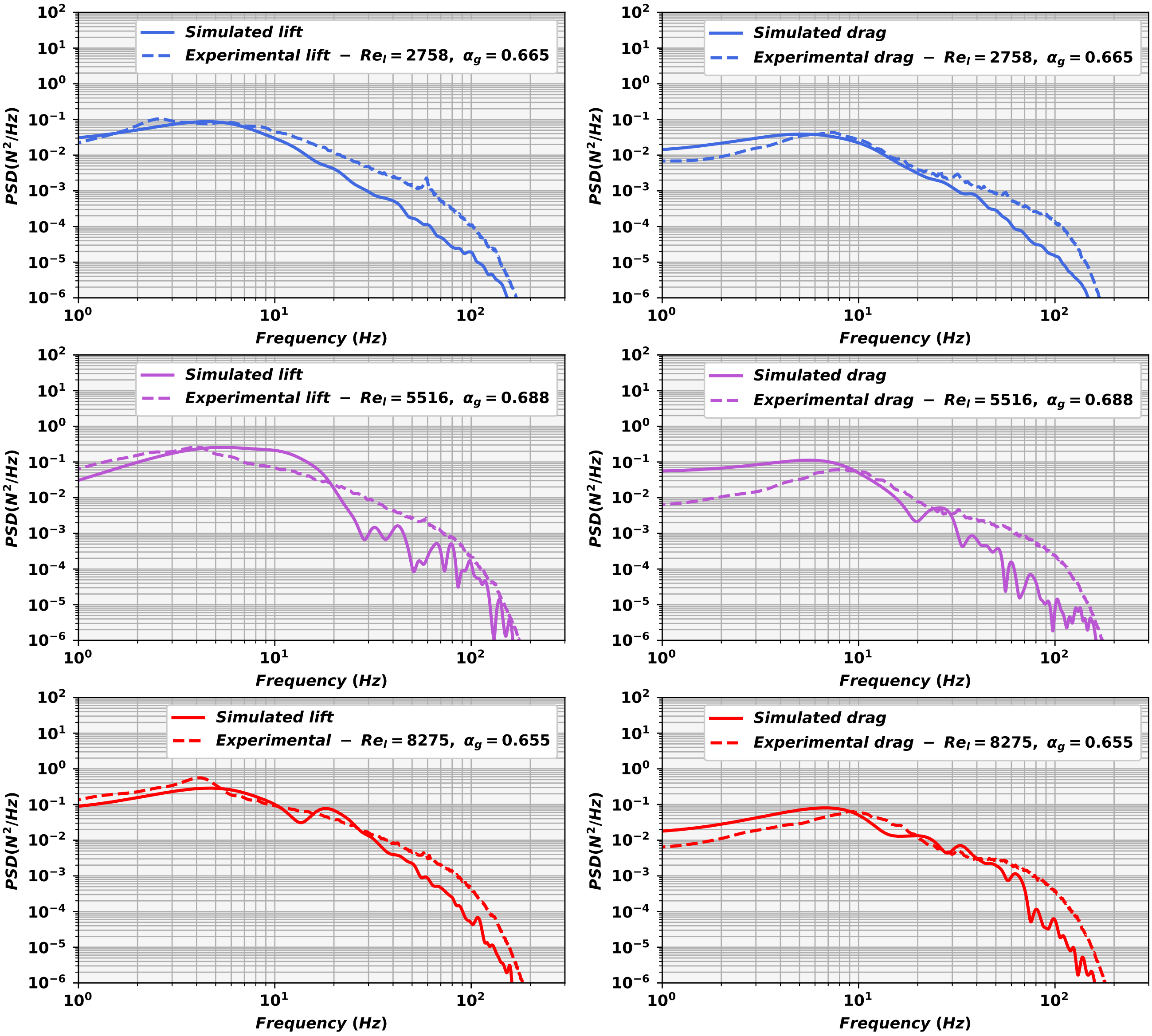

Figure 5.16: Lift (left) and drag (right) force spectra of simulated DIVA for $Re_l = 2758$ (top), $Re_l = 5516$ (middle) and $Re_l = 8275$ (bottom) compared to experimental data. Simulations with new TRITON model.

Figure 5.16 shows the spectra of drag forces (bottom) and lift forces (top) for simulations with Reynolds numbers of 2758 (left), 5516 (middle), and 8275 (right), compared to experimental data.

Looking at the lift graph for the Reynolds number of 2758 (top-left), the experimental spectrum exhibits an almost constant trend between 1 Hz and 8 Hz, followed by a decrease up to the cutoff frequency. The simulation exhibits a slight increase between 1 Hz and 6 Hz, followed by a decrease until the cutoff frequency. This demonstrates a qualitatively similar behavior to the experimental data. Even the standard deviation of the lift (area under the curve) seems well reproduced.
Regarding the experimental drag spectrum (top-right), we observe an increase between 1 Hz

and 7 Hz and then a decrease towards the cutoff frequency. The simulated spectrum exhibits an increase between 1 Hz and 6 Hz, followed by a decrease until the cutoff frequency. Similar to the lift, we obtain a good simulated graph compared to experimental data. This behavior could be attributed to a better reproduction of the topology around the cylinder and the presence of the second group of bubbles.

Looking at the lift graph for the Reynolds number of 5516 (middle-left), the experimental spectrum shows an increase between 1 Hz and 4 Hz followed by a decreasing trend with a constant slope up to the cutoff frequency. In contrast, the simulated spectrum increases between 1 Hz and 4 Hz, then has a flat trend up to 11 Hz before decreasing. It seems that we can get parts of the distribution. This is due to too short simulation due to numerical problems.
Similarly, if we look at the experimental drag spectrum (bottom-right), we observe an increase between 1 Hz and 10 Hz, followed by a decreasing trend up to the cutoff frequency. The simulated graph shows a slightly increasing trend between 1 Hz and 6 Hz, then decreases up to the cutoff frequency. This shows that even though we do not have enough simulated time, we still find a good agreement between the simulation and the experimental behavior, and that our model works quite well.

If we look at the experimental lift spectrum for the Reynolds number of 8275 (bottom-left), we observe an increase between 1 Hz and 4 Hz, followed by a decrease towards the cutoff frequency. The simulation shows a slight increase between 1 Hz and 6 Hz, followed by a decrease up to the cutoff frequency, with a small bump at 20 Hz.
Examining the corresponding drag spectrum (bottom-right), the experimental data reveal an increase between 1 Hz and 10 Hz, followed by a decrease up to the cutoff frequency. In contrast, the simulated graph increases between 1 Hz and 8 Hz, then decreases up to the cutoff frequency. Consequently, this simulation has better reproduced the random force spectra than in the corresponding Re_l in bubbly flow.

An intriguing observation is that the simulations gave good results with a very rough approximation of the group 2 diameter and a lot of approximations for the distribution of void fraction. This suggests that the presence of the second group of bubbles has a significant positive impact on the accuracy of the simulation. It seems that the simulation is not that sensitive to the value of D_{sm2}, a phenomenon suggested on the experimental graphs. It surprisingly appears that spectra from bundle geometries are easier to get that the one from single tube. Indeed, the bundle mix well the simulations, the velocities before and behind the tubes are smaller, without stagnation point, and it seems that it also depends less on the prediction of the turbulent quantities. However, there is room for improvement. To identify the changes that may be necessary we can look at void fraction predictions.

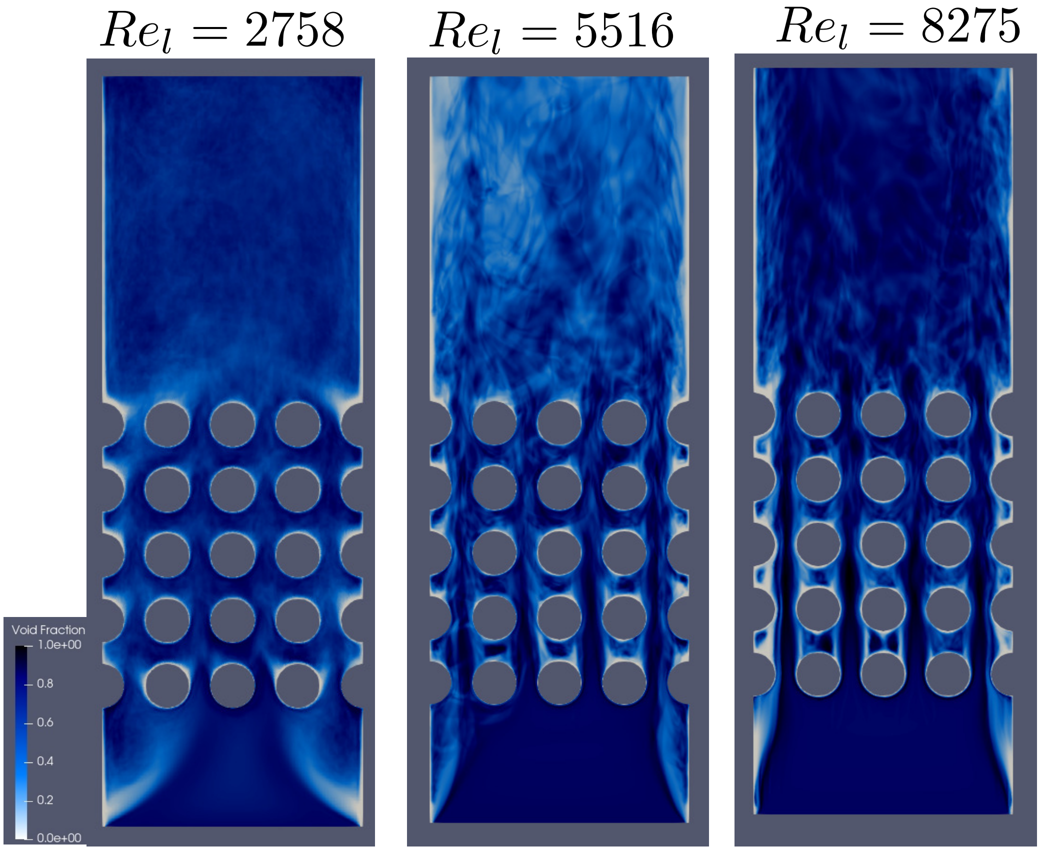
$Re_l = 2758$ $Re_l = 5516$ $Re_l = 8275$

Figure 5.17: Colormap of the averaged void fraction in simulated cap/churn DIVA for $Re_l = 2758$ (left), $Re_l = 5516$ (middle) and $Re_l = 8275$ (right). Simulations with new TRITON model.

Figure 5.17 depicts the averaged void fraction in a simulated cap/churn single-tube experiment for three different Reynolds numbers: $Re_l = 2758$ (left), $Re_l = 5516$ (middle), and $Re_l = 8275$ (right). In the case of the lowest Reynolds number (left), we observe detachment at the channel inlet due to the presence of group 2 bubbles. We observe a good symmetry of the computation. The asymmetries are primarily attributed to the averaging time step and the overall averaging time used to generate this figure. Qualitatively, we observe experimental characteristics of intermittent regimes: the void fraction is distributed very uniformly throughout the bundle. A detailed analysis of the distribution between the two gas fields will shed light on this phenomenon. We encounter nearly monophasic regions, largely due to lubrication forces. However, in this case, it does not seem to degrade the results for the force spectra. Additionally, unlike in bubbly flow, at the exit of the bundle, there is no longer evidence of intermittent alleys in the prediction of the averaged void fraction. Turning our attention to the other two cases with higher liquid Reynolds numbers, but equivalent void fractions, we observe the same phenomena: a homogeneous distribution of void fraction, detachment at the inlet, and the disappearance of balanced jet effects at the bundle exit. It seems that the distribution is then not sensitive to the injected diameter of group 2 and the distribution between the two groups.

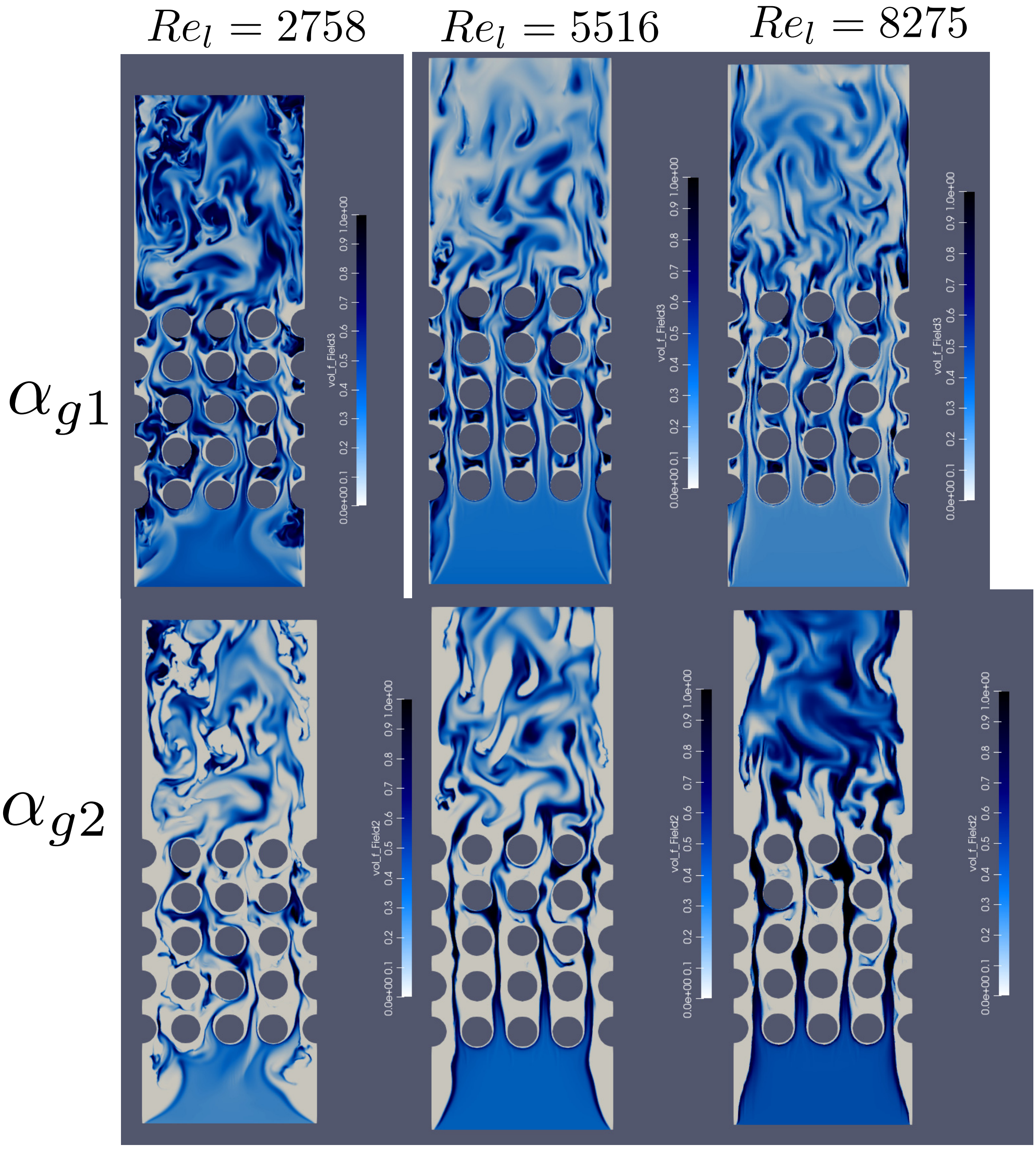

Figure 5.18: Colormap of the typical instantaneous void fraction fields, for group 1 α_{g1} and group 2 α_{g2}, from simulated cap/churn DIVA for $Re_l = 2758$ (left), $Re_l = 5516$ (middle) and $Re_l = 8275$ (right). Simulations with new TRITON model.

Figure 5.18 illustrates the instantaneous void fraction of group 1 (top) and group 2 (bottom) in simulated cap/churn tube bundle experiment DIVA for $Re_l = 2758$ (left), $Re_l = 5516$ (middle) and $Re_l = 8275$ (right). In the case of the lowest liquid Reynolds number (left), when we look at the group 1 field (top-left), we observe a much larger number of dynamic zones compared to bubbly flow, primarily due to the presence of group 2 bubbles. We also notice the absence of alleys at the bundle exit, similar to the average void fraction distribution. In the group 2 field, we observe that the LIM is rarely activated in the calculation, except at the bundle exit. We observe a narrowing of the jet at the entrance, similar to bubbly flow, followed by a concentration of the field towards the center between the cylinders, with a deviation to a horizontal flow. However, it is challenging to provide qualitative validation for this field in this case.

In the case of intermediate Reynolds numbers (middle) and the group 1 field (top-middle), we can qualitatively observe behavior similar to that of bubbly regimes. We see zones of strong presence behind the cylinders, but the exit jets appear to be less prominent. This is likely why the average void fraction does not capture this effect. Turning to the group 2 bubble field, we observe a more moderate narrowing of the jet at the entrance and fewer horizontal deviations between the cylinders, likely due to the strong presence of group 1 bubbles in these areas. Here, we notice the LIM activating between the cylinders, creating jets that are subsequently dispersed at the bundle exit. It appears that improvements are needed to better account for interactions between the LIM and the walls in order to accurately represent the jet width. However, despite vastly different topologies compared to the lowest Reynolds case, we obtain, on average, the same result for the void fraction, but achieve better results for the force spectra. To confirm the model's behavior when there are many group 2 bubbles, we can look at the last case.

Now, turning our attention to the case with the highest Reynolds number (right), especially in the context of the group 1 field (top-right), we still observe behavior similar to that of bubbly flow, but with confined jets at the bundle exit. In contrast, when we look at the group 2 bubble field (bottom-right), we see that the field is well-balanced, primarily because it is the dominant group. It is worth noting that the LIM predominantly activates between the cylinders and is subsequently dispersed at the bundle exit. This behavior is qualitatively interesting because it suggests that outside the bundle, we switch to a less dynamic regime with an average void fraction that does not lead to an annular flow pattern. Thus, it appears that the model is behaving correctly.

In summary, the force spectra in the lift and drag directions are reasonably well reproduced compared to experiments, for bubbly and cap/churn flows. Indeed, despite the complexity of the modeling, the URANS aspect, and the poor results obtained with a single cylinder we have a model able to reproduce the global trends of forces spectra. Additionally, the averaged distribution of void fraction aligns with experimental observations. It is obvious that for this regime, we can achieve very similar averages, but encounter rather different dynamic behaviors depending on the liquid Reynolds number. Interestingly, the diameter of the group 2 bubbles appears to have little influence on the response of random forces. It is worth noting that the presence of the second group of bubbles has improved the force spectra, likely due to a more even distribution of void fraction in group 1, which is influenced by the presence of group 2. This underscores the value of our modeling approach in replicating force spectra in two-phase water-air flows. Nevertheless, there are still areas where improvements are possible:

- Improving validation of the interaction between the LIM and the walls appears necessary to better account for annular regions between the cylinders.
- Further work is required to identify the appropriate injection parameters for achieving an annular flow regime, as the experimental data do not provide a clear definition for the required input conditions.

Conclusion and perspectives

In this thesis, our focus has been on developing a modeling approach that aligns with experimental data to replicate drag and lift force spectra on the central cylinder of a tube bundle. Our research encompassed the consistency of turbulence modeling and involved comparisons of different models in vertical channel configurations. Notably, we highlighted the successful reproduction of void fraction and liquid velocity trends, especially near the walls, using the EBRSM [77] and turbulence induced by bubbles. After observing modeling challenges, particularly for high void fractions, we tried to modify and adapt source terms in the IATE 2 groups [121] to enhance simulation stability and coherence while preserving physical consistency. This allowed for a better consideration of both bubble groups and regions with high void fractions. We also investigated the coupling forces between gas and liquid fields to address modeling issues associated with high void fractions. Changes in the drag coefficient and the transition from the Zuber [90] added mass model to the Cai and Wallis model [6] proved necessary. We proposed a new coefficient for turbulent dispersion force [64], along with its anisotropy adjustment, to accurately account for regions with high void fractions. Due to numerical challenges in simulating scenarios with high void fractions and a significant proportion of group 2 bubbles, we introduced an original modeling approach for group 2 bubbles to address these issues. Specifically, increasing the added-mass coefficient better accounted for the inertia of deformed bubbles, leading to reduced activation of the LIM [16] and enhanced diffusion in the second-group bubble diameter equation. We also attempted to justify the use of some experimental limits for flow regimes and bubble group distributions through simple calculations and the consideration of turbulent dispersion, aiming to support our modeling approach. Theoretical justifications were provided for limiting void fractions of 0.62, 0.33, and 0.8, commonly found in models based on correlations. Additionally, we initiated changes in the modeling approach to replicate experiments involving water-steam mixtures, aiming for a better understanding of the differences compared to the water-air cases.

We subsequently studied a single-tube configuration to assess the relevance of experimental results and identify key parameters. This investigation revealed that the liquid Reynolds number and void fraction were the most influential parameters. We then simulated experimental cases using the new model, encompassing bubbly and churn/cap-bubbly regimes, with liquid Reynolds numbers ranging from 7500 to $30,000$ and void fractions around 0.2 and 0.65. We encountered challenges with this configuration due to containment effects and the model's sensitivity to equilibrium conditions around the cylinder. Nonetheless, our simulations demonstrated that the model could replicate experimental topologies, though it appeared to lack in modeling for induced turbulence by group 1 bubbles and exhibited near-wall problems, particularly around the stagnation point. However, we achieved a more robust modeling approach for obtaining force spectra, and it was possible to qualitatively obtain good power distributions.

Nevertheless, obtaining the standard deviation of these forces proved to be more challenging. Furthermore, our investigations highlighted that churn/cap-bubbly flow cases could yield quantitatively better results because group 1 was constrained by group 2. This phenomenon was particularly pronounced with the significant presence of group 2 and liquid injection velocities high enough to balance the dynamics between the two groups. In conclusion, we identified potential improvements related to a better consideration of void fraction effects on drag and lift coupling forces, as well as the embodiment of a new force or coefficient modification to enhance the dynamic balance between the two gas fields in the model.

Finally, we turned our attention to the simulation of DIVA. We proposed a simplistic method for identifying flow regimes and void fraction distributions between the two bubble groups to obtain the distribution of void fractions between the two groups to be injected and, in some cases, bubble diameters for both groups. Using this method, we successfully replicated the characteristic void fractions associated with different flow regimes. These results were compared to those calculated in Chapter 3 to validate our approach. Furthermore, our investigation highlighted key parameters, particularly the liquid Reynolds number and void fraction, as significant factors, as discerned from the study of force spectra. It is noteworthy that, in the case of DIVA, void fraction behavior appears more 'linear' in spectra compared to the single-cylinder configuration. Additionally, a distinct behavior in the lift spectrum was identified for the annular and bubbly flow regimes. Subsequently, we conducted simulations in bubbly and churn/cap-bubbly regimes for injection liquid Reynolds numbers ranging from 2700 to 8200, with void fractions around 0.2 and 0.66. These simulations demonstrated that achieving quantitatively accurate spectra is easier with a bundle of tubes than with a single cylinder. This can be attributed to the containment effects imposed by the cylinders, which result in a more complex topology. The lower impact of turbulence effects in regions with relatively low velocities, such as the front and rear of the cylinders, contributes to this improvement. Thus, our modeling approach proved to be interesting, yielding promising qualitative and quantitative results for force spectra and void fraction distributions. However, areas for improvement were also identified, particularly concerning the LIM. It is imperative to conduct a more detailed investigation into the interaction between LIM and the walls to validate its relevance. The model appears to encounter difficulties in accurately representing the size of the annular regions between the cylinders. This is one of the reasons why we did not present calculations for purely annular flow. The other reason lies in the uncertainty surrounding how to inject the bubble field to faithfully reproduce this regime and the large interfaces it entails. Ultimately, despite the extensive modeling, the URANS aspect of the model, we have achieved encouraging and promising results. Nevertheless, there is a continued need for improvement, particularly in accounting for the interactions between the liquid and gas phases, with the aim of developing a model able to simulate two-phase flows involving water and steam.

This thesis has also brought to light suspended issues related to two-phase modeling, as well as potential challenges in forthcoming comparisons.
First, one could consider the broader development of a lubrication force applicable across all void fractions and flow topologies. In a general sense, it would be insightful to compare and validate force modeling for extremely high void fractions, particularly drag and lift forces. Connected to this issue, a more precise study and comparison involving model bubbles, such as the Taylor bubble, for interfacial force modeling, would hold significant interest for the overall modeling, especially the LIM interacting with walls.
In terms of additional modeling, it is of paramount importance to conduct a comprehensive investigation into the averaged two-phase turbulence, in order to accurately capture the under-

lying mechanisms. Furthermore, a more in-depth study than the one proposed in this thesis would be valuable in enhancing our understanding and inclusion of the complete theoretical mechanisms leading to the transition into a continuous modeling framework.

From the perspective of experimental validation, it remains imperative to both verify and better modeling at extremely high void fractions, applicable to both channels and bundles. Indeed, the scarcity of literature on these void fraction levels can be attributed to challenges in instrumentation and the determination of parameters required for accurate simulation of such regimes. Following an investigation into the square pitch bundle configuration, like DIVA experiment, there arises an opportunity to study a triangular pitch configuration, which could lead to similar issues as in the single-cylinder case (especially with the stagnation points). This exploration holds promise for a more comprehensive understanding of the underlying phenomena. Moreover, triangular pitch configurations should replace square pitch bundles in future steam generators (EPR).

Ultimately, it becomes imperative to couple the two-phase model with a method that takes into account the solid movement, in order to validate the physics in the context of a vibrating tube. We attempted to numerically compute the mechanical loading exerted by a two-phase flow on a rigid tube in a square pitch bundle. To compute DIVA, simulations will need to consider tube vibrations, thus implementing a coupling model between the structure and the fluid, as a complete fluid-structure problem. This expanded approach holds the potential better understand and model the vibrations of U tubes in steam generators.

Appendix A

Appendice : Additional modeling

A.1 Additional turbulence models

The $k-\varepsilon$ model

The $k-\varepsilon$ model [47] is given by the following set of equations :

$$\begin{gathered}
\frac{\partial k}{\partial t}+\overline{U_i}\frac{\partial k}{\partial x_i}=\frac{\partial}{\partial x_i}[(\nu+\frac{\nu_t}{\sigma_k})\frac{\partial k}{\partial x_i}]+P-\varepsilon \\
\frac{\partial \varepsilon}{\partial t}+\overline{U_i}\frac{\partial \varepsilon}{\partial x_i}=\frac{\partial}{\partial x_i}[(\nu+\frac{\nu_t}{\sigma_\varepsilon})\frac{\partial \varepsilon}{\partial x_i}]+C_{\varepsilon 1}P\frac{\varepsilon}{k}-C_{\varepsilon 2}\frac{\varepsilon^2}{k} \\
P=2\nu_t S_{ij}S_{ij} \\
\nu_t=C_\mu\frac{k^2}{\varepsilon} \\
S_{ij}=\frac{1}{2}(\frac{\partial\overline{U_i}}{\partial x_j}+\frac{\partial\overline{U_j}}{\partial x_i}) \\
C_\mu=0.09,\ \sigma_k=1,\ C_{\varepsilon 1}=1.44,\ C_{\varepsilon 1}=1.92,\ \sigma_\varepsilon=1.3
\end{gathered} \tag{A.1}$$

The SSG model

The SSG [9] model is given by the following set of equations :

$$
\begin{aligned}
\frac{\partial R_{ij}}{\partial t} + \overline{U_k}\frac{\partial R_{ij}}{\partial x_k} &= \phi_{ij} + P_{ij} - \frac{2}{3}\varepsilon\delta_{ij} + D^{p}_{ij} + \nu\frac{\partial^2 R_{ij}}{\partial x_k x_k} \\
\frac{\partial \varepsilon}{\partial t} + \overline{U_i}\frac{\partial \varepsilon}{\partial x_i} &= \frac{\partial}{\partial x_i}[\nu\frac{\partial \varepsilon}{\partial x_i}] + C_{\varepsilon 1}P\frac{\varepsilon}{k} - C_{\varepsilon 2}\frac{\varepsilon^2}{k} + \frac{\partial}{\partial x_i}(C_\varepsilon\frac{k}{\varepsilon}R_{il}\frac{\partial \varepsilon}{\partial x_l}) \\
P_{ij} &= -(R_{ik}\frac{\partial U_j}{\partial x_k} + R_{jk}\frac{\partial U_i}{\partial x_k}) \\
D^{P}_{ij} &= \frac{\partial}{\partial x_k}(C_s\frac{k}{\varepsilon}R_{kl}\frac{\partial R_{ij}}{\partial x_l}) \\
\phi_{ij} =& \phi_{ij,1} + \phi_{ij,2} + \phi_{ij,w} \\
\phi_{ij,1} =& -C_1\frac{\varepsilon}{k}(R_{ij} - \frac{2}{3}\delta_{ij}k) \\
\phi_{ij,2} =& -C_2((P_{ij} - \overline{U_k}\frac{\partial R_{ij}}{\partial x_k}) - \frac{1}{3}\delta_{ij}(P_{ij} - \overline{U_k}\frac{\partial R_{ij}}{\partial x_k}))
\end{aligned}
$$

$$
\phi_{ij,w} = \frac{C_{mu}^{3/4}k^{3/2}}{\kappa\varepsilon D_w}(C'_1\frac{\varepsilon}{k}(R_{km}n_kn_m\delta_ij - \frac{3}{2}R_{ik}n_jn_k - \frac{3}{2}R_{jk}n_in_k) + C'_2(\phi_{km,2}n_kn_m - \frac{3}{2}\phi_{ik,2}n_jn_k - \frac{3}{2}\phi_{jk,2}n_in_k))
$$

$$
\begin{gathered}
S_{ij} = \frac{1}{2}(\frac{\partial\overline{U_i}}{\partial x_j} + \frac{\partial\overline{U_j}}{\partial x_i}) \\
C_\mu = 0.09,\ C_\varepsilon = 0.18,\ C_{\varepsilon 1} = 1.44,\ C_{\varepsilon 1} = 1.92,\ C_1 = 1.8,\ C_2 = 0.6,\ C_3 = 0.55, \\
C_s = 0.22,\ C'_1 = 0.5,\ C'_2 = 0.3,\ \kappa = 0.418
\end{gathered}
\tag{A.2}
$$

A.2 Bubble coalescence/break-up source terms

Random collision (RC)

The source/sink terms of Random Collision (RC) are modeled as follows :

$$
\phi^{(1)}_{RC} = -0.17C^{(1)}_{RC}\lambda^{(1)}_{RC}\frac{\varepsilon^{1/3}\alpha_{g1}a_{i1}^{5/3}}{\alpha_{g1,max}^{1/3}\left(\alpha_{g1,max}^{1/3} - \alpha_{g1}^{1/3}\right)}\left[1 - \exp\left(-C_{RC1}\frac{\alpha_{g1,max}^{1/3}\alpha_{g1}^{1/3}}{\alpha_{g1,max}^{1/3} - \alpha_{g1}^{1/3}}\right)\right], \tag{A.3}
$$

$$
\phi^{(11,2)}_{RC,2} = 4.1C^{(1)}_{RC}\lambda^{(1)}_{RC}\frac{\varepsilon^{1/3}\alpha_{g1}a_{i1}^{5/3}}{\alpha_{g1,max}^{2/3}}\left[1 - \exp\left(-C_{RC1}\frac{\alpha_{g1,max}^{1/3}\alpha_{g1}^{1/3}}{\alpha_{g1,max}^{1/3} - \alpha_{g1}^{1/3}}\right)\right]\left(1 - \frac{2}{3}D^*_{c1}\right), \tag{A.4}
$$

$$
\phi^{(12,2)}_{RC,1} = -1.14C^{(12,2)}_{RC}\lambda^{(12,2)}_{RC}\varepsilon^{1/3}\alpha_{g1}^{2/3}\alpha_{g2}^{4/3}a_{i1}a_{i2}^{2/3}\left[1 - \exp\left(-C_{RC1}\frac{\alpha_{g1,max}^{1/3}\alpha_{g1}^{1/3}}{\alpha_{g1,max}^{1/3} - \alpha_{g1}^{1/3}}\right)\right], \tag{A.5}
$$

$$
\phi^{(12,2)}_{RC,2} = 1.80C^{(12,2)}_{RC}\lambda^{(12,2)}_{RC}\varepsilon^{1/3}\alpha_{g1}^{5/3}\alpha_{g2}^{1/3}a_{i2}^{5/3}\left[1 - \exp\left(-C_{RC1}\frac{\alpha_{g1,max}^{1/3}\alpha_{g1}^{1/3}}{\alpha_{g1,max}^{1/3} - \alpha_{g1}^{1/3}}\right)\right], \tag{A.6}
$$

$$
\phi^{(2)}_{RC} = -95.7C^{(2)}_{RC}\lambda^{(2)}_{RC}\varepsilon^{1/3}\frac{\alpha_{g2}^{7/3}}{D_h^2}\frac{1}{a_{i2}^{1/3}}\left[1 - \exp\left(-C_{RC2}\alpha_{g2}^{1/2}\right)\right]\left(1 - 0.37D^{*3}_{c2}\right), \tag{A.7}
$$

$$\eta_{RC,2}^{(11,2)} = 3.15 C_{RC}^{(1)} \lambda_{RC}^{(1)} \frac{\varepsilon^{1/3} \alpha_{g1}^2 a_{i1}^{2/3}}{\alpha_{g1,max}^{2/3}} \left[1 - \exp\left(-C_{RC1} \frac{\alpha_{g1,max}^{1/3} \alpha_{g1}^{1/3}}{\alpha_{g1,max}^{1/3} - \alpha_{g1}^{1/3}} \right) \right] \left(1 - \frac{2}{3} D_{c1}^{*} \right), \quad (A.8)$$

$$\eta_{RC,2}^{(12,2)} = 1.44 C_{RC}^{(12,2)} \lambda_{RC}^{(12,2)} \varepsilon^{1/3} \alpha_{g1}^{5/3} \alpha_{g2}^{4/3} a_{i2}^{2/3} \left[1 - \exp\left(-C_{RC1} \frac{\alpha_{g1,max}^{1/3} \alpha_{g1}^{1/3}}{\alpha_{g1,max}^{1/3} - \alpha_{g1}^{1/3}} \right) \right]. \quad (A.9)$$

$\lambda_{RC}^{(1)}$, $\lambda_{RC}^{(12,2)}$, $\lambda_{RC}^{(2)}$ are defined as follows:

$$\lambda_{RC}^{(1)} = \exp\left(-C_{RC0} \frac{D_{sm1}^{5/6} \rho_l^{1/2} \varepsilon^{1/3}}{\sigma^{1/2}} \right), \quad (A.10)$$

$$\lambda_{RC}^{(2)} = \exp\left(-C_{RC0} \frac{D_{sm2}^{5/6} \rho_l^{1/2} \varepsilon^{1/3}}{\sigma^{1/2}} \right), \quad (A.11)$$

$$\lambda_{RC}^{(12,2)} = \lambda_{RC}^{(2)}. \quad (A.12)$$

In the above equations, $C_{RC}^{(1)}$, $C_{RC}^{(12,2)}$, $C_{RC}^{(2)}$ are three constant coefficients. C_{RC1}, C_{RC2} are coefficients accounting for effective range of influence of turbulent eddies. $\alpha_{g1,max}$ is the dense packing limit for Group 1 bubbles. D_h is the hydraulic diameter. C_{RC0} is a constant coefficient.

- $C_{RC}^{(1)} = 0.005$, $C_{RC}^{(12,2)} = 0.005$, $C_{RC}^{(2)} = 0.01$.
- $C_{RC1} = 3.0$, $C_{RC2} = 3.0$.
- $\alpha_{g1,max} = 0.62$.
- $C_{RC0} = 3.0$.

Wake entrainment (WE)

The source/sink terms of Wake Entrainment (WE) are modeled as follows :

$$\phi_{WE}^{(1)} = -0.17 C_{WE}^{(1)} C_{D1}^{1/3} U_{r1} a_{i1}^2, \quad (A.13)$$

$$\phi_{WE,2}^{(11,2)} = 2.57 C_{WE}^{(11,2)} C_{D1}^{1/3} U_{r1} a_{i1}^2 \left(1 - \frac{2}{3} D_{c1}^{*} \right), \quad (A.14)$$

$$\phi_{WE,l1}^{(12,2)} = -0.33 C_{WE}^{(12,2)} U_{w12} a_{i1} a_{i2}, \quad (A.15)$$

$$\phi_{WE,g2}^{(12,2)} = 0.922 C_{WE}^{(12,2)} U_{w12} \alpha_{g1} \frac{a_{i2}^2}{\alpha_{g2}}, \quad (A.16)$$

$$\phi_{WE}^{(2)} = -1.02 C_{WE}^{(2)} \left[1 - \exp(-0.7 \alpha_{g2}) \right] U_{rw2} \frac{a_{i2}^2}{\alpha_{g2}} \left(1 - 0.10 D_{c2}^{*2} \right), \quad (A.17)$$

$$\eta_{WE,2}^{(11,2)} = 3.85 C_{WE}^{(1)} C_{D1}^{1/3} U_{r1} \alpha_{g1} a_{i1} \left(1 - \frac{2}{3} D_{c1}^{*} \right), \quad (A.18)$$

$$\eta_{WE,2}^{(12,2)} = 0.33 C_{WE}^{(12,2)} U_{w12} \alpha_{g1} a_{i2}. \quad (A.19)$$

In the above equation

$$\begin{aligned} U_{rw2} &= 0.94 U_{r2} C_{D2}^{1/3}, \\ U_{w12} &= U_{rw2} + U_{r1} - U_{r2}, \\ D_{c2}^{*} &= \frac{D_c}{D_{sm2}}, \end{aligned}$$

and

$$\begin{aligned} C_{D1} &= \frac{2}{3} D_{sm1} \sqrt{\frac{g\Delta\rho}{\sigma}} \left(\frac{1 + 17.67 [f(\alpha_{g1})]^{6/7}}{18.67 f(\alpha_{g1})} \right)^{2} \text{ with } f(\alpha_{g1}) = (1 - \alpha_{g1})^{1.5}, \\ C_{D2} &= \frac{8}{3} (1 - \alpha_{g2})^2. \end{aligned}$$

In the above equations $C_{WE}^{(1)}$, $C_{WE}^{(11,2)}$, $C_{WE}^{(12,2)}$, $C_{WE}^{(2)}$ are constant coefficients.

- $C_{WE}^{(1)} = 0.002$, $C_{WE}^{(12,2)} = 0.002$, $C_{WE}^{(2)} = 0.005$.

Turbulent impact (TI)

The source/sink terms of Turbulent Impact (TI) are modeled as follows :

$$\phi_{TI}^{(1)} = 0.12 C_{TI}^{(1)} \varepsilon^{1/3} (1 - \alpha_g) \left(\frac{a_{i1}^{5/3}}{\alpha_{g1}^{2/3}} \right) \exp\left(-\frac{We_{cr1}}{We_1} \right) \sqrt{1 - \frac{We_{cr1}}{We_1}}, \tag{A.20}$$

$$\phi_{TI,1}^{(2,1)} = 6.165 C_{TI}^{(2,1)} \varepsilon^{1/3} (1 - \alpha_g) \left(\frac{a_{i2}^{5/3}}{\alpha_{g2}^{2/3}} \right) \exp\left(-\frac{We_{cr2}}{We_2} \right) \sqrt{1 - \frac{We_{cr2}}{We_2}} \left(0.212 D_{c2}^{*13/3} - 0.167 D_{c2}^{*5} \right), \tag{A.21}$$

$$\phi_{TI,2}^{(2)} = 0.378 C_{TI}^{(2)} \varepsilon^{1/3} (1 - \alpha_g) \left(\frac{a_{i2}^{5/3}}{\alpha_{g2}^{2/3}} \right) \exp\left(-\frac{We_{cr2}}{We_2} \right) \sqrt{1 - \frac{We_{cr2}}{We_2}} \left(1 - 0.212 D_{c2}^{*13/3} \right), \tag{A.22}$$

$$\eta_{TI,2}^{(2,1)} = -11.65 C_{TI}^{(2,1)} \varepsilon^{1/3} (1 - \alpha_g) \alpha_{g2}^{1/3} a_{i2}^{2/3} \exp\left(-\frac{We_{cr2}}{We_2} \right) \sqrt{1 - \frac{We_{cr2}}{We_2}} \left(0.15 D_{c2}^{*16/3} - 0.117 D_{c2}^{*6} \right), \tag{A.23}$$

$$\eta_{TI,1}^{(2,1)} = -\eta_{TI,2}^{(2,1)}, \tag{A.24}$$

with the following expressions for We_1 and We_2 :

$$\begin{aligned} We_1 &= \frac{2\rho_l \varepsilon^{2/3} (D_{sm1})^{5/3}}{\sigma}, \\ We_2 &= \frac{2\rho_l \varepsilon^{2/3} (D_{sm2})^{5/3}}{\sigma}. \end{aligned}$$

$C_{TI}^{(1)}$, $C_{TI}^{(2,1)}$, $C_{TI}^{(2)}$ are constant coefficients. We_{cr1}, We_{cr2} are critical Weber number for breakup due to turbulent impact.

- $C_{TI}^{(1)} = 0.1$, $C_{TI}^{(2,1)} = 0.02$, $C_{TI}^{(2)} = 0.02$.
- $We_{cr1} = 6.5$, $We_{cr2} = 7$.

Shearing-off (SO)

The source/sink terms of Shearing-off (SO) are modeled as follows :

$$\phi_{SO,1}^{(2,12)} = 8.0C_{SO}\frac{\rho_l^{3/5}U_{g2}^{1/5}\sigma^{2/5}}{\rho_g D_h^{2/5} We_c^{3/5}}\frac{a_{i2}^2}{\alpha_{g2}}\left[1-\left(\frac{We_{c,SO}}{We_{m2}}\right)^4\right] \tag{A.25}$$

$$\phi_{SO,2}^{(2,12)} = -0.36C_{SO}\left(\frac{\sigma}{\rho_g U_{g2}}\right)\frac{a_{i2}^3}{\alpha_{g2}^2}\left[1-\left(\frac{We_{c,SO}}{We_{m2}}\right)\right], \tag{A.26}$$

$$\eta_{SO,2}^{(2,12)} = -2.33C_{SO}\left(\frac{\sigma}{\rho_g U_{g2}}\right)\frac{a_{i2}^2}{\alpha_{g2}}\left[1-\left(\frac{We_{c,SO}}{We_{m2}}\right)^4\right], \tag{A.27}$$

$$\eta_{SO,1}^{(2,12)} = -\eta_{SO,2}^{(2,12)}, \tag{A.28}$$

$$\phi_{SO,1}^{(2,12)} = 7.17C_{SO}\frac{\rho_l^{3/5}U_{r1}^{1/5}\sigma^{2/5}}{\rho_g D_h^{2/5}}\frac{a_{i2}^2}{\alpha_{g2}}\left[1-\left(\frac{We_{c,SO}}{We_{m2}}\right)^4\right]. \tag{A.29}$$

C_{SO} is a constant coefficient. $We_{c,SO}$ is a critical weber number for shearing-off of small bubbles from large cap bubbles. We_{m2}, We_c, D_h.

- $C_{SO} = 3.8 \times 10^{-5}$, $We_{c,SO} = 4500$.

Surface instability (SI)

The source/sink terms of Surface Instability (SI) are modeled as follows :

$$\begin{aligned}\phi_{SI}^{(2)} &= 2.616\times 10^{-4}C_{RC}^{(2)}\varepsilon^{1/3}\frac{1}{D_h^2}\alpha_{g2}^2\left(\frac{\sigma}{g\Delta\rho}\right)^{1/6}\left[1-\exp\left(-C_{RC2}\alpha_{g2}^{1/2}\right)\right],\\ &+ 1.425\times 10^{-7}C_{WE}^{(2)}(1-\exp(-0.7\alpha_{g2}))U_{rw2}\alpha_{g2}^2\left(\frac{\sigma}{g\Delta\rho}\right)^{-1},\end{aligned} \tag{A.30}$$

$C_{RC}^{(2)}$ and $C_{WE}^{(2)}$ are constant coefficients from Random collision and Wake Entrainment source terms. D_h is the hydraulic diameter.

Appendix B

Appendice: Résumé substantiel en français

Introduction

Les générateurs de vapeur (GV) des centrales nucléaires sont composés de faisceaux de tubes soumis à des écoulements diphasiques eau-vapeur ascendants, comme illustré sur la Figure B.1. Les forces exercées par le fluide sur ces tubes peuvent entraîner leur endommagement par usure ou fatigue (section 1.1). Des expériences effectuées en eau-air sur la maquette DIVA [95] (faisceau réduit de tubes droits, illustré sur la Figure B.2) n'ont pas permis de comprendre pleinement l'interaction complexe entre un fluide diphasique et le mouvement des tubes (section 1.2).

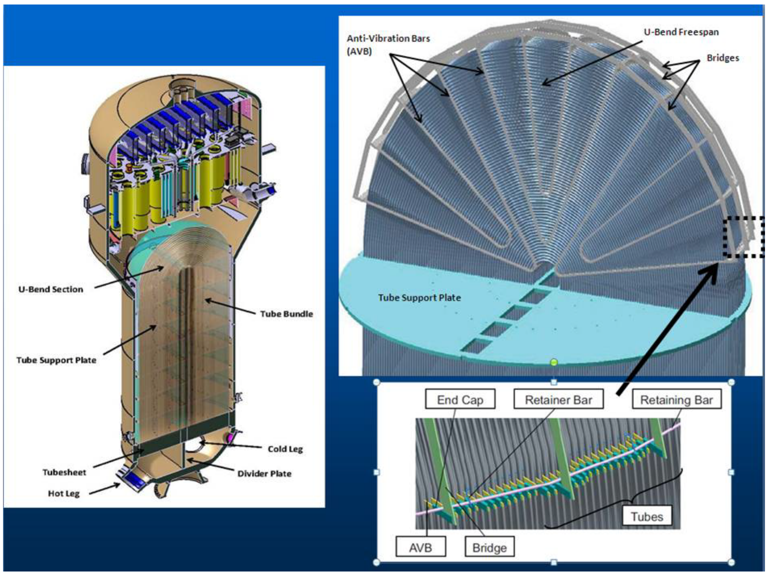

Figure B.1: Schéma d'un générateur de vapeur. Extrait du site internet de la US Nuclear Regulatory Commision (NRC).

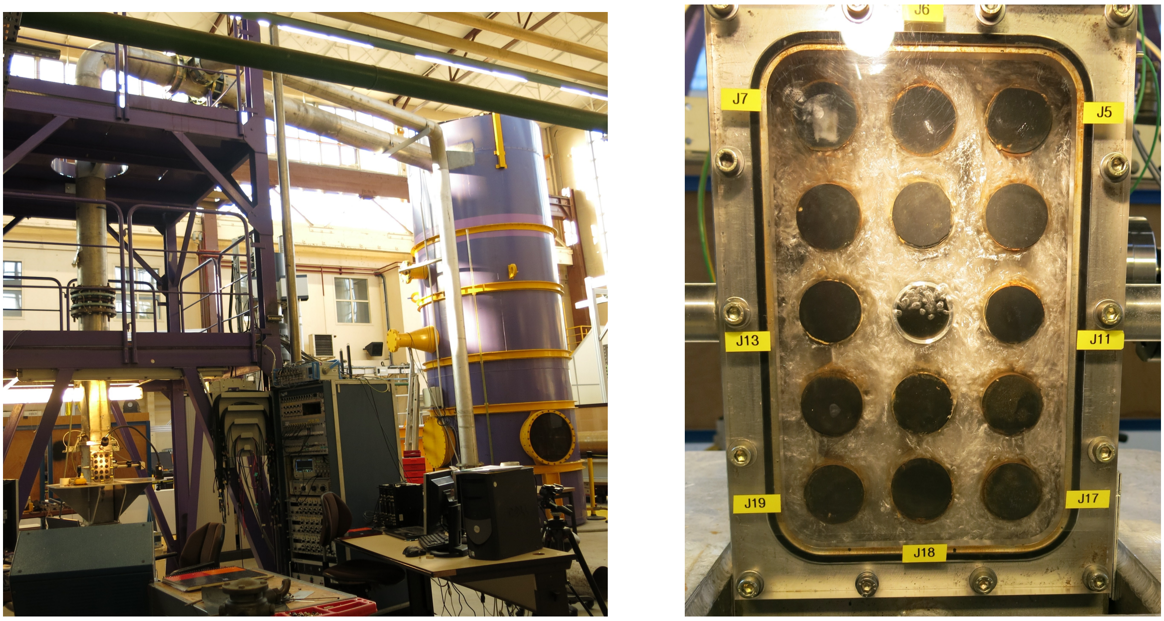

Figure B.2: Photographies de la plateforme DIVA.

Ainsi, la simulation numérique permettrait d'accéder à des données et des informations qui ne sont pas accessibles ou observables expérimentalement (section 1.3). Cependant, la difficulté de la modélisation diphasique tient dans la multiplicité des topologies d'écoulement, appelées régimes et illustrés dans la Figure B.3.

L'objectif de cette thèse est de simuler les expériences en faisceau de tubes à pas carré (DIVA), à l'aide du code NEPTUNE_CFD, afin de reproduire le chargement mécanique exercé sur les tubes (section 1.4), comme illustré sur la Figure B.4.

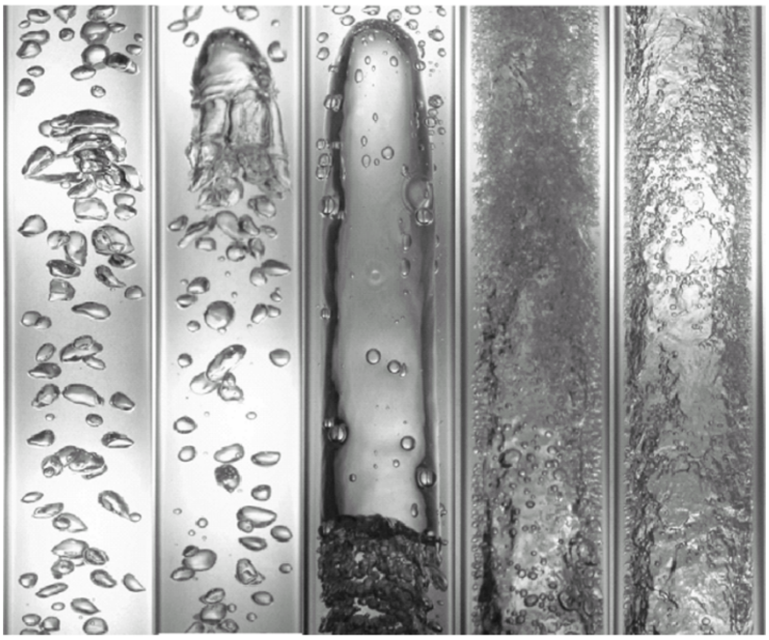

Figure B.3: Photographies prises dans un tube vertical de dimaètres 25.4 mm pour différents régimes d'écoulement. De gauche à droite sont représentés les régimes bubbly, cap-bubbly, slug, churn-turbulent et annulaire. Extrait de [85].

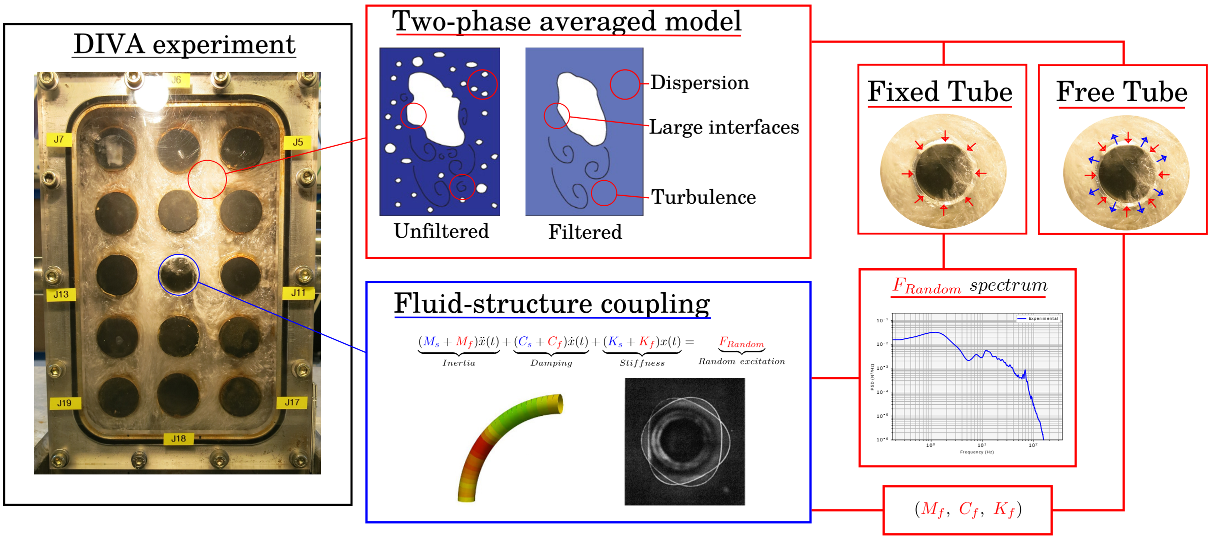

Figure B.4: Illustration de la simulation numérique de DIVA pour étudier les vibrations des tubes de générateurs de vapeur. Images issues du site internet d'Europlexus, de [93] et de [3].

Modélisation moyennée diphasique

La modélisation employée dans cette thèse repose sur un modèle à deux-fluides – trois-champs (section 2.1), comprenant un champ liquide continu, un champ de gaz dispersé, composé de bulles peu déformées (plus petites que 10.8 mm), et un champ hybride dispersé-continu pour tenir compte des bulles très déformées (entre 10.8 mm et 108 mm) et des poches de gaz (section 2.2), comme illustré sur la Figure B.5.

Cette distinction entre deux groupes de bulles et l'utilisation d'une modélisation de reproduction d'interface se base sur des observations faites dans la littérature, sur la distribution des diamètres, illustrées sur la Figure B.6, et celles obtenues via les données expérimentales de taux de vide obtenues avec la maquette DIVA, comme illustrées sur la Figure B.7.

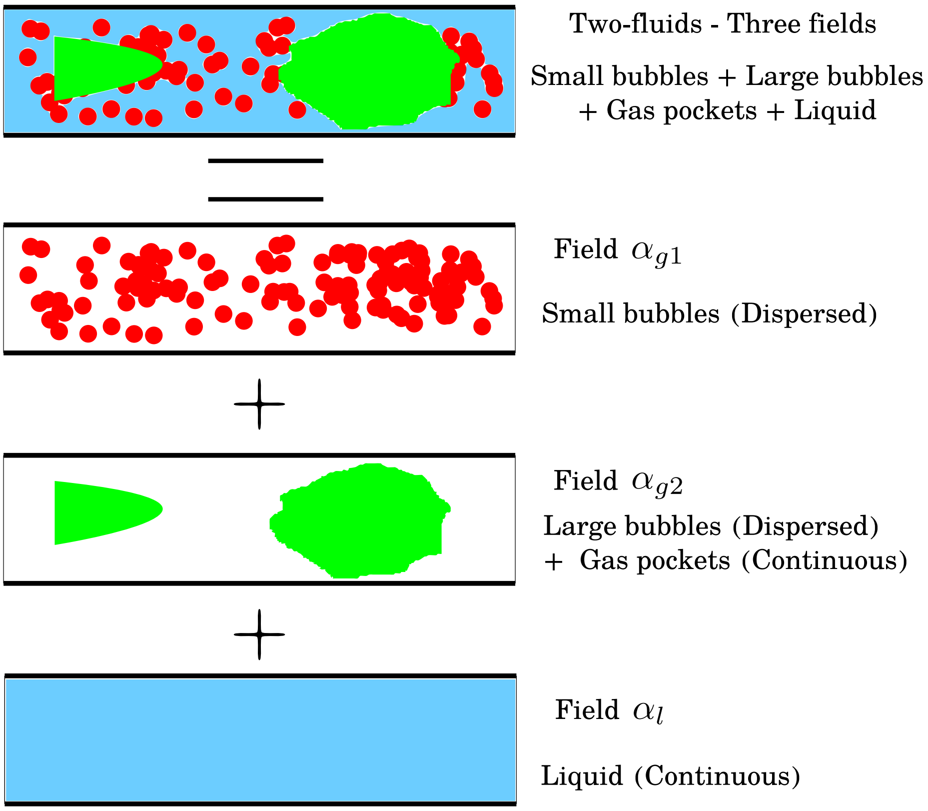

Figure B.5: Principe du modèle "Tous-régimes" utilisé dans cette thèse. 🟥 petites bulles, 🟩 Gaz continu et bulles larges, 🟪 Liquide.

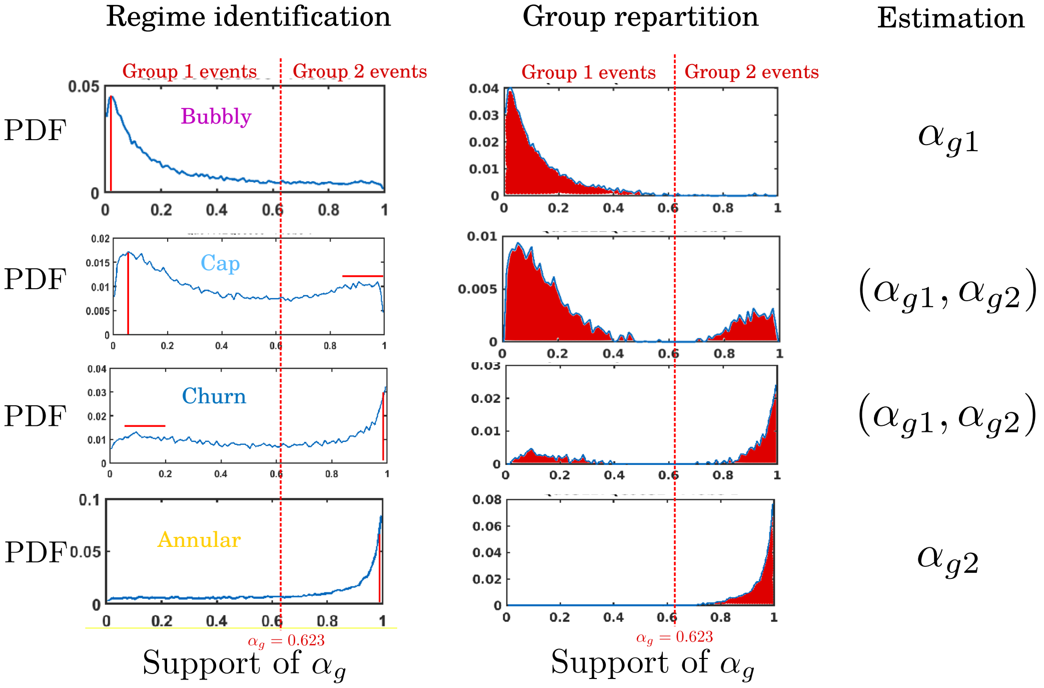

Figure B.7: Méthode de mesure de la répartition entre le groupe des petites bulles (groupe 1 de taux de présence α_{g1}) et le groupe des grandes bulles et poches de gaz (groupe 2 de taux de présence α_{g2}) basée sur le support du taux de présence du gaz par mesure de la PDF. Légende : 🟪 Régime bubbly, 🟦 Régime cap-bubbly, 🟦 Régime churn, 🟨 Régime Annulaire.

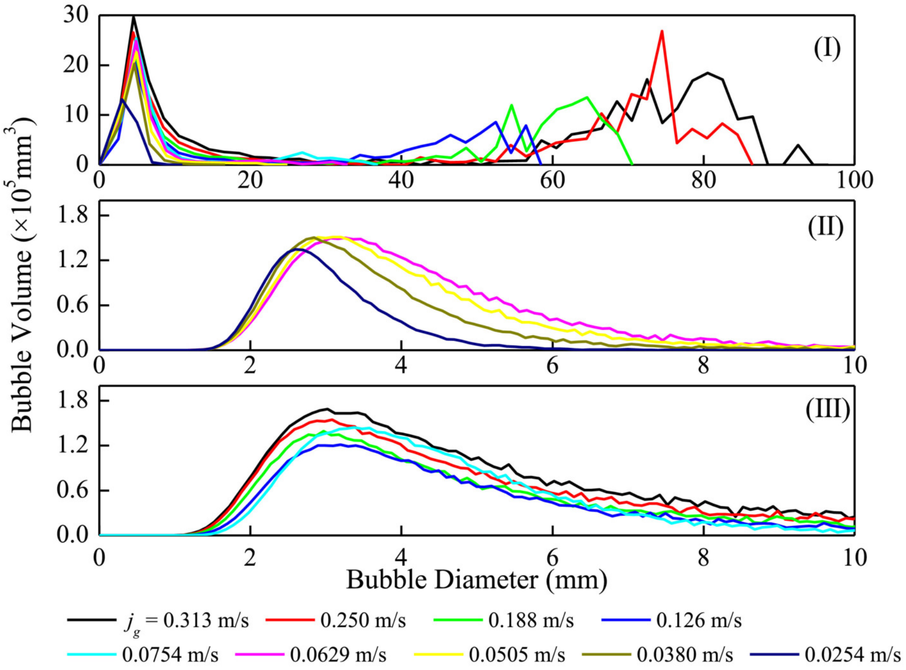

Figure B.6: Répartition des tailles de bulles pour une vitesse superficielle liquide $j_l = 0.765$ m/s et différentes injections de gaz dans un canal carré de côté 66 mm. Sous-figures : (I) répartition des tailles de bulles avec une largeur de classe de 2 mm pour les régimes de bubbly et de cap/churn, (II) répartition des tailles de bulles en zoom avec une largeur de classe de 0.1 mm pour le régime de bubbly, (III) répartition des tailles de bulles en zoom avec une largeur de classe de 0.1 mm pour le régime de cap/churn-bubbly. Extrait de [153].

La simulation repose également sur la modélisation de la turbulence liquide pour correctement reproduire les efforts au niveau des tubes (section 2.3). Cependant, les modèles diphasiques de la littérature sont validés sur des configurations sans obstacle. La présence des tubes engendre une topologie particulière de l'écoulement qui empêche l'utilisation directe du modèle de base (section 2.4).

Validation et changements dans la modélisation

Une étape d'adaptation et de validation du modèle a donc été nécessaire avant de réaliser les simulations. En premier lieu, un changement de paradigme a été necessaire. Un critère basé sur la taille du maillage pour passer du modèle dispersé au modèle continu est couramment utilisé dans la littérature, bien que sa sophistication puisse varier. Contrairement aux modèles existants qui introduisent la confusion entre la modélisation dispersée et la vision dispersée à travers un maillage de capteurs, notre méthode repose sur des considérations physiques, illustrées sur la Figure B.8. Nous supposons d'abord que la coalescence des petites bulles du Groupe 1 engendre les bulles du Groupe 2. Ensuite, les bulles déformées du Groupe 2 peuvent se transformer en grandes poches de gaz et en interfaces étendues. Cette perspective découle de la croissance naturelle des interfaces, passant d'une catégorie à une autre et finalement à un champ continu. Cette transition se produit lorsque le diamètre équivalent devient trop grand, créant une grande interface, ou lorsque la fraction de vide devient trop élevée, limitant l'arrangement des grosses bulles et conduisant ainsi à la présence d'un régime annulaire.

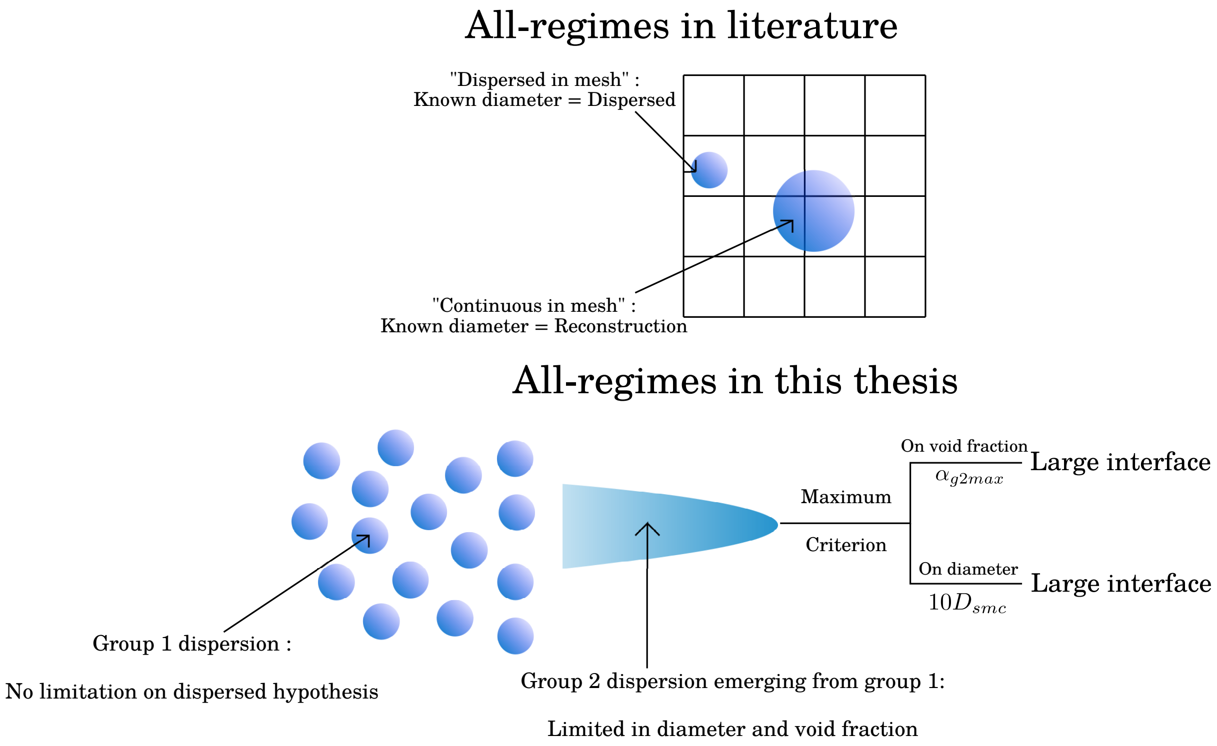

Figure B.8: Comparaison du paradigme des modèles à tous les régimes entre ceux présents dans la littérature et notre modélisation

Ensuite, une étape de validation et d'étude du couplage diphasique-turbulence liquide sur des expériences en canaux (étroit et large) a été conduite (section 3.1). Préalablement, nous avons sélectionné quatre modèles de turbulence fréquemment cités dans la littérature liée à notre sujet : le modèle $k-\varepsilon$ [47], le modèle SSG [9], l'EBRSM [77] et l'EBRSM avec turbulence diphasique [81]. Cette comparaison avec des données expérimentales nous a permis d'acquérir une meilleure compréhension de l'interaction entre les modèles de turbulence et le modèle diphasique. L'étude a révélé le potentiel du modèle EBRSM, que ce soit avec ou sans turbulence diphasique, dans la reproduction des tendances des profils de taux de vide et de vitesse. Ces résultats ont conduit à la décision de poursuivre notre travail en se concentrant sur le modèle EBRSM.

Par la suite, un travail de recherche et d'ajustement a été entrepris pour adapter la modélisation diphasique en tenant compte des taux de vide élevés (section 3.2. Nous avons initialement étudié les forces d'interaction liquide-gaz, qui présentent des dépendances non linéaires par rapport au taux de vide. Le coefficient adimensionnel de traînée diverge avec le taux de vide, nécessitant ainsi une correction. La force classique de masse ajoutée de [90] montre également une divergence avec le taux de vide. Nous avons donc opté pour une formulation plus générale, celle de [6], qui ne diverge pas et dépend du rapport de masse volumique. De plus, nous avons proposé une nouvelle expression corrigée du coefficient de dispersion turbulente de [64] pour éviter ces divergences, comme illustré dans la Figure B.9.

Dans le même souci d'amélioration, des corrections ont été apportées aux termes sources de coalescence et de fragmentation des bulles pour résoudre les problèmes près de la paroi et dans les zones à fort taux de vide. Parallèlement, des défis ont émergé concernant la dynamique du Groupe 2. Les simulations ont révélé des problèmes liés à des accélérations élevées, des sauts dans la prédiction du diamètre et une reproduction inhabituelle des interfaces dans le champ

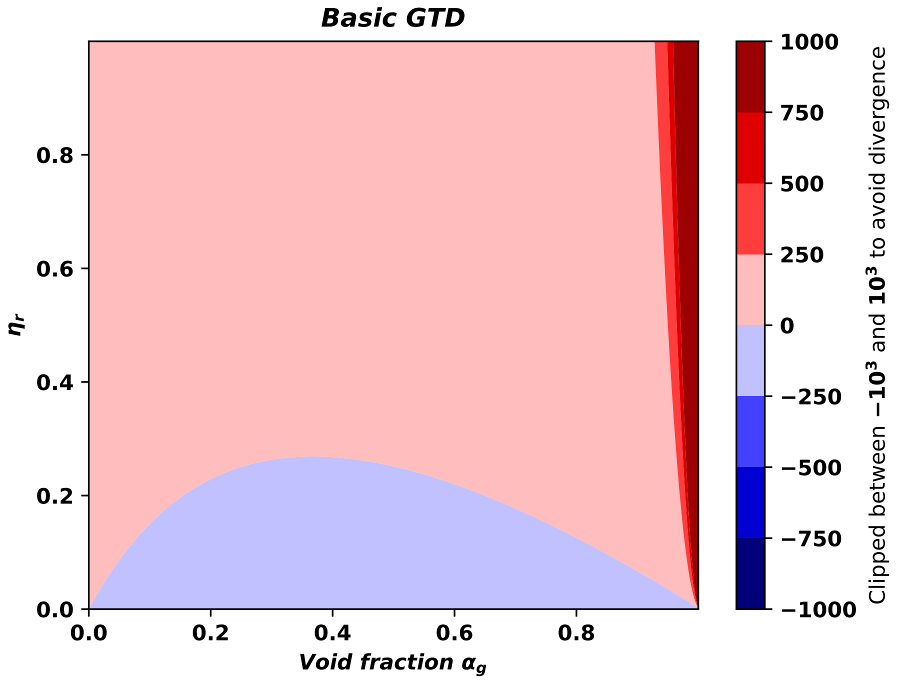

(a) Avant modification. Les valeurs sont limitées entre -10^3 et 10^3 afin d'éviter toute divergence.

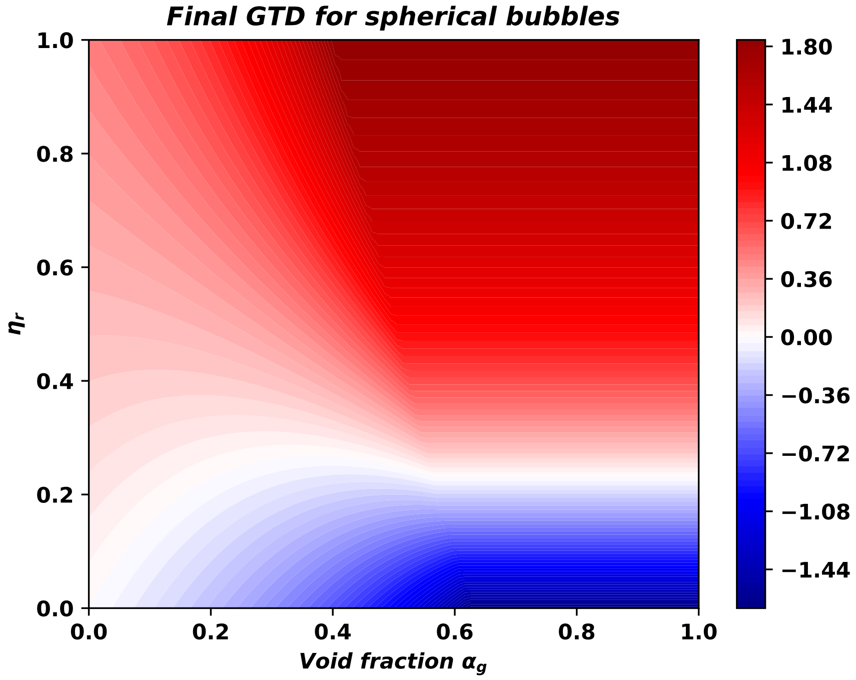

(b) Après modifications.

Figure B.9: Coefficient la dispersion turbulente GTD pour le groupe 1 avant (a) et après (b) modifications suivant les valeurs de η_r et α_g (c.f. equation 3.19).

continu (parfois similaire à la formation des grains dans les microstructures des métaux). Pour résoudre ces problèmes, nous avons proposé d'ajuster le coefficient de masse ajoutée du Groupe 2 en se basant sur des calculs tirés de la littérature, ce qui a permis de modifier le coefficient de dispersion turbulente, comme illustré dans la Figure 2.

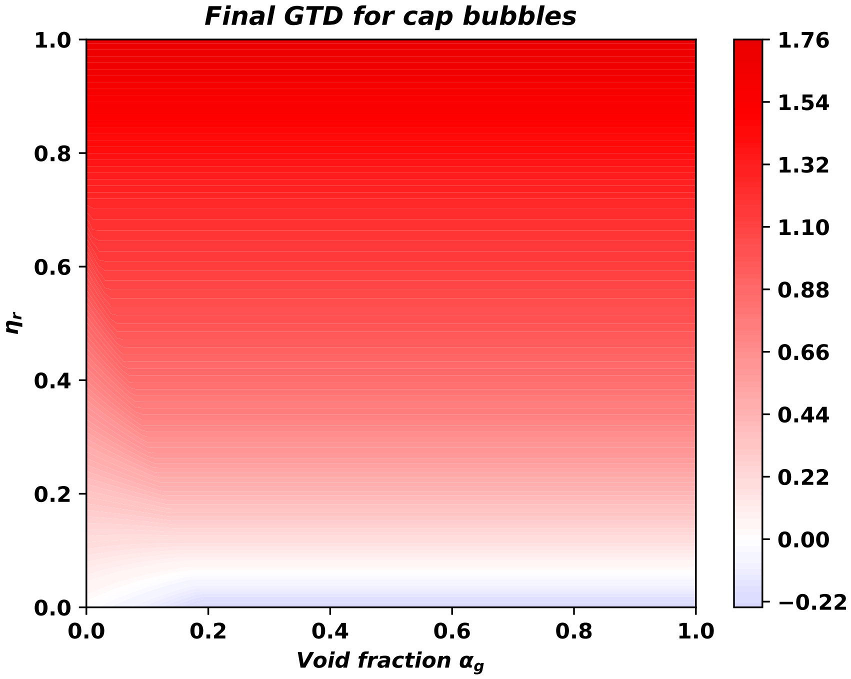

Figure B.10: Coefficient la dispersion turbulente GTD pour le groupe 2 après modifications suivant les valeurs de η_r et α_g (c.f. equation 3.19)

De plus, l'augmentation du coefficient de masse ajoutée a permis d'augmenter la diffusion dans l'équation du diamètre pour atténuer les problèmes de sauts. Enfin, nous avons établi un critère de taux de vide pour activer le champ continu en nous appuyant sur des calculs analytiques simples basés sur les équations moyennées, assurant ainsi une transition fluide de la vision dispersée à la vision continue.

Simulations moyennées diphasiques avec un cylindre unique

L'étape suivante a eu pour but de simuler des écoulements diphasiques eau-air autour tube unique afin de comprendre la réponse du modèle proposé dans cette thèse. En premier lieu, une étude de sensibilité du modèle diphasique en régime bubbly est proposée afin de comprendre la physique reproduite dans les simulations à travers les spectres de forces exercées sur le tube (section 4.1). Cette étape permet notamment d'axer la réflexion sur les aspects numériques de la modélisation physique. La partie suivante s'intéresse à la comparaison et à la compréhension des résultats numériques et expérimentaux (section 4.2).

Nous avons constaté que le nombre de Reynolds liquide et le taux de vide homogène étaient les paramètres les plus influents pour la reproduction des spectres de force numériques. Il a été observé que l'obtention de spectres de force correspondant au régime à bulles était la plus difficile en raison de sa sensibilité aux fluctuations du liquide, de la topologie autour du cylindre et de l'accélération causée par le confinement. Cependant, pour la configuration en faisceau de

tubes (DIVA), les cylindres en amont et en aval du cylindre central contraignent la topologie de l'écoulement autour de lui, la rapprochant de l' expérimentale. De plus, les vitesses à l'arrière et à l'avant du cylindre central devraient être plus modérées, réduisant l'influence des fluctuations du liquide et potentiellement conduisant à une meilleure reproduction de l'écoulement expérimental. Par conséquent, nous avons été optimiste quant à l'obtention de résultats relativement bons en faisceau de tubes. De plus, nous avons pu montrer que les régimes cap-bulles/churn sont plus résilients aux fluctuations du liquide et aux variations du taux de vide. Finalement, les spectres de force obtenus sont cohérents avec la topologie simulée, et nous observons certaines tendances favorables par rapport aux données expérimentales. Bien que des améliorations soient nécessaires, les résultats obtenus sont plutôt encourageants.
Au cours de cette étude, nous avons identifié des pistes d'améliorations :

- La force de portance semble avoir une influence trop importante par rapport à la force de traînée dans la modélisation. Il est particulièrement important d'étudier de manière approfondie l'effet du taux de vide sur la portance. De plus, il semble que des améliorations soient nécessaires pour modéliser les forces de portance pour les bulles du groupe 2.

- Une force ou un nouveau coefficient de traînée favorisant un meilleur équilibre entre les deux groupes de bulles semble nécessaire lorsqu'il s'agit de zones dynamiques, en particulier lorsque la vitesse d'injection est faible ou lorsque la présence du groupe 2 est nettement moins dominante. En effet, ces bulles plus inertes ont tendance à perturber la dynamique globale lorsqu'elles sont en minorité ou lorsque le débit est faible.

- Une amélioration de la force de lubrification pour mieux prendre en compte les effets proche parois, notamment les problèmes de point d'arrêt en dispersé, est nécessaire.

Simulations moyennées diphasiques en faisceau de tubes à pas carré

Enfin, la dernière partie s'intéresse à la comparaison des résultats expérimentaux et numériques dans le cas d'un écoulement diphasique eau-air dans un faisceau de tubes à pas carré (DIVA). En premier lieu, une analyse des résultats expérimentaux a pour but de renseigner nos simulations sur les conditions opératoires et sur les paramètres clés pour la simulation des spectres de force et justifier les cas tests dans la suite (section 5.1). Cela a permis de comprendre que les spectres de forces numériques devraient être sensibles à la vitesse moyenne liquide au premier ordre et au régime d'écoulement au second ordre, avec peu d'influence des diamètres. Il est à noter que les régimes bubbly et annulaire présentent des comportements distincts par rapport aux autres régimes concernant les spectres de traînée et de portance, respectivement, les rendant sûrement plus difficile à obtenir numériquement.
La dernière partie permet de comparer les résultats expérimentaux aux simulations pour 3 injections liquides différentes, pour les régimes bubbly et cap/churn (section 5.2). Les spectres de force dans les directions de portance et de traînée sont raisonnablement bien reproduits par rapport aux expériences, pour les écoulements à bulles, illustrés dans la Figure B.11 et les écoulements cap/churn, illustrés dans la Figure B.12.

En effet, malgré la complexité de la modélisation, l'aspect URANS et les résultats mitigés obtenus avec un seul cylindre, nous disposons d'un modèle capable de reproduire les tendances

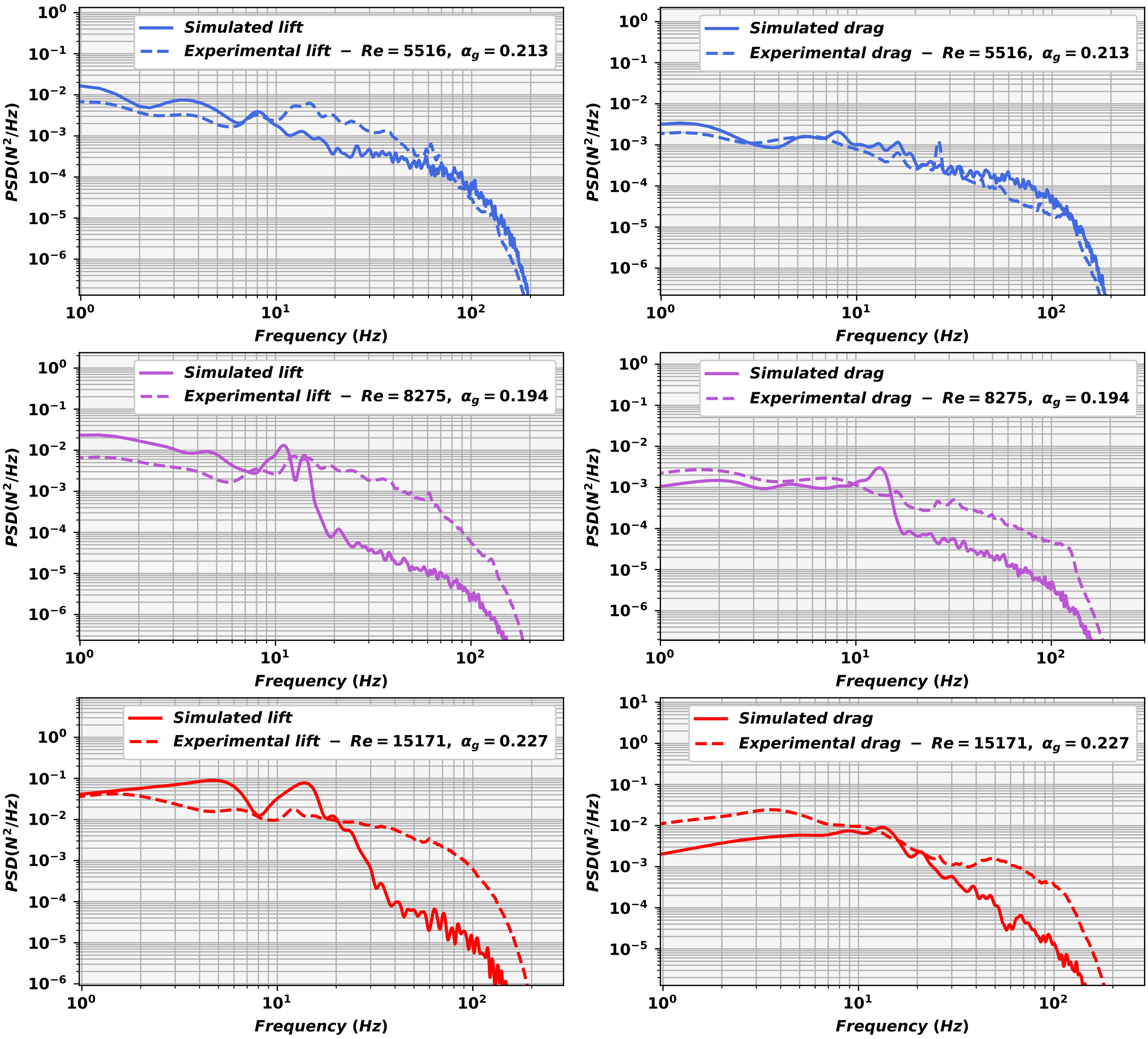

Figure B.11: Spectres de forces de portance (à gauche) et de traînée (à droite) simulés avec DIVA pour $Re_l = 5516$ (en haut), $Re_l = 8275$ (au milieu) et $Re_l = 15171$ (en bas) comparés aux données expérimentales, pour le régime bubbly. Simulations avec le nouveau modèle TRITON.

globales des spectres de forces. Il est intéressant de noter que le diamètre des bulles du groupe 2 semble avoir peu d'influence sur la réponse des forces aléatoires. Il est à noter que la présence du second groupe de bulles a amélioré les spectres de force, probablement en raison d'une distribution plus uniforme du taux de vide global, qui est influencé par la présence du groupe 2. Cela souligne la valeur de notre approche de modélisation dans la reproduction des spectres de force dans les écoulements diphasiques eau-air. Néanmoins, il existe encore des pistes d'améliorations possibles :

- Améliorer l'interaction entre le LIM et les parois semble nécessaire pour mieux rendre compte des régions annulaires entre les cylindres.

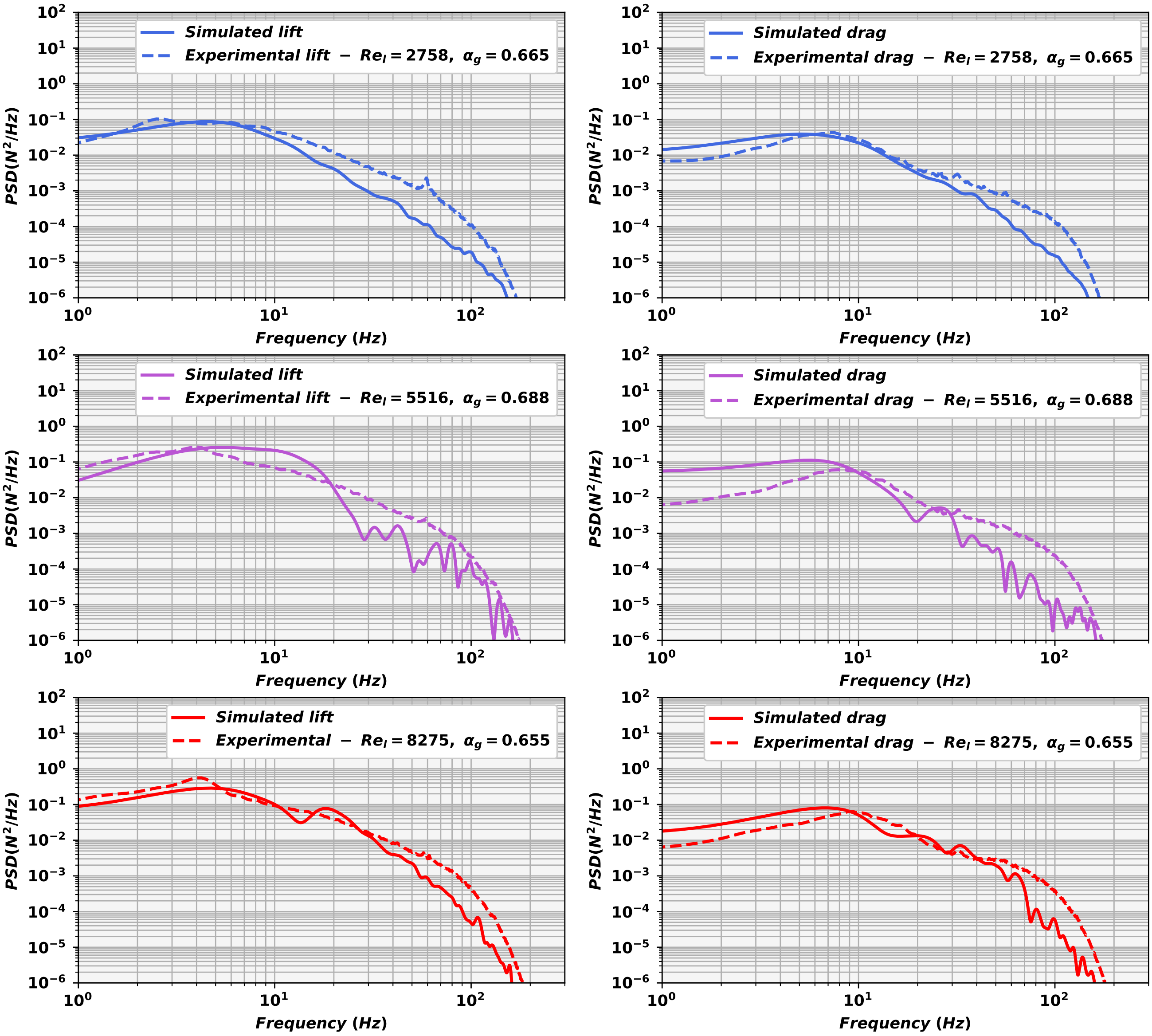

Figure B.12: Spectres de forces de portance (à gauche) et de traînée (à droite) simulés avec DIVA pour $Re_l = 2758$ (en haut), $Re_l = 5516$ (au milieu) et $Re_l = 8275$ (en bas) comparés aux données expérimentales, pour le régime cap-bubbly/churn. Simulations avec le nouveau modèle TRITON.

- Des travaux supplémentaires sont nécessaires pour identifier les paramètres d'injection appropriés afin d'obtenir un régime d'écoulement annulaire correct.

Bibliography

[1] S. Benhamadouche, I. Afgan, and R. Manceau. Numerical simulations of flow and heat transfer in a wall-bounded pin matrix. *Flow, Turbulence and Combustion*, 104(1):19–44, 2020.

[2] D. Bestion. Applicability of two-phase cfd to nuclear reactor thermalhydraulics and elaboration of best practice guidelines. *Nuclear Engineering and Design*, 253:311–321, 2012. doi: 10.1016/j.nucengdes.2011.08.068.

[3] D. Bestion. The difficult challenge of a two-phase cfd modelling for all flow regimes. *Nuclear Engineering and Design*, 279:116–125, 2014. ISSN 00295493. doi: 10.1016/j.nucengdes.2014.04.006. URL `http://dx.doi.org/10.1016/j.nucengdes.2014.04.006`.

[4] C. S. Brooks, S. S. Paranjape, B. Ozar, T. Hibiki, and M. Ishii. Two-group drift-flux model for closure of the modified two-fluid model. *International Journal of Heat and Fluid Flow*, 37:196–208, 2012. ISSN 0142-727X. doi: https://doi.org/10.1016/j.ijheatfluidflow.2012.04.002. URL `https://www.sciencedirect.com/science/article/pii/S0142727X12000495`.

[5] A. Burns, T. Grank, I. Hamill, and J.-M. Shi. The favre averaged drag model for turbulent dispersion in eulerian multi-phase flows. *In: 5th International Conference on Multiphase Flow, ICMF, Yokohama, Japan*, 2004.

[6] X. Cai and G. B. Wallis. A more general cell model for added mass in two-phase flow. *Chemical Engineering Science*, 49(10):1631–1638, may 1994. doi: 10.1016/0009-2509(93)e0042-b.

[7] M. D. Carelli, L. Conway, L. Oriani, B. Petrovic, C. Lombardi, M. Ricotti, A. Barroso, J. Collado, L. Cinotti, N. Todreas, D. Grgic, M. Moraes, R. Boroughs, H. Ninokata, D. Ingersoll, and F. Oriolo. The design and safety features of the iris reactor. *Nuclear Engineering and Design*, 230(1-3):151–167, may 2004. doi: 10.1016/j.nucengdes.2003.11.022.

[8] G. Cerne, S. Petelin, and I. Tiselj. Coupling of the interface tracking and the two-fluid models for the simulation of incompressible two-phase flow. *Journal of Computational Physics*, 171(2):776–804, 2001. ISSN 00219991. doi: 10.1006/jcph.2001.6810. URL `http://linkinghub.elsevier.com/retrieve/pii/S002199910196810X`.

[9] C.G.Speziale, S.Sarkar, and T.B.Gatski. Modelling the pressure–strain correlation of turbulence: an invariant dynamical systems approach. *Journalof Fluid Mechanics*, 227:245–272, 1991. doi: 10.1017/s0022112091000101.

[10] T. J. Chuang and T. Hibiki. Vertical upward two-phase flow cfd using interfacial area transport equation. *Progress in Nuclear Energy*, 85(2015):415–427, 2015. ISSN 01491970. doi: 10.1016/j.pnucene.2015.07.008. URL `http://dx.doi.org/10.1016/j.pnucene.2015.07.008`.

[11] T.-J. Chuang and T. Hibiki. Interfacial forces used in two-phase flow numerical simulation. *International Journal of Heat and Mass Transfer*, 113:741–754, oct 2017. doi: 10.1016/j.ijheatmasstransfer.2017.05.062.

[12] A. D. Cluzeau. Modelisation physique de la dynamique des ecoulements a bulles par remontee d'echelle a partir de simulations fines (french). *PhD Dissertation. Universite de Perpignan*, 2019.

[13] M. Colombo and M. Fairweather. Multiphase turbulence in bubbly flows: Rans simulations. *International Journal of Multiphase Flow*, 77:222–243, 2015. doi: 10.1016/j.ijmultiphaseflow.2015.09.003.

[14] M. Colombo and M. Fairweather. Influence of multiphase turbulence modelling on interfacial momentum transfer in two-fluid eulerian-eulerian cfd models of bubbly flows. *Chemical Engineering Science*, 195:968–984, 2019. doi: 10.1016/j.ces.2018.10.043.

[15] M. Colombo and M. Fairweather. Multi-fluid computational fluid dynamic predictions of turbulent bubbly flows using an elliptic-blending reynolds stress turbulence closure. *Frontiers in Energy Research*, 8:44, 2020. doi: 10.3389/fenrg.2020.00044.

[16] P. Coste. A large interface model for two-phase cfd. *Nuclear Engineering and Design*, 255:38–50, feb 2013. doi: 10.1016/j.nucengdes.2012.10.008.

[17] P. Coste and J. Lavieville. A turbulence model for large interfaces in high reynolds two-phase cfd. *Nuclear Engineering and Design*, 284:162–175, 2015. ISSN 00295493. doi: 10.1016/j.nucengdes.2014.12.004. URL `http://dx.doi.org/10.1016/j.nucengdes.2014.12.004`.

[18] P. Coste and N. Merigoux. Two-phase cfd validation: Topflow-pts steady-state steam-water tests 3-16, 3-17, 3-18 and 3-19. *Nuclear Engineering and Design*, 299:18–27, 2016. ISSN 00295493. doi: 10.1016/j.nucengdes.2015.08.006. URL `http://dx.doi.org/10.1016/j.nucengdes.2015.08.006`.

[19] B. J. Daly. Transport equations in turbulence. *Physics of Fluids*, 13(11):2634, 1970. doi: 10.1063/1.1692845.

[20] A. K. Das and P. K. Das. Modelling bubbly flow and its transitions in vertical annuli using population balance technique. *International Journal of Heat and Fluid Flow*, 31(1):101–114, 2010. ISSN 0142727X. doi: 10.1016/j.ijheatfluidflow.2009.11.006. URL `http://dx.doi.org/10.1016/j.ijheatfluidflow.2009.11.006`.

[21] A. Dave, A. Manera, M. Beyer, D. Lucas, and H.-M. Prasser. Uncertainty analysis of an interfacial area reconstruction algorithm and its application to two group interfacial area transport equation validation. *Nuclear Engineering and Design*, 310:620–637, 2016. ISSN 00295493. doi: 10.1016/j.nucengdes.2016.10.038. URL `http://dx.doi.org/10.1016/j.nucengdes.2016.10.038`.

[22] A. J. Dave. Interfacial area transport equation models and validation against high resolution experimental data for small and large diameter vertical pipes by. *PhD dissertation, University of Michigan*, 2016.

[23] A. J. Dave, A. Manera, M. Beyer, D. Lucas, and M. Bernard. Evaluation of two-group interfacial area transport equation model for vertical small diameter pipes against high-resolution experimental data. *Chemical Engineering Science*, 162:175–191, 2017. ISSN 00092509. doi: 10.1016/j.ces.2017.01.001. URL `http://dx.doi.org/10.1016/j.ces.2017.01.001`.

[24] M. L. de Bertodano, X.Sun, M.Ishii, and A.Ulke. Phase distribution in the cap bubble regime in a duct. *Journal of Fluids Engineering*, 128(4):811–818, 01 2006. doi: 10.1115/1.2201626.

[25] P. Durbin. Near-wall turbulence closure modeling without "damping functions". *Theoret. Comput. Fluid Dynamics*, 3:1–13, 1991. doi: https://doi.org/10.1007/BF00271513.

[26] T. Frank, P. J. Zwart, E. Krepper, H. M. Prasser, and D. Lucas. Validation of cfd models for mono- and polydisperse air-water two-phase flows in pipes. *Nuclear Engineering and Design*, 238(3):647–659, 2008. ISSN 00295493. doi: 10.1016/j.nucengdes.2007.02.056.

[27] E. Frederix, D. Dovizio, A. Mathur, and E. Komen. All-regime two-phase flow modeling using a novel four-field large interface simulation approach. *International Journal of Multiphase Flow*, 145:103822, dec 2021. doi: 10.1016/j.ijmultiphaseflow.2021.103822.

[28] X. Y. Fu and M. Ishii. Two-group interfacial area transport in vertical air-water flow i. mechanistic model. *Nuclear Engineering and Design*, 219:143–168, 2002.

[29] V. H. Gada, M. P. Tandon, J. Elias, R. Vikulov, and S. Lo. A large scale interface multi-fluid model for simulating multiphase flows. *Applied Mathematical Modelling*, 44:189–204, 2017. ISSN 0307-904X. doi: https://doi.org/10.1016/j.apm.2017.02.030. URL `https://www.sciencedirect.com/science/article/pii/S0307904X17301269`.

[30] G.Bois. Direct numerical simulation of a turbulent bubbly flow in a verticalchannel: Towards an improved second-order reynolds stress model. *Nuclear engineering and Design 321*, pages 92–103, 2017. doi: 10.1016/j.nucengdes.2017.01.023.

[31] X. Han, X. Shen, T. Yamamoto, K. Nakajima, H. Sun, and T. Hibiki. Experimental study on local interfacial parameters in upward air-water bubbly flow in a vertical 6x6 rod bundle. *International Journal of Heat and Mass Transfer*, 144:118696, 2019. ISSN 0017-9310. doi: https://doi.org/10.1016/j.ijheatmasstransfer.2019.118696. URL `https://www.sciencedirect.com/science/article/pii/S0017931019333551`.

[32] Y. Hassan. *12 – An overview of computational fluid dynamics and nuclear applications.* Number 1994. Elsevier Ltd., 2017. ISBN 9780081006627. doi: 10.1016/B978-0-08-100662-7.00012-9. URL `http://dx.doi.org/10.1016/B978-0-08-100662-7.00012-9`.

[33] K. Hayashi, H. Hessenkemper, D. Lucas, D. Legendre, and A. Tomiyama. Scaling of lift reversal of deformed bubbles in air-water systems. *International Journal of Multiphase Flow*, 142:103653, sep 2021. doi: 10.1016/j.ijmultiphaseflow.2021.103653.

[34] T. Hibiki and M. Ishii. One-group interfacial area transport of bubbly flows in vertical round tubes. *International Journal of Heat and Mass Transfer*, 43(15):2711–2726, 2000. ISSN 00179310. doi: 10.1016/S0017-9310(99)00325-7.

[35] T. Hibiki and M. Ishii. Two-group interfacial area transport equations at bubbly-to-slug flow transition. *Nuclear Engineering and Design 202*, (1):39–76, 2000. doi: https://doi.org/10.1016/S0029-5493(00)00286-7.

[36] T. Hibiki and M. Ishii. Lift force in bubbly flow systems. *Chem. Eng. Sci. 62*, pages 6457—-6474, 2007. doi: 10.1016/j.ces.2007.07.034.

[37] T. Hibiki and M. Ishii. Interfacial area transport equations for gas-liquid flow. (1), 2017.

[38] T. Hibiki, J. P. Schlegel, T. Ozaki, S. Miwa, and S. Rassame. Simplified two-group two-fluid model for three-dimensional two-phase flow computational fluid dynamics for vertical upward flow. *Progress in Nuclear Energy*, (September), 2018. ISSN 01491970. doi: 10.1016/j.pnucene.2017.12.003. URL `http://linkinghub.elsevier.com/retrieve/pii/S0149197017303037`.

[39] C. Hirt and B. Nichols. Volume of fluid (vof) method for the dynamics of free boundaries. *Journal of Computational Physics*, 39(1):201–225, 1981. doi: 10.1016/0021-9991(81)90145-5.

[40] T. Hohne and J. P. Mehlhoop. Validation of closure models for interfacial drag and turbulence in numerical simulations of horizontal stratified gas-liquid flows. *International Journal of Multiphase Flow*, 62:1–16, 2014. ISSN 03019322. doi: 10.1016/j.ijmultiphaseflow.2014.01.012.

[41] T. Hohne, Deendarlianto, and D. Lucas. Numerical simulations of counter-current two-phase flow experiments in a pwr hot leg model using an interfacial area density model. *International Journal of Heat and Fluid Flow*, 32(5):1047–1056, 2011. ISSN 0142727X. doi: 10.1016/j.ijheatfluidflow.2011.05.007.

[42] B. G. Huh, D. J. Euh, H. Y. Yoon, B. J. Yun, C. H. Song, and C. H. Chung. Mechanistic study for the interfacial area transport phenomena in an air/water flow condition by using fine-size bubble group model. *International Journal of Heat and Mass Transfer*, 49(21-22):4033–4042, 2006. ISSN 00179310. doi: 10.1016/j.ijheatmasstransfer.2005.11.037.

[43] S. Hänsch, D. Lucas, E. Krepper, and T. Höhne. A multi-field two-fluid concept for transitions between different scales of interfacial structures. *International Journal of Multiphase Flow*, 47:171–182, dec 2012. doi: 10.1016/j.ijmultiphaseflow.2012.07.007.

[44] A. Inoue, Y. Kozawa, M. Yokosawa, and S. Aoki. Studies on two-phase cross flow. part i: Flow characteristics around a cylinder. *International Journal of Multiphase Flow*, 12(2):149–167, 1986. ISSN 0301-9322. doi: https://doi.org/10.1016/0301-9322(86)90023-6. URL `https://www.sciencedirect.com/science/article/pii/0301932286900236`.

[45] M. Ishii, S. Kim, and J. Uhle. Interfacial area transport equation: Model development and benchmark experiments. *International Journal of Heat and Mass Transfer*, 45(15):3111–3123, 2002. ISSN 00179310. doi: 10.1016/S0017-9310(02)00041-8.

[46] C. Iwaki, K. H. Cheong, H. Monji, and G. Matsui. Vertical, bubbly, cross-flow characteristics over tube bundles. *Experiments in Fluids*, 39(6):1024–1039, oct 2005. doi: 10.1007/s00348-005-0036-2.

[47] W. Jones and B. Launder. The calculation of low-reynolds-number phenomena with a two-equation model of turbulence. *International Journal of Heat and Mass Transfer*, 16(6):1119–1130, jun 1973. doi: 10.1016/0017-9310(73)90125-7.

[48] J.P.Schlegel, T.Hibiki, X.Shen, S.Appathurai, and H.Subranami. Evaluation of interfacial area transport equation in coupled two-fluid model computation. *NURETH-16*, pages 389–402, 2015.

[49] J. E. Julia and T. Hibiki. Flow regime transition criteria for two-phase flow in a vertical annulus. *International Journal of Heat and Fluid Flow*, 32(5):993–1004, 2011. ISSN 0142727X. doi: 10.1016/j.ijheatfluidflow.2011.06.001. URL `http://dx.doi.org/10.1016/j.ijheatfluidflow.2011.06.001`.

[50] J. E. Julia, Y. Liu, T. Hibiki, and M. Ishii. Local flow regime analysis in vertical co-current downward two-phase flow. *Experimental Thermal and Fluid Science*, 44:345–355, jan 2013. doi: 10.1016/j.expthermflusci.2012.07.006.

[51] I. Kataoka, K. Yoshida, M. Naitoh, H. Okada, and T. Morii. Modeling of turbulent transport term of interfacial area concentration in gas liquid two-phase flow. *Nuclear Engineering and Design*, 253:322–330, dec 2012. doi: 10.1016/j.nucengdes.2011.08.062.

[52] S. Kim, X. Sun, M. Ishii, S. G. Beus, and F. Lincoln. Interfacial area transport and evaluation of source and sink terms for confined air-water bubbly flow. *Nuclear Engineering and Design*, 219(1):61–75, 2003. ISSN 00295493. doi: 10.1016/S0029-5493(02)00289-3.

[53] S. Kim, M. Ishii, R. Kong, and G. Wang. Progress in two-phase flow modeling: Interfacial area transport. *Nuclear Engineering and Design*, 373:111019, 2021. doi: https://doi.org/10.1016/j.nucengdes.2020.111019.

[54] K.Mishima and M.Ishii. Flow regime transition criteria for upward two-phase flow in vertical tubes. *Int. J. Heat Mass Transf., 27 (5)*, pages 723–737, 1984. doi: 10.1016/0017-9310(84)90142-x.

[55] G. Kocamustafaogullari and M. Ishii. Foundation of the interfacial area transport equation and its closure relations. *Int. J. Heat Mass Transfer 38*, pages 481–493, 1994. doi: 10.1016/0017-9310(94)00183-v.

[56] G. Kocamustafaogullari, W. D. Huang, and J. Razi. Measurement and modeling of average void fraction, bubble size and interfacial area. *Nuclear Engineering and Design*, 148(2-3):437–453, 1994. ISSN 00295493. doi: 10.1016/0029-5493(94)90124-4.

[57] E. Krepper, D. Lucas, and H.-M. Prasser. On the modelling of bubbly flow in vertical pipes. *Nuclear Engineering and Design 235*, (5):597–611, 2005. doi: https://doi.org/10.1016/j.nucengdes.2004.09.006.

[58] E. Krepper, D. Lucas, T. Frank, H.-M. Prasser, and P. J. Zwart. The inhomogeneous musig model for the simulation of polydispersed flows. *Nuclear Engineering and Design*, 238(7):1690–1702, 2008. ISSN 0029-5493. doi: https://doi.org/10.1016/j.nucengdes.2008.01.004.

[59] E. Krepper, M. Beyer, T. Frank, D. Lucas, and H. M. Prasser. Cfd modelling of polydispersed bubbly two-phase flow around an obstacle. *Nuclear Engineering and Design*, 239(11):2372–2381, 2009. ISSN 00295493. doi: 10.1016/j.nucengdes.2009.06.015.

[60] E. K. Kuidjo. Towards a predictive model to reproduce flow regime transitions in gas-liquid flows with neptune_cfd: from a dispersed to a separated regime. *PhD dissertation.Université d'Aix en Provence*, 2019.

[61] R. T. Lahey and D. A. Drew. The analysis of two-phase flow and heat transfer using a multidimensional, four field, two-fluid model. *Nuclear Engineering and Design*, 204(1-3):29–44, feb 2001. doi: 10.1016/s0029-5493(00)00337-x.

[62] M. Lance and J. Bataille. Turbulence in the liquid phase of a uniform bubbly air–water flow. *Journal of Fluid Mechanics*, 222:95–118, 1991. doi: 10.1017/S0022112091001015.

[63] Y. Lau, I. Roghair, N. Deen, M. van Sint Annaland, and J. Kuipers. Numerical investigation of the drag closure for bubbles in bubble swarms. *Chemical Engineering Science*, 66 (14):3309–3316, jul 2011. doi: 10.1016/j.ces.2011.01.053.

[64] J. Lavieville, N. Merigoux, M. Guingo, C. Baudry, and S. Mimouni. A generalized turbulent dispersion model for bubbly flow numerical simulation in neptune cfd. *NURETH 16*, pages 4167–4181, 2015. doi: 10.1016/j.nucengdes.2016.11.003.

[65] J. Lee and H. Park. Bubble dynamics and bubble-induced agitation in the homogeneous bubble-swarm past a circular cylinder at small to moderate void fractions. *Physical Review Fluids*, 5(5):054304, may 2020. doi: 10.1103/physrevfluids.5.054304.

[66] K.-H. Lee, H.-S. Kang, D.-H. Hong, and J.-I. Kim. Fluidelastic instability of a curved tube array in single phase cross flow. *Nuclear Engineering and Technology*, 55(3):1118–1124, mar 2023. doi: 10.1016/j.net.2022.11.007.

[67] D. LEGENDRE and J. MAGNAUDET. The lift force on a spherical bubble in a viscous linear shear flow. *Journal of Fluid Mechanics*, 368:81–126, aug 1998. doi: 10.1017/s0022112098001621.

[68] D. Legendre, C. Colin, and T. Coquard. Lift, drag and added mass of a hemispherical bubble sliding and growing on a wall in a viscous linear shear flow. *Philosophical Transactions of the Royal Society A: Mathematical, Physical and Engineering Sciences*, 366(1873): 2233–2248, mar 2008. doi: 10.1098/rsta.2008.0009.

[69] Y. Liao, D. Lucas, E. Krepper, and M. Schmidtke. Development of a generalized coalescence and breakup closure for the inhomogeneous musig model. *Nuclear Engineering and Design*, 241(4):1024–1033, 2011. ISSN 00295493. doi: 10.1016/j.nucengdes.2010.04.025. URL http://dx.doi.org/10.1016/j.nucengdes.2010.04.025.

[70] S. Liu, L. Liu, H. Gu, and K. Wang. Experimental study of gas-liquid flow patterns and void fraction in prototype 5 x 5 rod bundle channel using wire-mesh sensor. *Annals of Nuclear Energy*, 171:109022, 2022. ISSN 0306-4549. doi: https://doi.org/10.1016/j.anucene.2022.109022. URL https://www.sciencedirect.com/science/article/pii/S0306454922000573.

[71] N. Lubchenko, B. Magolan, R. Sugrue, and E. Baglietto. A more fundamental wall lubrication force from turbulent dispersion regularization for multiphase cfd applications. *International Journal of Multiphase Flow*, 98:36–44, jan 2018. doi: 10.1016/j.ijmultiphaseflow.2017.09.003.

[72] D. Lucas, E. Krepper, R. Rzehak, Y. Liao, T. Ma, and T. Ziegenhein. Status and challenges of cfd-modelling for poly-disperse bubbly flows. *NURETH-16*, pages 1980–1991, 2015.

[73] R. T. L. J. M. LOPEZ DE BERTODANO and O. C. JONES. Phase distributionin bubbly two-phasein vertical ducts. 1994.

[74] T. Ma, D. Lucas, S. Jakirlic, and J. Fröhlich. Progress in the second-moment closure for bubbly flow based on direct numerical simulation data. *Journal of Fluid Mechanics*, 883: A9, 2020. doi: 10.1017/jfm.2019.851.

[75] B. Magolan and E. Baglietto. Assembling a bubble-induced turbulence model incorporating physical understanding from dns. *International Journal of Multiphase Flow*, 116: 185–202, jul 2019. doi: 10.1016/j.ijmultiphaseflow.2019.04.009.

[76] H. B. Mahood, A. N. Campbell, R. B. Thorpe, and A. O. Sharif. A new model for the drag coefficient of a swarm of condensing vapour–liquid bubbles in a third immiscible liquid phase. *Chemical Engineering Science*, 131:76–83, 2015. ISSN 0009-2509. doi: https://doi.org/10.1016/j.ces.2015.03.053. URL `https://www.sciencedirect.com/science/article/pii/S0009250915002341`.

[77] R. Manceau. Recent progress in the development of the elliptic blending reynolds-stress model. *International Journal of Heat and Fluid Flow 51*, pages 195–220, 2015. doi: 10.1016/j.ijheatfluidflow.2014.09.002.

[78] R. Manceau and K. Hanjalić. Elliptic blending model: A new near-wall reynolds-stress turbulence closure. *Physics of Fluids 14*, pages 744–754, 2002. doi: 10.1063/1.1432693.

[79] K. Mao and T. Hibiki. Flow regime transition criteria for upward two-phase cross-flow in horizontal tube bundles. *Applied Thermal Engineering*, 112:1533–1546, 2017. doi: 10.1016/j.applthermaleng.2016.10.182.

[80] D. L. Marchisio and R. O. Fox. *Computational Models for Polydisperse Particulate and Multiphase Systems*. Cambridge University Press, mar 2013. doi: 10.1017/cbo9781139016599.

[81] O. Marfaing, M. Guingo, J. Lavieville, S. Mimouni, E. Baglietto, and al. Comparison and uncertainty quantification of two-fluid models forbubbly flows with neptune_cfd and starccm+. *Nuclear Engineering and Design*, 337:1–16, 2018. doi: 10.1016/j.nucengdes.2018.05.028.

[82] A. Mathur, D. Dovizio, E. Frederix, and E. Komen. A hybrid dispersed-large interface solver for multi-scale two-phase flow modelling. *Nuclear Engineering and Design*, 344:69–82, apr 2019. doi: 10.1016/j.nucengdes.2019.01.020.

[83] R. A. M.G. Rodio, E. Kuidjo and P. Sagaut. Beyond bubbly two-phase flow investigation using a cfd three-field two-fluid model. *Submitted to International Journal of Multiphase Flow*, 2022.

[84] M.Ishii and N.Zuber. Drag coefficient and relative velocity in bubbly, droplet or particulate flows. *AIChE J. 25*, pages 843–855, 1979. doi: 10.1002/aic.690250513.

[85] M.Ishii and T.Hibiki. *Thermo-Fluid Dynamics of Two-Phase Flow*. Springer, 2011, Second Edition.

[86] C. Morel. Modeling approaches for strongly non-homogeneous two-phase flows. *Nuclear Engineering and Design*, 237(11):1107–1127, jun 2007. doi: 10.1016/j.nucengdes.2007.01.005.

[87] C. Morel, P. Ruyer, N. Seiler, and J. M. Lavieville. Comparison of several models for multi-size bubbly flows on an adiabatic experiment. *International Journal of Multiphase Flow*, 36(1):25–39, 2010. ISSN 03019322. doi: 10.1016/j.ijmultiphaseflow.2009.09.003. URL `http://dx.doi.org/10.1016/j.ijmultiphaseflow.2009.09.003`.

[88] R. V. Mukin. Modeling of bubble coalescence and break-up in turbulent bubbly flow. *International Journal of Multiphase Flow*, 62:52–66, 2014. ISSN 03019322. doi: 10.1016/j.ijmultiphaseflow.2014.02.008. URL `http://dx.doi.org/10.1016/j.ijmultiphaseflow.2014.02.008`.

[89] H. Murakawa, M. Baba, T. Miyazaki, K. Sugimoto, H. Asano, and D. Ito. Local void fraction and heat transfer characteristics around tubes in two-phase flows across horizontal in-line and staggered tube bundles. *Nuclear Engineering and Design*, 334:66–74, aug 2018. doi: 10.1016/j.nucengdes.2018.05.005.

[90] N.Zuber. On the dispersed two-phase flow in the laminar flow regime. *Chem. Engng Sci. 19*, pages 897–917, 1964. doi: 10.1016/0009-2509(64)85067-3.

[91] B. Ozar, A. Dixit, S. W. Chen, T. Hibiki, and M. Ishii. Interfacial area concentration in gas-liquid bubbly to churn-turbulent flow regime. *International Journal of Heat and Fluid Flow*, 38(2012):168–179, 2012. ISSN 0142727X. doi: 10.1016/j.ijheatfluidflow.2012.08.006. URL `http://dx.doi.org/10.1016/j.ijheatfluidflow.2012.08.006`.

[92] B. Ozar, C. Brooks, D. Euh, T. Hibiki, and M. Ishii. Investigation of one-dimensional interfacial area transport for vertical upward air–water two-phase flow in an annular channel at elevated pressures. *Nuclear Engineering and Design*, 263:362–379, 2013. ISSN 0029-5493. doi: https://doi.org/10.1016/j.nucengdes.2013.05.018. URL `https://www.sciencedirect.com/science/article/pii/S0029549313002811`.

[93] M. Paidoussis. Real-life experiences with flow-induced vibration. 2006. doi: doi:10.1016/j.jfluidstructs.2006.04.002.

[94] S. Pascal-Ribot and Y. Blanchet. Buffeting lift forces and local air water flow aspects around a rigid cylinder. *International Journal of Multiphase Flow*, 33(11):1237–1254, nov 2007. doi: 10.1016/j.ijmultiphaseflow.2007.05.007.

[95] P. Piteau, X. Delaune, J. Antunes, and L. Borsoi. Experiments and computations of a loosely supported tube in a rigid bundle subjected to single-phase flow. *Journal of Fluids and Structures*, 28:56–71, 2012. ISSN 0889-9746. doi: https://doi.org/10.1016/j.jfluidstructs.2011.08.007. URL `https://www.sciencedirect.com/science/article/pii/S0889974611001289`.

[96] D. Prabhudharwadkar, A. Vaidheeswaran, M. L. de Bertodano, J. Buchanan, and P. Guilbert. Two-fluid cfd simulations of cap bubble flow using the two-group interfacial area transport equations. *The Journal of Computational Multiphase Flows*, 4(4):363–374, 2012. doi: 10.1260/1757-482X.4.4.363. URL `https://doi.org/10.1260/1757-482X.4.4.363`.

[97] S. Rassame and T. Hibiki. Modeling of turbulent diffusion terms for one-dimensional interfacial area transport equation in vertical round channels. *Progress in Nuclear Energy*, 157:104568, mar 2023. doi: 10.1016/j.pnucene.2023.104568.

[98] F. Risso. Agitation, mixing, and transfers induced by bubbles. *Annual Review of Fluid Mechanics*, 50(1):25–48, jan 2018. doi: 10.1146/annurev-fluid-122316-045003.

[99] I. Roghair, M. V. S. Annaland, and H. J. A. M. Kuipers. Drag force and clustering in bubble swarms. *AIChE Journal*, 59(5):1791–1800, nov 2012. doi: 10.1002/aic.13949.

[100] P. Ruyer and N. Seiler. Modelisation avancee de la polydispersion en taille des ecoulements bouillants. *La Houille Blanche*, 95(4):65–71, aug 2009. doi: 10.1051/lhb/2009046.

[101] R. Rzehak and E. Krepper. Bubble-induced turbulence: Comparison of cfd models. *Nuclear Engineering and Design*, 258:57–65, 2013. doi: 10.1016/j.nucengdes.2013.02.008.

[102] A. D. Santis, M. Colombo, B. Hanson, and M. Fairweather. A generalized multiphase modelling approach for multiscale flows. *Journal of Computational Physics*, 436:110321, jul 2021. doi: 10.1016/j.jcp.2021.110321.

[103] S. Sari, S. Ergun, M. Barik, C. Kocar, and C. N. Sokmen. Modeling of isothermal bubbly flow with interfacial area transport equation and bubble number density approach. *Annals of Nuclear Energy*, 36(2):222–232, 2009. ISSN 03064549. doi: 10.1016/j.anucene.2008.11.016.

[104] J. Schlegel and T. Hibiki. A correlation for interfacial area concentration in high void fraction flows in large diameter channels. *Chemical Engineering Science*, 131:172–186, jul 2015. doi: 10.1016/j.ces.2015.04.004.

[105] J. Schlegel, P. Sawant, S. Paranjape, B. Ozar, T. Hibiki, and M. Ishii. Void fraction and flow regime in adiabatic upward two-phase flow in large diameter pipes. *Nuclear Engineering and Design 238*, pages 2864–2874, 2009.

[106] J. Schlegel, S. Sharma, R. Cuenca, T. Hibiki, and M. Ishii. Local flow structure beyond bubbly flow in large diameter channels. *International Journal of Heat and Fluid Flow*, 47: 42–56, jun 2014. doi: 10.1016/j.ijheatfluidflow.2014.03.001.

[107] J. Schlegel, T. Hibiki, and M. Ishii. Two-group modeling of interfacial area transport in large diameter channels. *Nuclear Engineering and Design 293*, pages 75–86, 2015. doi: https://doi.org/10.1016/j.nucengdes.2015.07.011.

[108] S. L. Sharma, T. Hibiki, M. Ishii, C. S. Brooks, J. P. Schlegel, Y. Liu, and J. R. Buchanan. Turbulence-induced bubble collision force modeling and validation in adiabatic two-phase flow using cfd. *Nuclear Engineering and Design*, 312:399–409, 2017. doi: 10.1016/j.nucengdes.2016.05.006. 16th International Topical Meeting on Nuclear Reactor Thermal Hydraulics.

[109] S. L. Sharma, M. Ishii, T. Hibiki, J. P. Schlegel, Y. Liu, and J. R. Buchanan. Beyond bubbly two-phase flow investigation using a cfd three-field two-fluid model. *International Journal of Multiphase Flow*, 113:1–15, 2019. doi: https://doi.org/10.1016/j.ijmultiphaseflow.2018.12.010.

[110] M. Shawkat, C. Ching, and M. Shoukri. On the liquid turbulence energy spectra in two-phase bubbly flow in a large diameter vertical pipe. *International Journal of Multiphase Flow*, 33(3):300–316, 2007. doi: https://doi.org/10.1016/j.ijmultiphaseflow.2006.09.002.

[111] M. Shawkat, C. Ching, and M. Shoukri. Bubble and liquid turbulence characteristics of bubbly flow in a large diameter vertical pipe. *International Journal of Multiphase Flow*, 34(8):767–785, 2008. doi: https://doi.org/10.1016/j.ijmultiphaseflow.2008.01.007.

[112] X. Shen and T. Hibiki. One-group interfacial area transport equation and its sink and source terms in narrow rectangular channel. *International Journal of Heat and Fluid Flow*, 44(2013):312–326, 2013. ISSN 0142727X. doi: 10.1016/j.ijheatfluidflow.2013.06.010. URL `http://dx.doi.org/10.1016/j.ijheatfluidflow.2013.06.010`.

[113] X. Shen and T. Hibiki. Interfacial area concentration in gas–liquid bubbly to churn flow regimes in large diameter pipes. *International Journal of Heat and Fluid Flow 54*, pages 107–118, 2015. doi: https://doi.org/10.1016/j.ijheatfluidflow.2015.05.002.

[114] X. Shen and T. Hibiki. Bubble coalescence and breakup model evaluation and development for two-phase bubbly flows. *International Journal of Multiphase Flow*, 109:131–149, 2018. ISSN 0301-9322. doi: https://doi.org/10.1016/j.ijmultiphaseflow.2018.07.008. URL `https://www.sciencedirect.com/science/article/pii/S0301932218302040`.

[115] X. Shen, Y. Saito, K. Mishima, and H.Nakamura. A study on the characteristics of upward air–water two-phase flow in a large diameter pipe. *Experimental Thermal and Fluid Science 31*, pages 21–36, 2006. doi: 10.1016/j.expthermflusci.2006.01.007.

[116] S. Shi, D. Wang, Y. Qian, X. Sun, Y. Liu, and A. Tentner. Liquid-phase turbulence measurements in air-water two-phase flows using particle image velocimetry. *Progress in Nuclear Energy*, 124:103334, jun 2020. doi: 10.1016/j.pnucene.2020.103334.

[117] M. Simcik, M. Puncochar, and M. C. Ruzicka. Added mass of a spherical cap body. *Chemical Engineering Science*, 118:1–8, oct 2014. doi: 10.1016/j.ces.2014.07.015.

[118] O. Simonin, E. Deutsch, and J. P. Minier. Eulerian prediction of the fluid/particle correlated motion in turbulent two-phase flows. *Applied Scientific Research*, 51(1-2):275–283, jun 1993. doi: 10.1007/bf01082549.

[119] S.Mimouni, M.Boucker, J.Lavieville, A.Guelfi, and D.Bestion. Modelling and computation of cavitation and boiling bubbly flows with the neptune_cfd code. *Nuclear engineering and Design 238*, pages 680–692, 2008. doi: 10.1016/j.nucengdes.2007.02.052.

[120] T. Smith, J. Schlegel, T. Hibiki, and M. Ishii. Mechanistic modeling of interfacial area transport in large diameter pipes. *International Journal of Multiphase Flow*, 47:1–16, 2012. doi: 10.1016/j.ijmultiphaseflow.2012.06.009.

[121] T. Smith, J. Schlegel, T. Hibiki, and M. Ishii. Two-phase flow structure in large diameter pipes. *International journal of Heat and Fluid Flows 33*, pages 156–167, 2012. doi: 10.1016/j.ijheatfluidflow.2011.10.008.

[122] H. Sun, T. Kunugi, X. Shen, D. Wu, and H. Nakamura. Upward air–water bubbly flow characteristics in a vertical square duct. *Journal of Nuclear Science and Technology 51:3*, pages 267–281, 2014.

[123] X. Sun, M. Ishii, and J. M. Kelly. Modified two-fluid model for the two-group interfacial area transport equation. *Annals of Nuclear Energy*, 30(16):1601–1622, 2003. doi: 10.1016/s0306-4549(03)00150-6.

[124] X. Sun, S. Kim, M. Ishii, and S. Beus. Modeling of bubble coalescence and disintegration in confined upward two-phase flow. *Nuclear Engineering and Design*, 230(1):3–26, 2004. doi: 10.1016/j.nucengdes.2003.10.008. 11th International Conference on Nuclear Energy.

[125] X. Sun, S. Kim, M. Ishii, and S. G. Beus. Model evaluation of two-group interfacial area transport equation for confined upward flow. *Nuclear Engineering and Design*, 230(1-3):27–47, 2004. ISSN 00295493. doi: 10.1016/j.nucengdes.2003.10.014.

[126] X. Sun, S.Kim, L.Cheng, M. Ishii, and S. Beus. Interfacial structures in confined cap-turbulent and churn-turbulent flows. *International Journal of Heat and Fluid Flow*, 25(1):44–57, 2004. doi: 10.1016/j.ijheatfluidflow.2003.08.001.

[127] S. Tas-Koehler, M. Neumann-Kipping, Y. Liao, E. Krepper, and U. Hampel. Cfd simulation of bubbly flow around an obstacle in a vertical pipe with a focus on breakup and

coalescence modelling. *International Journal of Multiphase Flow*, 135:103528, 2021. ISSN 0301-9322. doi: https://doi.org/10.1016/j.ijmultiphaseflow.2020.103528.

[128] S. TEAM. Salome 8.5.0. https://www.salome-platform.org/, 2021.

[129] T.Hibiki and M.Ishii. One-dimensional drift-flux model for two-phase flow in a large diameter pipe. *International Journal of Heat and Mass Transfer 46*, pages 1773–1790, 2003.

[130] T.Marcel. Simulation numérique et modélisation de la turbulence statistique et hybride dans un écoulement de faisceau de tubes à nombre de reynolds élevé dans le contexte de l'interaction fluide-structure. *PhD Thesis. Université de Toulouse*, 2011.

[131] A. Tomiyama. Struggle with computational bubble dynamics. *Multiphase Sci. Tech.*, pages 369–405, 1998.

[132] A. TOMIYAMA, I. KATAOKA, I. ZUN, and T. SAKAGUCHI. Drag coefficients of single bubbles under normal and micro gravity conditions. *JSME International Journal Series B*, 41(2):472–479, 1998. doi: 10.1299/jsmeb.41.472.

[133] A. Tomiyama, H. Tamai, I. Zun, and S. Hosokawa. Transverse migration of single bubbles in simple shear flows. *Chem. Eng. Sci. 57*, pages 1849–1858, 2002. doi: 10.1016/s0009-2509(02)00085-4.

[134] T.R.Auton, J. Hunt, and M.Prud'Homme. The force exerted on a body in inviscid unsteady non-uniform rotational flow. *J. Fluid Mech. 197*, pages 241–257, 1988. doi: 10.1017/s0022112088003246.

[135] G. Tryggvason, R. Scardovelli, and S. Zaleski. *Direct numerical simulations of gas-liquid multiphase flows.* Cambridge University Press, 2011.

[136] R. Ulbrich and D. Mewes. Vertical, upward gas-liquid two-phase flow across a tube bundle. *International Journal of Multiphase Flow*, 20(2):249–272, 1994. doi: 10.1016/0301-9322(94)90081-7.

[137] B. M. Waite, H.-M. Prasser, and M. Z. Podowski. Computational and experimental analysis of gas/liquid two-phase flow in rod bundles with mixing-vane spacer grids. *Nuclear Engineering and Design*, 360:110499, 2020. ISSN 0029-5493. doi: https://doi.org/10.1016/j.nucengdes.2019.110499. URL `https://www.sciencedirect.com/science/article/pii/S0029549319305308`.

[138] G. Wang, P. Sawant, and M. Ishii. A new entrainment rate model for annular two-phase flow. *International Journal of Multiphase Flow*, 124:103185, 2020. ISSN 0301-9322. doi: https://doi.org/10.1016/j.ijmultiphaseflow.2019.103185. URL `https://www.sciencedirect.com/science/article/pii/S0301932219303994`.

[139] T. Wang, J. Wang, and Y. Jin. Theoretical prediction of flow regime transition in bubble columns by the population balance model. *Chemical Engineering Science*, 60(22):6199–6209, 2005. ISSN 00092509. doi: 10.1016/j.ces.2005.04.027.

[140] X. Wang and X. Sun. Three-dimensional simulations of air–water bubbly flows. *International Journal of Multiphase Flow*, 36(11):882–890, 2010. doi: https://doi.org/10.1016/j.ijmultiphaseflow.2010.08.004.

[141] X. Wang and X. Sun. Numerical simulations of air–water cap-bubbly flows using two-group interfacial area transport equation. *Annals of Nuclear Energy*, 71:399–410, 2014. doi: https://doi.org/10.1016/j.anucene.2014.04.026.

[142] W.Benguigui. Numerical simulation of two-phase flow induced vibration. *PhD dissertation. Universite Paris-Saclay*, 2018.

[143] Q. Wu, S. Kim, and M. Ishii. One-group interfacial area transport in vertical bubbly flow. *Int. J. Heat Mass Transfer.*, 41(8-9):1103–1112, 1998. ISSN 00179310. doi: 10.1016/S0017-9310(97)00167-1.

[144] G. Xu, C. Tso, and K. Tou. Hydrodynamics of two-phase flow in vertical up and down-flow across a horizontal tube bundle. 1998.

[145] X.Wang and X.Sun. Simulations of two-phase flows using interfacial area transport equation. *Graduate Program Dissertation. Ohio State University*, 2010.

[146] X. Yang, J. Schlegel, Y. Liu, S. Paranjape, T. Hibiki, and M. Ishii. Experimental study of interfacial area transport in air–water two phase flow in a scaled 8 x 8 bwr rod bundle. *International Journal of Multiphase Flow*, 50:16–32, 2013. ISSN 0301-9322. doi: https://doi.org/10.1016/j.ijmultiphaseflow.2012.10.006. URL `https://www.sciencedirect.com/science/article/pii/S0301932212001498`.

[147] X. Yang, J. Schlegel, Y. Liu, S. Paranjape, T. Hibiki, M. Ishii, S. Bajorek, and A. Ireland. Prediction of interfacial area transport in a scaled 8x8 bwr rod bundle. *Nuclear Engineering and Design*, 310:638–647, 2016. ISSN 0029-5493. doi: https://doi.org/10.1016/j.nucengdes.2016.10.037. URL `https://www.sciencedirect.com/science/article/pii/S0029549316304149`.

[148] G. H. YEOH and J. TU. *COMPUTATIONAL TECHNIQUES FOR MULTIPHASE FLOWS*. Butterworth-Heinemann, SECOND EDITION,2019.

[149] G. H. Yeoh, S. C. P. Cheung, and J. Y. Tu. On the prediction of the phase distribution of bubbly flow in a horizontal pipe. *Chemical Engineering Research and Design*, 90(1):40–51, 2012. ISSN 02638762. doi: 10.1016/j.cherd.2011.08.004.

[150] G. H. Yeoh, C. P. Cheung, and J. Tu. *Multiphase Flow Analysis Using Population Balance Modeling: Bubbles, Drops and Particles.* Butterworth-Heinemann, 2014, First Edition.

[151] Y.Liao and T.Ma. Study on bubble-induced turbulence in pipes and containers with reynolds-stress models. *Exp. Comput. Multiph. Flow 4*, page 121–132, 2022. doi: 10.1007/s42757-021-0128-0.

[152] H. Yoshida, A. Ohnuki, T. Misawa, K. Takase, and H. Akimoto. Development of analytical procedures of two-phase flow in tight-lattice fuel bundles for innovative water reactor for flexible fuel cycle. *Nuclear Technology*, 164(1):45–54, oct 2008. doi: 10.13182/nt08-a4007.

[153] H. Zhang, Y. Xiao, H. Gu, and D. Liu. Study on bubbly and cap-bubbly flow in a square channel using dual wire-mesh sensors. *International Journal of Multiphase Flow*, 133:103461, dec 2020. doi: 10.1016/j.ijmultiphaseflow.2020.103461.

[154] X. Zhou, X. Sun, and Y. Liu. Liquid-phase turbulence measurements in air-water two-phase flows over a wide range of void fractions. *Nuclear Engineering and Design*, 310:534–543, dec 2016. doi: 10.1016/j.nucengdes.2016.10.048.

[155] T. Ziegenhein and D. Lucas. Observations on bubble shapes in bubble columns under different flow conditions. *Experimental Thermal and Fluid Science*, 85:248–256, jul 2017. doi: 10.1016/j.expthermflusci.2017.03.009.

ECOLE
DOCTORALE

Titre : Etudes numériques et expérimentales des écoulements diphasiques en intéraction avec un faisceau de tubes

Mots clés : écoulement diphasique, approche multi-champ, faisceau de tubes, simulation numérique, couplage de modèles, interaction fluide-structure.

Résumé : Les générateurs de vapeur (GV) des centrales nucléaires sont composés de faisceaux de tubes soumis à des écoulements diphasiques eau-vapeur. Les vibrations liées à cette interaction peuvent induire des dommages (fatigue et usure par frottement et chocs) pouvant entraîner de graves conséquences pour la sûreté nucléaire. Dans le cadre de la prévention des risques vibratoires des tubes de GV des études expérimentales sont réalisées à l'aide de faisceaux analytiques de tubes droits soumis à un écoulement transverse diphasique. En parallèle, il est également important de développer un outil de simulation numérique permettant d'accéder à des données et des informations difficilement mesurables. L'objectif de cette thèse est donc de simuler l'interaction entre un fluide diphasique et une structure rigide (tube unique ou faisceau de tubes), à l'aide du code NEPTUNE_CFD. Ces simulations doivent permettre de reproduire le chargement mécanique exercé par le fluide sur les tubes. La modélisation employée dans cette thèse repose sur un modèle à deux-fluides - trois-champs, comprenant un champ liquide continu, un champ de gaz dispersé, composé de bulles peu déformées, et un champ hybride dispersé-continu pour tenir compte des bulles très déformées et des poches de gaz. La première partie de ce travail s'est concentrée sur la validation du couplage diphasique-turbulence liquide ainsi que sur la modification et l'adaptation de la modélisation pour mieux prendre en compte la présence d'une structure immergée. De nouvelles modélisations pour la force de dispersion turbulente, les termes sources de coalescence et fragmentation, la masse ajoutée et le critère d'activation du champ continu ont été proposées. Dans la deuxième partie de ce travail, nous avons simulé l'écoulement diphasique autour d'un tube unique fixe, afin d'en extraire une physique sous-jacente et d'identifier ses limites et lacunes. Enfin, dans la dernière partie de ce travail, nous avons simulé l'interaction d'un écoulement diphasique avec un faisceau de tubes rigides. Les résultats numériques ont été comparés aux mesures expérimentales. Cette approche nous a permis de justifier l'intérêt de notre modélisation, de trouver des similitudes entre les résultats numériques et expérimentaux, tout en proposant des pistes d'amélioration.

Title : Numerical and experimental studies of two-phase flows interacting with a bundle of tubes

Keywords : Two-phase flow, multi-field approach, bundle of tubes, numerical simulation, model coupling, fluid-structure interaction.

Abstract : The steam generators (SG) in nuclear power plants are made up of bundles of tubes subjected to two-phase water-steam flows. Vibrations related to this interaction can cause damage (fatigue, wear due to friction and shocks) that can lead to serious consequences for nuclear safety. In the context of preventing vibrational risks in SG tubes, experimental studies are conducted using analytical bundles of straight tubes subjected to transverse two-phase flow. In parallel, it is also important to develop a numerical simulation tool to access data and information that are difficult to measure. The goal of this work is to simulate the interaction between a two-phase fluid and a rigid structure (single tube or bundle of tubes) using the NEPTUNE_CFD code. These simulations aim to reproduce the mechanical loading exerted by the fluid on the tubes. The modeling used in this work is based on a two-fluid - three-field model, including a continuous liquid field, a dispersed gas field made up of slightly deformed bubbles, and a dispersed-continuous hybrid field to account for highly deformed bubbles and gas pockets. The first part of this work focused on the validation of the two-phase liquid-turbulence coupling as well as the modification and adaptation of the modeling to better account for the presence of an immersed structure. New models for turbulent dispersion force, source terms of coalescence and break-up, added mass, and the activation criterion of the continuous field were proposed. In the second part of this work, we simulated the two-phase flow around a fixed single tube to extract underlying physics, and identify its limitations and shortcomings. Finally, in the last part of this work, we simulated the interaction of a two-phase flow with a bundle of rigid tubes. The numerical results were compared to experimental measurements. This approach allowed us to justify the relevance of our modeling, find similarities between numerical and experimental results, while also suggesting areas for improvement.

Institut Polytechnique de Paris
91120 Palaiseau, France